Titre: Title:	Synthesized Waveguide Technology for Ultra-Broadband Signal Transmission
Auteur: Author:	Desong Wang
Date:	2021
Type:	Mémoire ou thèse / Dissertation or Thesis
Référence: Citation:	Wang, D. (2021). Synthesized Waveguide Technology for Ultra-Broadband Signal Transmission [Thèse de doctorat, Polytechnique Montréal]. PolyPublie. https://publications.polymtl.ca/9920/

POLYTECHNIQUE MONTRÉAL

affiliée à l'Université de Montréal

Synthesized waveguide technology for ultra-broadband signal transmission

DESONG WANG

Département de génie électrique

Thèse présentée en vue de l'obtention du diplôme de *Philosophiæ Doctor*

Génie électrique

Décembre 2021

POLYTECHNIQUE MONTRÉAL

affiliée à l'Université de Montréal

Cette thèse intitulée :

Synthesized waveguide technology for ultra-broadband signal transmission

présentée par **Desong WANG**

en vue de l'obtention du diplôme de *Philosophiæ Doctor*

a été dûment acceptée par le jury d'examen constitué de :

Raman KASHYAP, président
Ke WU, membre et directeur de recherche
Serioja Ovidiu TATU, membre
Yahia ANTAR, membre externe

DEDICATION

To my wife and my parents

ACKNOWLEDGEMENTS

I am deeply grateful to my supervisor Prof. Ke Wu for his inspirational guidance, constant encouragement, and supreme confidence especially when our work was being questioned. I would like to thank him for offering me the opportunity to pursue my Ph.D. study in his research group, and for recommending me the industrial internship at Huawei Ottawa R&D Centre, Canada, and the academic exchange at the University of Duisburg-Essen, Germany.

I wish to acknowledge with special thanks to the technical and administrative team at Poly-Grames Research Center, especially Jules Gauthier, Traian Antonescu, and Steve Dube for their wonderful work on the circuit fabrications, Louis-Philippe Carignan, David Dousset, and Maxime Thibault for their support on the measurements. My gratitude extends to Rachel Lortie and Jean-Sebastien Décarie for their help on IT, financial, and administrative issues.

I appreciate Prof. Raman Kashyap, Prof. Serioja Ovidiu Tatu, and Prof. Yahia Antar serving as jury members of my Ph.D. examination committee and reviewing this thesis.

I would like to take this opportunity to thank the following colleagues for valuable academic discussions and suggestions: Faezeh Fesharaki, Dongze Zheng, Yue-Long Lyu, Amirhossein Askarian, Ben You, Mohammad Reza Rahimi, Ping Zhao, Wentao Lin, Pascal Burasa, Chunmei Liu, Chao Li, Intikhab Hussain, Muhib Ur Rahman, and Kang Zhou. I would also like to thank Yifan Yin, Xiaoqiang Gu, Srinaga Nikhil Nallandhigal, Kai Wang, Fang Zhu, Long Zhang, Lei Guo, Amir Afshani, Luzhou Chen, Wencui Zhu, Jiming Li, Omar Masood Khan, Nhu Huan Nguyen, Marko Zivanovic, Tongfeng Guo, Jiapin Guo, Yangping Zhao, Kuangda Wang, Xiaoyi Wang, Lianfeng Zou, and Qingtao Chen for building together a pleasant and active research environment. I extend my thanks to the visiting scholars and students: Xiaoxiong Song, Hao Chen, Yuanwei Tong, Wenwen Yang, Peng Chu, Gaoming Xu, Yunlong Lu, Jun Xu, Yihong Su, Yunjie Geng, and Bengeng Cai, who made my stay at Polytechnique Montreal memorable.

I am grateful to my parents, sister, and parents-in-law for their support, understanding, and endless love. Finally yet importantly, I would like to express my deepest love and thanks to my wife Yingying Tian who has accompanied me through the highs and lows of the past 14 years. Without her support and encouragement, I would not achieve what I have today.

RÉSUMÉ

Les signaux électromagnétiques à très large bande (dc-à-ondes millimétriques ou dc-à-térahertz) sont essentiels pour de nombreuses applications telles que l'imagerie, la détection, la sécurité, les communications à haute capacité, les interconnexions à grande vitesse, les mesures dans le domaine temporel et les traitements biologiques avancés. Ceci a suscité un intérêt et une attention particulière concernant le problème technique fondamental, à savoir la transmission de signaux ultra-large bande [au niveau de la picoseconde (ps)] avec une intégrité du signal très élevée, ce qui nécessite une structure de guide d'ondes assez particulière à très faibles pertes, faible dispersion, et avec une transmission qui laisse tout passer (tout-passe). A notre connaissance, ce type de support de transmission n'existe pas encore du moins en pratique ; tous les supports conventionnels souffrent généralement des effets indésirables tels que des pertes et/ou de la dispersion liées à la coupure basse fréquence (passe-haut) et/ou à l'atténuation haute fréquence (passe-bas), sans oublier de mentionner la bande passante monomode habituellement limitée avec référence aux modes d'ordre supérieur. Bien que des efforts importants aient été faits pour explorer des supports de transmission à haute performance au cours des dernières décennies, ils sont souvent des améliorations incrémentales des structures conventionnelles. Afin de remédier et ainsi apporter une contribution à cette situation, le concept de ligne de transmission sélective de mode (MSTL) a récemment été proposé. Elle fonctionne sélectivement dans un mode dominant souhaité à différentes fréquences ou sur différentes gammes de fréquences (la sélectivité de mode dépendante de la fréquence). Cette propriété unique offre à MSTL la possibilité de guider efficacement les ondes électromagnétiques ultra-large-bandes avec les propriétés de transmission souhaitées. MSTL peut être considéré comme un système de transmission synthétisé en mode couplé qui diffère largement des lignes de transmission et des guides d'ondes conventionnels. Inspirée par ce concept MSTL, cette recherche vise à étudier et développer des systèmes de guide d'ondes synthétisés pour l'électronique ultrarapide du futur.

Cette recherche débute par un traitement des guides d'ondes intégrés au substrat (SIW) demi-mondes couplés. En tant que système de guide d'ondes simple, son comportement modal est d'abord examiné, et ensuite ses applications pratiques dans la conception de balun sont explorées. Une balun compact à large bande est présentée, fonctionnant à des fréquences micro-ondes et à ondes millimétriques avec des performances supérieures en termes de bande passante, de pertes, ainsi que

de déséquilibres d'amplitude et de phase. Cette étude fournit un concept intuitif utile pour comprendre les propriétés d'un système de transmission couplé. Ensuite, nous nous concentrons sur certaines propriétés de base de MSTL. La comparaison avec les structures conventionnelles montre que MSTL se distingue avec des différences substantielles dans les caractéristiques structurelles, le model comportemental, ainsi que dans la façon de guidage d'ondes. La sélectivité de mode de MSTL est traitée à l'aide de propriétés physiques identifiées (c'est-à-dire des distributions de champ en rapport avec le model comportemental). Dans la même optique, une analyse plus rigoureuse est effectuée en définissant et en formulant les fréquences caractéristiques par lesquelles la bande passante de fonctionnement de MSTL est divisée en plusieurs régions de fréquences distinctes, associées au mode dominant variable et dépendant de la fréquence. Ceci permet de prédire le comportement en rapport avec la sélectivité de mode de MSTL.

Une étude plus approfondie de MSTL est menée pour mieux comprendre le contexte théorique, le mécanisme physique et l'excitation. Le mécanisme physique du model comportemental dépendant de la fréquence est présenté avec des variations du model de champ. À cette fin, MSTL est traité comme un système à lignes couplées utilisant une analyse conjointe des modes normal et couplé, soutenue par la comparaison des champs approximatifs dérivés et des champs exacts extraits d'une simulation numérique rigoureuse. L'excitation MSTL est expliquée par comparaison avec un guide d'ondes coplanaire à conducteur soutenu (CBCPW). Pour produire une excitation de mode spécifique, une transition entre CBCPW et MSTL est ensuite proposée. Cette transition peut supporter une conversion efficace du mode CPW fixe de CBCPW au mode dominant dépendant de la fréquence de MSTL. De plus, il peut supprimer efficacement les modes d'ordre supérieur dans MSTL en limitant les couplages indésirables, procurant ainsi une pureté de mode sur une plage de fréquences ultra-large.

Pour démontrer davantage les potentiels des systèmes de transmission couplés, un autre guide d'ondes synthétisé est présenté. Il permet un guidage efficace et une bonne transmission des impulsions de signaux ultrarapides. Ce guide d'ondes a un mode propre dominant qui est entièrement remodelé d'un mode quasi-TEM CPW à un mode quasi-TE_{10} en rapport avec fréquence. En conséquence, la polarisation de l'onde tourne de 90° (de l'horizontal au vertical), et les pertes de transmission aux hautes fréquences diminuent, tandis que la dispersion du signal s'améliore. Pour démontrer la preuve de principe, deux de ces guides d'ondes sont développés et caractérisés

dans des gammes de fréquences ultra-larges allant du dc aux fréquences à ondes millimétriques (dc à 67 GHz) et aux fréquences térahertz (dc à 300 GHz).

Cette recherche montre que la technologie des guides d'ondes synthétisés présente de nombreux avantages en termes de bande passante, de perte de transmission et de dispersion de fréquence, offerts et assurés par le mode de fonctionnement à fréquence variable. Ce travail ouvre la voie à une transmission à faible perte et à faible dispersion pour les signaux ultra-large bande et ultrarapides, et pour de futures applications potentielles à large bande, hautes performance, haute densité et haute vitesse. Les systèmes de transmission synthétisés tels que MSTL pourraient devenir le pilier des futurs circuits, interconnections et systèmes électroniques ultrarapides. Cette recherche conduirait à une quantité importante de recherche dans les guides d'ondes synthétisés et les applications connexes.

ABSTRACT

Ultra-broadband (dc-to-millimeter-wave or dc-to-terahertz) electromagnetic signals are instrumental for many applications such as imaging, sensing, security scanning, high-capacity communications, high-speed interconnects, time-domain measurements, and advanced biological treatments. This fact has drawn extensive interest and attention to the underlying fundamental but critical issue, namely ultra-broadband ultrafast signal transmission with picosecond (ps)-level high signal integrity, which requires a waveguiding structure in support of low-loss, low-dispersion, and all-pass transmission. To our knowledge, this type of transmission medium does not exist in practice yet; all conventional ones generally suffer from the prohibited effects of loss and/or dispersion in connection with low-frequency cutoff (high-pass) and/or high-frequency attenuation (low-pass), needless to mention usually limited mono-mode bandwidth with reference to high-order modes. Although significant efforts have been made for exploring high-performance transmission media over the past decades, they are often concerned with incremental or limited improvements in conventional structures. To remedy this situation, the concept of mode-selective transmission line (MSTL) has recently been proposed, which is set to selectively operate in a desired dominant mode at different frequencies or over different frequency ranges, namely frequency-dependent mode selectivity. This unique property offers MSTL the possibility of efficiently guiding ultra-broadband electromagnetic waves with desired transmission properties. MSTL can be viewed as a synthesized coupled-mode transmission system that differs greatly from common transmission lines and waveguides. Inspired by this MSTL concept, this research aims to investigate and develop promising synthesized waveguiding systems for ultrafast electronics.

This research begins with a treatment of coupled half-mode substrate-integrated waveguides (SIWs). As a simple waveguiding system, its modal behavior is first examined, and its practical applications in balun design are then explored. A compact wideband balun is presented, operating at microwave and millimeter-wave frequencies with superior in-band performance in terms of bandwidth, loss, as well as amplitude and phase imbalances. This study provides a helpful intuitive concept for understanding the properties of a coupled transmission system. We then turn our attention to some basic properties of MSTL. Comparison with conventional structures shows that MSTL distinguishes itself by manifesting substantial differences in structural features, modal behavior, and wave guidance. The mode selectivity of MSTL is treated by means of identified

physical evidence (i.e., field distributions in connection with modal behavior). Following this thread, a more rigorous analysis is carried out by defining and formulating the characteristic frequencies by which the operating bandwidth of MSTL is divided into several distinct frequency regions associated with the frequency-related variable dominant mode. This helps quantify the mode-selectivity behavior of MSTL.

A more in-depth treatment of MSTL is conducted subsequently to reveal theoretical background, physical mechanism, and excitation scheme. The physical mechanism of the frequency-dependent modal behavior is presented with modal field variations. To this end, MSTL is treated as a coupled-line system using a joint normal- and coupled-mode analysis, supported by comparing the derived approximate fields and the exact fields extracted from rigorous numerical simulation. The MSTL excitation is explained by comparison with a conductor-backed coplanar waveguide (CBCPW). To produce a specific mode excitation, a tapered transition between CBCPW and MSTL is then proposed. This taper can support smooth evolution from the fixed CPW mode of CBCPW to the frequency-dependent dominant mode of MSTL. In addition, it can effectively suppress higher-order modes in MSTL by limiting undesired couplings, thus sustaining a mode purity over an ultra-broad frequency range.

To further demonstrate the potentials of coupled transmission systems, another synthesized waveguide is presented, which enables the efficient guidance and proper manipulation of ultrafast electrical pulses. This all-pass waveguide has a dominant eigenmode that is fully reshaped from a quasi-TEM CPW mode to a quasi-TE_{10} mode with frequency. As a result, the wave polarization rotates by 90° (from horizontality to verticality), and the transmission loss at high frequencies decreases anomalously, while the signal dispersion improves. To demonstrate the proof-of-principle, two such waveguides are developed and characterized for use in ultra-broad frequency ranges from dc to millimeter-wave (dc to 67 GHz) and to terahertz (dc to 300 GHz), respectively.

This research illustrates that synthesized waveguide technology has many advantages in terms of operating bandwidth, transmission loss, and frequency dispersion, which are offered and granted by the frequency-varying mode of operation. This work provides a path towards low-loss and low-dispersion transmission for ultra-broadband ultrafast signals and establishes the foundations for potential broadband applications toward high-performance, high-density, and high-speed operations. Synthesized transmission systems such as MSTL may become the backbone of future

ultrafast electric circuits, interconnects, and systems. This research would drive a significant amount of research in synthesized waveguides and related applications.

TABLE OF CONTENTS

LIST OF TABLES

LIST OF FIGURES

LIST OF SYMBOLS AND ABBREVIATIONS

2-D	Two-dimensional
5G	Fifth generation
ADS	Advanced Design System
CBCPW	Conductor-backed coplanar waveguide
CMOS	Complementary metal-oxide-semiconductor
CPW	Coplanar waveguide
dc	Direct current
DRW	Dielectric ribbon waveguide
DUT	Device under test
DW	Dielectric waveguide
EM	Electromagnetic
ENZ	ε-near-zero
FWHM	Full width at half maximum
GCPW	Grounded coplanar waveguide
GHz	Gigahertz
GSG	Ground-signal-ground
HBT	Heterojunction bipolar transistor
HFSS	High frequency structural simulator
HM-MSTL	Half-mode mode-selective transmission line
HMSIW	Half-mode substrate-integrated waveguide
ICT	Information and communications technology
IFFT	Inverse fast Fourier transform

LTCC	Low temperature co-fired ceramic
MHz	Megahertz
ML	Microstrip line
mmW	Millimeter-wave
MSTL	Mode-selective transmission line
PCB	Printed circuit board
PGL	Planar Goubau line
PHEMT	Pseudomorphic high-electron-mobility transistor
PPLWG	Parallel-plate ladder waveguide
PPWG	Parallel-plate waveguide
RWG	Rectangular waveguide
SEM	Scanning electron microscope
SIW	Substrate-integrated waveguide
SL	Stripline
SOLT	Short-open-load-through
SPP	Surface plasmon polariton
S-WG	Synthesized waveguide
TE	Transverse electric
TEM	Transverse electromagnetic
THz	Terahertz
TM	Transverse magnetic
TRL	Thru-reflect-line
VDI	Virginia Diodes Inc.
VPC	Valley photonic crystal

LIST OF APPENDICES

CHAPTER 1 INTRODUCTION

1.1 Research background

Fiber is widely used to transmit optical waves over a long distance, whereas metal wire is used for direct current (dc) transmission, both showing a lot of advantages including low cost, low loss, light weight, etc. In microwave, millimeter-wave (mmW), and terahertz (THz) frequency ranges, high-performance transmission media are instrumental in support of current and future applications in wireless communications, chip-to-chip interconnects, electro-optic modulators, detectors, etc. Many transmission media such as coaxial lines, metallic waveguides, dielectric waveguides, microstrip lines, and coplanar waveguides (CPWs) have been used for guiding electromagnetic (EM) waves. These transmission structures are the foundation for building analog and digital electronic and photonic circuits and systems, and are responsible for signal integrity of ultrafast signal transmissions (e.g., picosecond pulse transmission) and for broadband responses ranging from dc to THz.

Over the past decades, many research groups have participated in searching for high-performance transmission structures, which are often concerned with incremental or limited improvements in conventional transmission lines and waveguides. As we know, the two basic parameters of EM signals, namely transmission loss (or attenuation) and dispersion (e.g., group velocity stability), are critical to evaluate the performance of transmission structures. Although the performance of conventional transmission structures has been continually improved, they still suffer from high transmission loss and/or high dispersion, especially in high-frequency ranges. The conventional transmission lines and waveguides are still unable to meet the stringent requirements for high-quality ultra-broadband guided-wave signal transmission and sophisticated high-performance applications over the dc-to-THz range. This strongly motivates researchers to realize ultra-broadband structures with low loss and low dispersion. Few revolutionary research results, however, have been reported within the past few years. Metal-wire waveguide has been applied to propagate THz signals; however, it suffers from poor mode confinement and difficult mode excitation, and it cannot be integrated with and used in chip interconnects. High-frequency metallic and dielectric waveguides have been proposed for low-loss THz applications; nevertheless, they suffer from high

dispersion at low frequency due to their inherent frequency-cutoff performance. It can be concluded that the reported so-called high-performance transmission structures cannot operate well over a wide frequency range starting from dc.

1.2 Research objectives

The principal objective of this research is to investigate and develop synthesized waveguide technologies that support low-loss, low-dispersion, and all-pass transmission for ultra-broadband signals, which are expected to become a suitable candidate for future ultrafast electronic circuits, interconnects, and systems. Specifically, this research work focuses on the following aspects:

1) To investigate a simple waveguide system, coupled half-mode substrate-integrated waveguides (HMSIWs), and to develop promising applications, which can provide the basic understanding of a coupled-mode transmission system.
2) To analyze the typical mode-selective transmission line (MSTL) especially its modal (field) behavior and propagation characteristics, and then to reveal the physical mechanism behind the unique frequency-enabled mode-selectivity phenomenon appearing along MSTL, which can help us gain in-depth physical insight into the MSTL mode-guidance behavior.
3) To examine the excitation scheme of MSTL and then to produce the required excitation by innovative transition designs, which facilitate experimental verifications of dc-to-mmW and dc-to-THz MSTLs and expedite the practical applications in broadband circuits and systems.
4) To explore other high-performance synthesized waveguide structures that enable efficient transmission and proper manipulation of ultrafast (picosecond, for example) electrical pulses.
5) To apply the synthesized waveguides in promising applications foreseen for future ultrafast electronic circuits, interconnects, and systems.

Ultra-broadband-signal transmission is the most fundamental and critical issue in the future development of ultrafast electronics; however, there is no available transmission medium existing

in practice to support low-loss, low-dispersion, and all-pass transmission for ultra-broadband ultrafast signals. This research work attempts to remedy this situation by developing promising synthesized waveguide technologies. In addition, this systematic research is intended to establish the foundations for potential ultra-broadband applications toward high performance, high density, and high speed.

1.3 Thesis outline

This Ph.D. thesis presents original research dedicated to a synthesized waveguide technology for ultrafast ultra-broadband signal transmission. Based on this technology, several versatile synthesized waveguides are presented and investigated, including coupled-HMSIW systems, MSTLs, and synthesized all-pass waveguides (S-WGs). They demonstrate superior transmission performance and find promising applications in leaky-wave antenna (LWA), wideband balun, power divider, etc. This thesis is organized in an article-based format, in which five published papers form the main content (Chapters 3-7), as outlined below.

Chapter 1 introduces the background and objectives of this research work on synthesized waveguide systems, and outlines this thesis briefly.

Chapter 2 provides a review of reported research results on various transmission structures and discusses their respective advantages and disadvantages, with the purpose of unfolding the state-of-the-art of this topic.

Chapter 3 treats coupled HMSIWs, a relatively simple coupled-mode transmission system, from which a compact wideband balun design is developed for mmW applications. This chapter also introduces a straightforward slotline feeding method to excite the odd mode of interest and presents the numerical and experimental verifications of this design concept. This design provides a helpful intuitive way for understanding the properties of a coupled-mode transmission system.

Chapter 4 focuses on some fundamental but critical issues in MSTL, including distinctive frequency characteristics, mode-selectivity phenomenon, and modal behavior quantification. First, a comparative study between MSTLs and conventional waveguide structures is made through two MSTL examples (respectively operating from dc to 60 GHz and to 500 GHz). The unique

phenomenon of frequency-enabled mode selectivity appearing in MSTLs is then examined by means of identified physical evidence (i.e., field distributions in connection with modal behavior). It is followed by a more rigorous analysis that is carried out by defining and formulating three characteristic frequencies, and the operating frequency ranges of MSTLs are thus divided into several distinct frequency regions associated with the frequency-related variable dominant modes. In addition, a general analysis of the attenuation characteristics of MSTLs and higher-order modes in MSTLs is conducted. To facilitate practical measurements and to expedite the integration applications of MSTLs, a low-loss and ultra-broadband transition between MSTL and microstrip line is presented. The numerical and theoretical analyses of MSTLs are carried out with experimental verifications. At the end of this chapter, different fabrication and measurement techniques for the two MSTLs are briefly described.

Chapter 5 reveals the theoretical background and physical mechanism of MSTL. The mechanism of the frequency-dependent modal behavior is presented via modal field variations. Coupled-mode theory and normal-mode analysis are combined to sequentially analyze the half-mode MSTL and MSTL. A comparison between approximate fields derived from the theoretical analysis and exact fields extracted from the rigorous numerical simulation is performed, followed by a parametric study to examine the effect of geometrical parameters on the MSTL characteristics and performance. A further discussion of mode selectivity is also given at the end of this chapter.

Chapter 6 is devoted to the excitation scheme, transition design, and experimental verification of MSTL. The MSTL excitation is first explained by comparison with a conductor-backed coplanar waveguide (CBCPW). An ultra-broadband transition between CBCPW and MSTL is then proposed to produce this specific mode excitation. It has a tapered structure that supports smooth evolution from the fixed CPW mode of CBCPW to the frequency-dependent dominant mode of MSTL. For experimental demonstration purposes, back-to-back CBCPW-to-MSTL transition circuits are physically realized. Finally, this chapter demonstrates the measured scattering parameters and the extracted propagation characteristics of MSTL.

Chapter 7 presents another synthesized waveguide to further demonstrate the potentials of coupled-mode waveguide systems for ultrafast-electrical-pulse transmission. This type of synthesized waveguide is constructed by elaborate geometric tailoring; its dominant eigenmode can be fully reshaped with frequency in an ultra-broad operating range. As frequency of transmitted

RF signals continues to increase, we can rotate the wave polarization from horizontality to verticality and reduce the transmission loss at high frequencies while improving the signal dispersion. To demonstrate the proof-of-principle, two such waveguides are studied and developed, which respectively operate over two different frequency ranges well into the mmW (dc to 67 GHz) and THz (dc to 300 GHz) ranges. At the end of this chapter, eigenmode analysis, device fabrication, and waveguide characterization are briefly described.

Chapter 8 presents a general discussion on some issues involved in this research to help clarify this work on the synthesized waveguide technology and demonstrate its potential impact.

Chapter 9 summarizes the entire research work and describes some promising outlook of this research in which it may be worthwhile for us to engage in the future.

It should be noted that since this thesis is mainly developed through the assembly of several published papers on the presented waveguiding technology, it would be appropriate to create a logical connection among different chapters, especially Chapters 3-7, for better readability. To make this thesis easier to read and understand with a smooth flow of the text, a work breakdown structure of this research is shown in Fig. 1.1, which summarizes the salient points and principal contributions of this research in connection with the synthesized waveguides and anticipated applications.

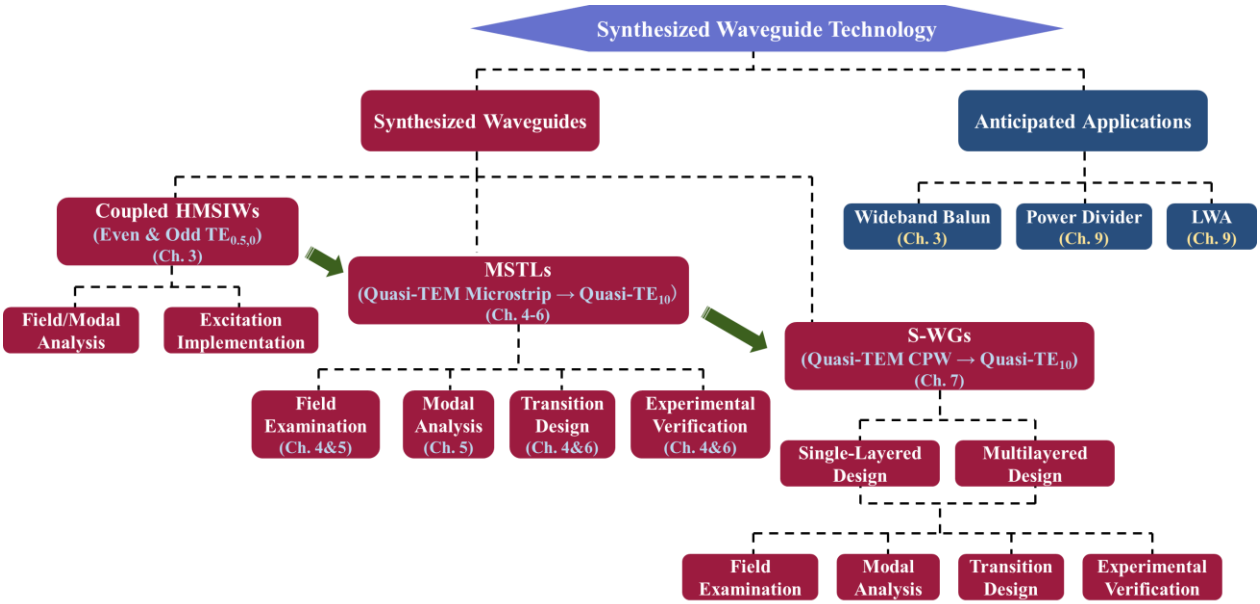

Figure 1.1 Work breakdown structure (WBS) of this research

CHAPTER 2 LITERATURE REVIEW

Transmission and processing of ultra-broadband EM signals present a technological foundation for a wide range of applications in many fields such as basic science, imaging, sensing, detection, communications, high-speed interconnects, time-domain measurements, and biological treatment. Nevertheless, signal transmission quality has been recognized as a primary issue that fundamentally hampers the development of ultrafast electronics beyond the current time scale of nanoseconds. Obviously, it requires a transmission line or waveguide having an all-pass response for ultra-broadband signals on the scale of frequency starting from dc. Such high-performance transmission media operating at microwave, mmW, and THz frequencies, in support of ultra-broadband ultrafast signal generation, transmission, and processing, are indispensable building blocks for realizing and advancing cutting-edge semiconductor and system technologies and applications for aerospace, defense, communications, sensing, data center, and high-tech segments and markets. They are instrumental for current and future ICT-related hardware developments, such as chip-to-chip interconnects, electro-optic modulators, and detectors.

Conventional transmission media, however, are generally subject to low-frequency cutoff (high-pass) and/or high-frequency attenuation (low-pass). Significant efforts have been devoted to exploring high-performance transmission structures over the past several decades, which are often concerned with incremental or limited improvements in conventional ones. The performance of conventional structures has been improved continually thanks to structural and processing innovations; nevertheless, they are still not good enough to meet the stringent requirements for high-quality ultra-broadband ultrafast signal transmission judging from transmission loss, frequency dispersion, and field confinement.

2.1 TEM mode transmission lines

The commonly used transmission lines include coaxial cables, microstrip lines, CPWs, and striplines (see Fig. 2.1), which operate in a ground-plane referenced transverse electromagnetic (TEM) or quasi-TEM (TEM-like) mode. They do not have a cutoff frequency and thus present an

inherent low-pass capability of guiding wideband signals starting from dc (or a very low frequency). However, these conventional transmission lines suffer from weak field confinement and severe signal attenuations, especially at mmW and THz frequencies. In addition, undesired higher-order modes may appear at high frequencies, thereby limiting their maximum operating frequencies. These drawbacks fundamentally hinder their widespread applications that require low-loss, low-dispersion, and ultra-broadband (e.g., dc to THz) signal transmission.

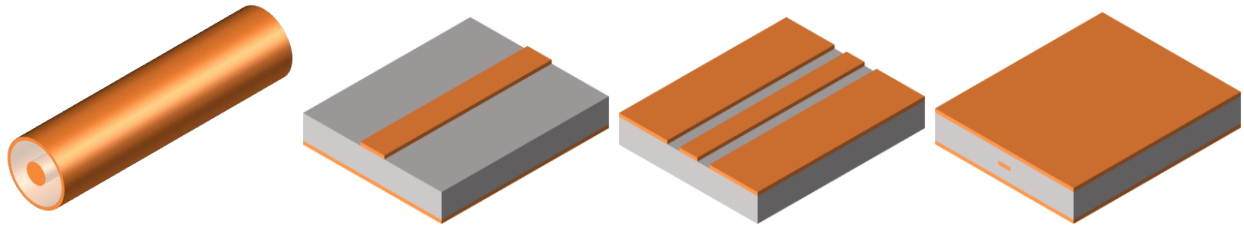

(a) (b) (c) (d)

Figure 2.1 Typical TEM mode transmission lines: (a) Coaxial cable, (b) microstrip line, (c) CPW, and (d) stripline

Several significant improvements in TEM mode lines have been reported in the recent decade. For example, a planar Goubau line was modified by adding corrugations (see Fig. 2.2) in order to slow down and confine EM waves [1]. With an efficient planar excitation, this modified line has been presented for applications in phase shifters, six-port reflectometers, microfluidic systems, etc. Furthermore, the corrugating line can avoid unwanted substrate modes. In [2], a low-loss and low-crosstalk surface-wave transmission line (T-line) was presented at sub-THz frequencies (see Fig. 2.3). Periodic sub-wavelength structures are introduced onto a metal transmission line; as a result, the so-called surface plasmon polaritons (SPPs) are excited to transmit electromagnetic signals through strictly bonded surface waves. This SPP T-line has an interesting application potential in future highly dense on-chip sub-THz communications. Despite the aforementioned advantages, the high-frequency losses of these two transmission lines are still too high. As an open structure, these lines may be easily affected by crosstalk. These drawbacks essentially prohibit them from practical applications in ultrafast pulse transmission.

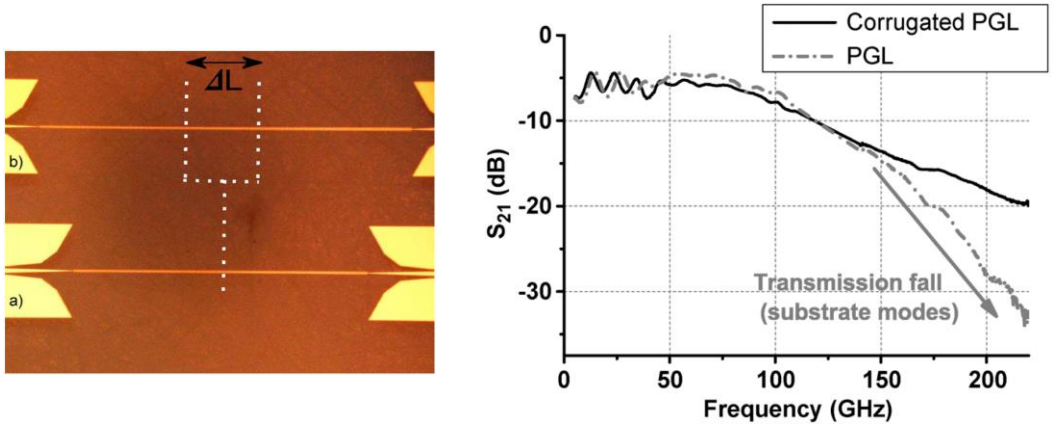

(a) (b)

Figure 2.2 (a) Corrugated planar Goubau lines (PGLs) and (b) measured transmission responses for 4.7-mm-long PGLs [1]

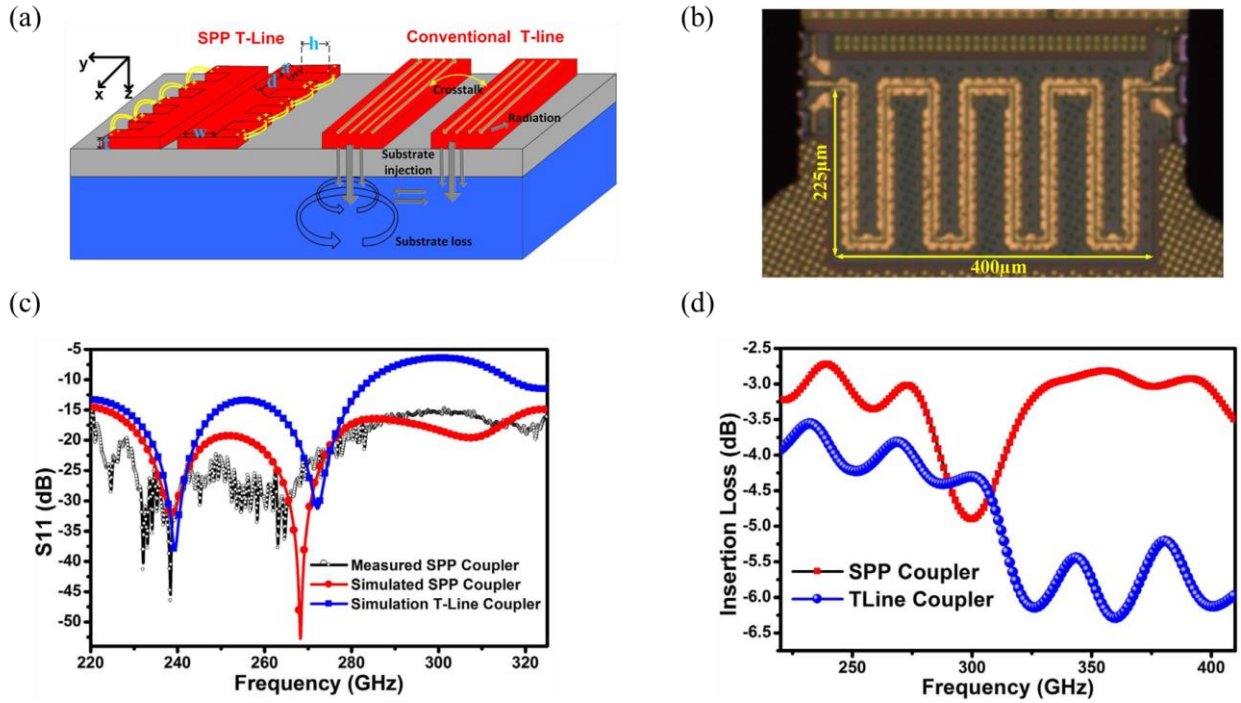

Figure 2.3 (a) On-chip SPP and conventional T-lines, (b) fabricated SPP line prototype, (c) reflection coefficient, and (d) insertion loss [2]

In [3], a modified parallel-plate waveguide (PPWG), called parallel-plate ladder waveguide (PPLWG, see Fig. 2.4), was proposed for confining and guiding THz waves, with main features of

high-degree field confinement, single-mode propagation with widely designable characteristics, and ease of coupling to TE modes of a conventional PPWG. PPLWG is a promising choice for realizing a variety of THz circuits and guided-wave devices. However, this modified structure, which consists of parallel plates connected by metallic posts, becomes a single-conductor structure; it is thus prone to a low-frequency cutoff. This means that this structure cannot support efficient transmission for dc or vey low-frequency signals.

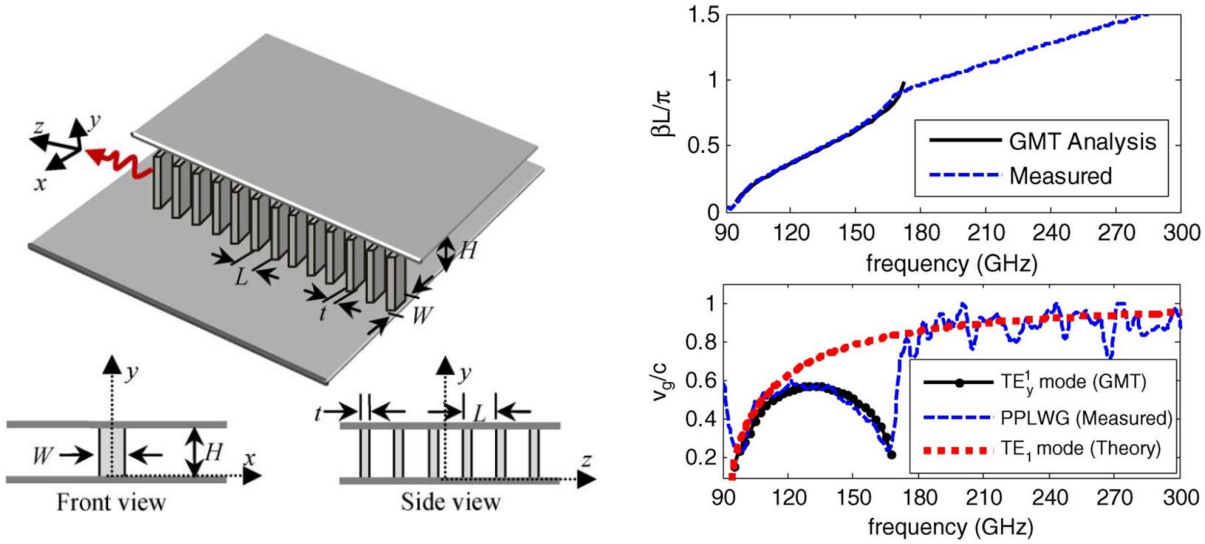

(a) (b)

Figure 2.4 (a) Parallel-plate ladder waveguide and (b) frequency responses [3]

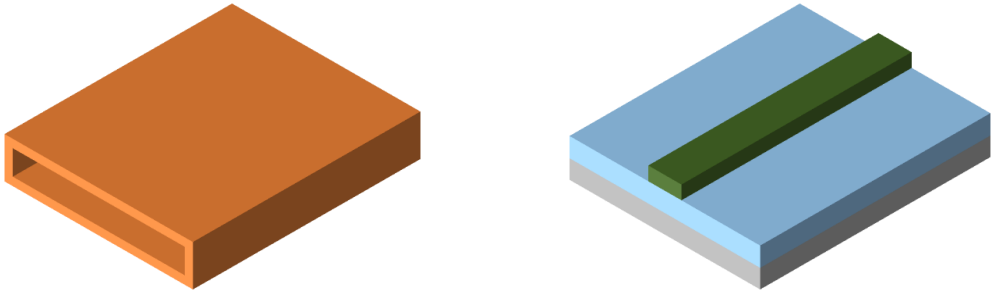

(a) (b)

Figure 2.5 Typical Non-TEM mode waveguides: (a) Rectangular waveguide and (b) dielectric waveguide

2.2 Non-TEM mode waveguides

The most popular non-TEM waveguides in use today include rectangular metallic waveguides and dielectric waveguides (see Fig. 2.5), which operate in a dominant transverse electric (TE) or magnetic (TM) mode, or in a hybrid modal form. They have a relatively low in-band attenuation but possess a low-frequency cutoff, thus yielding a relatively strong dispersion near the cutoff frequencies of the guided modes. In addition, possible higher-order modes greatly limit broadband applications of these waveguides. In fact, transmission loss of these waveguides becomes a serious problem that cannot be ignored when the operating frequency is increased into the THz range.

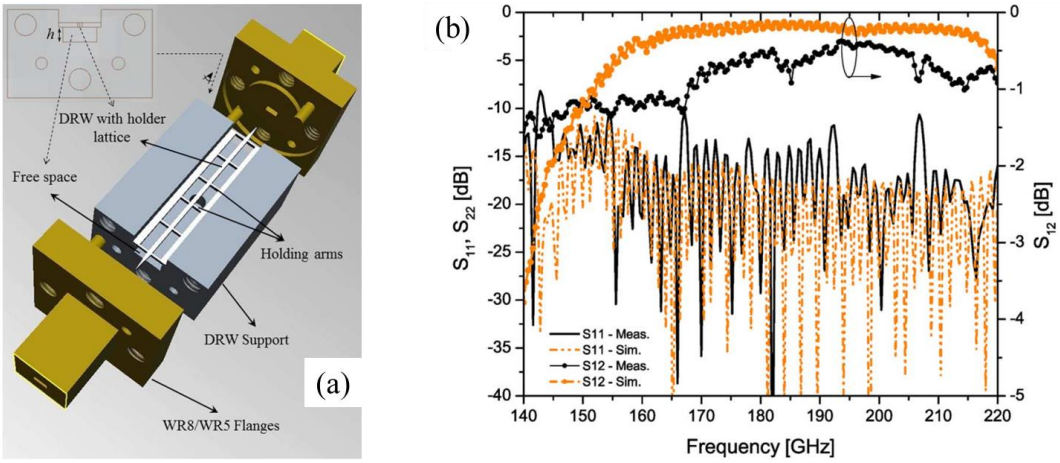

Figure 2.6 (a) Dielectric ribbon waveguide (DRW) connected to measurement setup and (b) simulated and measured S-parameters for a 15-mm-long DRW [4]

Material selection is of critical importance for realizing a high-performance waveguide (especially dielectric waveguide) to efficiently transmit mmW/THz EM signals. Although the common conductors such as gold, silver, copper, and aluminum introduce more or less conductor (Ohmic) losses, there are not better alternatives in practice. Some dielectric materials such as polymers and crystal materials demonstrate good material characteristics in infrared and optical ranges, but they have unacceptable frequency-dependent absorption losses in the THz gap. Another large barrier limiting possible applications of waveguides is the group velocity dispersion. That is, when different components operate in different group velocities, it could lead to distorted pulse shapes.

Transmission structures are often subject to both material and structure dispersions. It has been shown that material dispersion is negligible in non-TEM waveguides; the dominant dispersion is caused by the waveguide structure. While the dispersion zone can be tailored such that a flat dispersion region is achieved, it is always challenging to design waveguides to provide low frequency dispersion over an ultra-broad frequency range.

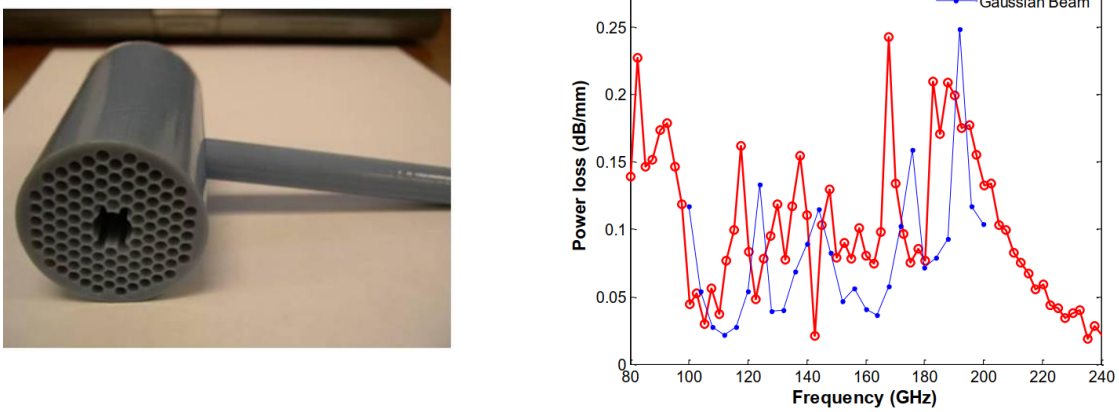

(a) (b)

Figure 2.7 (a) Printed THz waveguide and (b) power loss factors [5]

Due to the high transparency and low fabrication cost, high-resistivity silicon (HR-silicon) and alumina have popularly been used in mmW and THz dielectric waveguide designs. For example, in [4], HR-silicon was selected to implement dielectric ribbon waveguides (DRWs) operating in the F-band (90–140 GHz) and G-band (140–220 GHz) (see Fig. 2.6). These DRWs demonstrate high frequency performance in terms of in-band loss and dispersion, thus making them a good candidate for THz wave transmission. In order to further reduce dielectric loss, in [5], hollow-core electromagnetic crystal waveguide was proposed and implemented by polymer-jetting rapid prototyping (see Fig. 2.7). This waveguide has a low transmission loss of 0.03 dB/mm at 105 GHz. Thanks to the systematic fabrication manor of a rapid prototyping technique, this waveguide can be easily integrated with other THz components.

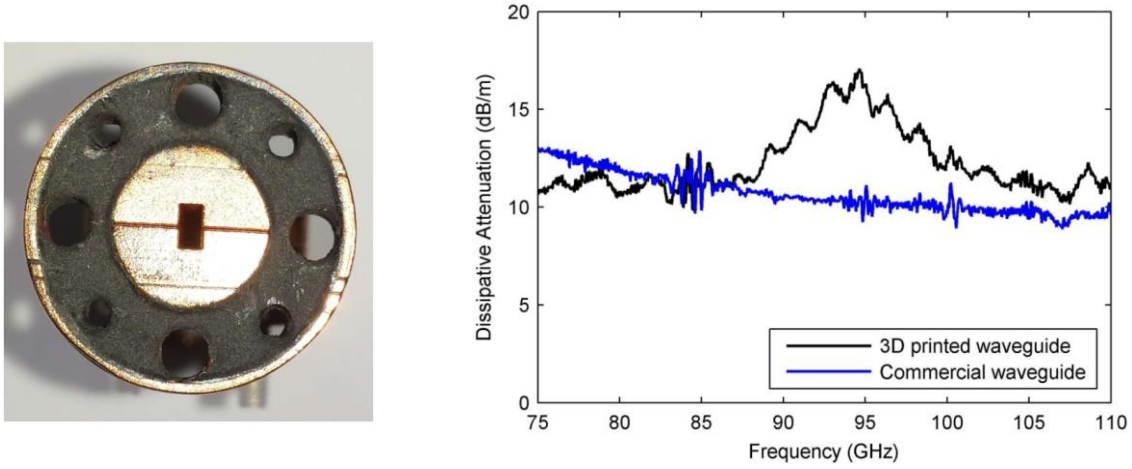

(a) (b)

Figure 2.8 (a) 3-D printed W-band waveguide and (b) measured dissipative attenuations [6]

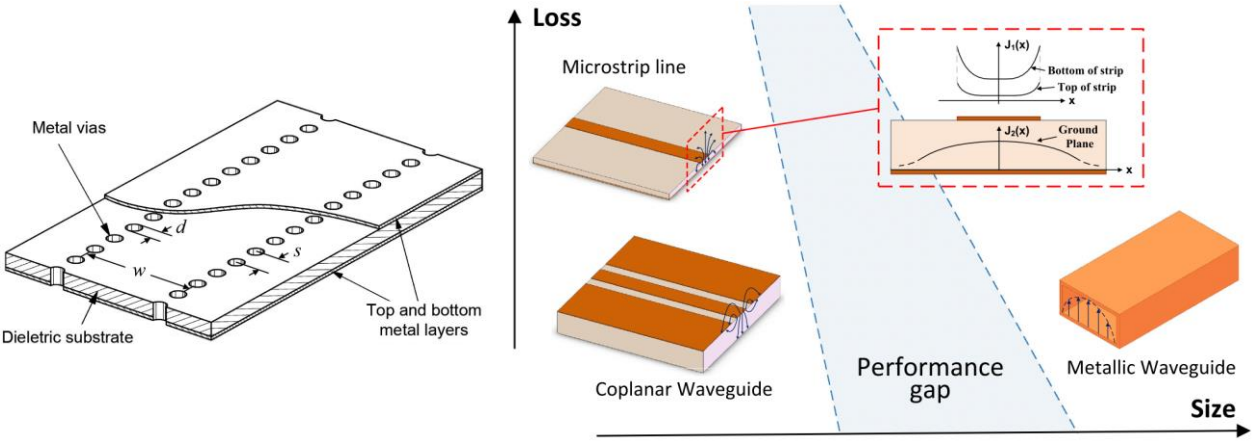

(a) (b)

Figure 2.9 (a) SIW model and (b) its role in filling the performance gap between planar transmission lines and metallic waveguides [7]

As discussed above, there is not much room for obviously reducing conductor losses of metallic waveguides. Many researchers have tried different advanced fabrication processes instead of reducing the fabrication cost. For instance, 3-D printing process has widely been used for realizing air-filled metal-pipe waveguides for microwave and mmW applications. In [6], two different 3-D

printing technologies including low-cost low-resolution fused deposition modeling and higher-cost higher-resolution stereolithography were used to implement X-band (8–12 GHz) and W-band (75–110 GHz) rectangular waveguides (see Fig. 2.8). It has been found that the performance of the 3-D printed waveguides is comparable with that of commercial waveguides. To facilitate the integration with other planar components, SIW technology has been developed rapidly for the implementation of classical rectangular waveguides in a planar form. This technology combines the advantages of planar technologies and conventional metallic waveguides (see Fig. 2.9) [7]. SIW can be manufactured by adopting well-established and cost-effective processing techniques such as printed circuit board (PCB) and low temperature co-fired ceramic (LTCC) processes among many others. At the same time, SIW exhibits high power-handling capability and practically complete electromagnetic shielding. Moreover, SIW can be easily connected to other planar transmission lines (e.g., microstrip lines and CPWs) in the same substrate.

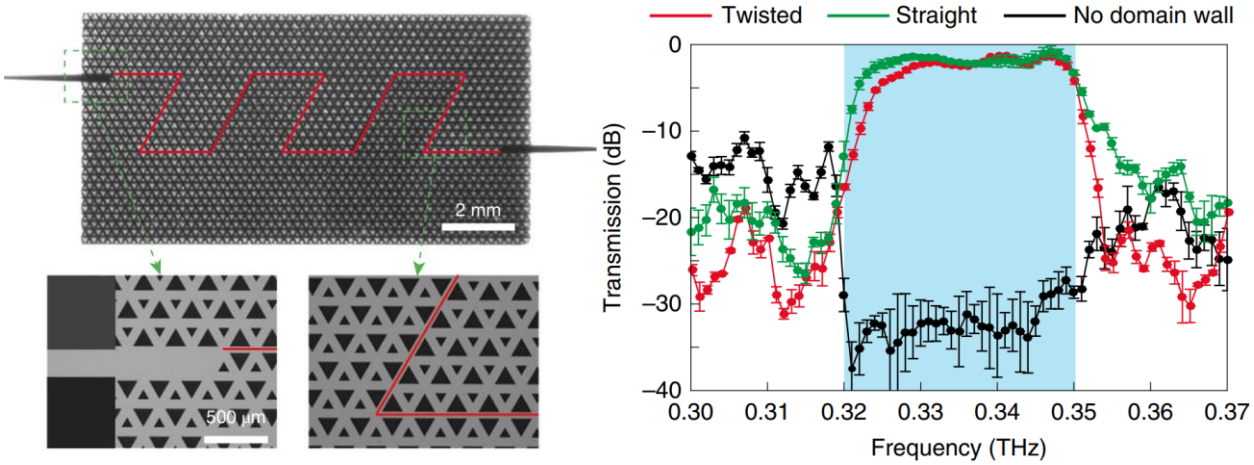

(a) (b)

Figure 2.10 (a) Silicon-platform-based on-chip valley photonic crystal and (b) measured transmission curves [8]

In addition to the continuous improvements in the classical dielectric waveguides and metallic waveguides, substantial effort has been directed recently toward the design and development of some other promising waveguides. Researchers have experimentally demonstrated robust THz

topological valley transport through several sharp bends on an all-silicon valley photonic crystal (VPC) chip (see Fig. 2.10) [8]. Topological valley kink states are excellent information carriers for THz communications, owing to their robustness, single-mode propagation, and linear dispersion. Silicon-platform-based on-chip VPCs have the additional merit of low loss. The silicon-based VPC would serve as an ideal platform for future THz integrated circuits, sensing, imaging, spectroscopy, and communications. On the other hand, ε-near-zero (ENZ) metastructures have been presented to support the tunneling of waves with longitudinal wave numbers near zero (see Fig. 2.11) [9]. The ENZ structures can transfer surface waves from one side to another by an anomalous squeezing effect. This phenomenon is totally independent of both the length and shape of the structures, suggesting potential applications in engineering flat photonic devices and components.

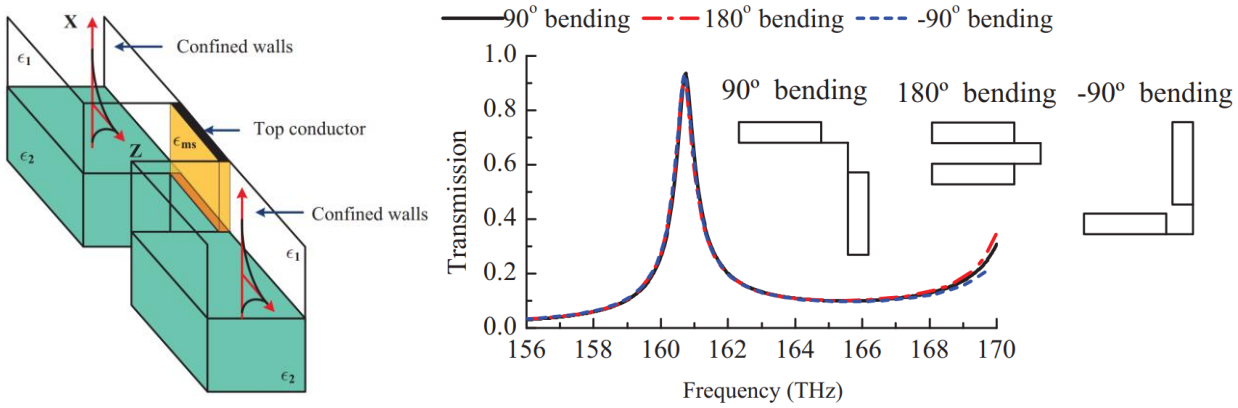

(a) (b)

Figure 2.11 (a) ENZ metastructure and (b) transmission coefficient magnitudes for tunneling through the ENZ region with different bending angles [9]

Despite the significant improvements and innovations involved in the recently reported waveguide structures, the modified waveguides are still not suitable for the highly desired efficient transmission of ultra-broadband signals starting from dc (or a very low frequency). The primary causes are the limited bandwidth and strong frequency dispersion, as for other non-TEM mode waveguides. In addition, undesired modes such as higher-order modes are easily excited. The fundamental properties of conventional transmission lines and waveguides are primarily a result of

the guided-wave nature of respective dominant eigenmodes (eigen fields) that are generally assumed to remain unchanged for a given waveguide cross section. In a word, none of these conventional transmission media can support an all-pass signal transmission without distortion, covering a dc-to-THz (or dc-to-mmW) ultra-broad bandwidth in the frequency domain. These drawbacks (strong dispersion, high loss, and undesired modes) fundamentally limit their applications in which low-loss, low-dispersion, ultra-broadband (e.g., dc to THz), or ultrafast pulse (e.g., picosecond) transmission is often required. This poses the most fundamental challenge in the development of next-generation ultrafast electronics in support of picosecond and shorter pulse generation, transmission, and processing, which requires to break through the current nanosecond electronics barrier. Ground-breaking innovations and advances in transmission technology are desperately needed to mitigate this situation.

2.3 Mode-selective transmission line

The research status of transmission media presented in previous sections easily raises questions about whether we can successfully design a disruptive ultra-broadband transmission medium with superior performance, and about how we realize it in practice. Traditionally, due to the well-known facts of high loss and undesired modes, it is almost impossible to realize a transmission structure with sustained low loss and low dispersion from dc to mmW, THz, or even optical frequencies. However, if different operation modes in a same transmission structure are appropriately selected or converted as frequency changes, it is possible to maintain high frequency performance over a wide frequency range. Once this transmission structure is realized, it can bridge electronics and photonics and have a huge application potential in electro-optical fields.

Given the nonidealities of individual eigenmodes (TEM, TE, TM, etc.), as discussed at the end of Section 2.2, it is not so difficult to come up with an idea that if we could reshape the propagating eigenmode of a particular guiding structure, we should be able to precisely control the propagation of guided waves. For a given guided-wave structure, modal eigenvalues are the unique solutions of the wave equation corresponding to a set of appropriate boundary conditions. It is nevertheless of interest to note that these solutions are a function of frequency, which makes it possible to shape or configurate particular eigenmodes with frequency and thus to obtain various desired modal

behaviour. To this end, an attempt has been made to engineer a uniform transmission line, called mode-selective transmission line (MSTL), to reshape its dominant mode with frequency.

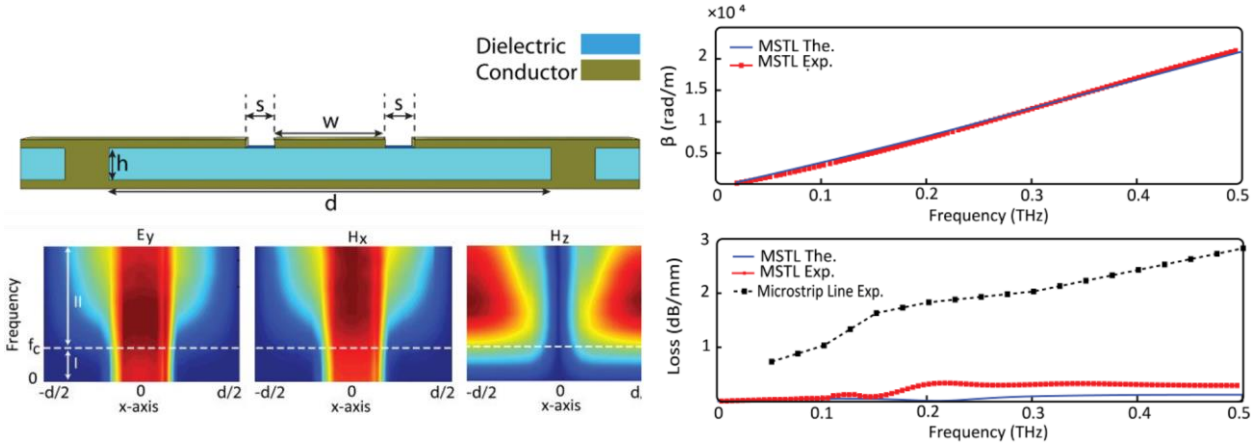

(a) (b)

Figure 2.12 (a) MSTL model and field distributions as well as (b) propagation constants [10]

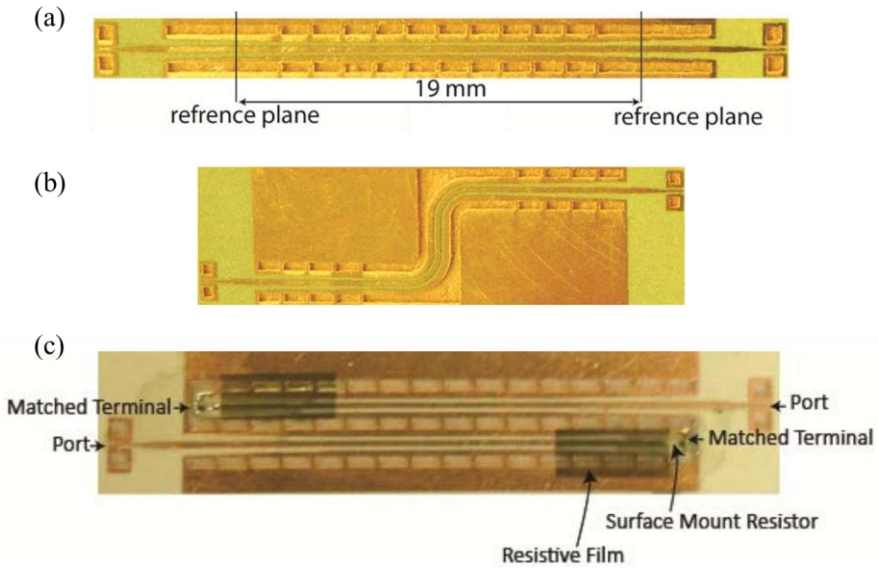

Figure 2.13 (a) Typical MSTL prototype, (b) MSTL bend prototype, and (c) fabricated MSTL circuit for crosstalk measurement [10]

The concept of MSTL was proposed and validated preliminarily by our research group (see Fig. 2.12) [10]. As the name indicates, MSTL can selectively operate in a desired dominant mode in different frequency ranges. Preliminary results have suggested that MSTL has a frequency-varying dominant mode changing smoothly but completely from a quasi-TEM mode to a quasi-TE_{10} mode as the operating frequency continues to increase, that is to say, its operation is mainly based on the frequency-enabled mode conversion (i.e., mode selectivity). This makes MSTL versatile to benefit from advantages of the two modes. The quasi-TEM mode gets rid of the cutoff characteristics, whereas the quasi-TE_{10} mode allows for a low propagation loss. This mode selectivity endows MSTL with efficiently guiding dc-to-mmW or dc-to-THz signals with low-loss and low-dispersion characteristics. The preliminary research on MSTL has also explored curved bend configuration's effects and the crosstalk of side-by-side lines (see Fig. 2.13). The results have indicated that MSTL significantly maintains very low crosstalk, noise, loss, and delay of ultra-broadband signal transmission.

In fact, MSTL is a synthesized coupled-mode transmission system that merges the desired waveguiding properties offered by different modes. The modal change occurring in MSTL, however, is not well reflected and studied in the related frequency characteristics (especially high-frequency attenuation and wave polarization). Motivated by this coupled-mode system concept, this research work attempts to explore promising synthesized waveguides for ultra-broadband signal transmission.

CHAPTER 3 ARTICLE 1: COMPACT WIDEBAND COUPLED-WAVEGUIDE BALUN FOR MILLIMETER-WAVE APPLICATIONS

Desong Wang and Ke Wu

Published in the *2020 IEEE MTT-S International Wireless Symposium (IWS)*, Sept. 2020.

This paper presents a compact wideband balun for millimeter-wave (mmW) applications, which is constructed from tightly coupled half-mode substrate-integrated waveguides (HMSIWs). This balun takes full advantage of the frequency-independent out-of-phase property of the odd $TE_{0.5,0}$ mode of the coupled-HMSIW system. As a result, a phase difference of 180° and balanced amplitudes between two balun outputs are obtained inherently over a wide frequency range. Thanks to the similarity of partial transverse fields, this odd mode can be excited by a conventional slotline in a straightforward manner. This design concept is verified by both simulation and measurement. Measurement shows that this balun has a fractional bandwidth of 97%, from 17 to 49 GHz, with a return loss of 10 dB at its unbalanced port; the in-band amplitude and phase imbalances between two balanced ports are within ±0.6 dB and ±5° (±10° at around 48 GHz), respectively. In addition, the core-circuit size of the proposed balun is about 0.2 λ_g × 0.57 λ_g, where λ_g is the guided wavelength at the center frequency of 33 GHz.

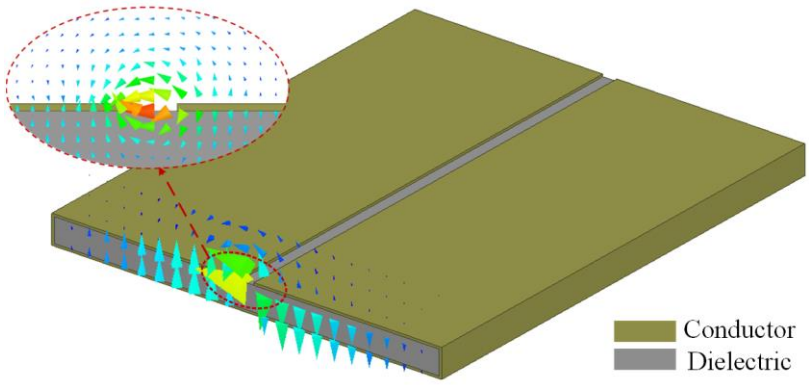

Figure 3.1 Coupled-HMSIW system and cross-sectional *E*-field distributions for its odd $TE_{0.5,0}$ mode

3.1 Introduction

Balun (balanced-to-unbalanced) is a device or circuit capable of converting an unbalanced signal to a balanced one, or vice versa. In the most commonly used communication systems today, there are a large number of microwave circuits and systems requiring balanced inputs or/and outputs to reduce environment noise, crosstalk, and high-order harmonics as well as to improve dynamic range. With the unique circuit functions, baluns are widely used in many critical building blocks, such as push-pull amplifiers, balanced mixers, antenna feed networks, etc. Furthermore, as the 5G mobile communication emerges, we can expect an increasing demand for low-cost, compact millimeter-wave (mmW) baluns with good operating performance in terms of bandwidth, power loss, as well as amplitude and phase imbalances. Recently, a variety of baluns have been studied and implemented for mmW applications using different processing techniques including CMOS [11], InGaP/GaAs HBT [12], GaAs [13], PHEMT [14], LTCC [15], and PCB schemes [16]. In view of cost and complexity, this work aims to design a compact wideband balun at mmW frequencies using a standard PCB process together with a typical substrate-integration technique.

Over the past two decades, substrate-integrated waveguide (SIW) techniques have been quickly developed for microwave, mmW, and even terahertz applications [17]. The concept of half-mode substrate-integrated waveguide (HMSIW) has also been proposed and demonstrated, which maintains the substantial advantages of SIW but has only half the size [18]. Placing two identical HMSIWs with their open edges facing each other forms a coupled-HMSIW system (Fig. 3.1). This coupled system is able to support even or odd modes. Coupled-HMSIW systems with even and odd $TE_{0.5,0}$ modes of operation each have been used to design power dividers [19] and leaky-wave antennas [20]. This work presents a wideband balun structure constructed from such a coupled-waveguide system in a compact manner. This balun can operate at microwave and mmW frequencies with superior in-band performance. The mode of operation in the coupled system is the odd $TE_{0.5,0}$ mode, for which the inherent 180° phase difference of the fields in the two individual HMSIWs ensures a wide operating bandwidth.

3.2 Analysis and design

As mentioned earlier, the balun proposed in this work is formed from a coupled-HMSIW system whose odd $TE_{0.5,0}$ mode offers the possibility of good in-band amplitude and phase balances over

a wide bandwidth. That is to say, its balun function is primarily determined by the coupled HMSIWs.

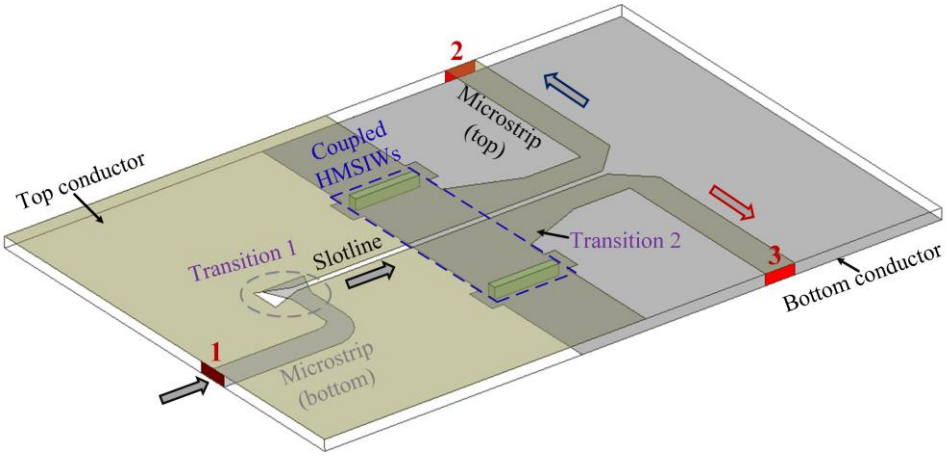

(a)

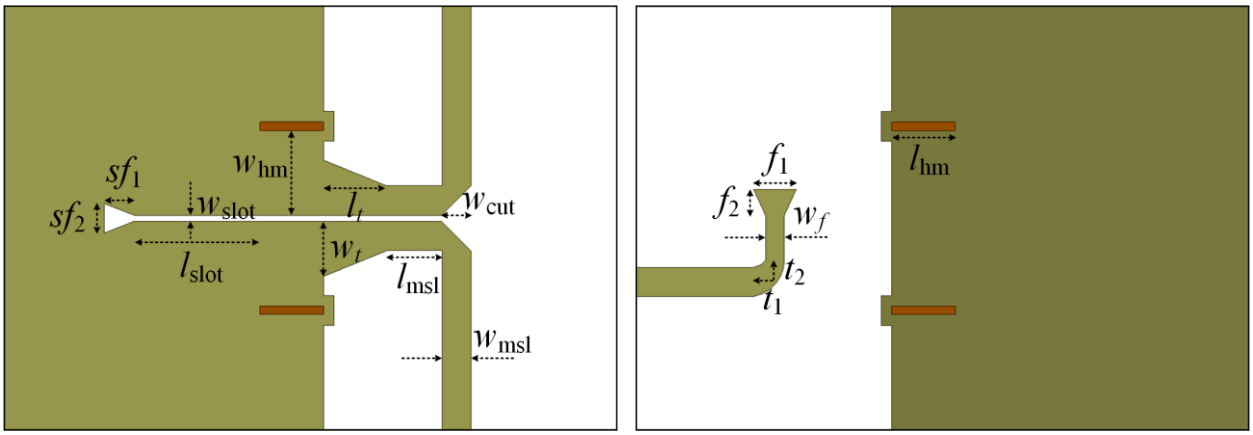

(b) (c)

Figure 3.2 Proposed wideband balun: (a) Perspective view; (b) top view; (c) bottom view

w_{hm} = 2, l_{hm} = 1.5, w_{slot} = 0.1524, l_{slot} = 3, w_t = 1.3, l_t = 1.5, l_{msl} = 1.31, w_{msl} = 0.69, sf_1 = 0.7, sf_2 = 0.7, w_f = 0.45, f_1 = 1, f_2 = 0.6, t_1 = 0.5, t_2 = 0.5, w_{cut} = 0.7, unit: mm.

3.2.1 Coupled HMSIWs

Fig. 3.1 shows the coupled-HMSIW system, in which two constituent HMSIWs are identical and closely spaced in a common conducting plane. Its geometry could be viewed as an SIW with a long

slot cut along the centerline of the top wall. Due to the presence of this additional slot, however, any transverse surface currents on the top wall would be truncated. In fact, this structure is a coupled-waveguide system, which supports even or odd waveguide modes rather than standard TE or TM modes in an SIW, as do the conventional coupled lines or waveguides [21]. Its modal behavior has been treated using a joint normal- and coupled-mode analysis [22], which will be detailed in future expanded version. Here we restrict our attention to the odd mode (i.e., odd $TE_{0.5,0}$ mode) in view of its frequency-independent 180° out-of-phase property. Its electric field (*E*-field) distributions in the transverse cross section of the structure are plotted in Fig. 3.1, in which the partial fields around the thin slot are deliberately enlarged for clarity. As can be seen, the dominant fields are distributed between the top and bottom conducting planes, with opposite orientations in the two individual HMSIWs (i.e., 180° out-of-phase property). Upon a close inspection of the inset of Fig. 3.1, one can find that the fields around the slot are similar to those in a slotline. This fact indicates that this odd mode can be readily excited by a slotline.

3.2.2 Balun geometry

As discussed above, a conventional slotline is connected to the slot in the top conducting plane to excite the desired odd $TE_{0.5,0}$ mode of the coupled-HMSIW system. To facilitate the experimental characterization of the final balun, microstrip lines are used as the feedlines at its three ports. Transitions from the microstrip lines to the slotline and to the HMSIWs are built to connect the above-mentioned elements in a straightforward manner. The microstrip-to-slotline transition (Transition 1) is referred to the aperture-coupling transition structure presented in [23], whereas the microstrip-to-HMSIW transition (Transition 2) is referred to the well-described tapered structure reported in [18]. Finally, the entire balun structure is built in planar form, as sketched in Fig. 3.2. Note that the dielectric substrate is set to be transparent to clearly show the balun structure. Here we let the length of the HMSIWs be close to one quarter-wavelength for our purposes of impedance matching and structure compactness.

This balun is constructed on a thin dielectric substrate with two conducting layers; the microstrip feedlines at input and output ports are placed on different sides of the dielectric substrate. The core part of this balun is the coupled HMSIW system, which is fed directly by a slotline whose width is the same as that of the slot between the HMSIWs. The coupled system ensures the equal-power

but 180° out-of-phase split and accounts for the operating bandwidth of the balun. Specifically, the minimum and maximum operating frequencies of the balun are primarily determined by the cutoff frequencies of the odd $TE_{0.5,0}$ mode and the next odd mode, respectively.

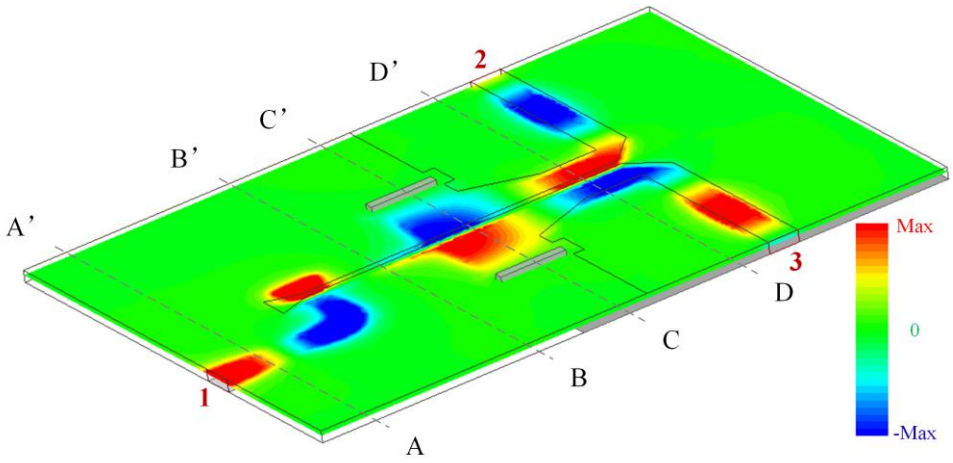

(a)

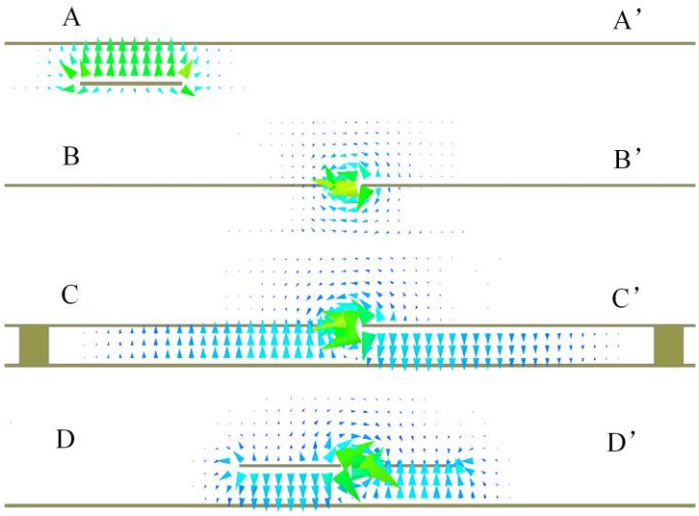

(b)

Figure 3.3 *E*-field distributions in (a) the proposed balun and (b) specified transverse cross sections

3.2.3 Field analysis

To show how an electromagnetic signal propagates down the balun structure, *E*-field distributions at the center frequency of the operating bandwidth are examined, as vividly depicted in Fig. 3.3(a). It can be observed that the input signal passes readily through the balun, from the microstrip line at port 1 to the slotline, then to the HMSIWs, and finally to the microstrip lines at the two output ports 2 and 3. In addition, the signal power entering port 1 is evenly divided into two out-of-phase components at ports 2 and 3. This signal flow is routed with the help of the specially designed transitions. To further demonstrate any possible mode conversions involved, *E*-field distributions in the specified transverse cross sections, namely A-A', B-B', C-C', and D-D' as labeled in Fig. 3.3(a), are treated and plotted in Fig. 3.3(b). It can be seen that several mode conversions occur over the whole length of the balun, from a microstrip mode (see A-A') to the slotline mode (see B-B'), then to the odd $TE_{0.5,0}$ mode of the HMSIWs (see C-C'), and finally to the odd microstrip mode of the coupled microstrip lines (see D-D'). The resulting *E*-fields at the two output ports have opposite orientations; this means a 180° phase difference. That is, an unbalanced signal applied to port 1 (unbalanced port) is converted to a balanced output signal at ports 2 and 3 (balanced ports), namely the balun function.

3.3 Simulation and measurement

To demonstrate the design methodology, a compact wideband balun at mmW frequencies is designed and fabricated on a 0.254-mm-thick Rogers RT/duroid 6002 substrate, with a relative dielectric constant of 2.94 and a dielectric loss tangent of 0.0012. Its physical dimensions are listed in Fig. 3.3. Photographs of the fabricated sample are shown in Fig. 3.4. In this work, the short sidewalls of HMSIWs are implemented with metallized slots, and the microstrip feedlines at the balanced ports are lengthened in opposite directions on account of measurement convenience. The core-circuit size of the balun is 1.5 mm × 4.1524 mm (i.e., 0.2 λ_g × 0.57 λ_g, where λ_g is the guided wavelength of coupled HMSIWs at the center frequency of 33 GHz). This mmW balun has advantages of small size, low cost, simple design, and integrability with planar circuitry.

Full-wave simulations are performed in a finite-element method software package (ANSYS Electronics Desktop 2018). The *S*-parameter measurements are carried out by connecting the DUT (device under test) to a PNA-X network analyser N5247A (Keysight Technologies) through three

Southwest 1.85 mm end launch connectors, as shown in Fig. 3.4. To remove the unwanted effects of the test system and the additional microstrip feedlines, the calibration work is conducted by using a thru-reflect-line calibration procedure.

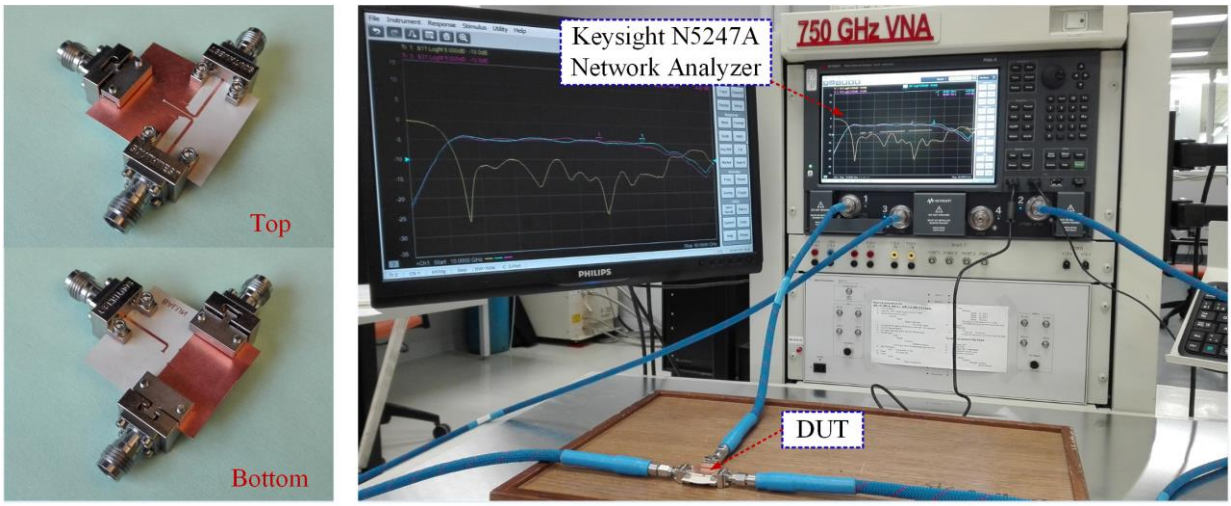

Figure 3.4 Photographs of fabricated balun and measurement setup

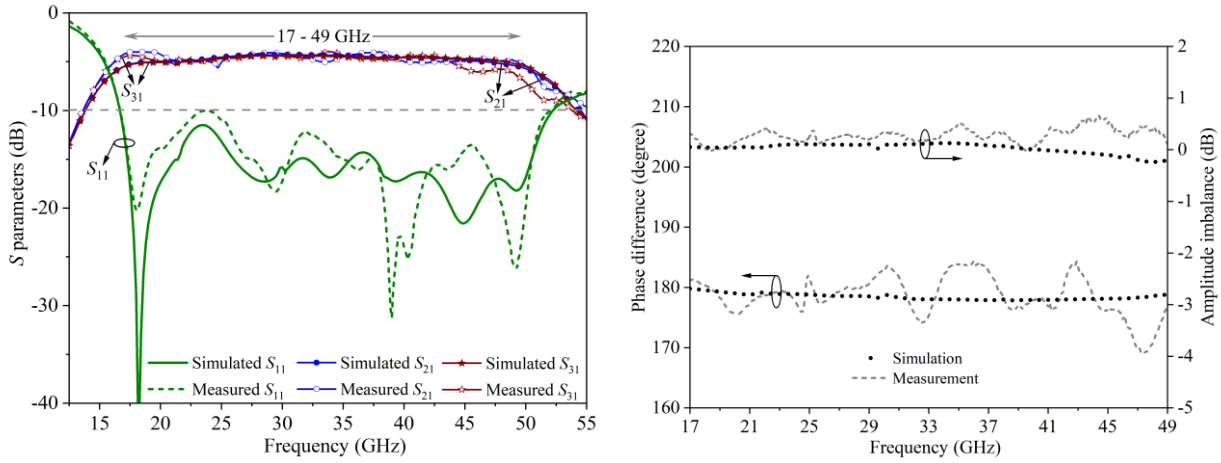

(a) (b)

Figure 3.5 Measured and simulated results of the proposed balun: (a) *S* parameters; (b) in-band phase difference and amplitude imbalance

Fig. 3.5 depicts the simulated and measured results for the amplitude response and imbalance, as well as phase difference of the proposed wideband balun. It can be seen that a good agreement between the measured and simulated results is achieved. The measured return loss at the unbalanced port (port 1) is better than 10 dB from 17 to 49 GHz (fractional bandwidth of 97%), and the measured minimum insertion loss is 0.94 dB, excluding the theoretical 3-dB power splitting loss. It is noteworthy that this insertion loss includes the additional losses introduced by the feeding slotline as well as the microstrip-to-slotline and microstrip-to-HMSIW transitions, which can usually be avoided in practical circuit integration applications. In the frequency range of operation, the measured amplitude and phase imbalances between the two balanced ports are within ±0.6 dB and ±5°, respectively, except that the phase imbalance reaches 10° at around 48 GHz. This discrepancy, mainly caused by both the calibration and measurement errors, is reasonable and is within an acceptable level.

3.4 Conclusion

A low-cost and compact balun has been proposed on the basis of the frequency-independent out-of-phase property of the odd $TE_{0.5,0}$ mode of the coupled-HMSIW system. This balun can operate at K-, Ka-, and Q-band with superior operating performance in terms of bandwidth, insertion loss, as well as amplitude and phase imbalances. The odd-mode excitation by a slotline facilitates the balun integration with other planar circuits and expedites its potential applications in microwave and mmW circuits and antenna feed networks, and particularly in 5G circuits and systems.

CHAPTER 4 ARTICLE 2: LONGITUDINALLY UNIFORM TRANSMISSION LINES WITH FREQUENCY-ENABLED MODE CONVERSION

Desong Wang, Faezeh Fesharaki, and Ke Wu

Published in the *IEEE Access*, vol. 6, pp. 24089-24109, Apr. 2018.

A class of longitudinally uniform transmission lines with low loss, low dispersion, and high-field confinement, called mode-selective transmission lines (MSTLs), has been proposed for ultra-broadband and ultrafast electromagnetic signal guidance and processing. Their operation is mainly based on the concept of frequency-enabled mode selectivity. This paper presents our latest research results on this emerging MSTL, including its operating mechanism, propagation characteristics, higher-order modes, and transition design. Throughout the detailed discussion, two MSTL structures operating in distinct frequency ranges (dc to 60 GHz and dc to 500 GHz as showcased here) are considered. First of all, a comparative study among MSTLs and several conventional transmission lines is made, illustrating significant differences in structural features, wave guidance, field distributions, and frequency characteristics. Secondly, the phenomenon of mode selectivity occurred in MSTLs is examined by means of identified physical evidence (i.e., field distributions in connection with modal behavior) and theoretical foundation. It is verified that, with increasing frequency, the dominant modes of MSTLs are converted from a quasi-TEM microstrip mode to a quasi-TE_{10} waveguide mode over a certain frequency range. Following this thread, a more rigorous analysis is carried out by defining and formulating three characteristic frequencies based on the observed inherent physical dispersions, and the operating frequency ranges of MSTLs are thus divided into several distinct frequency regions associated with the frequency-related variable dominant mode. In addition, a general analysis of the attenuation characteristics of MSTLs and higher-order modes in MSTLs is conducted. To facilitate practical measurements and to expedite the integrated applications of MSTLs, we propose a low-loss and ultra-broadband transition between MSTL and microstrip line, through which undesired higher-order modes are effectively suppressed. The numerical and theoretical analyses of MSTLs are carried out with experimental

verifications. At the end of this paper, different fabrication and measurement techniques for the two MSTLs of interest are briefly described.

4.1 Introduction

High-performance transmission lines and waveguides operating in the microwave, millimeter-wave, and terahertz (THz) frequency ranges, in support of ultra-broadband and ultrafast signal generation, transmission, and processing, are indispensable building blocks for realizing and advancing cutting edge semiconductor and system technologies and applications for aerospace, defense, communications, sensing, data center, and various high-tech segments and markets. They are instrumental for current and future ICT-related hardware developments, such as chip-to-chip interconnects [24], [25], electro-optic modulators [26], [27], and detectors [28]. Over the past decades, significant efforts have been made for exploring high-performance transmission media, which are often concerned with incremental or limited improvements of conventional transmission lines and waveguides. Although the performance of conventional transmission media has improved continually thanks to structure and processing innovations, they are still unable to meet the stringent requirements for high-quality ultra-broadband guided-wave signal propagation judging from propagation loss, frequency dispersion, and mode confinement. Non-TEM waveguides (such as rectangular waveguide (RWG) [29], [30], substrate integrated waveguide (SIW) [31], [17], and dielectric waveguide [32-34]) are subject to a strong frequency dispersion near the cutoff frequencies of guided modes. TEM-type lines (such as coplanar waveguide (CPW) [35], [36], microstrip line [37], [38], stripline [39], and coaxial line [40]) generally suffer from severe signal attenuations, especially at millimeter-wave and THz frequencies. In addition, higher-order modes are easily excited along these conventional transmission lines and waveguides [41]. These drawbacks (strong dispersion, high loss, and higher-order modes) fundamentally limit their applications in which low-loss, low-dispersion, ultra-broadband (e.g., dc to THz), or ultrafast pulse (pico- or femto-second) propagation is often required. On the other hand, parallel-plate waveguides (PPWGs) [42], [43] and metal wires [44], [45] have been demonstrated to potentially guide an ultra-broadband electromagnetic wave with low loss and low dispersion. However, a significant diffraction loss, especially for a long propagation length, deteriorates the performance of PPWGs.

Poor mode confinement and difficulty of mode excitation are few hurdles to the applications of metal wires.

A new concept of mode-selective transmission line (MSTL) has recently been proposed in [46-48]. This kind of transmission medium is capable of guiding an ultra-broadband (e.g., dc to THz) signal with low loss and low dispersion [46], [47]. Preliminary research results indicate that MSTL operates in a variable dominant mode, which can be converted from a quasi-TEM microstrip mode to a quasi-TE_{10} waveguide mode as frequency increases. A prevailing assumption or perception about a transmission medium with a given cross section has been that a mode conversion (or called mode coupling, mode transition, or mode transformation) can only occur when there is a geometrical discontinuity or perturbation along the propagation direction of the guided wave [49-51]. In [52], a mode conversion from a TEM-like mode to a plasmon-like mode has been observed in a PPWG when frequency goes up. Similarly, a phenomenon of frequency-enabled mode conversion appears in the longitudinally uniform MSTLs proposed in [46-48]. These facts reveal that a mode conversion may occur in a transmission medium without being subjected to any longitudinal irregularities.

This mode conversion makes MSTL versatile, benefitting from combined advantages of the two modes. The quasi-TEM microstrip mode gets rid of the cutoff frequency and dispersive behavior over a low-frequency range, whereas the quasi-TE_{10} waveguide mode allows a relatively low signal attenuation and reduced dispersion over a high-frequency range. In this paper, the specific phenomenon of frequency-enabled mode conversion is called “mode selectivity” to highlight its essential difference as opposed to the classical perception. The operation of MSTL, in fact, is mainly based on the mode selectivity. Field distributions for various field components of the dominant mode of a typical MSTL were examined in [53], becoming a first-hand physical evidence of the mode selectivity. In this work, we begin with reviewing our previous research on MSTL (referring to [46-48] and [53]) and then present our latest research findings through the analysis and demonstration of two practical MSTL examples (one is proposed in this paper, and the other MSTL was presented in our previous work [46], [47]). The main contributions of this work are listed as follows: (1) MSTLs are compared in detail to conventional transmission media; (2) Theoretical foundations of mode selectivity are provided; (3) Characteristic frequencies are defined and formulated to quantify the mode selectivity; (4) Propagation characteristics of MSTLs are

investigated based on the defined frequency regions; (5) Higher-order modes in MSTLs are treated for the first time, and the effective suppression of these undesired modes is demonstrated; (6) Field transformation in the tapered transition reported in [47] is examined; (7) Finally, the low-frequency (dc to 60 GHz) MSTL is experimentally verified to further examine the MSTL technique.

This paper is organized as follows. In Section 4.2, MSTLs are compared to conventional transmission media in terms of structural features, wave guidance, field distributions, and frequency characteristics. Section 4.3 is concerned with the mode selectivity in MSTLs, which is verified by both physical evidence and theoretical foundation. It is followed by a more rigorous analysis of the mode selectivity in Section 4.4. In this section, characteristic frequencies are defined, and several frequency regions are specified accordingly. In Section 4.5, a general analysis of signal attenuation and a brief discussion of higher-order modes in MSTLs are conducted. A low-loss and ultra-broadband microstrip-to-MSTL transition is presented in Section 4.6, and different fabrication and measurement techniques for the two MSTLs are briefly described. Finally, this work is concluded in Section 4.7.

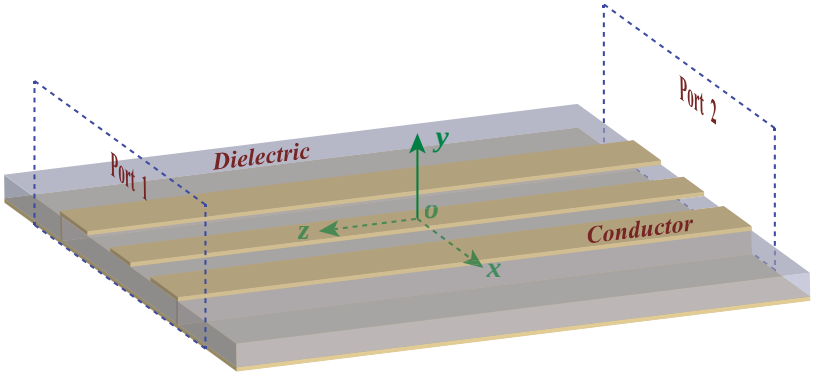

(a)

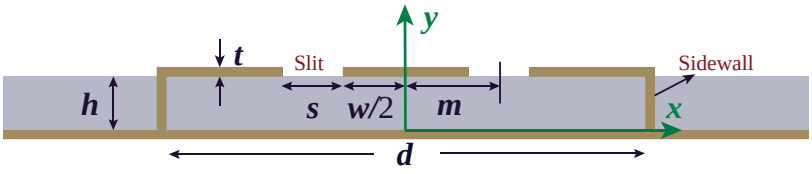

(b)

Figure 4.1 Typical topology of MSTL. (a) Perspective view. (b) Cross-sectional view

Table 4.1 Dimensions of both MSTL I and MSTL II

	h	d	m	w	s	t	ε_r	tanδ	σ
MSTL I	0.254 mm	3 mm	0.45 mm	0.65 mm	0.25 mm	18 μm	10.2 (ceramic PTFE)	0.0023	5.8×10^7 S/m (copper)
MSTL II	50 μm	600 μm	89 μm	140 μm	38 μm	2 μm	4.27 (crystal quartz)	0.0002	6.1×10^7 S/m (silver)

4.2 MSTL structure

A typical topology of MSTL is shown in Fig. 4.1, which may be regarded as a geometrical superposition of microstrip line, coplanar waveguide (CPW), substrate integrated waveguide, etc [54]. The geometrical parameters are also labeled in the figure. A conducting strip of width w is centered between two identical side conducting planes of thickness t and conductivity σ, constructing two identical slits of width s and offset distance m. They are printed on a thin conductor-backed dielectric substrate of thickness h, relative permittivity ε_r, and loss tangent tanδ. The side conducting planes are connected to the bottom conducting plane through two lateral conducting sidewalls of separation d. A close look of Fig. 4.1 shows that MSTL is symmetric about the *yoz* plane and uniform along the propagation direction of guided wave (z-axis in Fig. 4.1(a)); it is longitudinally uniform. On the other hand, MSTL is asymmetric and inhomogeneous with respect to the y-axis because of the hybrid air (for $y > h + t$) and dielectric regions (for $0 < y < h$). For this reason, the two-conductor MSTL cannot support the guidance of a pure TEM wave, resulting from an impossible phase-matching condition at the dielectric-air interface. As briefly mentioned earlier, MSTL can be viewed as a composite transmission line [55] from which we can see the footprints of different well-known transmission media, such as microstrip line, slotline, conductor-backed CPW (CBCPW), dielectric-filled RWG (i.e., SIW), half-mode SIW (or called half-width microstrip line), etc. This feature may cause higher-order modes in MSTL, which will be discussed in more detail in Section 4.5. Given the similarity of structures, we focus on comparing MSTL in this section with the conventional CBCPW and RWG in terms of structural features, wave guidance, field distributions, and frequency characteristics.

Two practical MSTL examples operating in distinct frequency ranges are considered for a comprehensive study. One operates from dc to 60 GHz, and the other operates from dc to 500 GHz

(proposed in [46]), which are called MSTL I and MSTL II for simplicity, respectively. Their dimensions are listed in Table 4.1. For the according discussions of these MSTLs later, it is necessary to introduce three characteristic frequencies, f_{ms1}, f_{ms}, and f_{ms2} ($f_{ms1} < f_{ms} < f_{ms2}$), ahead of time, which will be defined in Section 4.4 to quantify the mode selectivity in MSTL. When frequency f is below f_{ms1} ($f < f_{ms1}$), the dominant mode of MSTL is the quasi-TEM microstrip mode. In contrast, when f is above f_{ms2} ($f > f_{ms2}$), the dominant mode is converted to the quasi-TE_{10} waveguide mode. At a frequency in between (e.g., f_{ms}), the dominant mode is a kind of hybrid "transition" mode. In the following discussions, we will focus on the results and phenomena at these characteristic frequencies because of their applicability for different MSTLs.

Full-wave analyses are carried out using a commercially available finite-element method software package (ANSYS Electronics Desktop 2017) [56], [57]. Given that the dominant mode of MSTL would change with frequency, wave ports supporting various propagation modes are used to feed the uniform MSTL, as labeled in Fig. 4.1(a). For simplicity of analysis, the lateral sidewalls are modeled by conducting solid walls if no otherwise specified. Surface roughness of conductors, skin effect, and material dispersion are not considered in the simulation models.

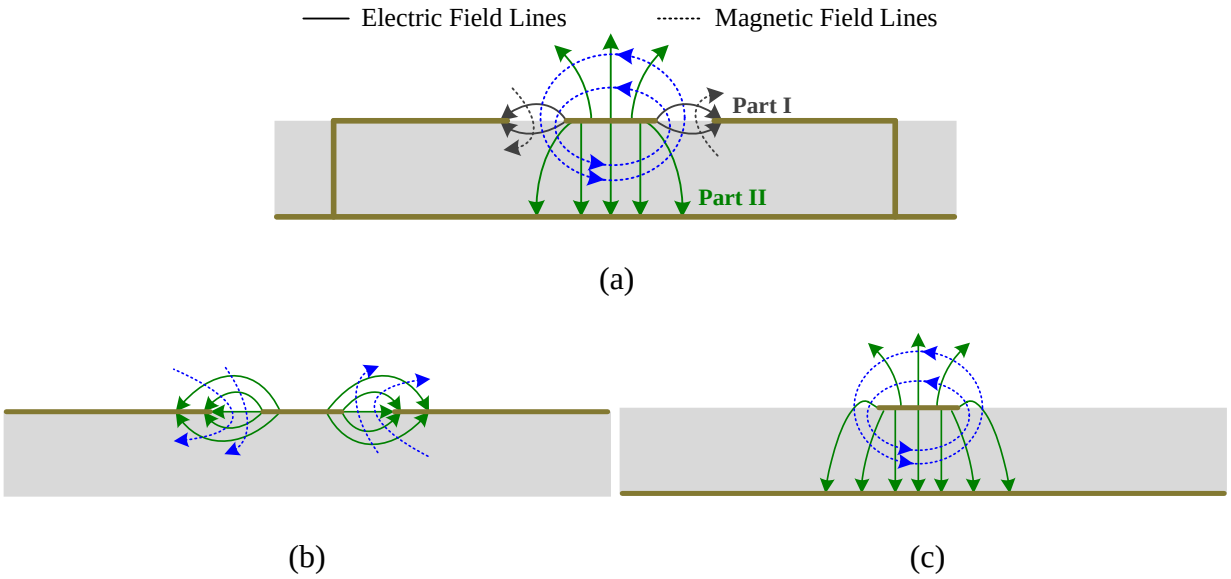

Figure 4.2 Cross-sectional electric and magnetic field lines in (a) MSTL when frequency f is below f_{ms1} (or CBCPW), (b) CPW, and in (c) microstrip line

4.2.1 Comparison with CBCPW

As we can see from Fig. 4.1, the typical MSTL structure itself resembles a conventional CBCPW with bilateral sidewalls [58-60] (also called channelized CPW [61] or grounded CPW [62]). There are, however, many important differences between MSTL and CBCPW, such as dominant modes, frequency characteristics, and excitation methods. The most significant and substantial difference lies in their dominant modes. The dominant mode of MSTL can be converted from a quasi-TEM microstrip mode to a quasi-TE_{10} waveguide mode with increasing frequency (i.e., mode selectivity), whereas the dominant quasi-TEM CPW mode of CBCPW remains unchanged over its frequency range of operation. The mode selectivity contributes to unique properties of MSTL, such as low loss, low dispersion, and ultra-broad frequency range of operation [46-48], which are rather challenging to obtain for a conventional CBCPW. Another difference is the excitation method. For a CBCPW, the feed point is generally located directly on the central strip [63]. In contrast, it is necessary for MSTL to feed the whole cross-sectional area with the aid of specially designed transitions, which will be discussed in Section 4.6.1.

In this subsection, the dominant mode of MSTL at frequencies f below f_{ms1} ($f < f_{ms1}$) is discussed and compared to that of CBCPW. A sketch of the cross-sectional electric and magnetic field lines for the dominant mode of MSTL when $f < f_{ms1}$ is given in Fig. 4.2(a). For comparison, the field lines for the standard CPW mode in a CPW and for the standard microstrip mode in a microstrip line are plotted in Figs. 4.2(b) and (c). The electric and magnetic field lines in MSTL are roughly divided into two parts, Part I (gray lines) and Part II (color lines) (as labeled in Fig. 4.2(a)), to simplify the following analysis. Part I is similar to the field lines in the CPW (see Fig. 4.2(b)), which is primarily determined by the central strip together with the side conducting planes of MSTL. Part II is similar to the field lines in the microstrip line (see Fig. 4.2(c)), which is primarily determined by the central strip together with the bottom conducting plane of MSTL. The dominant mode of MSTL at low frequencies ($f < f_{ms1}$), in fact, becomes analogous to that of a CPW or that of a microstrip line depending on the dimensions. For example, increasing the slit width s or decreasing the substrate thickness h of MSTL (Fig. 4.1) while keeping other parameters fixed can weaken Part I but strengthen Part II. That is, the dominant mode of MSTL tends to resemble that of a conventional microstrip line (i.e., quasi-TEM microstrip mode). On the other hand, as the slit width s decreases or the substrate thickness h increases, the dominant mode of MSTL tends to

resemble that of a conventional CPW (i.e., quasi-TEM CPW mode). In fact, the field lines in the conventional CBCPW are similar to those in MSTL in this case [58]. A similar phenomenon of the mode also exists in CBCPW [58], [64]. The CPW mode is generally preferable to the microstrip mode in CBCPW by strengthening Part I and weakening Part II. On the contrary, the microstrip mode is preferable in MSTL when $f < f_{ms1}$. The main reason is that the effective permittivity for the microstrip mode is in a level close to that for the high-frequency waveguide mode in MSTL, thus maintaining a relatively stable effective permittivity (i.e., low frequency dispersion) over the frequency range of interest [48]. For the two MSTL examples considered in this work, the dielectric substrates used are extremely thin ($h < (w + 2s)/4$) so that their dominant modes are the quasi-TEM microstrip mode when $f < f_{ms1}$. In one word, MSTL performs similarly to a microstrip line rather than a CBCPW or a CPW when frequency f is below f_{ms1}. When frequency continues to increase, the dominant mode of MSTL will be converted to a quasi-TE_{10} waveguide mode, becoming similar to the dominant mode of RWG, as discussed later.

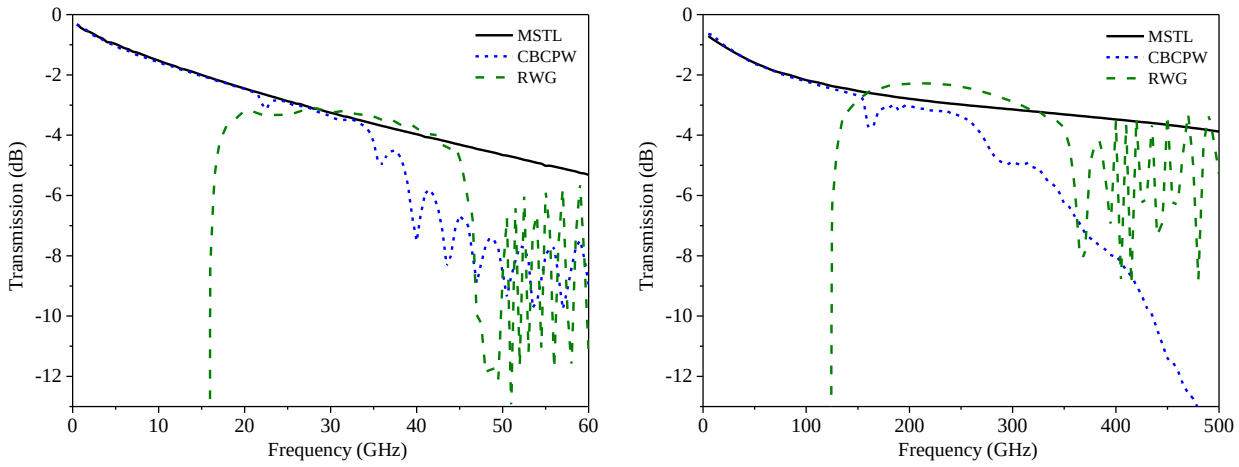

(a) (b)

Figure 4.3 Comparison between transmission responses of MSTLs and CBCPW and RWG counterparts. (a) MSTL I. (b) MSTL II

To demonstrate the difference of performance between MSTL and CBCPW, simulated transmission responses of the two MSTL examples (see Table 4.1) and their CBCPW counterparts are all plotted

in Fig. 4.3 for comparison. To emulate practical situations and to facilitate measurement interfaces, we use the microstrip-to-MSTL and microstrip-to-CBCPW feed lines into the corresponding simulation models. The overall lengths of MSTL I and MSTL II including transitions (see Section 4.6.1) are 76 and 14 mm, respectively. The CBCPW counterparts have the same shapes and sizes but different excitation methods [65]. From Fig. 4.3, the transmission curves of both MSTL I and MSTL II are smooth over the whole frequency ranges. In contrast, many sharp dips appear at high frequencies in the curves of CBCPW counterparts. This is because the resonances and leakage of laterally spreading fields cause these sharp dips, thus severely degrading the performance of CBCPWs [65]-[67].

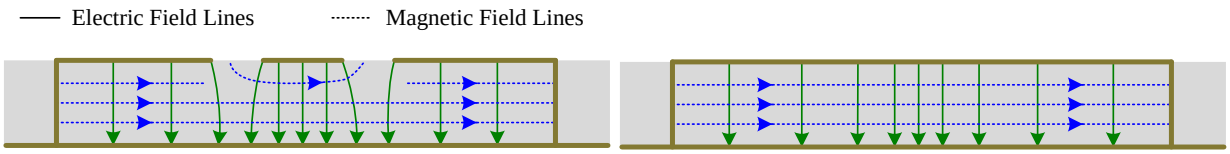

(a) (b)

Figure 4.4 Cross-sectional electric and magnetic field lines in (a) MSTL when frequency f is above f_{ms2} and in (b) RWG

4.2.2 Comparison with RWG

In addition to CBCPW, the typical MSTL structure also resembles a dielectric-filled RWG with two additional slits etched symmetrically in the top conducting plane. This feature contributes to the guided wave performance of MSTL at frequencies f above f_{ms2} ($f > f_{ms2}$). That is, MSTL performs similarly to a dielectric-filled RWG when $f > f_{ms2}$. In this case, the dominant mode of MSTL tends to resemble the dominant TE_{10} mode of RWG; in fact, it is a quasi-TE_{10} waveguide mode in MSTL because of the additional slits [25]. It should be noted that MSTL is a two-conductor transmission medium that its dominant mode does not possess a cutoff frequency. This high-frequency waveguide mode in MSTL is, in fact, converted from the low-frequency microstrip mode as frequency increases. A sketch of the electric and magnetic field lines for the dominant quasi-TE_{10} waveguide mode of MSTL at high frequencies ($f > f_{ms2}$) is described in Fig. 4.4(a), compared

to those for the dominant TE_{10} mode of the dielectric-filled RWG in Fig. 4.4(b). It can be observed that the field lines in MSTL in this case are similar to those in RWG except for a slight difference around the two slits. This indicates that MSTL should have the guided wave performance similar to that of a dielectric-filled RWG when $f > f_{ms2}$.

Similarly, the simulated transmission curves of the dielectric-filled RWG counterparts (i.e., SIWs) of both MSTL I and MSTL II are obtained and plotted in Fig. 4.3 for comparison. The microstrip-to-SIW transitions presented in [68] are used in the simulation models to emulate practical situations including measurement purposes. As can be seen, the RWG counterparts operate in narrow frequency ranges, resulting from the low-frequency cutoff and excitation of higher-order modes (e.g., TE_{30} mode) [69]. These MSTLs and their RWG counterparts show similar transmission responses over the common frequency ranges. The difference between the power losses, as a result of the additional slits in MSTLs, is negligible when considering practical influence factors such as conductor surface roughness and skin depth. This will be demonstrated by comparing the measured transmission responses of MSTL I and its RWG counterpart in Section 4.6 (see Fig. 4.20).

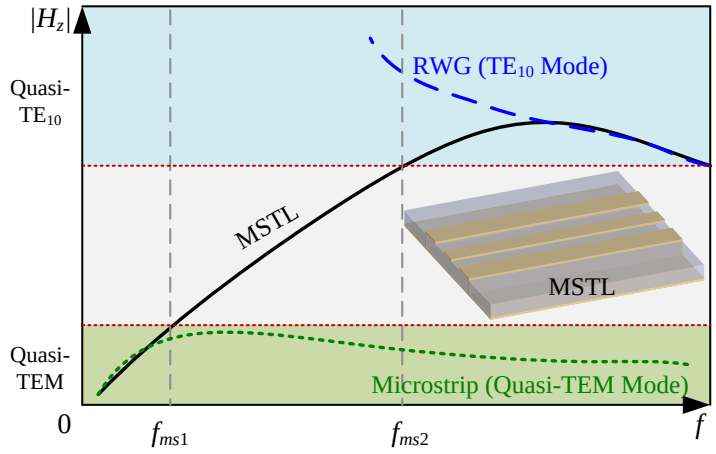

Figure 4.5 Schematic diagram of mode conversion in MSTL on the basis of the frequency-related variable longitudinal magnetic field component H_z

4.3 Mode selectivity

Now consider the phenomenon of mode selectivity occurring in MSTL in this section. As we know, the change of the dominant mode of MSTL is reflected directly in the change of electric and magnetic field distributions. Therefore, field distributions for the dominant mode of MSTL are examined thoroughly, which turn out to be an important physical evidence of mode selectivity. The orthogonality relations between the hybrid TM and TE modes in MSTL are then presented, providing a theoretical foundation of mode selectivity.

4.3.1 Physical evidence

To better understand the mechanism of physics, let us begin with the consideration of a simple microstrip line that supports the propagation of quasi-TEM mode. The use of terminology "quasi-TEM mode" is directly related to the existence of a longitudinal magnetic field component, which is generally negligible compared to its dominant TEM field components. The occurrence of such a longitudinal component is caused by the cross-sectional non-uniformity or discontinuity along the microstrip line. Generally, this longitudinal field may become more and more pronounced as frequency increases. This can be observed as dispersion becomes stronger. Still, the longitudinal field is relatively weak in most cases as long as the geometrical conditions of relevance favor the guidance of a quasi-TEM mode. Of course, this phenomenon may create a favorable condition for high-order mode leakage and also for high-order mode generations if a longitudinal discontinuity is introduced. On the other hand, one may also imagine that there is a special uniform geometry that can be designed and used to favor and strengthen this longitudinal magnetic field component such that it cannot be negligible beyond certain frequency point. Therefore, the resulting mode would be characterized by three field components, which in fact form a quasi-TE mode in this case. This would create a new mode conversion or simply MSTL, which spells out the fundamental physical mechanism. The schematic diagram of this kind of mode conversion is depicted in Fig. 4.5. As can be seen, the magnitude of the longitudinal magnetic field component $|H_z|$ for the dominant mode of MSTL continues to increase as frequency increases. As a result, $|H_z|$ of MSTL is becoming higher than that of microstrip (quasi-TEM mode) at around f_{ms1} and then approaching that of RWG (TE_{10} mode) at around f_{ms2}. This change of the important field component H_z results in the mode conversion between the quasi-TEM mode and the quasi-TE_{10} mode in MSTL. This

phenomenon will be further demonstrated and discussed by examining the practical field distributions in MSTL as follows.

For MSTL II, the field distribution curves for all the field components of the dominant mode have been extracted and discussed in [53], showing that the fields in MSTL smoothly change with frequency. The electric and magnetic field lines for the variable dominant mode of MSTL are also compared to those in conventional transmission media in the preceding section. In the present subsection, we further investigate and look into the field distributions in MSTL, which are compared to those in the RWG and microstrip counterparts at specific frequency points.

Table 4.2 Electric field distributions in MSTL, microstrip line, and RWG

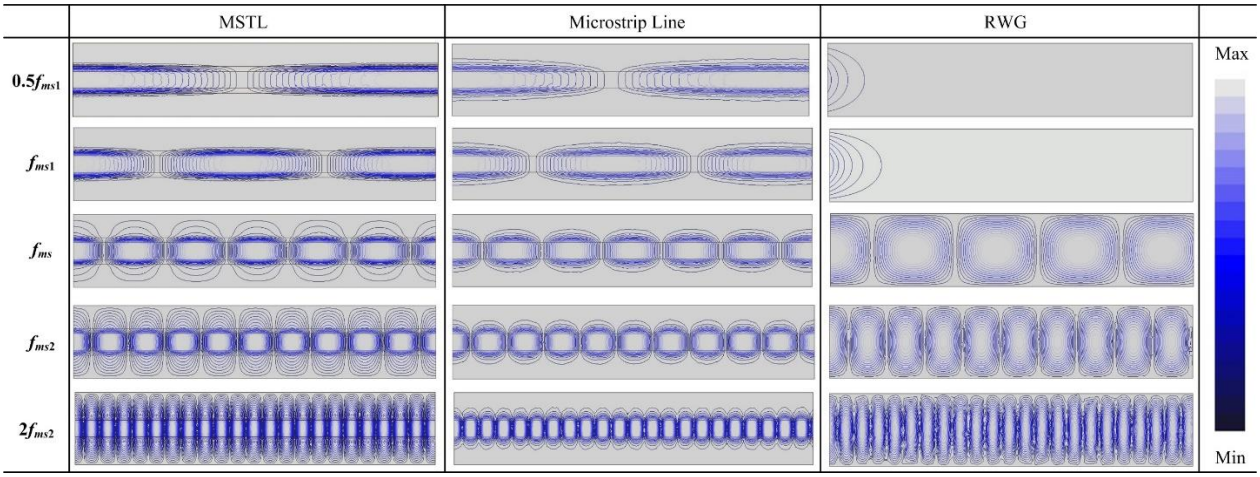

Table 4.3 Magnetic field distributions in MSTL, microstrip line, and RWG

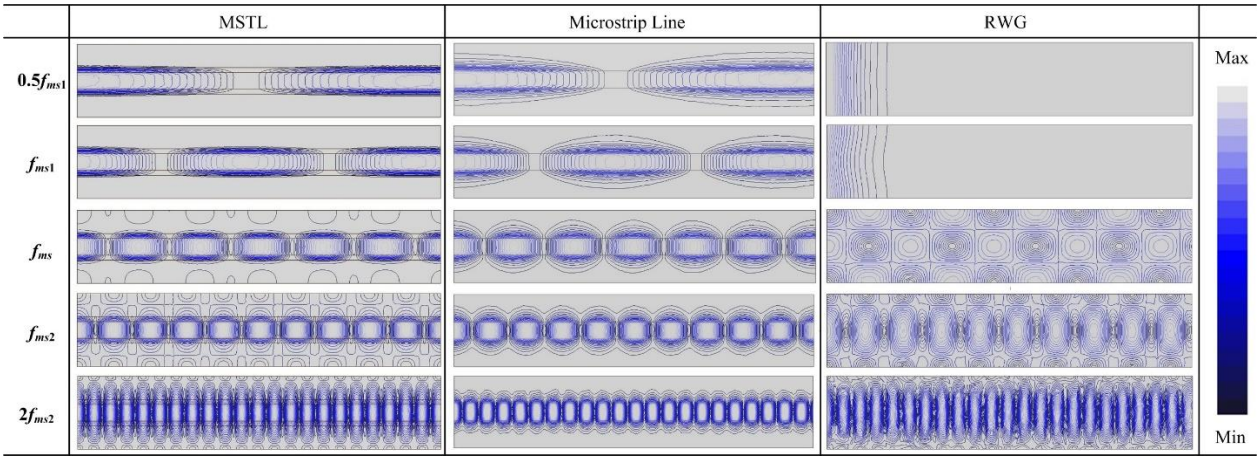

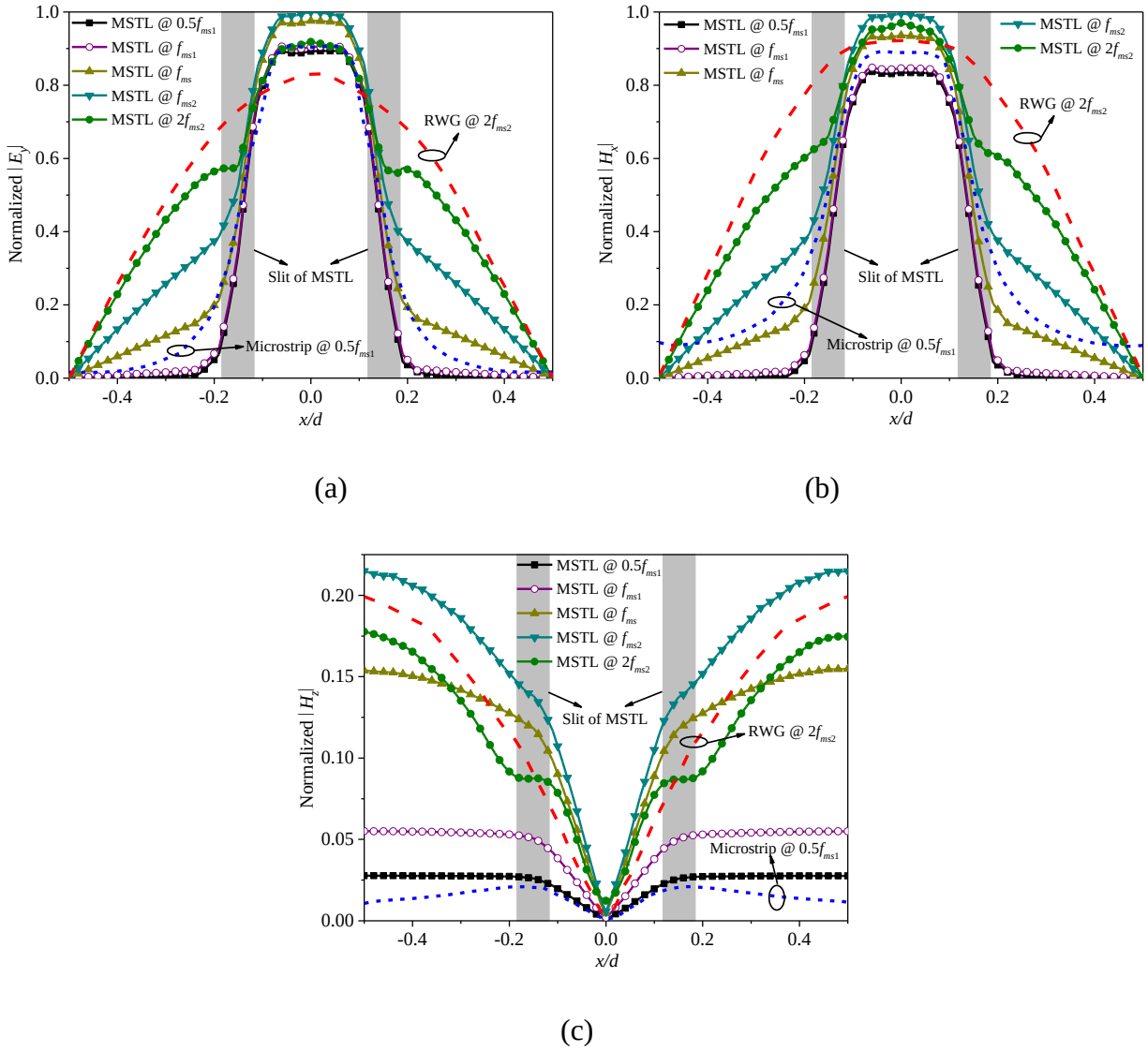

Figure 4.6 Normalized field magnitude curves of MSTL and the microstrip and RWG counterparts along the *x*-axis in Fig. 4.1. (a) E_y field component. (b) H_x field component. (c) H_z field component

In different MSTLs (e.g., MSTL I and MSTL II), field distributions at corresponding frequencies are almost the same, as a result of the same operating mechanism (i.e., mode selectivity). Electric and magnetic field distributions for the dominant modes of MSTLs at $0.5f_{ms1}$, f_{ms1}, f_{ms}, f_{ms2}, and $2f_{ms2}$ are considered here, as listed in Table 4.2 and Table 4.3. It should be emphasized that these frequency points are specified to simplify the unified analyses for different MSTLs. In fact, one can choose arbitrary frequencies; however, we suggest considering the frequencies across the

different frequency regions (to be specified in Section 4.4) for a clear comparison. Similarly, the field distributions for the dominant modes of the microstrip and RWG counterparts are also sketched and listed in Table 4.2 and Table 4.3 for comparison. The field distributions for the dominant mode of MSTL at different frequencies are different, as expected. To be specific, the fields in MSTL at $0.5f_{ms1}$ and f_{ms1} are bounded around the central strip, which are analogous to those in the microstrip counterpart. The dominant TE_{10} mode of RWG is below cutoff at these frequencies. At f_{ms2} and $2f_{ms2}$, partial fields spread to the side parts of MSTL, thus tending to resemble those in the RWG counterpart. This change of the field distributions in MSTL indicates the change of the dominant mode of MSTL. That is, the dominant mode of MSTL at a low frequency (e.g., $0.5f_{ms1}$ or f_{ms1}) is analogous to the dominant mode of the microstrip counterpart; that is a quasi-TEM microstrip mode. As frequency increases to a relatively high frequency (e.g., f_{ms2} or $2f_{ms2}$), the dominant mode of MSTL tends to be resemble the dominant mode of RWG; that is a quasi-TE_{10} waveguide mode. At a frequency in between (e.g., f_{ms}), the dominant mode of MSTL is a hybrid "transition" mode. The change of the dominant mode of MSTL is indeed describable by the mode selectivity, which occurs smoothly as frequency increases [53]. The reason is that the boundary conditions "seen" by the dominant propagating mode of MSTL change gradually with increasing frequency. Specifically, the boundary conditions for the dominant mode of MSTL at a low frequency (e.g., $0.5f_{ms1}$ or f_{ms1}) are almost the same as those for the dominant mode of the microstrip counterpart. As frequency increases to a higher frequency (e.g., f_{ms2} or $2f_{ms2}$), the side conducting planes together with the sidewalls (see Fig. 4.1) have a much-pronounced effect. Hence, the boundary conditions for the dominant mode of MSTL in this case become analogous to those for the dominant mode of the RWG counterpart.

In addition to the electric and magnetic field distributions in MSTL, it is worthwhile to further examine the major field components of the dominant mode of MSTL. As we know from [53], E_y, H_x, and H_z are the major field components. Their magnitude curves along the x-axis (at $y = h/2$) in Fig. 4.1 at $0.5f_{ms1}$, f_{ms1}, f_{ms}, f_{ms2}, and $2f_{ms2}$ are extracted using the HFSS field calculator [57], as plotted in Fig. 4.6. The field magnitude curves are normalized to the maximum magnitudes of the electric field component and the magnetic field component. The normalized field magnitude curves of the microstrip counterpart at $0.5f_{ms1}$ and the RWG counterpart at $2f_{ms2}$ are also plotted in Fig. 4.6 for comparison. For MSTL, the major field components (E_y, H_x, and H_z) have a noticeable change in

their distribution shape and magnitude as frequency increases gradually. It is found that the $|E_y|$, $|H_x|$, and $|H_z|$ curves of MSTL at $0.5f_{ms1}$ are similar to those of the microstrip counterpart at $0.5f_{ms1}$. As frequency continues to increase from $0.5f_{ms1}$ to $2f_{ms2}$, both the left and right parts of all the field curves of MSTL rise remarkably. As a result, the field curves of MSTL are becoming similar to those of the RWG counterpart, especially at $2f_{ms2}$. For the microstrip and RWG counterparts, on the other hand, the field magnitude curves have a slight change with increasing frequency [41], [53], [70]. This reveals the conversion of the dominant mode of MSTL. Given the changes of other field components E_x, H_y, and E_z of MSTL (both $|E_x|$ and $|H_y|$ decrease with frequency, and $|E_z| \approx 0$) [53], we can conclude that the dominant mode of MSTL is changed smoothly from a quasi-TEM microstrip mode to a quasi-TE_{10} waveguide mode with increasing frequency. The examination, comparison, and analyses of the field distributions in MSTL and its counterparts provide a substantial physics-based proof of the mode selectivity in MSTL.

4.3.2 Theoretical foundation

MSTL is asymmetric and inhomogeneous with respect to the *y*-axis because of the different (or hybrid) dielectric regions (see Fig. 4.1), as described in Section 4.2. For this reason, MSTL cannot support a pure dominant TEM mode or a pure dominant TE (or TM) waveguide mode. As described in Chapter 3 in [33] and [71], the fields in a composite transmission system (e.g., MSTL) can be expanded into a complete set of known modes. These known modes do not individually satisfy the boundary conditions of the composite system and hence couple to each other. In fact, the exact fields in MSTL constitute a hybrid TM-TE wave, as in a microstrip line or a CPW. The TE^y and TM^y hybrid modes with respect to the *y* direction are considered to simplify the study of the air-dielectric interface in the *y* direction. Due to the unbounded *y* and *z* directions (see Fig. 4.1), the hybrid TE^y and TM^y modes have complex propagation factors in the *y* and *z* directions, k_y and k_z. For a laterally shielded top-open transmission line like MSTL, the hybrid TE^y and TM^y modes satisfy the following orthogonality relations [72]:

$$P_{m,n}^{i,j} = \int_{-d/2}^{d/2} \left[\vec{e}_m^{\,i}(x) \times \left(\vec{h}_n^{\,j} \right)^* (x) \right] \cdot \hat{y} \cdot \mathrm{d}x = \begin{cases} 1, & \text{if } m = n \text{ and } i = j \\ 0, & \text{if } m \neq n \text{ and } i \neq j \\ C, & \text{if } m = n \text{ and } i \neq j \end{cases} \tag{4.1}$$

where $\vec{e}_m^{\,i}$ and $\vec{h}_n^{\,j}$ are the transverse vector modal functions with respect to the *y* direction. The indexes *m* and *n* represent the orders of modes, and *i* and *j* are used to distinguish between TE and TM polarizations with respect to the *y* direction. From [72], we know that the parameter *C* in (4.1) is nonzero as long as k_z is not a pure real number. These types of modes exist in MSTL because of the evanescent and leaky waves in the *z* propagation direction. This fact indicates that complex hybrid modes with the same orders (i.e., $m = n$) but different polarizations (i.e., $i \neq j$) are nonorthogonal. That is, a significant coupling effect can occur along the transverse direction (*y*-axis) between the TE^y and TM^y hybrid modes.

In MSTL, the TE^y modes could be coupled to the same-order TM^y modes with increasing frequency. The strength of coupling would decrease as the order ($m = n$) of the coupled modes increases [72]. This is consistent with the change of the field distributions in MSTL. As detailed in [53], when frequency increases, the magnitudes of the field components E_y, H_x, and H_z increase, and the magnitude of E_z is still close to zero, whereas the magnitudes of E_x and H_y decrease gradually. In addition to the change in magnitudes, there is an obvious change in shapes of the distribution curves of the field components [53]. As a result of the significant coupling effect, the change of field distributions in MSTL is reflected in the change of the dominant mode as a whole, i.e., mode selectivity. We emphasize that the dominant quasi-TEM mode at low frequencies and the dominant quasi-TE_{10} mode at high frequencies are confirmed by rigorously examining the field distributions at different frequencies. The above analysis provides a theoretical foundation of the phenomenon of mode selectivity in MSTL.

4.4 Characteristic frequencies

In the preceding section, it has been verified that the dominant mode of MSTL appears in two dissimilar forms (quasi-TEM and quasi-TE_{10} modes), supported by the mode selectivity. A more rigorous analysis of the mode selectivity is carried out in this section. The characteristic frequencies, f_{ms1}, f_{ms2}, and f_{ms}, are first defined and formulated. With these frequency points, the whole frequency range of MSTL can then be divided into several frequency regions, Region I, Region II (Region II-A and Region II-B), and Region III, associated with the variable dominant mode.

To quantify the mode selectivity in MSTL, it is necessary to treat and then model the quasi-TEM

and quasi-TE_{10} modes separately. For the individual quasi-TEM microstrip mode, the sidewalls (see Fig. 4.1) are placed close to the slits. This leads to that the "appearance" (cutoff) frequency of the waveguide mode increases and is thus completely outside the frequency ranges of interest. It should be noted that the sidewalls should not be too close to the slits, which may result in undesirable interference with the central bound fields of the quasi-TEM mode [73]. For the individual quasi-TE_{10} waveguide mode, all the top conductors (see Fig. 4.1) are set at the same voltage level. In fact, this realizes a dielectric-filled RWG with two symmetric slits etched in the top conducting plane, called two-slit RWG for short [74], which has a dominant quasi-TE_{10} mode [25]. In this way, the individual quasi-TEM and quasi-TE_{10} modes in MSTL can be analyzed numerically. The individual quasi-TE_{10} mode is also analyzed using empirical equations, which will be given later. The individual quasi-TEM mode is considerably similar to the dominant mode of a conventional microstrip line. Therefore, it is convenient to determine the propagation characteristics of the individual quasi-TEM mode by using the well-known equations about those of a microstrip line presented in [41] and [70], as well as considering the effect of the side conducting planes [75]. It is therefore not repeated in this work.

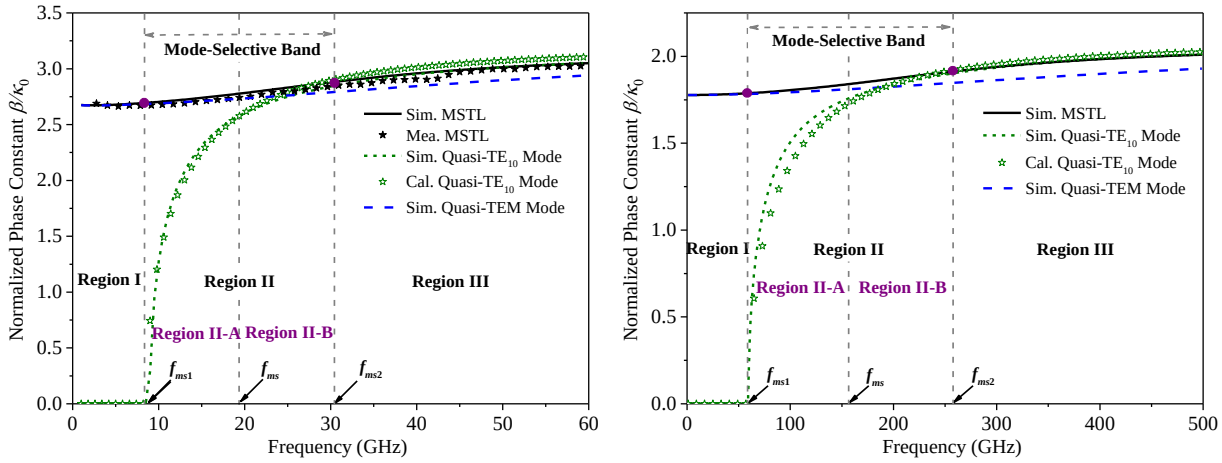

Figure 4.7 Comparison between normalized phase constants of MSTLs, individual quasi-TEM modes, and individual quasi-TE_{10} modes. (a) MSTL I. (b) MSTL II

Both MSTL I and MSTL II continue to be considered as examples for the following discussions. With the simulation models of MSTL and of the individual quasi-TEM and quasi-TE_{10} modes, their phase constants β are obtained and plotted in Fig. 4.7, normalized to the free-space phase constant k_0. It is found that the curves of the normalized phase constants of both MSTL I and MSTL II are continuous and flat all over the frequency ranges, indicating low frequency dispersion [46]-[48]. In Figs. 4.7(a) and (b), three critical frequency points, f_{ms1}, f_{ms2}, and f_{ms}, and several frequency regions, Region I, Region II (Region II-A and Region II-B), and Region III, are clearly labeled, which will be defined and discussed in more detail.

4.4.1 Appearance frequency of quasi-TE_{10} mode f_{ms1}

The first characteristic frequency f_{ms1} is defined as the "appearance" frequency of the quasi-TE_{10} mode in MSTL, meaning the quasi-TE_{10} mode begins to appear at this frequency. This indicates that the dominant mode of MSTL is the quasi-TEM mode when frequency f is below f_{ms1} ($f < f_{ms1}$). As seen from Fig. 4.7(a) or Fig. 4.7(b), f_{ms1} corresponds to the high-frequency end of the overlapping curve of MSTL and the individual quasi-TEM mode. This characteristic frequency is also the cutoff frequency of the individual quasi-TE_{10} mode. Its value can be determined with the help of the proposed models of the individual modes. It is also possible to determine its value directly by calculating the cutoff frequency of the individual quasi-TE_{10} mode. As described before, the individual quasi-TE_{10} mode can be modeled by a two-slit RWG. Many methods can be used to analyze slitted RWGs, such as transverse resonance analysis [25], [76], and numerical modeling [74]. In this work, we propose a simple but rigorous method to analyze the two-slit RWG (i.e., the individual quasi-TE_{10} mode). It is based on an assumption that the two-slit RWG evolves from a single-slit RWG, finally traced back to a dielectric-filled RWG. The method is detailed in Appendix. On the basis of the proposed method, an empirical equation is given to calculate the characteristic frequency f_{ms1} as

$$f_{ms1} = \frac{2}{M\sqrt{\mu_0\varepsilon_0(\varepsilon_r + 0.34)}} - \frac{1}{2d\sqrt{\mu_0\varepsilon_0\varepsilon_r}} \tag{4.2}$$

where μ_0 and ε_0 are the permeability and permittivity in free space, and ε_r represents the relative permittivity of the dielectric substrate used. The variable M is formulated as

$$M = \begin{cases} 2d + 3.69m + 2h - 2.25s & \text{for } s \geq 0.7h \\ 2d + 3.69m + \dfrac{h^2}{s} - h & \text{for } s < 0.7h \end{cases} \tag{4.3}$$

where all the parameters have been defined in Section 4.2. With the given dimensions (see Table 4.1), the characteristic frequencies f_{ms1} for MSTL I and MSTL II are calculated to be 8.6 and 59 GHz, respectively, in agreement with the simulated 8.5 and 58 GHz. The phase constant of the individual quasi-TE_{10} mode is also formulated (see (4.12) in Appendix) and plotted in Fig. 4.7. It can be observed that the calculated phase constants of the individual quasi-TE_{10} modes agree well with the simulated ones over the whole frequency ranges.

4.4.2 Maximum-coupling frequency f_{ms2}

The second characteristic frequency f_{ms2} is defined as the maximum-coupling frequency at which the maximum mode coupling between the quasi-TEM and quasi-TE_{10} modes takes place. This indicates that the dominant mode of MSTL is converted to the quasi-TE_{10} mode when frequency f is above f_{ms2} ($f > f_{ms2}$). With reference to Fig. 4.7(a) or Fig. 4.7(b), f_{ms2} corresponds to the low-frequency end of the overlapping curve of MSTL and the individual quasi-TE_{10} mode. This phenomenon is consistent with the coupled-mode theory [54], [77]. With a curve-fitting method [78], [18], an empirical equation is proposed to calculate this characteristic frequency as

$$f_{ms2} = \frac{1}{\left[1.34(d-h) - 1.55(w-2s)\right]\sqrt{\mu_0 \varepsilon_0 (\varepsilon_r - 1.23)}}. \tag{4.4}$$

The accuracy of (4.4) is verified through taking MSTL II as an example. As detailed in Appendix, comparison results indicate that, within the design region of MSTL defined in [48], (4.4) can be used to accurately predict the characteristic frequency f_{ms2} with a calculation error below 5%. For MSTL I and MSTL II, the characteristic frequency f_{ms2} calculated by (4.4) are 29.1 and 261 GHz, respectively, in agreement with the simulated 30.5 and 260 GHz. The frequency ranges of both MSTL I (dc to 60 GHz) and MSTL II (dc to 500 GHz) considered in this work are from dc to around $2f_{ms2}$, limited basically by the fabrication and measurement techniques, which will be described in Section 4.6.

Table 4.4 Simulated and calculated characteristic frequencies (unit: GHz)

		f_{ms1}	f_{ms}	f_{ms2}	Mode-Selective Band
MSTL I	Sim.	8.5	19.5	30.5	22 (8.5-30.5)
(dc-60 GHz)	Cal.	8.6	18.85	29.1	20.5 (8.6-29.1)
MSTL II	Sim.	58	159	260	202 (58-260)
(dc-500 GHz)	Cal.	59	160	261	202 (59-261)

Table 4.5 Frequency regions and corresponding dominant modes

Region I	Region II		Region III
	$f_{ms1} \le f \le f_{ms2}$		
$f < f_{ms1}$	Region II-A	Region II-B	$f > f_{ms2}$
	$f_{ms1} \le f < f_{ms}$	$f_{ms} < f \le f_{ms2}$	
Quasi-TEM Mode	Hybrid Mode		Quasi-TE_{10} Mode
	Quasi-TEM Mode	Quasi-TE_{10} Mode	

4.4.3 Mode-selective frequency f_{ms}

As described above, the dominant mode of MSTL is the quasi-TEM mode when $f < f_{ms1}$ and the quasi-TE_{10} mode when $f > f_{ms2}$, respectively. Within the frequency range from f_{ms1} to f_{ms2} ($f_{ms1} \le f \le f_{ms2}$), the dominant mode of MSTL experiences a gradual change from the quasi-TEM mode to the quasi-TE_{10} mode with increasing frequency. This change is evident from the field distributions [53]. This frequency range is therefore defined as the mode-selective band, as labeled in Fig. 4.7. The dominant mode of MSTL within this frequency band is a hybrid "transition" mode varying with frequency. A characteristic frequency termed the mode-selective frequency f_{ms} is defined to bound the mode-selective band in this paper. Due to the gradual change of the field distributions, the frequency point f_{ms} should be located around the center of the mode-selective band, thereby expressed as

$$f_{ms} \approx \frac{f_{ms1} + f_{ms2}}{2}. \tag{4.5}$$

The calculated f_{ms} for MSTL I and MSTL II are 18.85 and 160 GHz, respectively. The simulated and calculated values of all the characteristic frequencies are listed in Table 4.4. We can conclude that, within the mode-selective band ($f_{ms1} \le f \le f_{ms2}$), the quasi-TEM mode prevails when frequency f is below f_{ms} ($f < f_{ms}$), whereas the quasi-TE_{10} mode prevails when f is above f_{ms} ($f > f_{ms}$).

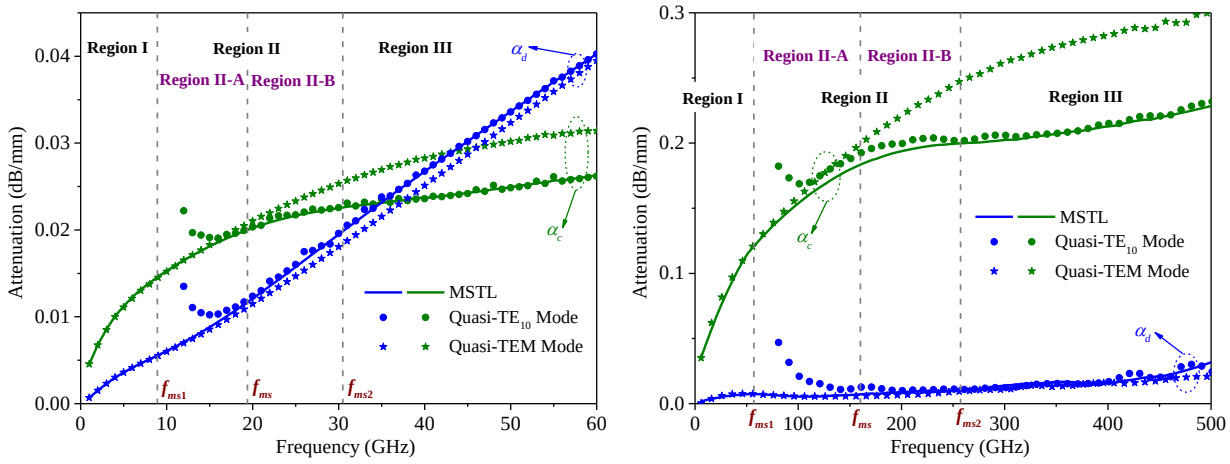

(a) (b)

Figure 4.8 Comparison between attenuation constants of MSTLs, individual quasi-TEM modes, and individual quasi-TE_{10} modes. (a) MSTL I. (b) MSTL II

With these characteristic frequencies, the whole frequency range of MSTL can be divided into several frequency regions including Region I, Region II (Region II-A and Region II-B), and Region III, as labeled in Figs. 4.7(a) and (b). In Region I ($f < f_{ms1}$), the dominant mode of MSTL is the quasi-TEM mode and its frequency characteristics are remarkably analogous to those of a microstrip line. In Region II ($f_{ms1} \le f \le f_{ms2}$), i.e., mode-selective band, the dominant mode is a hybrid "transition" mode performing as a quasi-TEM mode in Region II-A ($f_{ms1} \le f < f_{ms}$) and as a quasi-TE_{10} mode in Region II-B ($f_{ms} < f \le f_{ms2}$). In Region III ($f > f_{ms2}$), the dominant propagating mode of MSTL is the quasi-TE_{10} mode; its frequency characteristics closely resemble those of a dielectric-filled RWG. These conclusions are tabulated in Table 4.5. In one word, the mode selectivity enables the longitudinally uniform MSTL to operate in a dominant mode varying with frequency. It can be rigorously treated using these defined characteristic frequencies.

4.5 Attenuation characteristics and higher-order modes

The phase constants of both MSTL I and MSTL II have been examined when defining the characteristic frequencies in the preceding section (see Fig. 4.7). It implies that the phase characteristics of MSTL can be determined by treating the individual modes. In this section, we

focus on the attenuation characteristics of both MSTL I and MSTL II. We will also briefly discuss the higher-order modes in these MSTLs. As can be seen from Fig. 4.1, MSTL is a sort of composite transmission line from which we can see the footprints of different well-known transmission media. This feature may lead to higher-order modes in MSTL. In this section, the first three higher-order modes are examined and briefly discussed, which could be generated in both MSTL I and MSTL II over the frequency ranges of interest, i.e., dc to $2f_{ms2}$.

4.5.1 Attenuation characteristics

In general, the signal attenuation in a transmission line or waveguide is caused by dielectric loss and conductor loss [41]. The total attenuation constant α can be expressed as $\alpha = \alpha_d + \alpha_c$ where α_d and α_c represent the attenuation due to dielectric loss and the attenuation due to conductor loss, respectively. Fig. 4.8 shows the curves of α_d and α_c of both MSTL I and MSTL II, compared to those of the individual quasi-TEM and quasi-TE_{10} modes separately modeled in Section 4.4. It is seen that the attenuations, α_d and α_c, of these MSTLs are almost the same as those of the quasi-TEM modes when frequency f is below f_{ms} ($f < f_{ms}$) and as those of the quasi-TE_{10} modes when $f > f_{ms}$, respectively. This phenomenon is consistent with the previous comparison results among their phase constants (see Fig. 4.7). It implies that the attenuation characteristic of MSTL can be determined by separately treating the individual modes.

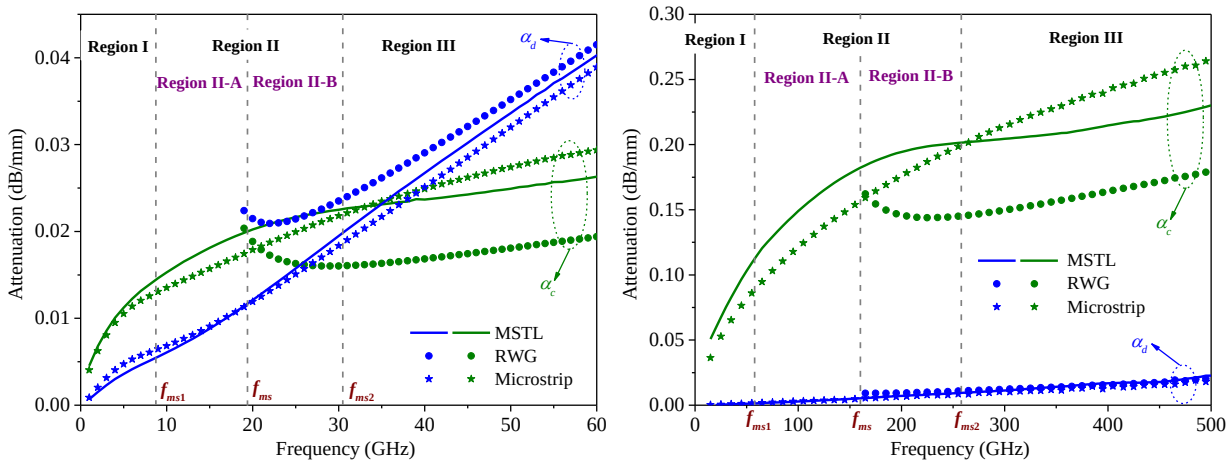

(a) (b)

Figure 4.9 Comparison between attenuation constants of MSTLs and RWG and microstrip counterparts. (a) MSTL I. (b) MSTL II

The simulated attenuation constants (α_d and α_c) of both MSTL I and MSTL II are compared to those of the RWG and microstrip counterparts for a further presentation of the attenuation characteristics of MSTL, as plotted in Fig. 4.9. The difference between the attenuation constants α_d of both MSTL I and MSTL II and their microstrip counterparts are small, especially when $f < f_{ms}$. The difference among the total attenuation constants α of these transmission media is mainly caused by the difference among the attenuations due to conductor loss α_c. As can be seen, α_c of the MSTLs are slightly higher than those of the microstrip counterparts in both Region I and Region II because of the effects of the side conducting planes [75]. However, α_c of the MSTLs are becoming smaller in Region III in which the dominant modes of the MSTLs have been converted to the quasi-TE_{10} waveguide mode. It is reasonable that α_c of the MSTLs are higher than those of the RWG counterparts in Region III, resulting from the two slits of the MSTLs. A closer examination of Fig. 4.9 shows that the α_c curves of the MSTLs are parallel to those of the RWG counterparts in Region III. This implies that we could consider an impact factor into the formula of the conductor loss of RWG (e.g., 3.96 of [41]) to determine the conductor loss of MSTL when $f > f_{ms2}$ (Region III).

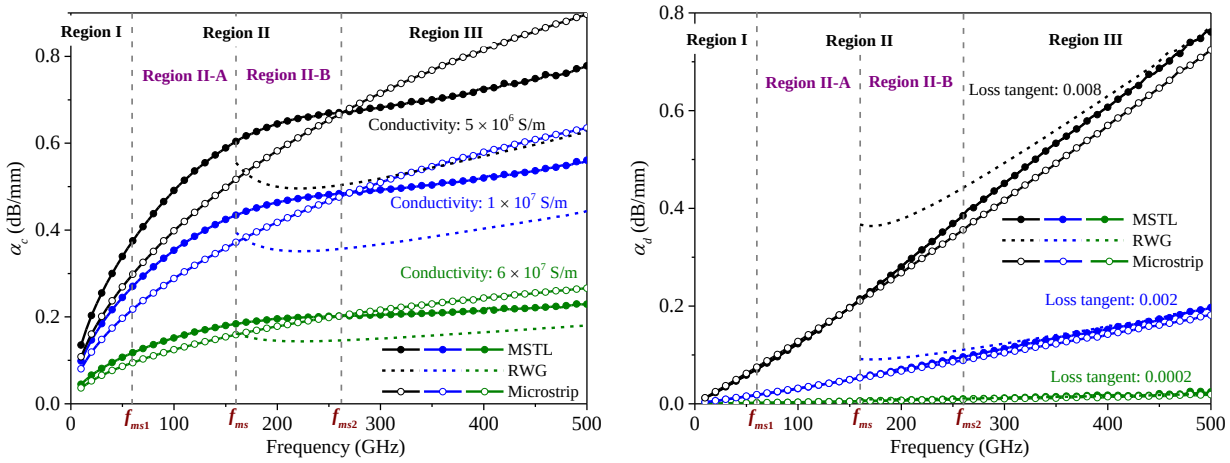

(a) (b)

Figure 4.10 Comparison between attenuation constants of MSTL II and its RWG and microstrip counterparts. (a) Attenuation due to conductor loss α_c. (b) Attenuation due to dielectric loss α_d

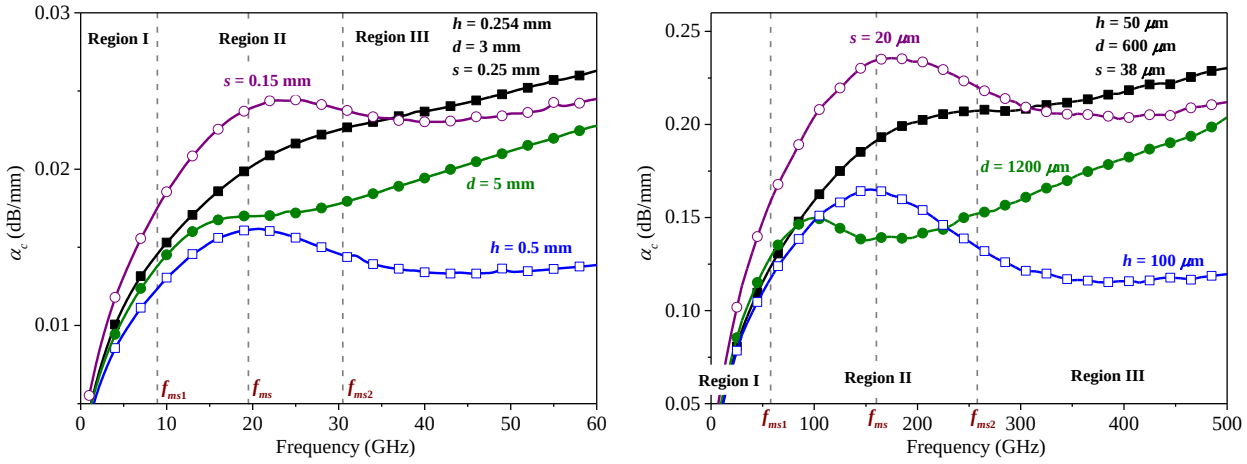

(a) (b)

Figure 4.11 Effects of parameters on the attenuation due to conductor loss of (a) MSTL I and (b) MSTL II

From Figs. 4.8 and 4.9, one can find that the attenuation due to dielectric loss α_d of MSTL II is considerably small when compared to the attenuation due to conductor loss α_c. This is attributed to the used dielectric material (crystal quartz) with an extremely low loss tangent of tanδ = 0.0002 [79]. Here the effects of the loss tangent tanδ of dielectric material and the conductivity σ of conductor material on the attenuation constants of MSTL II are investigated, compared to those of the RWG and microstrip counterparts. As depicted in Fig. 4.10, both the conductivity and loss tangent have effects on the attenuations as expected. This suggests that a proper material selection can help to reduce the power loss of MSTL to some extent. Despite these effects, the relationship between the attenuations of MSTL II and its RWG and microstrip counterparts remains the same, as described before.

With reference to Figs. 4.8, 4.9, and 4.10, the attenuations of both MSTL I and MSTL II increase gradually with frequency. We can also find that the difference among the attenuations of the transmission media is mainly caused by the different attenuations due to conductor loss α_c. To maintain a relatively low and stable attenuation over the frequency range of operation, it is necessary to further reduce the attenuations, in particular at higher frequencies. In addition to the material selection, we further study the effects of major geometrical parameters of the MSTLs,

including substrate thickness h, sidewall span d, and slit width s (labeled in Fig. 4.1), on the attenuation due to conductor loss α_c. As plotted in Fig. 4.11, the increase of d or h can reduce the attenuation constant α_c when $f > f_{ms}$, which is mainly because of the decreased power density [41]. They have little effects on the attenuation constant α_c when $f < f_{ms}$. In contrast, s has adverse effects on the attenuation constant α_c in Region II and Region III. The different effects of these parameters on the attenuation constant α_c in different frequency regions are due to the variable dominant modes of the MSTLs. The change in values of these parameters also affects the characteristic frequencies and then the frequency regions.

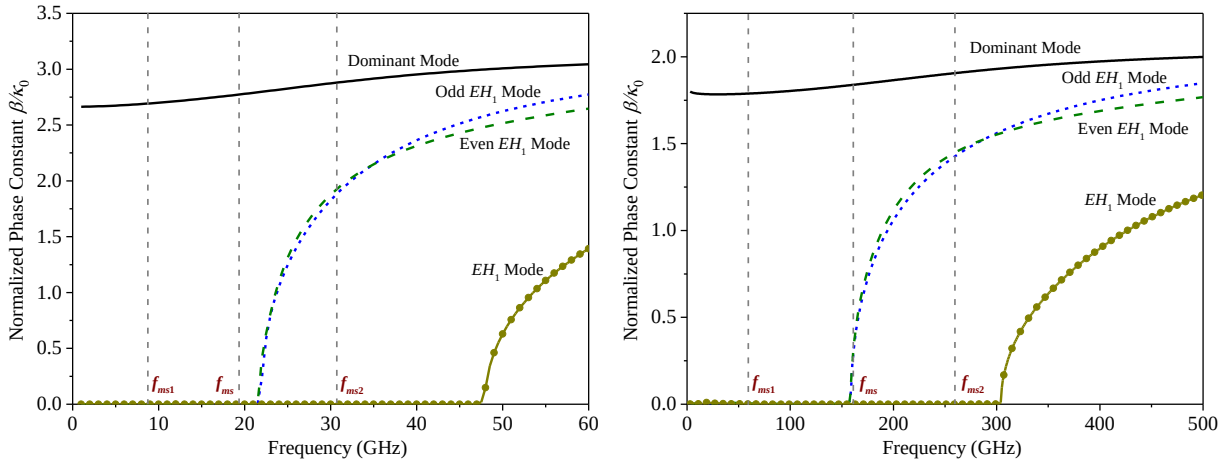

Figure 4.12 Normalized phase constants of various modes in (a) MSTL I and (b) MSTL II

4.5.2 Higher-order modes

The longitudinally uniform MSTL may support several higher-order modes. Phase constant curves plotted in Fig. 4.12 indicate that three higher-order modes could be generated in both MSTL I and MSTL II in the frequency ranges of interest (i.e., dc to $2f_{ms2}$). Their electric field distributions are sketched in Fig. 4.13. A close inspection of Figs. 4.13(a) and (b) shows that the electric fields of both the first and second higher-order modes concentrate mainly around the side parts of MSTL. The side parts, which consist of the side conducting planes, lateral sidewalls, and bottom conducting plane, can be considered as two symmetric half-width microstrips [20] (also called half-

mode SIWs [18]). Referring to [20] and [25], we know that the first and second higher-order modes are even and odd EH_1 modes (also called the quasi-$TE_{0.5,0}$ modes [18]), respectively. It is seen from Fig. 4.13(c) that the electric fields of the third higher-order mode concentrate mainly around the central part of MSTL. The central part, which consists of the central strip and the bottom conducting plane, can be considered as a microstrip line. This implies that the third higher-order mode of MSTL is the first higher-order mode of the central microstrip line, i.e., EH_1 mode. Note that for these higher-order modes, partial fields around the silts as observed from Fig. 4.13 contribute the portion of slotline modes; however, they are relatively weak when compared to the EH_1 mode.

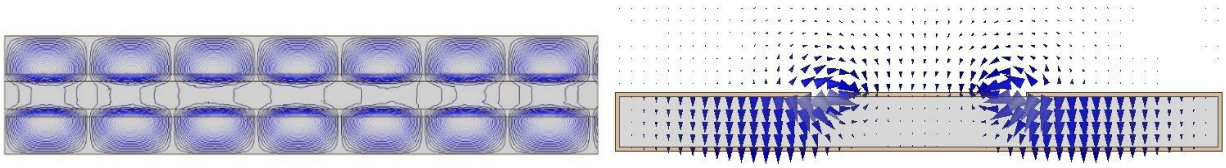

Top view Cross-sectional view

(a)

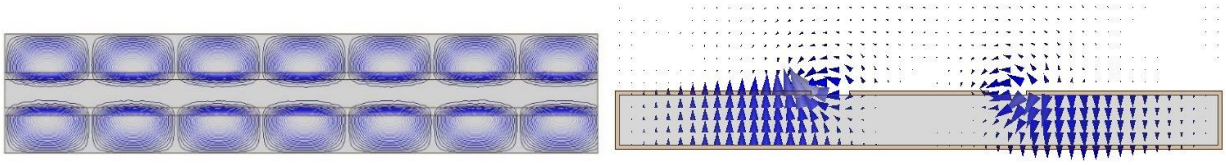

Top view Cross-sectional view

(b)

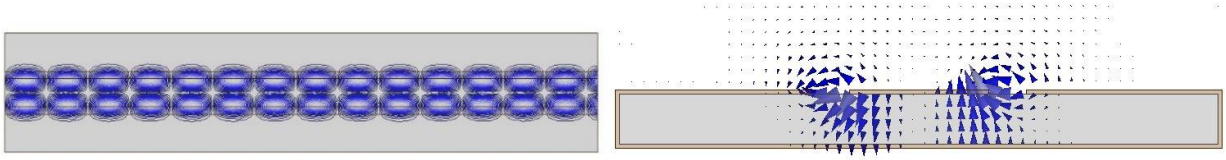

Top view Cross-sectional view

(c)

Figure 4.13 Electric field distributions for higher-order modes in MSTL. (a) Even EH_1 mode. (b) Odd EH_1 mode. (c) EH_1 mode

We have compared the field distributions and phase characteristics of these higher-order modes in both MSTL I and MSTL II with those of the corresponding modes in the separate side parts and

central part. The comparison results indicate that the corresponding modes show almost the same properties. This fact indicates that we can separately treat the higher-order modes by analyzing the separate side parts and central part of MSTL. This analysis can refer to the reported methods [18], [20]. It is not repeated here for simplicity. Other modes, such as slotline modes, surface wave modes, and other higher-order modes, could be generated in MSTL [47], [48] when frequency continues to increase, or any discontinuities are introduced. In practical applications, these undesired modes need to be suppressed or eliminated. To this end, a tapered transition is designed, able to effectively suppress the undesired modes over the frequency range of interest (i.e., dc to $2f_{ms2}$), to be presented in the following section.

4.6 Experimental verification

We have conducted numerical and theoretical analyses of MSTL. In this section, both MSTL I and MSTL II are implemented and characterized for an experimental verification. To facilitate the measurement and to suppress the higher-order modes, we will present a tapered microstrip-to-MSTL transition, showing properties of low loss and ultra-broad bandwidth.

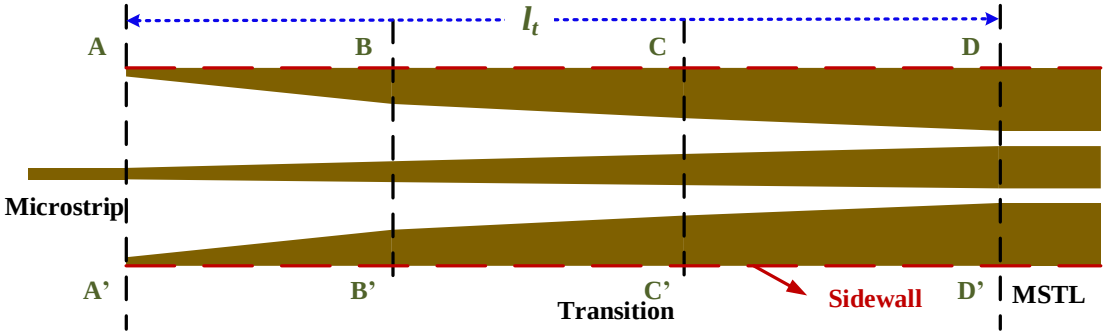

Figure 4.14 Top view of a tapered microstrip-to-MSTL transition

4.6.1 Microstrip-to-MSTL transition

Transitions between MSTL and conventional transmission media are required for practical measurement and circuit integration. A tapered transition between microstrip line and MSTL is designed, supporting a low-loss and ultra-broadband propagation. This transition is constructed by tapering the central strip inward and the side conducting planes outward symmetrically, as shown

in Fig. 4.14. It can ensure both impedance matching and field matching between the microstrip line and MSTL [80]. More specifically, the impedance matching is mainly realized by tapering the central signal line. The field matching is assured by the central tapered line alone when frequency is in Region I (labeled in Fig. 4.7). In Region II and Region III, the field matching is realized by the central tapered line together with the side tapered conducting planes, able to couple a partial field energy from the central part to the side parts. The field energy can be smoothly delivered from the microstrip line on the left side of the transition to MSTL on the right side by gradually changing the physical boundary conditions, as shown in Fig. 4.14. The tapered transition delivering power from the microstrip to MSTL is based on the coupled-mode mechanism [33], [71]; in fact, it provides an excitation on MSTL, which is the same as the wave port in the full-wave simulations (see Fig. 4.1(a)).

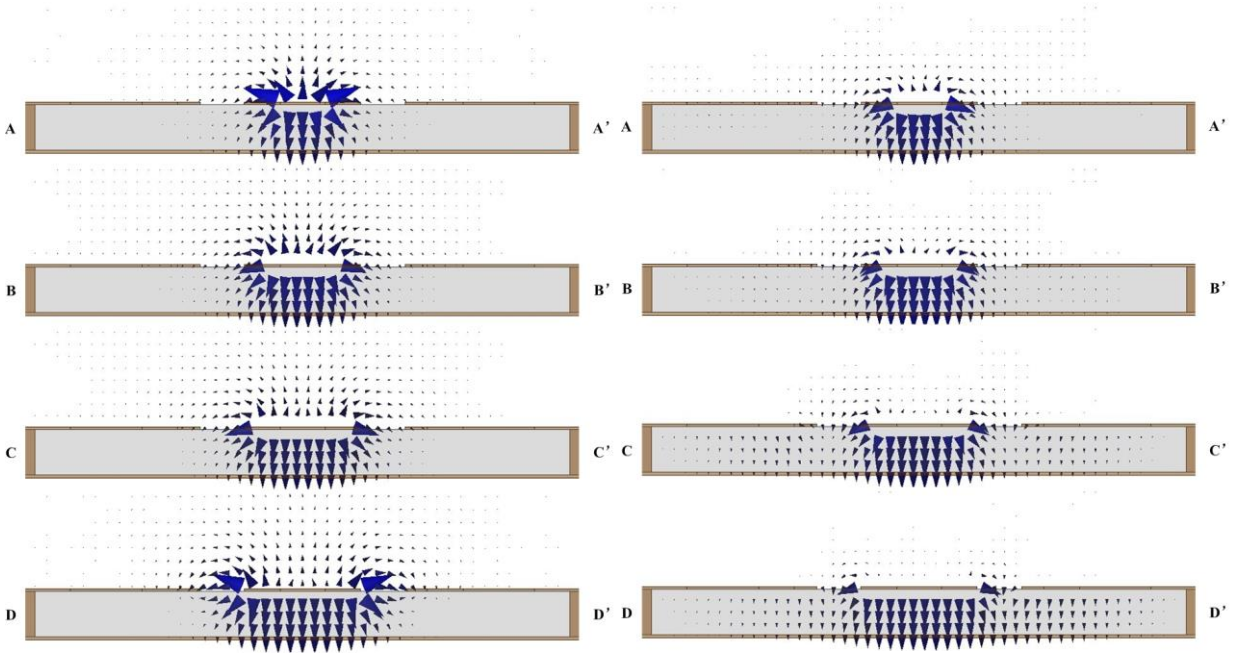

(a) (b)

Figure 4.15 Electric field distributions in various cross sections of the transition (see Fig. 4.14) at (a) $0.5f_{ms1}$ and (b) $2f_{ms2}$

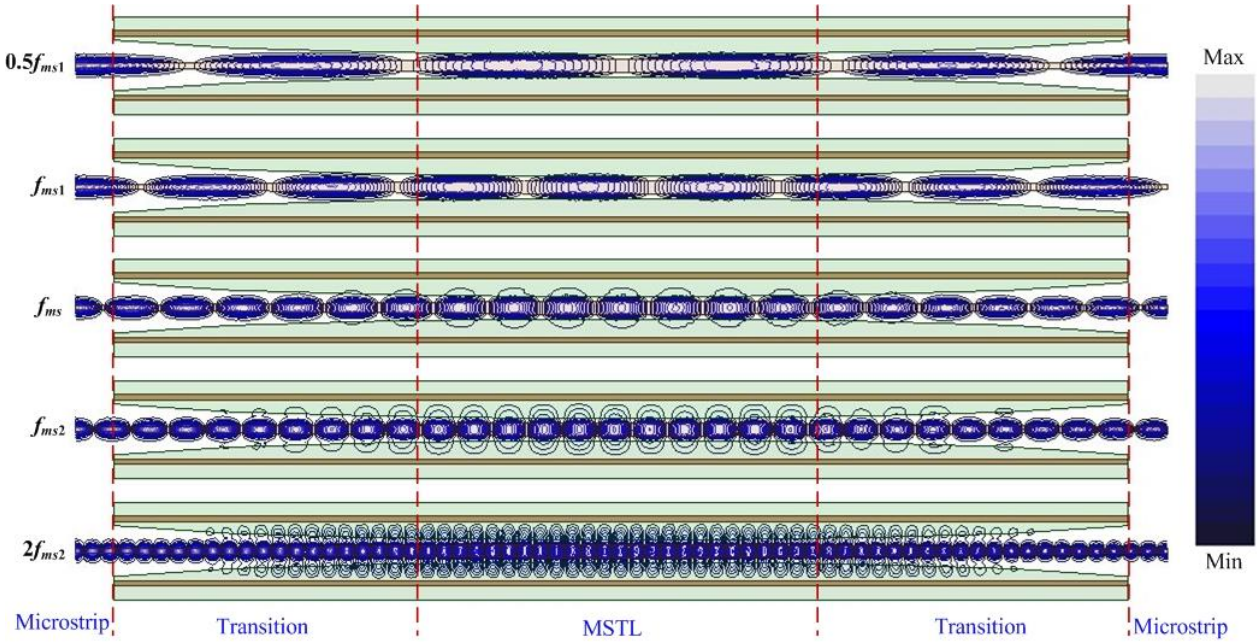

Figure 4.16 Electric field distributions along MSTL connected to two transitions at different frequencies

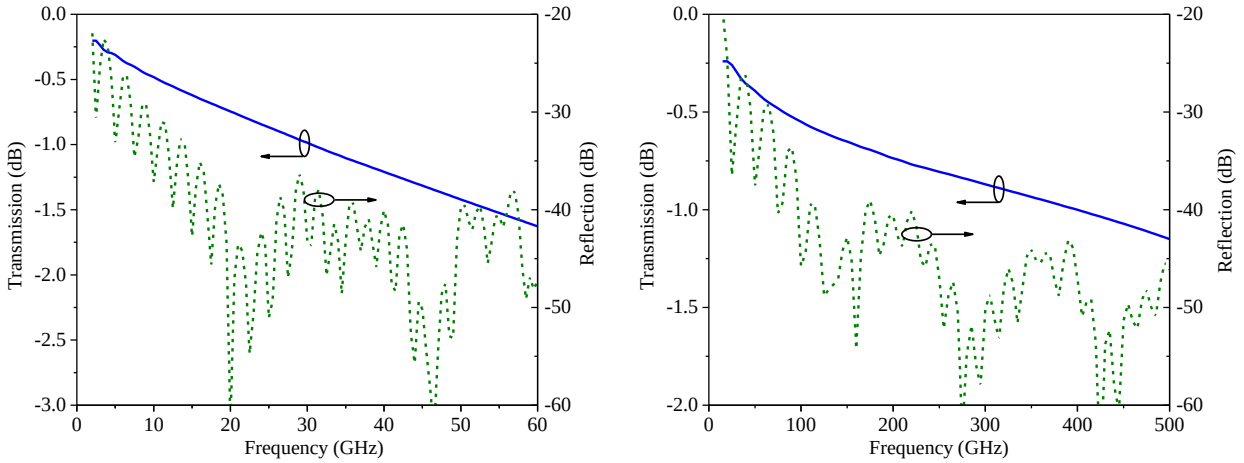

(a) (b)

Figure 4.17 Simulated transmission and reflection responses of the single microstrip-to-MSTL transitions for (a) MSTL I and (b) MSTL II

To check the field matching of the proposed transition, we examine the electric field distributions in various cross sections of the transition labeled as A-A', B-B', C-C', and D-D' in Fig. 4.14. As

we investigated earlier, the dominant mode of MSTL can change with frequency. Therefore, we examine the field distributions at two different frequencies, $0.5f_{ms1}$ and $2f_{ms2}$, at which the dominant mode of MSTL is the quasi-TEM mode and the quasi-TE_{10} mode of MSTL, respectively, as shown in Fig. 4.15. From the electric field distributions at $0.5f_{ms1}$ (see Fig. 4.15(a)), it is seen that the electric fields still concentrate around the central signal line, and the concentration region is changed slightly with tapering the central line. At $2f_{ms2}$ (see Fig. 4.15(b)), the electric fields gradually spread from the central line (see A-A') to the whole cross section (see D-D') along the transition. This phenomenon indicates that, at a low frequency (e.g., $0.5f_{ms1}$), the quasi-TEM microstrip mode of the microstrip line (see A-A' in Fig. 4.15(a)) is slightly adjusted to the quasi-TEM microstrip mode of MSTL (see D-D' in Fig. 4.15(a)). On the other hand, at a high frequency (e.g., $2f_{ms2}$), the microstrip mode of the microstrip line (see A-A' in Fig. 4.15(b)) is smoothly transformed to the quasi-TE_{10} waveguide mode of MSTL (see D-D' in Fig. 4.15(b)). In fact, the electric field distributions in A-A' are for the fixed dominant mode of the microstrip line on the left side of the transition (Fig. 4.14); therefore, there are slight changes at quite different frequencies. The electric field distributions in D-D' are for the variable dominant mode of MSTL on the right side of the transition, and one can thus find the significantly different field distributions at different frequencies. Shown in B-B' and C-C' are the "transition" fields in the microstrip-to-MSTL transition, which are found to be analogous to those in A-A' and in D-D', respectively, resulting from the corresponding positions.

Fig. 4.16 shows the electric field distributions along the MSTL structure connected to the transitions on two sides. Obviously, the delivery of the electric field energy along the structure at different frequencies, including $0.5f_{ms1}$, f_{ms1}, f_{ms}, f_{ms2}, and $2f_{ms2}$, is quite smooth. This further proves the capability of the proposed microstrip-to-MSTL transition in supporting well-behaved field and impedance matchings. Furthermore, at corresponding frequencies, the electric field distributions in the central MSTL of the whole structure shown in Fig. 4.16 are quite similar to the field distributions in a single MSTL (without transitions) listed in Table 4.2. This fact verifies that the microstrip-to-MSTL transition provides an excitation on MSTL, as the wave port in the full-wave simulations does (see Fig. 4.1(a)). Normally, a longer tapered transition could realize a smaller signal reflection, at the expense of a higher power loss [81]. This necessitates to find a trade-off between the reflection coefficient and power loss introduced by transitions. The full-wave analysis

result suggests that each microstrip-to-MSTL transition could be slightly longer than three times the guide wavelength λ_g at f_{ms}, namely $l_t \geq 3\lambda_g$ where l_t denotes the transition length as labeled in Fig. 4.14. This maintains a low insertion loss (below 0.42 dB/λ_g) and a good return loss (better than 20 dB) over the frequency ranges of interest. Fig. 4.17 shows the simulated transmission and reflection responses of the single microstrip-to-MSTL transitions for both MSTL I and MSTL II. It can be observed that the single transition for MSTL I (l_t = 21 mm ≈ 3.8λ_g) causes an insertion loss below 1.6 dB up to 60 GHz, and the single transition for MSTL II (l_t = 3 mm ≈ 3λ_g) causes an insertion loss below 1.1 dB up to 500 GHz. Their return losses are better than 20 dB over the ultra-broad frequency ranges of interest. These results indicate that the proposed microstrip-to-MSTL transition can operate in an ultra-broad frequency range and introduce a low power loss.

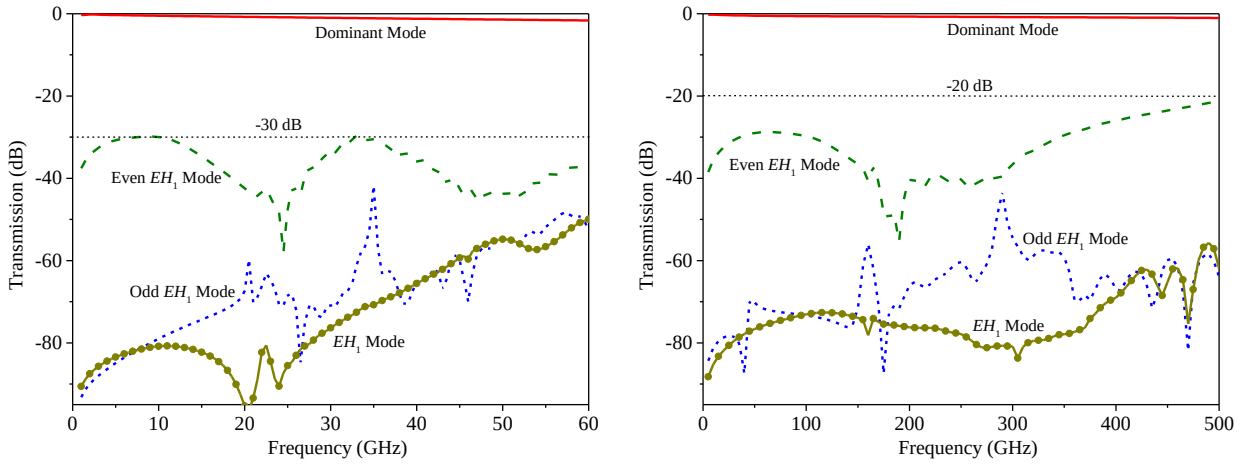

(a) (b)

Figure 4.18 Suppression of higher-order modes in (a) MSTL I and (b) MSTL II using the single microstrip-to-MSTL transitions

In addition to the requirement for practical measurement and circuit integration, the tapered microstrip-to-MSTL transition can also effectively suppress higher-order modes in MSTL over an ultra-broad frequency range (dc to 2f_{ms2}). As Fig. 4.18 shows, with the help of a single transition, the dominant mode propagates with a small loss, whereas the transmissions of the three higher-order modes (see Section 4.5.2) in MSTL I and MSTL II are below -30 and -20 dB when frequency is up to around 2f_{ms2} (i.e., 60 GHz for MSTL I and 500 GHz for MSTL II). The slight difference between

the suppression levels results from the different transition lengths, as described above. A close inspection of Fig. 4.18 shows that the transmission curves for the higher-order modes slightly rise when frequency goes below the cutoff frequencies (see Fig. 4.12), mainly resulting from the unwanted mode coupling. The reason for successful suppression of higher-order modes is that the transition operates in the coupled-mode approach [33], [71], and it is impossible to realize a good impedance matching and particularly a proper field matching between the dominant microstrip mode of the microstrip line and the higher-order modes in MSTL. This fact is directly observed and deduced by comparing the field distributions in microstrip line (see Fig. 4.2(c)) and the field distributions for higher-order modes in MSTL (see Fig. 4.13).

4.6.2 MSTL implementation

MSTL II has been experimentally verified in [46] and [47]. Due to a high requirement for fabrication precision, a microfabrication process was used to implement MSTL II with micro-scale features. Detailed fabrication steps have been described in [47]. MSTL I was also fabricated to further demonstrate the practical properties of MSTL. The RT/duroid 6010LM laminate from Rogers Corporation is intentionally chosen as the MSTL substrate. Its high relative permittivity ε_r of 10.2 allows to examine the wide parameter ε_r range of the proposed empirical equations given in Section 4.4. The substrate thickness h needs to be as small as possible to weaken and even suppress the CPW mode (or slotline modes), as explained in Section 4.2.1. The microstrip-to-MSTL transitions are used to facilitate the measurement. Given the operating frequency and the limited line width of the microstrip feeds, a dielectric substrate with a thickness of 0.254 mm is chosen rather than the commercially available thinnest counterpart with a thickness of 0.127 mm. Detailed dimensions of MSTL I are listed in Table 4.1. A standard printed circuit board (PCB) process technology was adopted to implement MSTL I. Note that the sidewalls of MSTL I are realized with periodically plated rectangular slots based on the SIW technology [17], [31]. Simulation results have indicated that this realization method does not cause an obvious deterioration of the MSTL performance over the frequency range of interest. The photograph of the fabricated samples of MSTL I is shown in Fig. 4.19. For comparison, the RWG and microstrip counterparts of MSTL I were also fabricated using the same fabrication technique. Similarly, the sidewalls of the dielectric-filled RWG are realized using the periodically plated rectangular slots; in fact, the implemented structure is an SIW.

Microstrip-to-SIW transitions [17] are used to facilitate the characterization of the dielectric-filled RWG (SIW). For impedance matching, the microstrip counterpart of MSTL I is connected to two 50-Ω microstrip feed lines via two tapered lines.

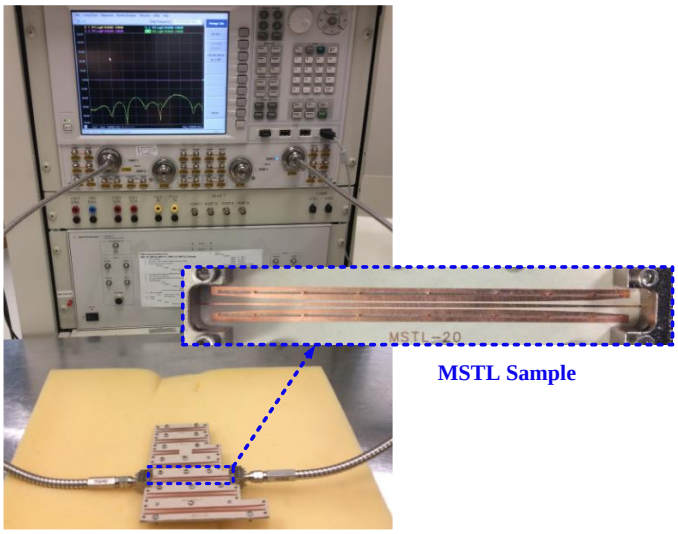

Figure 4.19 Photograph of the measurement setup and samples of MSTL I

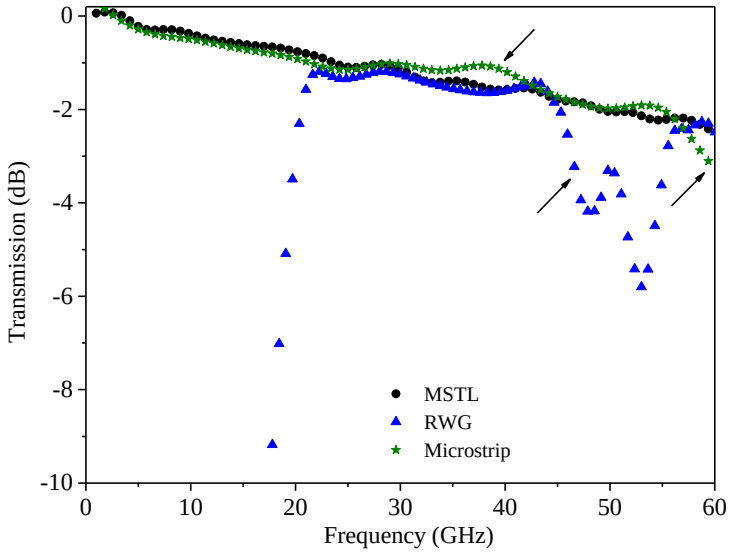

Figure 4.20 Comparison between measured transmission responses of MSTL I and its RWG and microstrip counterparts

4.6.3 MSTL characterization

For MSTL II, the measurement was carried out on a THz station. A multiline thru-reflect-line (TRL) calibration method [82] was adopted to de-embed the effects of the test system and the transitions. A PNA-X network analyzer N5247A (Keysight Technologies) is connected to VDI transmitting and receiving frequency extenders to perform full two-port scattering parameter measurements up to 500 GHz. Measured results of MSTL II are presented in [47], revealing that MSTL II can guide an ultra-broadband (dc-500 GHz) signal with low loss and low dispersion. For MSTL I, the network analyzer is connected to MSTL I through Southwest 1.85 mm end launch connectors. The photograph of the measurement setup is shown in Fig. 4.19. A measurement was carried out up to 60 GHz using the multiline TRL calibration method. The RWG and microstrip counterparts were also characterized using the same methods. Note that, the lowest measured frequency is 10 MHz, limited by the measurement setup; however, it is sufficient to demonstrate the performance near dc.

A comparison between the simulated transmission responses of MSTL I and MSTL II and their RWG and CBCPW counterparts has been carried out in Section 4.2 (see Fig. 4.3). Shown in Fig. 4.20 is the comparison between the measured transmission responses of the 20-mm-long MSTL I and its RWG and microstrip counterparts. It can be observed that MSTL I shows a smooth transmission over the whole frequency range (i.e., dc to 60 GHz). In contrast, a sharp drop at around 60 GHz in the transmission curve of the microstrip line is observed, which is due to the excitation of the first higher-order mode, EH_1 mode. Small fluctuations at around 38 GHz are also found. Consistent with the simulation results shown in Fig. 4.3, the RWG counterpart operates in a narrow frequency range due to the low frequency cutoff and excitation of higher-order modes at high frequencies. Through the comparison, one can find that MSTL I can operate in a wider frequency range than the microstrip and RWG counterparts. A close examination of Fig. 4.20 also shows that the power loss of MSTL I is comparable to the counterparts over the common frequency range of operation. In addition to the transmission response, the phase constant of MSTL I is also extracted from the measured scattering parameters [83], which is plotted in Fig. 4.7(a). As can be seen, the measured phase constant agrees well with the simulated one, showing a smooth phase constant curve, thus meaning a low dispersion. From these comparison results, it can be concluded that this measurement verifies the properties of MSTL.

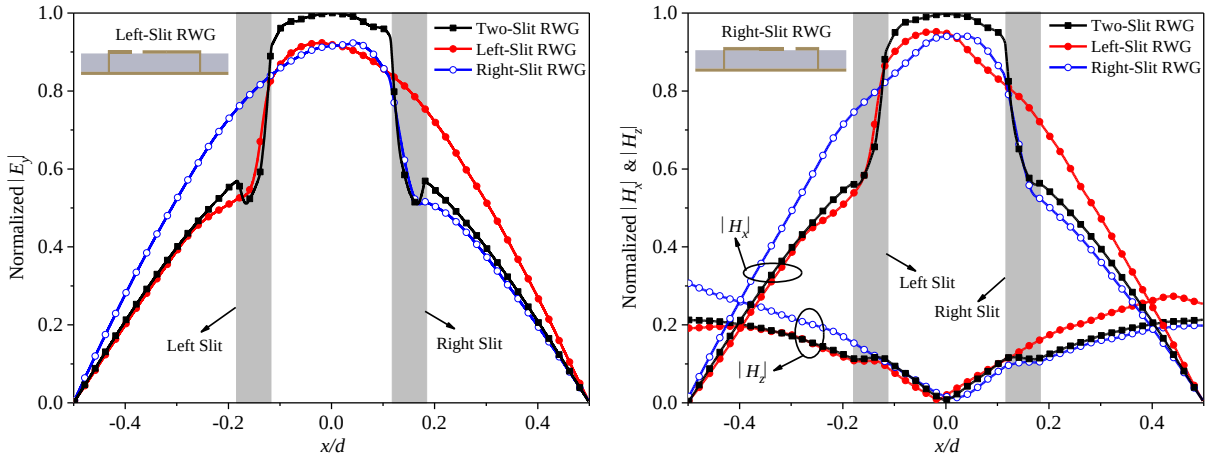

(a) (b)

Figure 4.21 Normalized field distribution curves of the two-slit RWG, left-slit RWG, and right-slit RWG along the *x*-axis at 400 GHz. (a) E_y field component. (b) H_x and H_z field components

4.7 Conclusion

In this paper, we have investigated MSTLs comprehensively, including numerical analysis, theoretical analysis, and experimental verification. To demonstrate the applicability of the MSTL design, we have considered two MSTLs as practical examples, which operate in different frequency ranges and require different fabrication and measurement techniques. The specific phenomenon of mode selectivity in MSTLs has been verified by both the physical evidence (field distributions) and theoretical foundation (orthogonality relations). This means that a frequency-enabled mode conversion can occur in a transmission medium with a given cross section. Similar phenomenon possibly occurs in other composite transmission media. The mode selectivity has been treated rigorously by defining characteristic frequencies and then specifying several frequency regions. This will be useful for the MSTL designs with given specifications. We have also analyzed the propagation characteristics of MSTLs and have briefly discussed their higher-order modes. Higher-order modes in MSTLs can be suppressed by the proposed microstrip-to-MSTL transition, thus expanding the frequency range of operation. The comparison between the frequency characteristics of MSTLs and the conventional transmission media indicates that MSTLs can support the

transmission and processing of low-loss, low-dispersion, and particularly ultra-broadband and ultrafast signals.

Given the conditions of mode selectivity, it is possible to realize other MSTLs with frequency-enabled mode conversion among other modes, such as CPW mode and waveguide mode. Such MSTLs are promising candidates for THz chip-to-chip interconnects and other ultra-broadband applications. In addition, we could implement various MSTL-based components with high performance through benefiting from the advantages of different modes.

Appendix

We propose a simple but rigorous method to analyze slitted RWGs in this work. MSTL II is considered as an example to introduce the method. To begin with, it is assumed that the effect of the two slits on the frequency characteristics (without considering power loss) of a two-slit RWG is a combination (linear superposition) of the effect of individual slits. The field distribution curves of the two-slit RWG and two single-slit RWGs (left-slit RWG and right-slit RWG) at 400 GHz are plotted in Fig. 4.21 for a visual comparison. Since the two-slit RWG in this case is used to model the individual quasi-TE_{10} waveguide mode in MSTL II, the chosen frequency point (400 GHz in this case) should be higher than the characteristic frequency f_{ms2} (defined in Section 4.4.2). The single-slit RWG is a dielectric-filled RWG with only one slit asymmetrically etched in the top broad wall, as shown in the insets of Fig. 4.21. Its dominant mode is also a quasi-TE_{10} waveguide mode. Inspection of Fig. 4.21 shows that the effect of both the left and right slits on the field distributions in the two-slit RWG is approximately equal to the combination (or linear superposition) of their individual effect on the left-slit RWG and right-slit RWG. This confirms the above assumption, and we can thus investigate the effect of single slit on the single-slit RWG and then simply double the effect for the two-slit RWG.

The single-slit RWG (left-slit RWG or right-slit RWG) is first analyzed in terms of phase constant and cutoff frequency. On the basis of the waveguide theory [84], empirical equations are given to calculate the phase constant β_1 and cutoff frequency f_c of the dominant quasi-TE_{10} mode of the single-slit RWG as follows:

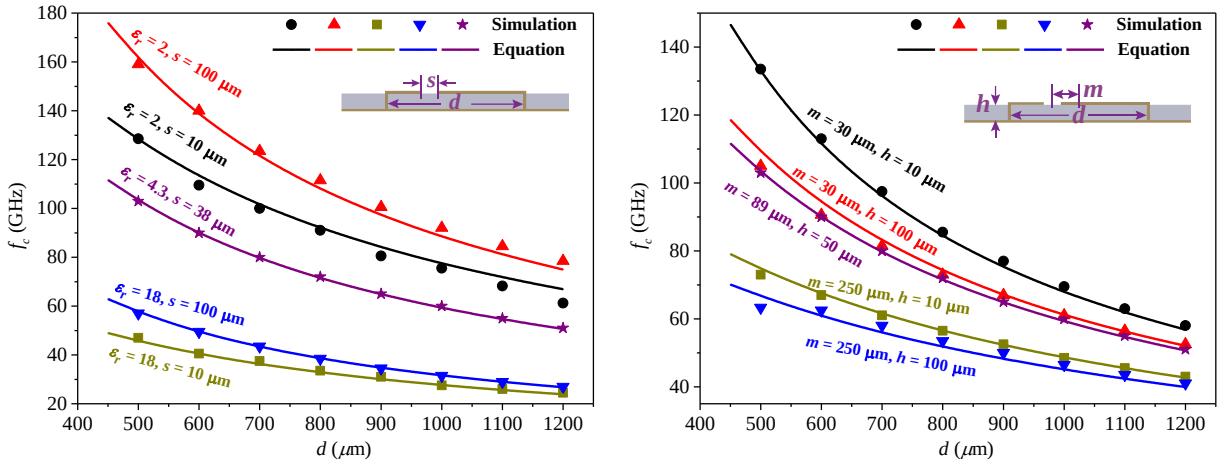

(a) (b)

Figure 4.22 Cutoff frequency f_c of the single-slit RWG versus sidewall span d as functions of parameters: (a) ε_r and s. (b) m and h

$$\beta_1^2 = \varepsilon_r k_0^2 - \frac{k_0^2}{\left(k_0 + \Delta k\right)^2} k_{c0}^2 \tag{4.6}$$

$$f_c = \frac{1}{M\sqrt{\mu_0 \varepsilon_0 (\varepsilon_r + 0.34)}} \tag{4.7}$$

where

$$\Delta k = \frac{2\pi \cdot \Delta f}{c} = \frac{2\pi \cdot \left(f_c - f_{c0}\right)}{c} \tag{4.8}$$

$$k_{c0} = \pi / d \tag{4.9}$$

$$k_0 = \frac{2\pi f}{c} \tag{4.10}$$

$$f_{c0} = \frac{k_{c0}}{2\pi\sqrt{\mu\varepsilon}} = \frac{1}{2d\sqrt{\mu_0 \varepsilon_0 \varepsilon_r}} \tag{4.11}$$

where c, μ_0, ε_0, and ε_r are the speed of light, free-space permeability, free-space permittivity, and the relative permittivity of the dielectric substrate used, respectively, and f is the operating

frequency. The variable M is expressed in (4.3). The parameters d, h, s, and m of the single-slit RWG are labeled in the insets of Fig. 4.22. Fig. 4.22 compares the calculated and simulated cutoff frequencies f_c of the single-slit RWG versus the sidewall span d for different parameter values. Due to the limited space, the comparison is conducted for a few sets of parameter values. The value range of each parameter is expanded sufficiently. Other parameter values remain the same, as listed in Table 4.1. To obtain the required variable dominant mode of MSTL and to suppress undesired modes, we have defined the design region of MSTL in [48]. Within this design region, the calculation error is estimated to be less than 2%. A similar comparison for the phase constant β_1 of the single-slit RWG was also carried out, showing an acceptable calculation error of 5%.

Through comparing (4.6) with the equation for the phase constant of a standard RWG [41], [84], it is deduced that the term Δk in (4.6) and (4.8) is a result of the effect of the slit on the frequency characteristics of the single-slit RWG. By doubling this effect, we obtain the following empirical equations (4.12) and (4.13) to calculate the phase constant β and cutoff frequency f_{ms1} of the two-slit RWG.

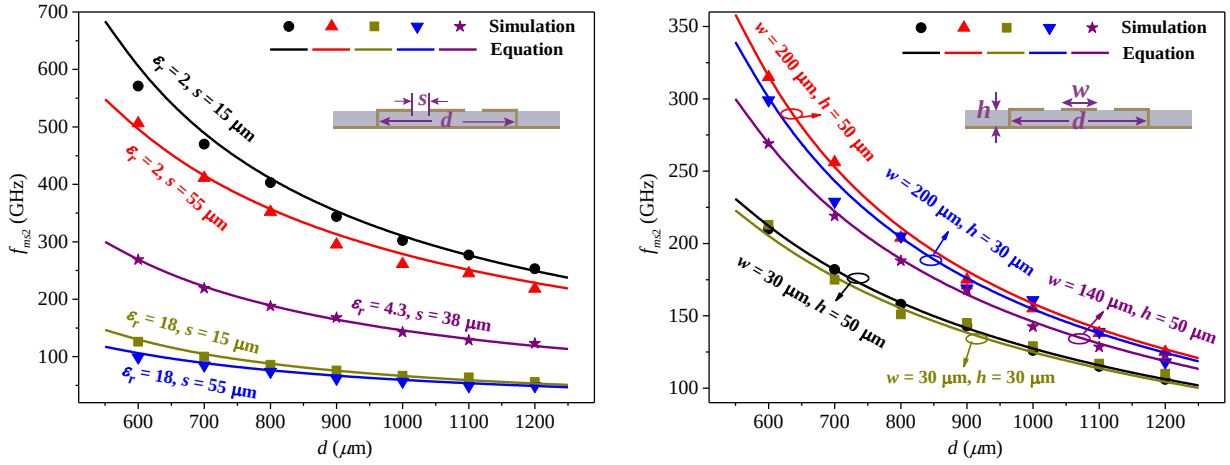

(a) (b)

Figure 4.23 Maximum-coupling frequency f_{ms2} versus sidewall span d as functions of parameters: (a) ε_r and s. (b) w and h

$$\beta^2 = \varepsilon_r k_0^2 - \frac{k_0^2}{(k_0 + 2\Delta k)^2} k_{c0}^2 \tag{4.12}$$

and

$$f_{ms1} = 2 f_c - f_{c0} \tag{4.13}$$

where f_{ms1} is ultimately expressed as (4.2). As described in Section 4.4, the individual quasi-TE_{10} mode in MSTL can be modeled by the two-slit RWG, and thus (4.12) and (4.13) are also applicable to the individual quasi-TE_{10} mode in MSTL. For both MSTL I and MSTL II, the calculated phase constants and cutoff frequencies agree well with the simulated ones (see Fig. 4.7).

In addition to the characteristic frequency f_{ms1}, f_{ms2} is also formulated in (4.4). MSTL II is also considered as an example to examine the accuracy of (4.4). The calculated and simulated f_{ms2} for various parameter values are compared, as shown in Fig. 4.23. The simulation results are obtained by locating the low-frequency end of the overlapping curve of MSTL II and the individual quasi-TE_{10} mode for various parameter values. Comparison results indicate that, within the design region of MSTL defined in [48], (4.4) can be used to accurately predict the characteristic frequency f_{ms2} with a calculation error below 5%. Note that from the comparison results, the empirical equations given above are valid for the relative permittivity of dielectric substrate ranging from 2 to 18.

CHAPTER 5 ARTICLE 3: MODE-SELECTIVE TRANSMISSION LINE——PART I: THEORETICAL FOUNDATION AND PHYSICAL MECHANISM

Desong Wang and Ke Wu

Published in the *IEEE Transactions on Components, Packaging and Manufacturing Technology*, vol. 10, no. 12, pp. 2072-2086, Dec. 2020.

Mode-selective transmission line (MSTL) has been studied and realized in support of ultra-broadband and ultrafast electromagnetic signal guidance. Its operation is based on the fact that its dominant mode behaves as a quasi-TEM microstrip mode at low frequencies and is gradually converted into a quasi-TE_{10} waveguide mode at higher frequencies notwithstanding its longitudinal uniformity. In the first part of this work (Chapter 5), the physical mechanism of the frequency-dependent modal behavior is presented. From the viewpoint of mode coupling, MSTL is heuristically considered as a coupled system consisting of one microstrip line and two half-mode substrate-integrated waveguides (HM-SIWs). Coupled-mode theory and normal-mode analysis are combined to sequentially analyze HM-MSTL, a relatively simple case, and MSTL. The coupled-mode theory provides an approximate representation for the normal modes of each coupled system, thus gaining in-depth physical insight into the MSTL mode-guidance behavior. A comparison between approximate fields derived from the theoretical analysis and exact fields extracted from the rigorous numerical simulation is made to support the modal analysis. A parametric study is then carried out to examine the effect of geometrical parameters on the MSTL characteristics and performance, thereby providing meaningful guidance in the MSTL design and optimization. A further discussion of mode selectivity is given at the end of this article.

5.1 Introduction

Mode-selective transmission line (MSTL) has recently been proposed and demonstrated, showing its unprecedented capability in the high-performance guidance of ultra-broadband and ultrafast

electromagnetic signals covering the continuous spectrum of operation from dc through THz [46], [47], [85]. The most distinguishing and astonishing feature of MSTL as compared with any other transmission media reported and developed to date is its dominant mode, which can be gradually but completely converted in a self-adaptive manner from a quasi-TEM microstrip mode to a quasi-TE_{10} waveguide mode as frequency increases [53], [86]. This happens even though the MSTL structure preserves its longitudinal uniformity in geometry. In this way, the MSTL scheme offers combined advantages of the two dissimilar guided modes for veritable full-pass frequency spectrum operations, including low power loss, low frequency dispersion, no cutoff frequency, ultra-broadband operation, and excellent field confinement [48], [87]. In [86], a comparison with the conventional microstrip line, coplanar waveguide (CPW), and rectangular waveguide (RWG) has illustrated the superior performance of MSTL. Surprisingly, this guided mode diversity observed in MSTL seems to be in contradiction with the prevailing assumption or popular perception with regard to the condition for mode conversion. It has been always commonly postulated in the community and definitely in the classical textbooks, since the birth of waveguide, that in any transmission medium of a given cross section, mode conversion might occur if and only if a geometrical discontinuity or perturbation is introduced along the longitudinal or propagation direction [51], [88], [89]. However, MSTL is completely uniform in the direction of propagation; the conversion in its dominant mode is enabled only by frequency change. This seemingly conflicting outcome will be discussed in more detail in Section 5.6.

To qualify this fundamental feature from the well-known physical mechanism of mode conversion attributed to longitudinal discontinuity, this unique MSTL phenomenon was referred to as the *frequency-enabled mode selectivity* [86]. To understand this phenomenon, the field distributions along MSTL were examined in [53], becoming a first-hand physical evidence of this phenomenon. In [86], characteristic frequencies were defined and formulated to quantify the behavior of frequency-enabled mode selectivity. In order to gain a robust insight into the guided-wave behavior of MSTL, a more in-depth treatment is urgently required from theoretical grounds, physical mechanism, excitation scheme, and practical demonstration. In the present part of this work (Chapter 5), coupled-mode theory and normal-mode analysis are combined to mathematically and physically explore and explain the mode-selectivity phenomenon observed in MSTL, which provides clear evidence in

support of this unique feature. Part II (Chapter 6) of this work focuses on the excitation scheme of MSTL, practical transition design for demonstration purpose, and experimental verification [90].

The coupled-mode theory is a perturbation approach that describes a mode-coupled system with the uncoupled or unperturbed modes of individual constituent elements [77], [91], [92]. It is rather useful in providing simple and intuitive analytical solutions that give insight into the mode-coupling process occurring in an electromagnetically coupled system. In contrast, the normal-mode analysis yields exact solutions based on Maxwell's equations for an entire mode-coupled system of interest [91], [93], [94]. With reference to the solutions, normal modes (i.e., eigenmodes) are orthogonal, thereby meaning that no mode coupling occurs between them. In fact, the coupled-mode theory can provide an approximate representation for the normal modes of the coupled system [91], [92]. The mutual relation between these two analytical approaches has been derived in [22]. In [26] and [54], they have been successfully combined to analyze the coupling mechanism in mode-composite transmission systems. In this work, MSTL is geometrically viewed as an electromagnetically coupled system, which is composed of one microstrip line and two half-mode substrate-integrated waveguides (HM-SIWs) [95]. The normal- and coupled-mode analysis is conducted to explore and understand the physical mechanism behind the mode-selectivity phenomenon observed in MSTL. Together with field distributions plotted in the transverse cross section through a full-wave modeling method, this analysis provides a simple and intuitive yet rigorous description of guided-wave propagation and modal interaction in MSTL.

This article is organized as follows. The unique phenomenon of mode selectivity seen in a typical MSTL is presented and described narratively and briefly in Section 5.2. In Section 5.3, the half-mode MSTL (HM-MSTL), a relatively simple case, is introduced and treated by the normal- and coupled-mode analysis. A similar phenomenon of mode selectivity is also found to occur in this half-mode case, which is presented by both approximate analysis and numerical simulation. Section 5.4 is concerned with the modal characteristics of the typical MSTL. Thanks to the geometrical symmetry of this MSTL, its coupled-mode equations are simplified to those of the HM-MSTL case; this greatly simplifies and clarifies the modal analysis of MSTL. A parametric study is then carried out in Section 5.5, revealing the effect of geometrical parameters on MSTL characteristics and performance. It is followed by subsequent discussions of mode selectivity in Section 5.6, in which a special case is presented to further demonstrate our analysis. Finally, conclusions are given in Section 5.7.

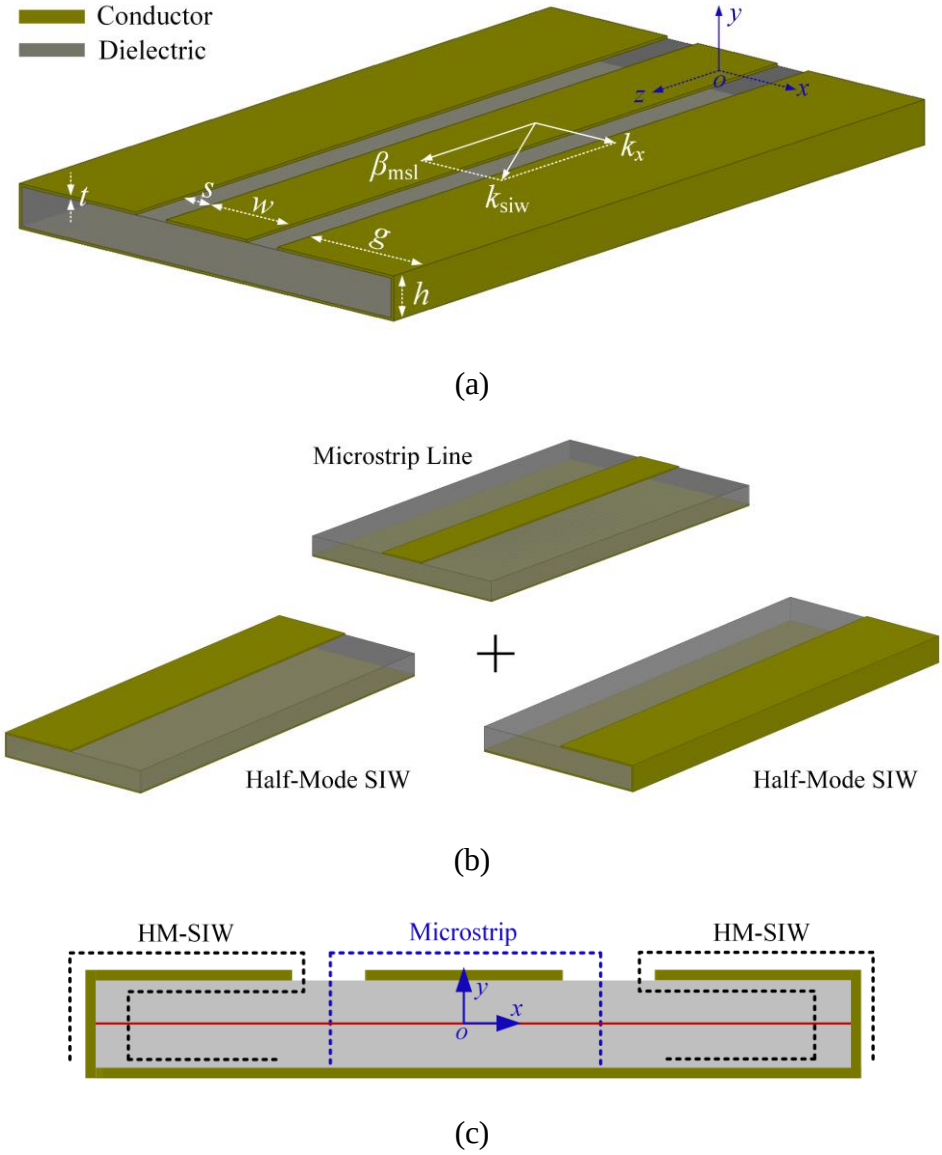

Figure 5.1 Geometry of a typical MSTL. (a) Perspective view. (b) Schematic illustration of the MSTL coupled system. (c) Cross-sectional view

5.2 Frequency-enabled mode selectivity

5.2.1 MSTL geometry and field variation

The geometry of a typical MSTL is shown in Fig. 5.1. It is constructed on a thin dielectric substrate; on the top side, a conducting strip is centered between two side conductors that are connected to

the bottom conducting plane via two lateral conducting sidewalls. This transmission structure is uniform along the *z*-axis (i.e., the direction of propagation) and semi-enclosed along the *y*-axis, thus creating its physical features of longitudinal uniformity and transverse inhomogeneity. To simplify our discussion, we assume that this MSTL is lossless and symmetric about the *yz* plane. This typical MSTL resembles a conventional conductor-backed CPW (CBCPW) [also called grounded CPW (GCPW)] with bilateral sidewalls [61], [62] and also resembles a dielectric-filled RWG with two additional slits etched symmetrically in the top conducting plane (called slitted RWG) [25], [74]. The choice of its structural dimensions has nothing to do with what CBCPW does where the bilateral grounding is used to suppress unwanted waveguide modes. MSTL actually behaves as a folded-ground microstrip line with a dominant quasi-TEM microstrip mode at low frequencies and as a slitted RWG with a dominant quasi-TE_{10} waveguide mode at higher frequencies, which will be discussed in Sections 5.4 and 5.6. To treat this mode-selectivity phenomenon, here, we consider a dc-to-110-GHz MSTL as an example, which was mentioned in [96]. Its structural dimensions are listed in Table 5.1. For comparison, a numerical simulation is performed through both full-wave modal and eigenmode solutions in a finite-element method software, ANSYS Electronics Desktop 2017 [57].

Table 5.1 Dimensions of the dc-to-110 GHz MSTL

Parameter	Description	Value
g	Side conductor width	0.925 mm
h	Substrate thickness	0.254 mm
w	Center strip width	0.65 mm
s	Slit width	0.25 mm
t	Conductor thickness	17.5 μm
ε_r	Relative permittivity of substrate	10.2

The frequency-enabled mode selectivity of the dominant mode (i.e., first normal mode) of MSTL is directly reflected in its normal modal fields (i.e., eigen fields). Fig. 5.2 shows a progressive change in field distributions versus frequency, which are obtained from the full-wave eigenmode solutions. At low frequencies, the electric fields (*E*-fields) are mostly distributed around the center strip. As frequency increases, the *E*-fields start to spread away from the central region and finally

get spilled over the entire cross section of MSTL. Because of this field spreading, the dominant mode of MSTL undergoes a shape change with reference to its fundamental properties. Regardless of how the field distribution varies with frequency, the fields are still mostly confined within MSTL, suggesting tight field confinement. In [53], we have identified the frequency-varying dominant mode over different frequency ranges by examining the corresponding field components. Specifically, the dominant mode of MSTL in a low-frequency range has been identified as a quasi-TEM microstrip mode, mainly governed by the central region. It is then converted into a quasi-TE_{10} waveguide mode in a high-frequency range, conditioned by the enclosure waveguide. In other words, an incident signal with frequency f_{in} below specific frequency f_c is transmitted through MSTL via a quasi-TEM propagating mode, whereas an incident signal with higher signal frequency components is transmitted selectively via a quasi-TE_{10} propagating mode, as sketched on the bottom right of Fig. 5.2. The specific frequency f_c is the cutoff frequency of HM-SIW, which will be investigated in detail in Section 5.5. This incident signal can be imagined as a broadband signal covering dc to very high frequencies of the electromagnetic spectrum such as THz. This is the unique phenomenon of frequency-enabled mode selectivity or conversion seen in MSTL [86].

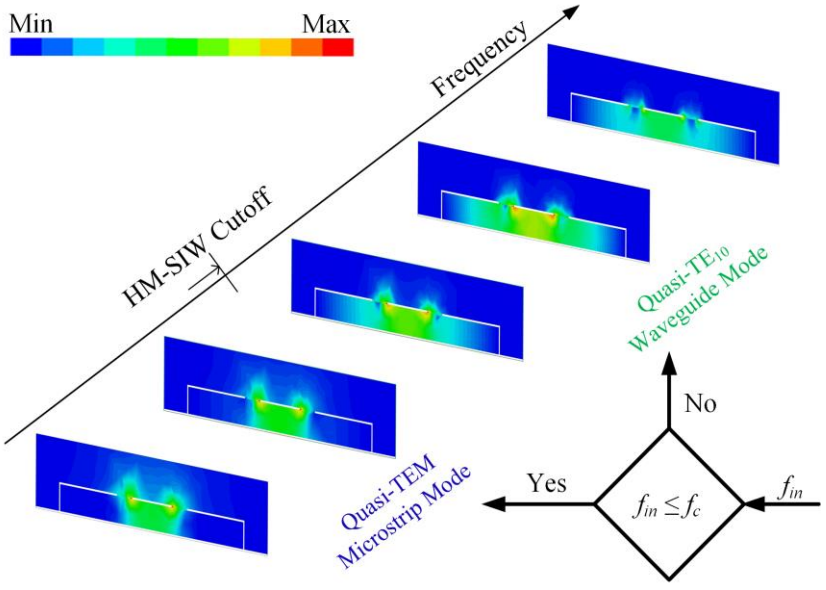

Figure 5.2 Frequency-enabled cross-sectional *E*-field conversion and mode selectivity in a typical MSTL

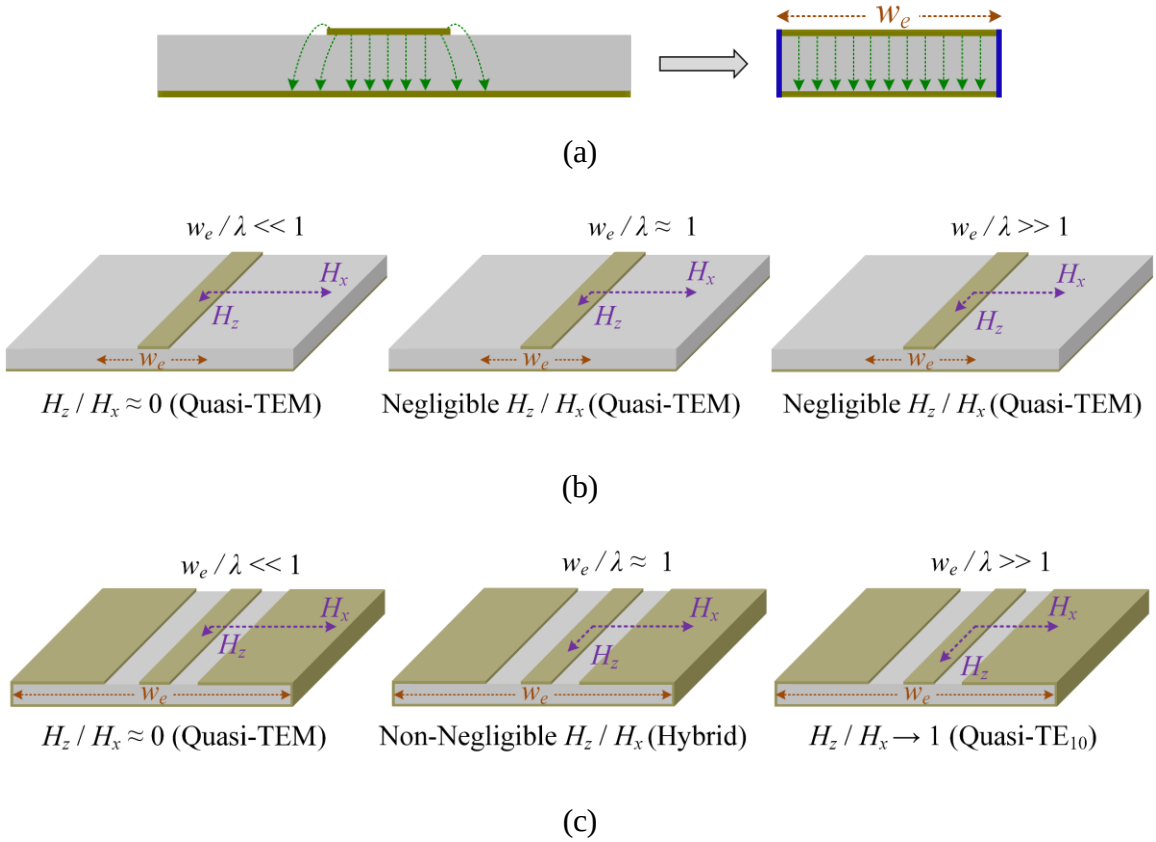

Figure 5.3 Ratio H_z/H_x variation with frequency (wavelength λ). (a) Definition of effective width w_e. (b) Microstrip line case. (c) MSTL case

5.2.2 Essence of mode-selectivity phenomenon

There is a rather straightforward physical explanation to describe this mode-selective behavior from the viewpoint of frequency-dependent modal evolution, which is described in Fig. 5.3. For the sake of illustration, we define variable w_e in Fig. 5.3(a) to present the maximum effective width of field distributions in an unbounded structure. For an open transmission medium such as microstrip line, the effective width w_e should be somewhat larger than the physical width because of the field fringing [see Fig. 5.3(b)]. For a laterally shielded structure such as MSTL, by contrast, the effective width w_e is fairly close or equal to the distance between the bilateral sidewalls [see Fig. 5.3(c)]. Note that w_e is also frequency dependent. It is well-known that a quasi-TEM mode implies a negligible longitudinal field component (essentially H_z component in this case) compared with its transverse and orthogonal electric and magnetic field components [see Fig. 5.3(b)]. On the

other hand, a quasi-TE_{10} mode means there are three intensity-comparable field components, including two transverse orthogonal electric (mainly E_y) and magnetic field components (mainly H_x) as well as one well-pronounced longitudinal magnetic field component (H_z). Interestingly, the transverse fields for the quasi-TEM and quasi-TE_{10} modes may be highly similar in spite of the fact that their confinement is slightly different. Of course, these two modes have different dispersion dynamics because of their different longitudinal components: one is negligible; the other is strong. Let us imagine that a transmission structure can be geometrically engineered such that the initially negligible longitudinal magnetic field component (H_z) gradually becomes non-negligible as frequency increases, as shown in Fig. 5.3(c). In this way, it can be anticipated that the "transformed" quasi-TEM mode with a "strong" longitudinal component holds the fundamental properties of a quasi-TE_{10} mode. Therefore, the mode selectivity or conversion happens. Without any doubt, such an "engineered" frequency-enabled phenomenon is not subject to any geometrical discontinuity in the propagation direction but is conditioned by the making of a topological condition along the cross section. More precisely, the dimensionality of the boundary condition is conditioned by frequency or wavelength. This also explains why some "inductive" structures in RF and microwave engineering can exhibit certain "capacitive" effects beyond a specific frequency range or vice versa. This explanation can supplement and substantiate our discussions on the physical mechanism of mode selectivity from the mode-coupling point of view.

From the viewpoint of mode coupling [91], MSTL can be regarded as a coupled system that is constructed from three parallel or joint transmission elements, including the center microstrip line and the two outer HM-SIWs, as shown in Fig. 5.1(b) and (c). The reason for this way of combination will be presented in Section 5.6.1. Unlike conventional coupled lines [21], [97] or coupled waveguides [91], [98], the constituent elements of MSTL have quite different dispersion characteristics. More specifically, the individual microstrip line has a dominant quasi-TEM microstrip mode freeing it from a frequency cutoff, whereas the individual HM-SIWs each have a dominant quasi-$TE_{0.5,0}$ waveguide mode exhibiting a low-frequency cutoff phenomenon. Once the condition for coupling is satisfied [99], [100], mode couplings occur between the uncoupled modes, whose strength may vary rapidly with frequency. The normal modes (i.e., eigenmodes) of the entire MSTL system can be represented approximately by the uncoupled modes of individual constituent elements. As a result, the frequency-dependent variation of the coupling strength, which is closely

related to the geometrical conditions and material parameters, would affect the eigen fields in MSTL. The resulting dominant mode of MSTL has distinctly different modal behavior in different frequency ranges. Further discussion of mode selectivity can be found in Section 5.6.

5.3 Normal- and coupled-mode analysis of half-mode MSTL

The typical MSTL shown in Fig. 5.1 is a complicated coupled system that involves several dissimilar modes even though its geometry looks like a CBCPW as discussed earlier. In the following, we will reveal that such a structure has masked an interesting electromagnetic reality. To facilitate the following formulations and discussions, we first treat a relatively simple half-mode case, HM-MSTL, to start the normal- and coupled-mode analysis.

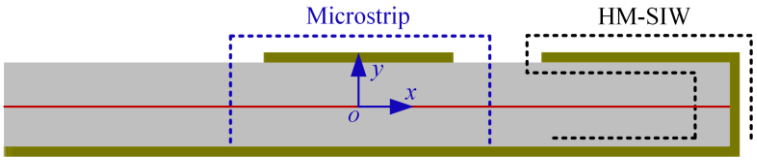

Figure 5.4 Transverse cross-sectional geometry of HM-MSTL

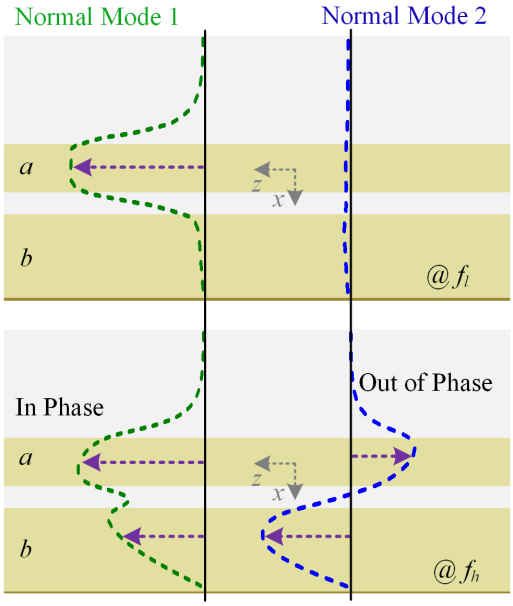

Figure 5.5 Electromagnetic field distributions for the first and second normal modes of HM-MSTL at two frequency points, f_l and f_h (as labeled in Figs. 5.6 and 5.7)

The individual microstrip line and HM-SIW are labeled as *a* and *b*, respectively.

5.3.1 Coupled-mode formalism

As depicted in Fig. 5.4, HM-MSTL is a typical MSTL with one-side HM-SIW removed. It can be considered as a two-guide coupled system that consists of one microstrip line and one HM-SIW. A significant mode coupling occurs between the individual microstrip line and HM-SIW when its dominant mode is above cutoff. The entire HM-MSTL coupled system can support two distinct propagating modes. Similar to those of conventional coupled lines (e.g., CPW) or coupled waveguides, the first normal mode should have in-phase electromagnetic field distributions in the two constituent elements as for the even mode of CPW, whereas the second normal mode should have out-of-phase field distributions as for the odd mode of CPW. However, this is true only at frequencies above the cutoff frequency, f_c, of the quasi-$TE_{0.5,0}$ waveguide mode of HM-SIW. At frequencies below f_c, there exists no appreciable coupling between the microstrip mode and the waveguide mode. In this case, only the first normal mode of HM-MSTL has well-behaved field distributions concentrated primarily in the central microstrip region, whereas the second normal mode is at cutoff. Fig. 5.5 shows this unique feature of HM-MSTL, in which the individual microstrip line and HM-SIW are labeled as *a* and *b*, respectively. Two different frequency points, f_l and f_h (satisfying $f_l < f_c < f_h$, as labeled in Figs. 5.6 and 5.7), are chosen for comparison, where the subscripts stand for "low" and "high". It can be observed that there is a significant difference between the fields of the first normal mode (dominant mode), which reveals the dominant mode of HM-MSTL undergoing a shape change. This feature basically explains the frequency-enabled mode selectivity of HM-MSTL, which is similar to that of MSTL.

Here, it is of interest to treat the first two normal modes of HM-MSTL. To this end, we only need to consider the first guided mode of each constituent element in isolation (e.g., uncoupled element). The coupled-mode theory describing the codirectional coupling in this coupled system can be established in a simple and intuitive way. Referring to the Appendix, the coupled-mode equations can be expressed as

$$\frac{da(z)}{dz} = -j\beta_a a(z) - jK_{ab} b(z) \tag{5.1a}$$

$$\frac{db(z)}{dz} = -j\beta_b b(z) - jK_{ba} a(z) \tag{5.1b}$$

where β_a and β_b are the propagation constants of the uncoupled modes of individual microstrip line and HM-SIW, respectively, $a(z)$ and $b(z)$ are the coupled-mode amplitudes, and K_{ab} and K_{ba} are the coupling coefficients, and they satisfy [101]

$$K_{ba} \approx K_{ab}^{*} + 2\delta c_{ab}^{*} \tag{5.2}$$

where δ denotes the difference of propagation constants between constituent elements, c_{ab} represents the butt coupling coefficient, and the asterisk indicates conjugation. Compared with the mode couplings, the butt couplings in this lossless HM-MSTL system are weak and negligible, so we have

$$K_{ba} \approx K_{ab} = K \tag{5.3}$$

where K is real [94], [102].

5.3.2 Normal-mode solution

For the uniform HM-MSTL system, the propagation constants and coupling coefficients are independent of z; (5.1) can then be solved analytically. As derived in the Appendix, the normal modes (eigenmodes) of the HM-MSTL system can be represented approximately as a linear superposition of the uncoupled modes; their scalar field patterns are

$$\psi_{e1} \approx m\psi_a + n\psi_b \tag{5.4a}$$

$$\psi_{e2} \approx -n\psi_a + m\psi_b \tag{5.4b}$$

where ψ_{e1} and ψ_{e2} represent the electromagnetic field profiles of the first and second normal modes of HM-MSTL, and ψ_a and ψ_b represent the field profiles of the uncoupled quasi-TEM microstrip mode and quasi-$TE_{0.5,0}$ waveguide mode, respectively. The normal modes of HM-MSTL are orthogonal, so we have

$$\int_C \psi_{e1}\psi_{e2}^{*} ds = 0 \tag{5.5}$$

where C denotes the entire cross section of HM-MSTL. After some algebraic manipulations (see the Appendix), we obtain

$$m = \sqrt{\frac{1}{2}\left[1+\frac{\beta_a-\beta_b}{\sqrt{(\beta_a-\beta_b)^2+(2K)^2}}\right]} \tag{5.6a}$$

$$n = \sqrt{\frac{1}{2}\left[1 - \frac{\beta_a - \beta_b}{\sqrt{(\beta_a - \beta_b)^2 + (2K)^2}}\right]}. \tag{5.6b}$$

The coupling coefficient K is generally calculated by a field overlap integral of transverse fields. Here, the normal-mode analysis and coupled-mode theory are combined, and K can then be calculated as (see (5.22) in the Appendix)

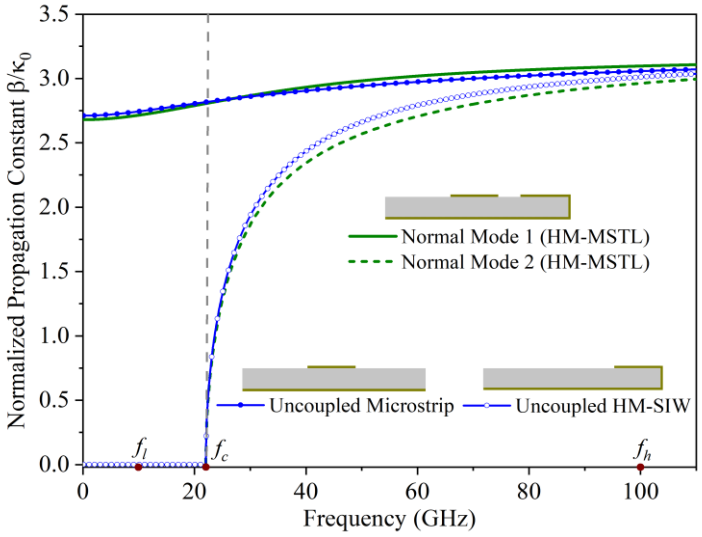

Figure 5.6 Normalized propagation constants β/κ_0 of normal modes of HM-MSTL, compared with those of uncoupled microstrip line and HM-SIW

Insets show simulation models of HM-MSTL, HM-SIW, and microstrip line.

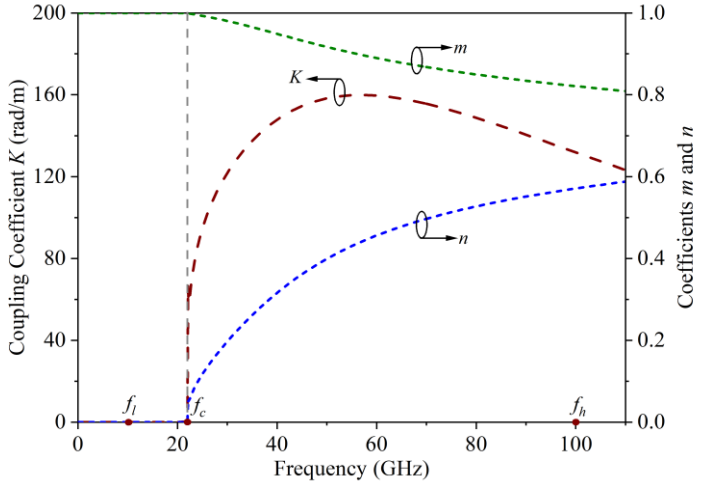

Figure 5.7 Calculated coefficients, K, m, and n, for HM-MSTL

Table 5.2 Coefficients and field profiles of HM-MSTL versus frequency

	$f \le f_c$	$f > f_c$
m	1	$\neq 0$, ↘
n	0	$\neq 0$, ↗
$\psi_{e1} \approx m\psi_a + n\psi_b$	ψ_a	ψ_a & ψ_b
$\psi_{e2} \approx -n\psi_a + m\psi_b$	ψ_b (at cutoff)	$-\psi_a$ & ψ_b
ψ_{e1}, ψ_{e2}: First and second normal modes of HM-MSTL ψ_a: Quasi-TEM microstrip mode ψ_b: Quasi-$TE_{0.5,0}$ waveguide mode		
Conclusion: The first normal mode (dominant mode) of HM-MSTL has the frequency-enabled mode selectivity.		

$$K = \frac{1}{2}\sqrt{(\beta_{e1} - \beta_{e2})^2 - (\beta_a - \beta_b)^2} \tag{5.7}$$

where β_{e1} and β_{e2} are the propagation constants of the first two normal modes of HM-MSTL. It can be seen from (5.6) and (5.7) that to evaluate the complete coupling behavior, we only need to know the four propagation constants, β_{e1}, β_{e2}, β_a, and β_b. They can be obtained from analytical expressions, empirical formulas, or rigorous numerical methods. Here, the numerical simulation through full-wave modal and eigenmode solutions is conducted to extract these parameters.

Fig. 5.6 shows the normalized propagation constants β/k_0 of the first two normal modes of HM-MSTL and those of the two uncoupled modes of the individual microstrip line and HM-SIW, where k_0 is the free-space wavenumber. The insets show simulation models of the HM-MSTL, HM-SIW, and microstrip line structures. Their sizes are kept the same as those of the dc-to-110-GHz MSTL (see Table 5.1) for comparison. It can be observed that both the second normal mode of HM-MSTL and the uncoupled quasi-$TE_{0.5,0}$ waveguide mode of HM-SIW exhibit a cutoff phenomenon and have the same cutoff frequency that is labeled as f_c (= 22 GHz). With these results, the coefficients, K, m, and n, are calculated from (5.6) and (5.7). As plotted in Fig. 5.7, all these coefficient curves are divided by the specific frequency point f_c into two different segments. When frequency f is lower than or equal to f_c ($f \le f_c$), we have $K \approx 0$ rad/m, indicating that there is no coupling between the microstrip mode and the waveguide mode. Accordingly, the curves of m and n are fairly flat in this case; $m \approx 1$ and $n \approx 0$. The resulting first normal mode of HM-MSTL resembles the uncoupled microstrip mode [i.e., $\psi_{e1} = \psi_a$, see (5.4a)], whereas the second normal mode of HM-MSTL resembles the uncoupled waveguide mode of HM-SIW [i.e., $\psi_{e2} = \psi_b$, see (5.4b)], which is at cutoff in this case.

When $f > f_c$, the coupling tends to occur. As frequency continues to increase, the coupling coefficient K increases rapidly to its peak value and then decreases somewhat. Both m and n are nonzero ($0 < m < 1$ and $0 < n < 1$) but vary inversely with frequency. The value of m decreases slowly with frequency, whereas the value of n increases gradually. As a result, both the first and second normal modes of HM-MSTL are approximately viewed as a superposition of the two uncoupled modes, but in different manners. These results are listed in Table 5.2.

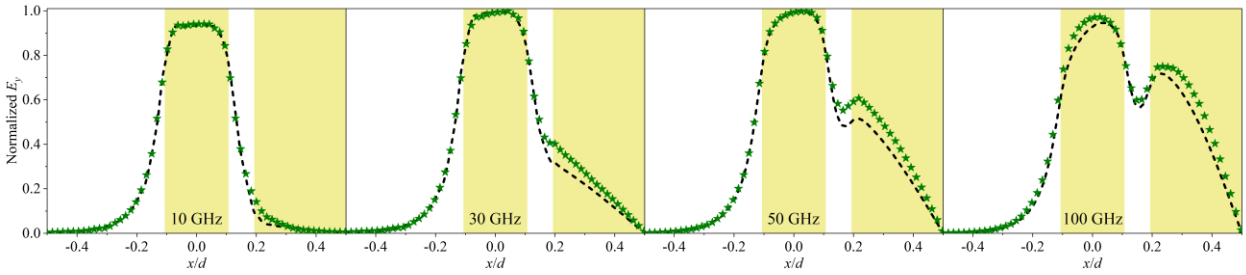

(a)

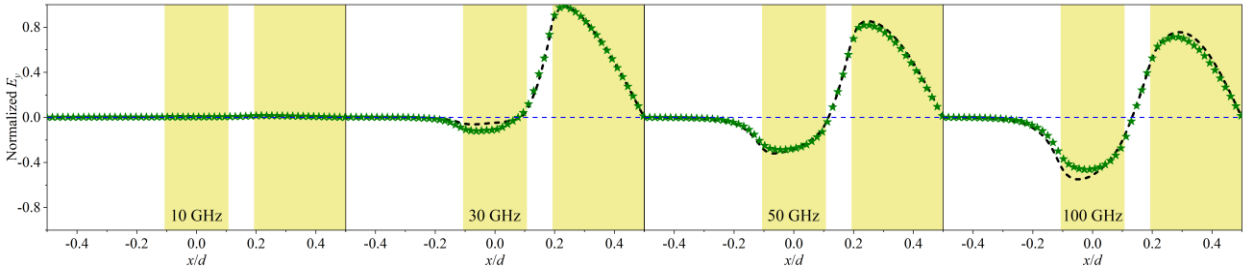

(b)

Figure 5.8 Normalized E_y fields at 10, 30, 50, and 100 GHz for (a) the first and (b) second normal modes of HM-MSTL, which are obtained from numerical simulation (black dashed lines) and (5.4) (green stars)

Yellow regions represent the top conductors of HM-MSTL with regard to the x-axis (Fig. 5.4); parameter d denotes the distance along the x-axis and satisfies $d = 2g + 2s + w$, where g, s, and w are defined in Table 5.1.

5.3.3 Normal modal fields

The above theoretical prediction describes how the modal behavior of the first two normal modes of HM-MSTL varies with frequency. As an example, we examine their E_y field components to visualize this phenomenon and to verify the prediction. The E_y fields along the x-axis at $y = 0$ (see the red line

drawn in Fig. 5.4) at 10, 30, 50, and 100 GHz are approximated by (5.4) (i.e., analytical modal solution), compared with the exact fields extracted by the field calculator [57] (i.e., full-wave modal solution). They are normalized to the corresponding maximum E_y field magnitudes. As shown in Fig. 5.8, the yellow regions represent the top conductors of HM-MSTL with regard to the x-axis (Fig. 5.4); parameter d denotes the distance along the x-axis and satisfies $d = 2g + 2s + w$, where g, s, and w are defined in Table 5.1. For both the first and second normal modes, the approximate field curves agree with the exact field curves at different frequencies. At 10 GHz ($< f_c$), both the dominant mode of individual HM-SIW and the second normal mode of HM-MSTL are at cutoff. As a result, the field intensity of the first normal mode is concentrated around the center microstrip line, whereas the second normal mode has no well-behaved field distributions. In contrast, at 30, 50, and 100 GHz ($> f_c$), the coupling between the microstrip line and HM-SIW appears (i.e., $K \neq 0$ rad/m, causing $m \neq 1$ and $n \neq 0$). For the first normal mode of HM-MSTL, the right parts of the field curves rise remarkably with frequency. In other words, the fields are spread away from the center microstrip line to the side HM-SIW, implying that the first normal mode is being converted. It suggests the phenomenon of mode selectivity or conversion. The fields of the second normal mode just have a change in magnitude with frequency. This phenomenon of field variation with frequency is consistent with the above description, therefore verifying the modal analysis of HM-MSTL.

5.4 Normal- and coupled-mode analysis of MSTL

In this section, we consider the typical MSTL. As described in Section 5.2.2, this MSTL can effectively be considered as a three-guide coupled system that consists of one microstrip line and two HM-SIWs [Figs. 5.1(b) and (c)]. This suggests that a generalized asymmetry be possible in the analysis even though we consider two identical HM-SIWs for the condition of symmetry in the following joint normal- and coupled-mode analysis.

5.4.1 Coupled-mode formalism

A coupled-mode analysis is conducted for the MSTL coupled system. At frequencies above the cutoff frequency f_c of the quasi-$TE_{0.5,0}$ waveguide mode of HM-SIWs, the first normal mode of MSTL has in-phase field distributions in its constituent elements, whereas the second normal mode has out-of-phase field distributions. At frequencies below f_c, only the first normal mode has well-behaved field

distributions concentrated primarily in the central microstrip region; the second normal mode is at cutoff. Fig. 5.9 depicts this unique feature, in which the individual microstrip line and HM-SIWs are labeled as *A*, *B*, and *C*. This is analogous to the HM-MSTL case. Two different frequency points, f_l and f_h (satisfying $f_l < f_c < f_h$), are chosen, as labeled in Figs. 5.10 and 5.11. A close inspection of Fig. 5.9 shows that the field distributions for the first normal mode change significantly with frequency, implying that the dominant mode (i.e., the first normal mode) of MSTL undergoes a mode conversion, namely the mode-selectivity phenomenon.

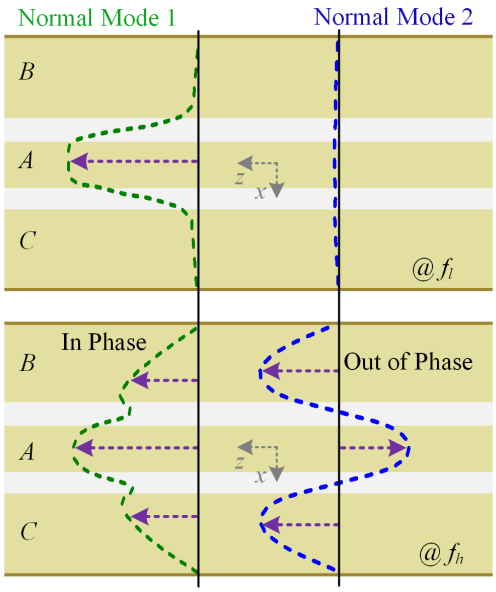

Figure 5.9 Electromagnetic field distributions for the first and second normal modes of MSTL at two frequency points, f_l and f_h (as labeled in Figs. 5.10 and 5.11)

The individual microstrip line and HM-SIWs are labeled as *A*, *B*, and *C*, respectively.

Under the same assumptions (negligible butt couplings and losses) involved in the analysis of the HM-MSTL, this typical MSTL can also be treated by the coupled-mode analysis. Coupled-mode equations describing this MSTL system are

$$\frac{dA(z)}{dz} = -j\beta_A A(z) - jK_{AB}B(z) - jK_{AC}C(z) \tag{5.8a}$$

$$\frac{dB(z)}{dz} = -j\beta_B B(z) - jK_{BA}A(z) - jK_{BC}C(z) \tag{5.8b}$$

Table 5.3 Parameters for both HM-MSTL and MSTL

HM-MSTL	MSTL	Description	
a(z), b(z)	A(z), B(z), C(z)	Coupled-mode amplitudes	Individual microstrip line and HM-SIW
β_a, β_b	β_A, β_B, β_C	Propagation constants	
K_{ab}, K_{ba}, K	K_{AB}, K_{AC}, K_{BC}, K_{BA}, K_{CA}, K_{CB}	Coupling coefficients	
ψ_a, ψ_b	ψ_A, ψ_B, ψ_C	Field profiles	
β_{e1}, β_{e2}	β_{E1}, β_{E2}	Propagation constants	Normal modes of coupled systems
ψ_{e1}, ψ_{e2}	ψ_{E1}, ψ_{E2}	Field profiles	
m, n	M, N	Coefficients	Mutual relation

$$\frac{dC(z)}{dz} = -j\beta_C C(z) - jK_{CA}A(z) - jK_{CB}B(z) \tag{5.8c}$$

where $A(z)$, $B(z)$, and $C(z)$ are the coupled-mode amplitudes; β_A is the mode propagation constant of the individual microstrip line; β_B and β_C are those of the individual HM-SIWs; K_{AB} (= K_{BA}) and K_{AC} (= K_{CA}) are the coupling coefficients between the microstrip line and each HM-SIW; K_{BC} (= K_{CB}) is the coupling coefficient between the two outer HM-SIWs. Note that we use capital subscripts such as A, B, and C when referring to MSTL. Due to the symmetry of MSTL, as it is considered in this work, we have $K_{AB} = K_{BA} = K_{AC} = K_{CA}$, $B(z) = C(z)$, and $\beta_B = \beta_C$. In addition, the propagation equations for this three-guide system (MSTL), (5.8a)-(5.8c), can be simplified to the equations for the two-guide system (HM-MSTL), (5.1a) and (5.1b), using the following substitutions [103]:

$$a(z) = A(z) \tag{5.9a}$$

$$b(z) = \frac{1}{\sqrt{2}}[B(z) + C(z)] \tag{5.9b}$$

$$\beta_a = \beta_A \tag{5.9c}$$

$$\beta_b = \beta_B + K_{BC} \tag{5.9d}$$

$$K = \sqrt{2}K_{AB}. \tag{5.9e}$$

The left- and right-hand sides of (5.9) correspond to the two-guide HM-MSTL system and the three-guide MSTL system, respectively. The coupling coefficients, K_{AB} and K_{BC}, can be obtained by

combining the coupled-mode theory and normal-mode analysis, as in (5.7). For clarity, the parameters for both MSTL and HM-MSTL are listed in Table 5.3.

5.4.2 Normal-mode solution

With the above simplification of the coupled-mode equations for the three-guide MSTL system, its normal-mode solutions can be straightforwardly obtained in a manner similar to that for the HM-MSTL case. After substituting (5.9c)-(5.9e) into (5.22) (see the Appendix), the propagation constants (eigenvalues) of the first two normal modes of MSTL, β_{E1} and β_{E2}, are given by

$$\beta_{E1} = \frac{\beta_A + \beta_B + K_{BC}}{2} + \sqrt{\left(\frac{\beta_A - \beta_B - K_{BC}}{2}\right)^2 + 2K_{AB}^2} \tag{5.10a}$$

$$\beta_{E2} = \frac{\beta_A + \beta_B + K_{BC}}{2} - \sqrt{\left(\frac{\beta_A - \beta_B - K_{BC}}{2}\right)^2 + 2K_{AB}^2}. \tag{5.10b}$$

As in the case of HM-MSTL, the normal modes of the entire MSTL coupled system can be represented approximately as a linear superposition of the uncoupled modes of individual constituent elements. Here, we restrict our attention to the first two symmetric normal modes (eigenmodes) of MSTL, whose scalar field patterns are expressed approximately as [103]

$$\psi_{E1} \approx \frac{N}{\sqrt{2}}\psi_B + M\psi_A + \frac{N}{\sqrt{2}}\psi_C \tag{5.11a}$$

$$\psi_{E2} \approx \frac{M}{\sqrt{2}}\psi_B - N\psi_A + \frac{M}{\sqrt{2}}\psi_C \tag{5.11b}$$

where ψ_{E1} and ψ_{E2} represent the field profiles of the first and second normal modes of MSTL, respectively, and ψ_B (= ψ_C) and ψ_A represent the field profiles of the uncoupled quasi-$TE_{0.5,0}$ waveguide mode and the quasi-TEM microstrip mode, respectively. Substituting (5.9c)-(5.9e) into (5.6) gives the following expressions of the coefficients M and N:

$$M = \sqrt{\frac{1}{2}\left[1 + \frac{\beta_A - \beta_B - K_{BC}}{\sqrt{(\beta_A - \beta_B - K_{BC})^2 + 8K_{AB}^2}}\right]} \tag{5.12a}$$

$$N = \sqrt{\frac{1}{2}\left[1 - \frac{\beta_A - \beta_B - K_{BC}}{\sqrt{(\beta_A - \beta_B - K_{BC})^2 + 8K_{AB}^2}}\right]}. \tag{5.12b}$$

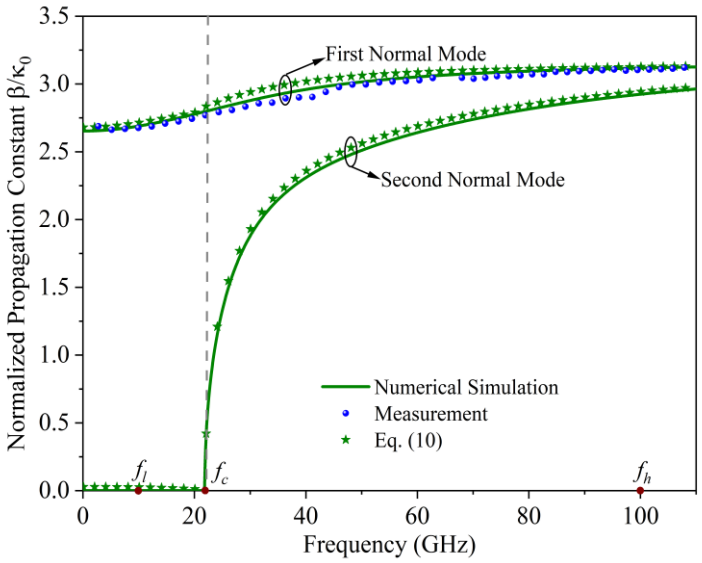

Figure 5.10 Normalized propagation constants β/κ_0 of both the first and second normal modes of MSTL, which are obtained from both numerical simulation and (5.10) for comparison

Measurement-extracted propagation constant of MSTL is also shown here for experimental verification.

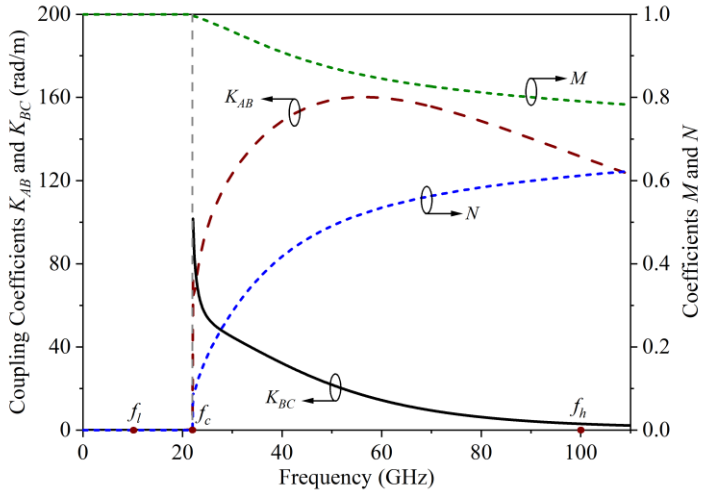

Figure 5.11 Calculated coefficients, K_{AB}, K_{BC}, M, and N, for MSTL

With the extracted β_A, β_B, K_{AB}, and K_{BC}, we can calculate β_{E1} and β_{E2} from (5.10). A comparison with the exact eigenvalues extracted through the full-wave simulation is shown in Fig. 5.10 where the

propagation constants are normalized to k_0. It can be observed that the calculated results are in a reasonable agreement with the simulated results. The propagation constant of MSTL extracted from the measured *S*-parameters is also shown in Fig. 5.10. It agrees with the calculated and simulated counterparts of the first normal mode (i.e., dominant mode) of MSTL, which verifies our analysis to some extent. It is important to note that the measurement-extracted propagation constant is only for the first normal mode of MSTL. This is because the dominant mode of MSTL is selectively excited, to the exclusion of all other modes, with the help of the specially designed transitions. The specific excitation scheme, design illustrations, and experimental measurements are presented in Part II (Chapter 6) of this work [90]. The second normal mode of MSTL has a cutoff frequency equal to that of the uncoupled quasi-$TE_{0.5,0}$ waveguide mode (i.e., f_c = 22 GHz). The coefficients M and N for MSTL are calculated from (5.12), as plotted in Fig. 5.11, in which the extracted K_{AB} and K_{BC} are also plotted. When $f \le f_c$, we have $K_{AB} \approx 0$ rad/m, $K_{BC} \approx 0$ rad/m, $M \approx 1$, and $N \approx 0$. When $f > f_c$, however, they are nonzero and show similar variation trends as those for HM-MSTL (see Fig. 5.7) except for K_{BC}, which are not repeated here. As shown in Fig. 5.11, K_{BC} is much smaller than K_{AB} ($K_{BC} < K_{AB}$) at frequencies above f_c; by definition, it is reasonable. Therefore, the coupling coefficient mentioned below will be K [$= \sqrt{2}\,K_{AB}$, see (5.9e)] if not otherwise specified. As a result of the changes in M and N, the field profiles of the normal modes of MSTL get modified with frequency. They are similar to those of HM-MSTL, as listed in Table 5.4.

Table 5.4 Coefficients and field profiles of MSTL versus frequency

	$f \le f_c$	$f > f_c$
M	1	$\neq 0$, ↘
N	0	$\neq 0$, ↗
$\psi_{E1} \approx \frac{N}{\sqrt{2}}\psi_B + M\psi_A + \frac{N}{\sqrt{2}}\psi_C$	ψ_A	ψ_A & ψ_B & ψ_C
$\psi_{E2} \approx \frac{M}{\sqrt{2}}\psi_B - N\psi_A + \frac{M}{\sqrt{2}}\psi_C$	ψ_B & ψ_C (at cutoff)	-ψ_A & ψ_B & ψ_C
ψ_{E1}, ψ_{E2}: First and second normal modes of MSTL ψ_A: Quasi-TEM microstrip mode ψ_B, ψ_C: Quasi-$TE_{0.5,0}$ waveguide mode		
Conclusion: The first normal mode (dominant mode) of MSTL has the frequency-enabled mode selectivity.		

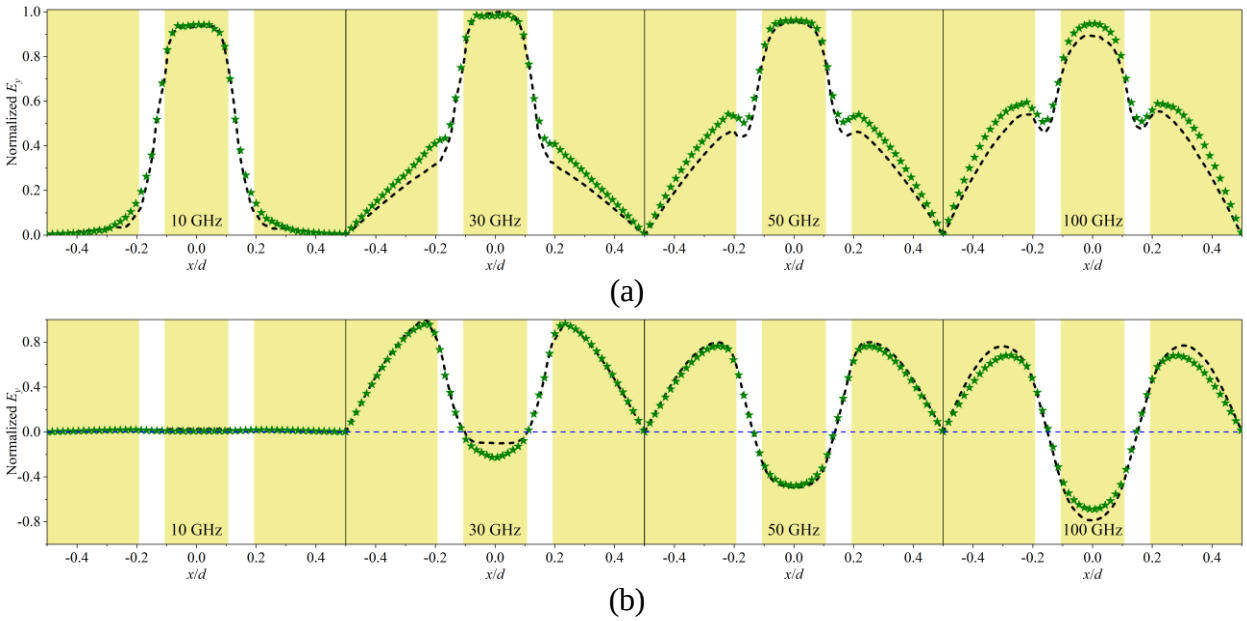

Figure 5.12 Normalized E_y fields at 10, 30, 50, and 100 GHz for (a) the first and (b) second normal modes of MSTL, which are obtained from numerical simulation (black dashed lines) and (5.11) (green stars)

Yellow regions represent the top conductors of MSTL with regard to the x-axis (Fig. 5.1); parameter d denotes the distance along the x-axis and satisfies $d = 2g + 2s + w$, where g, s, and w are defined in Table 5.1.

5.4.3 Normal modal fields

To illustrate the frequency-dependent modal behavior, we first examine the E_y field components of both the first and second normal modes of MSTL in a similar way as in the case of HM-MSTL. The normalized magnitude curves along the x-axis [see the red line drawn in Fig. 5.1(c)] at 10, 30, 50, and 100 GHz are all plotted in Fig. 5.12, which are obtained from both (5.11) and numerical simulation (i.e., analytical and full-wave modal solutions) for comparison. As can be seen, the two methods produce almost identical results, thus affirming the correctness of the above normal- and coupled-mode analysis. It can be observed from Fig. 5.12(b) that at 10 GHz ($< f_c$), the second normal mode of MSTL is at cutoff and has no visible field distributions. At 30, 50, and 100 GHz ($> f_c$), the field curves have similar shapes but different magnitudes. Let us now closely examine the first normal mode of MSTL. From Fig. 5.12(a), its fields are highly concentrated around the central microstrip region at 10 GHz. In this case, the two outer HM-SIWs are at cutoff; the couplings in this MSTL

coupled system are extremely weak (basically zero) and can be ignored (i.e., $K_{AB} \approx 0$ rad/m and $K_{BC} \approx 0$ rad/m, causing $M \approx 1$ and $N \approx 0$, and finally $\psi_{E1} = \psi_A$). At frequencies above f_c (e.g., 30, 50, and 100 GHz), both the left and right parts of the field curves rise remarkably, which end up being analogous to those in an RWG. In this case, the couplings, K_{AB} and K_{BC}, can no longer be considered negligible, causing the fields to be spread out from the center microstrip line to the outer HM-SIWs. Finally, the E_y field in MSTL becomes approximately a linear superposition of those in the individual microstrip line and HM-SIWs. This large change in field distributions indicates the conversion of the first normal mode of MSTL, and it is consistent with the phenomenon reported in [53].

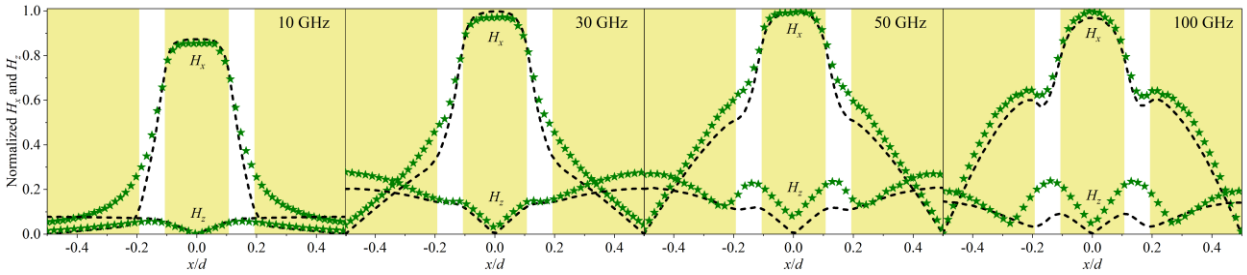

Figure 5.13 Normalized H_x and H_z fields at 10, 30, 50, and 100 GHz for the first normal mode of MSTL, which are obtained from numerical simulation (black dashed lines) and (5.11) (green stars)

Yellow regions represent the top conductors of MSTL with regard to the x-axis (Fig. 5.1); parameter d denotes the distance along the x-axis and satisfies $d = 2g + 2s + w$, where g, s, and w are defined in Table 5.1.

To further demonstrate the mode conversion of the first normal mode, we also examine its normalized magnetic field components, H_x and H_z, in a manner similar to E_y, as plotted in Fig. 5.13. Similarly, the approximate magnetic fields derived from the theoretical analysis [see (5.11)] are in reasonable agreement with the exact fields extracted from the rigorous numerical simulation except near the two slits, where some deviations of the H_z field at 50 and 100 GHz can be observed. As can be seen, the H_x field undergoes an obvious change similar to that of the E_y field. The H_z field at 10 GHz ($< f_c$) is relatively weak, and it increases significantly at a frequency above f_c (e.g., 30, 50, or 100 GHz). By rigorously looking into the field components at different frequencies in [53] and [86], we have already

confirmed that the first normal mode (i.e., dominant mode) of MSTL behaves as a quasi-TEM microstrip mode at low frequencies and is converted into a quasi-TE_{10} waveguide mode at higher frequencies. This mode selectivity of special interest can be readily understood with the aid of the above modal analysis.

5.5 Parametric study of MSTL

To obtain preliminary guidance in the design of an MSTL, a parametric study is carried out in this section. From the above modal analysis, it can be found that the specific frequency f_c plays a critical role in quantifying the mode-selectivity phenomenon observed in MSTL, as labeled in Figs. 5.7 and 5.11. The dominant mode of MSTL behaves as the quasi-TEM microstrip mode at frequencies lower than or equal to f_c ($f \le f_c$) and as the quasi-TE_{10} waveguide mode at frequencies higher than f_c ($f > f_c$). A complete conversion process of the dominant mode of MSTL has been presented in detail in [86] by defining several characteristic frequencies. In fact, f_c is the cutoff frequency of the second normal mode of MSTL and the uncoupled quasi-$TE_{0.5,0}$ waveguide mode of the individual HM-SIW as well. It can thus be expressed as

$$f_c = \frac{c}{4\sqrt{\varepsilon_r}(g+\Delta g)} \tag{5.13}$$

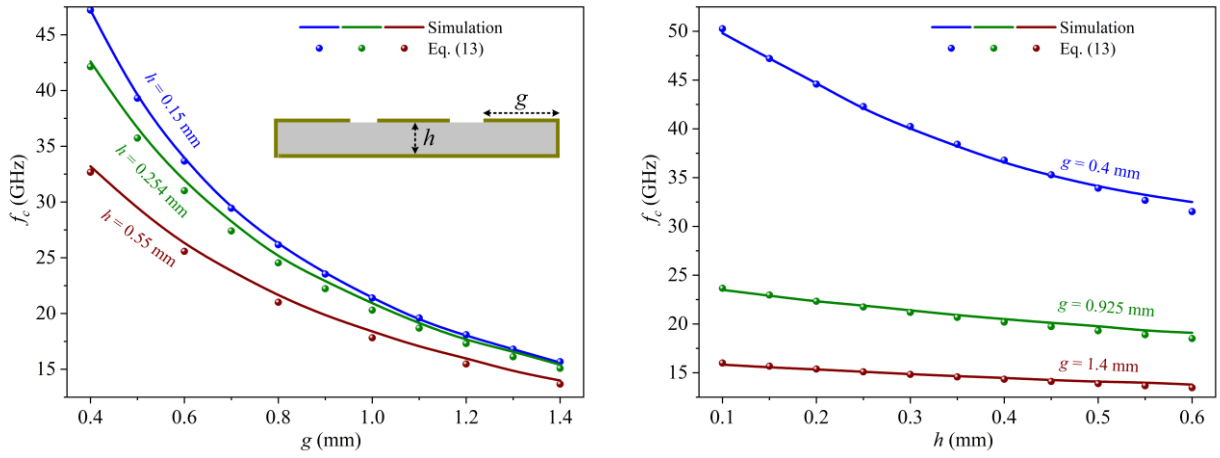

(a) (b)

Figure 5.14 Comparison of simulated and calculated frequency points f_c versus (a) side conductor width g and (b) substrate thickness h that are labeled in the inset of Fig. 5.14(a)

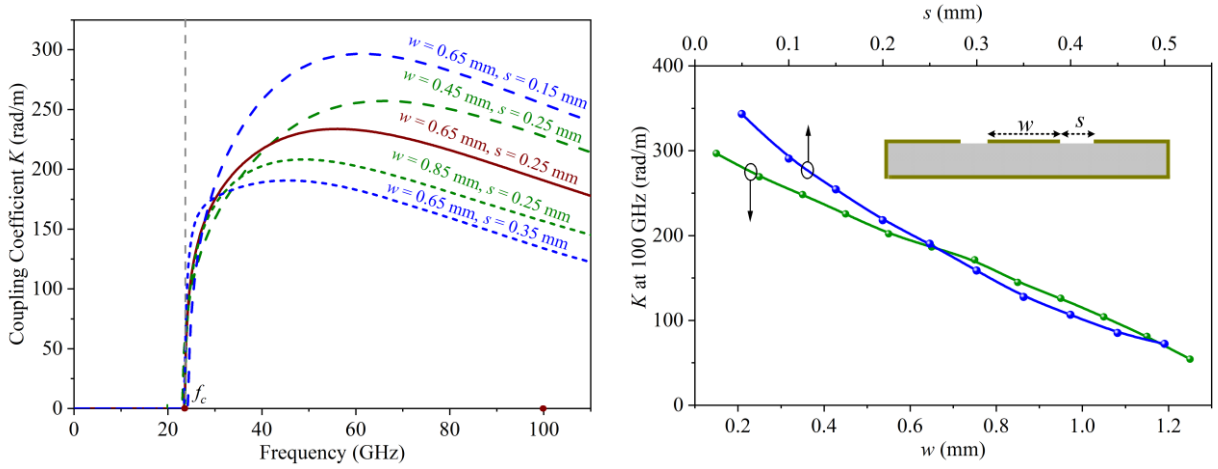

(a) (b)

Figure 5.15 Coupling coefficient K (a) in the entire frequency range and (b) at 100 GHz versus center strip width w and slit width s, which are labeled in the inset of Fig. 5.15(b)

where c is the speed of light in free space, and the additional width Δg accounting for the effect of fringing fields is estimated as (modified from [95])

$$\Delta g = \frac{h}{50}\times(1+\frac{4}{\varepsilon_r})\times\ln(0.79\frac{g^2}{h^3}+\frac{104g-261}{h^2}+\frac{38}{h}+2.77). \tag{5.14}$$

It can be found from (5.13) and (5.14) that f_c is determined by the two geometrical parameters, substrate thickness h and side conductor width g. Fig. 5.14 compares the calculated f_c from (5.13) with the simulation results for various values of h and g, in which other parameter values remain the same as listed in Table 5.1. The comparison shows that (5.13) provides an estimation of this specific frequency with a calculation error below 3%.

Other geometrical parameters including the center strip width w and the slit width s have no significant effect on f_c but affect the coupling strength in the MSTL system, as shown in Fig. 5.15(a). Here, we treat the coupling coefficient K in (5.9e). As observed, K experiences a considerable decrease at high frequencies ($> f_c$) when w increases from 0.45 to 0.85 mm in an increment of 0.2 mm, or s increases from 0.15 to 0.35 mm in an increment of 0.1 mm. In contrast, K is still near zero at frequencies below f_c. As a further check, the values of K at 100 GHz are extracted and depicted

in Fig. 5.15(b) as functions of w and s. It can be observed that K at 100 GHz is an approximate negative linear function of w, whereas there exists a nonlinear relationship between K and s.

This parametric study shows how the geometrical parameters affect the performance of MSTL, that is, g and h determine the critical frequency f_c, whereas w and s primarily determine the coupling strength between the microstrip line and HM-SIWs. Together with the empirical equations given in [86], this parametric study is instructive and provides some meaningful design guidance.

5.6 Discussion

5.6.1 Mode selectivity of MSTL

It is now found that the phenomenon of frequency-enabled mode selectivity occurring in the longitudinally uniform MSTL (or HM-MSTL) is special and unique. At low frequencies ($\leq f_c$), MSTL behaves as a microstrip line with a folded ground. Notably, the dominant mode of MSTL is a microstrip mode rather than a CPW mode in this case despite the fact that both are the quasi-TEM modes, regardless of the similarity of MSTL to the conventional CBCPW with bilateral sidewalls. Due to the relatively thin substrate of MSTL ($h < w$ and $h < w/2 + s$, see Table 5.1), the fringing fields around the two slits (see Fig. 5.1) are much weaker than the main fields between the top center strip and the bottom conductor, which has been discussed in detail in [47], [86], and [104]. This is the reason why we can decompose the MSTL system into a superposition of two HM-SIWs and one microstrip line rather than one CPW. At higher frequencies ($> f_c$), MSTL behaves as a slitted RWG (a dielectric-filled RWG with two additional slits etched symmetrically in the top conducting plane) with a dominant quasi-TE_{10} waveguide mode [25]. The specific mode-selectivity phenomenon occurring for the dominant mode of MSTL has been explained from a joint normal- and coupled-mode theory and visualized with full-wave modal and eigenmode solutions.

It is very difficult to experimentally examine the field distributions in MSTL across a wide frequency range. Instead, the propagation constant of MSTL is experimentally extracted (Fig. 5.10), providing an indirect experimental verification. The detailed experimental measurements are described in Part II (Chapter 6) of this work [90], in which the excitation scheme of MSTL and practical transition design are also presented for the demonstration purpose. This work only considers a typical MSTL structure which is symmetric about the yz plane (Fig. 5.1). In fact, an asymmetric MSTL, in which a

mode-selectivity phenomenon also occurs, can also be treated by solving the eigenvalue matrix of a three-guide system [22].

5.6.2 Frequency-varying mode coupling

As we have seen from the above normal- and coupled-mode analysis, the occurrence of the mode-selectivity phenomenon is attributable to the *frequency-varying mode coupling*, whose strength approaches zero at low frequencies and becomes sufficiently large at higher frequencies (Figs. 5.7 and 5.11). In fact, the leaky-wave theory can be used to help further interpret this special phenomenon. It starts by considering MSTL as a CBCPW (also called GCPW) bounded by bilateral conducting sidewalls, which are symmetrically located on the opposite sides along the thin substrate and electrically connect the upper and lower "ground planes." The thin CBCPW, which actually behaves more like a microstrip line, supports a "leaky" microstrip mode [104]. In this case, its power would leak away from the section of the central "microstrip" in the form of a parallel-plate waveguide mode (supported by the "ground planes") propagating at an angle. The "leaky" wave is reflected by the sidewalls and is therefore returned to the original "leaky" line [100]. The resulting guided mode will remain tightly bound to the entire guiding structure (i.e., MSTL) from which its guided power is no longer "lost" so that the mode wavenumber along the uniform MSTL is no longer complex but is real. The "ground planes" together with the sidewalls make up two HM-SIWs, which introduce HM-SIW guided modes (i.e., quasi-$TE_{0.5,0}$ modes). This means mode couplings occurring between the "leaky" microstrip mode and the HM-SIW modes, which require the well-known condition for coupling in which the propagation constant of the unperturbed microstrip mode should be equal or smaller than those of HM-SIW modes above some critical frequency. As a consequence, the fields associated with a coupling region become some combination of the microstrip mode and the HM-SIW modes through which the coupling takes place; the fields within the coupling region will be distributed throughout the entire composite MSTL system rather than concentrated near the microstrip itself [105]. Indeed, this is the mode-selectivity phenomenon we observed in MSTL.

It is worthwhile to point out that the extracted dispersion curve (β/κ_0) for the individual microstrip mode is above that for the HM-SIW mode over the complete operating range of interest (no intersection points observed from Fig. 5.6), but a mode coupling of significance between them has been observed (Figs. 5.7 and 5.11). We believe that this may be caused by an additional "leaky"

dominant mode of the individual microstrip line [106], which should be investigated in our future work.

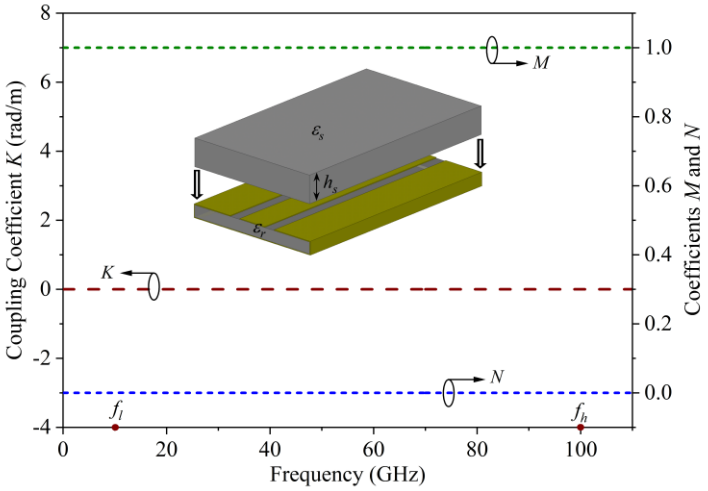

(a)

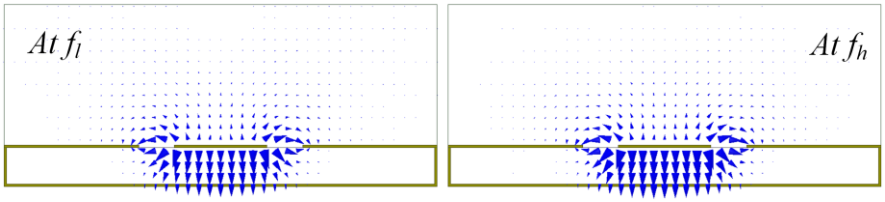

(b)

Figure 5.16 MSTL loaded with a dielectric superstrate. (a) Calculated coefficients, *K*, *M*, and *N*. Inset shows the simulation model where we set h_s = 1 mm and $\varepsilon_s = \varepsilon_r$ =10.2. (b) Cross-sectional *E*-field distributions for the dominant mode at frequency points, f_l and f_h [as labeled in Fig. 5.16(a)]

Both dielectric substrate and superstrate are set to be transparent to clearly show the fields.

We will now examine the possibilities of suppressing or avoiding the frequency-varying mode coupling, which can help to further understand the mode selectivity of MSTL. It is still true that the individual microstrip line and HM-SIWs taken separately have different propagation constants (i.e., $\beta_A \neq \beta_B$). With reference to (5.12a) and (5.12b), we have $M = 1$ and $N = 0$ at any frequency if the coupling coefficient *K* is still near zero (i.e., $K_{AB} = 0$ rad/m). Consequently, the first normal mode of

MSTL is still the microstrip mode [i.e., $\psi_{E1} = \psi_A$, see (5.11a)], thus meaning that the phenomenon of mode selectivity disappears. In fact, there are several methods that can be used to get rid of mode couplings. One is to enlarge the guide separation (i.e., slit width *s* labeled in Fig. 5.1), as expected. The other is to use multiple dielectric layers [73], [107]. For example, placing a superstrate onto the top of the original MSTL is an effective and simple way. It requires that the superstrate be thick enough, and its relative permittivity ε_s be fairly close or equal to that of the bottom (original) substrate ε_r ($\varepsilon_s \approx \varepsilon_r$). This forms a homogeneous dielectric region, within which all the fields are contained. This indicates that the individual microstrip line, whose effective permittivity is also close to ε_r, will no longer support a "leaky" guided mode. Therefore, there is no coupling between this microstrip line and the HM-SIWs. Fig. 5.16 depicts this scenario, in which the inset shows the simulation model of the MSTL loaded with a dielectric superstrate of permittivity $\varepsilon_s = 10.2$ and thickness $h_s = 1$ mm. The coefficients *K*, *M*, and *N* are calculated from (5.9e) and (5.12) and plotted in Fig. 5.16(a), obtaining $K \approx 0$ rad/m, $M \approx 1$, and $N \approx 0$ in the entire frequency range. Accordingly, the mode-selectivity phenomenon is not retained (i.e., $\psi_{E1} = \psi_A$), which has been verified by the full-wave simulation. As shown in Fig. 5.16(b), the extracted *E*-field distributions for the dominant mode at different frequency points, f_l and f_h, are almost the same; actually, this mode is still a TEM mode rather than a quasi-TEM or quasi-TE_{10} mode. This special case highlights the importance of the transverse inhomogeneity of MSTL to create the condition for mode coupling and to sustain the mode selectivity of guided waves.

5.6.3 Mode identification and variability

To avoid potential confusion, we would reiterate that the frequency-enabled mode selectivity described and discussed in this work is for the *dominant mode* (i.e., the first normal mode) of MSTL. Its physical mechanism has been presented in the present part of this work. Nevertheless, as it has been mentioned in Section 5.1, this unique phenomenon seems to be in contradiction with the popular perception well-documented in the textbooks, which claims that any mode conversion occurs if and only if a geometrical discontinuity or perturbation is introduced along the propagation direction. Before giving an intuitive explanation, let us look at the following two aspects of modal behavior.

One aspect is mode identification. It is well known that open guided-wave structures (such as dielectric waveguide, microstrip line, and CPW) suffer from mismatched phase velocities and irregular fringing fields at the dielectric interfaces, which stems from the different dielectric properties in different dielectric regions [108]. Therefore, it is difficult to derive exact analytical expressions for their modal behavior. Instead, their eigenmodes are usually identified and defined by examining the corresponding field components. For example, the dominant quasi-TEM mode of a microstrip line is identified after comparing its fields with those of the static (dc) case.

The other is mode variability. There is no doubt that once a transmission medium is assumed to be uniform in geometry with an infinitely long dimension in the *z*-direction, one can obtain the complete and unique eigenmode solutions of source-free Maxwell's equations together with the known boundary conditions. This is where the prevailing assumption about the classical mode conversion comes from. However, it should be noted that these eigenmode solutions are a function of frequency, that is, they are not invariant but change with frequency. If one or more field components undergo a significant change as frequency increases or decreases, as depicted in Fig. 5.3, the corresponding eigenmode may exhibit entirely different modal behavior. In fact, the frequency-dependent modal behavior of MSTL we discussed throughout this article is such a specific example. This means that there is no real conflict between our findings and the popular perception of mode conversion. Simply, the classical perception has ignored the dimension of frequency, which can play a fundamental role in the determination of modal behavior. One idea points out that changes in physical boundaries would trigger mode conversion (mode coupling, mode transition, or mode transformation), whereas the other idea suggests that an eigenmode of a uniform (*z*-invariant) structure (e.g., MSTL) have different modal behavior in the different frequency range.

As a type of open guided-wave structure, MSTL actually supports hybrid TM and TE modes [86], as do both the microstrip line and CPW. The difference in the dispersive nature could cause that the TM-TE element weights vary with frequency. The resulting dominant mode of MSTL has frequency-varying field components and thus behaves differently. After thoroughly examining all the six field components over a wide frequency range [53], we have found that at low frequencies, the dominant mode of propagation behaves as a quasi-TEM microstrip mode, whose fields are quite similar to those in a microstrip line. At high frequencies, the dominant mode behaves like a quasi-

TE_{10} waveguide mode, which resembles a TE_{10} mode as in an SIW and departs significantly from a TEM mode in its field distributions. Similar phenomena of frequency-dependent mode conversion can be observed in other open transmission media as well as in inhomogeneously filled waveguides, which are not subjected to any longitudinal irregularities. Collin [109] already reveals that the dominant mode of an inhomogeneously filled parallel-plate transmission line is a quasi-TEM mode at low frequencies and becomes an *E* (TM) mode at high frequencies. In [52], a mode conversion from a TEM-like mode to a plasmon-like mode is observed in a finite-width parallel-plate waveguide when frequency goes up. In [110], it is reported that a frequency-dependent mode conversion from a TEM mode to a TE_{10} mode occurs in a multi-mode waveguide. These findings are summarized in Table 5.5.

Table 5.5 Frequency-dependent mode conversion appearing in different guided-wave structures

Ref.	Guided-wave structure	Mode at low freq.	Mode at high freq.
[109]	Inhomogeneously filled parallel-plate transmission line	Quasi-TEM	*E* (TM)
[52]	Finite-width parallel-plate waveguide	TEM-like	Plasmon-like
[110]	Multi-mode waveguide	TEM	TE_{10}
This work	Mode-selective transmission line (MSTL)	Quasi-TEM	Quasi-TE_{10}

5.7 Conclusion

The physical mechanism of MSTL has been presented with modal field variations and discussed through the analysis of the unique phenomenon of frequency-enabled mode selectivity or conversion. In this work, the longitudinally uniform MSTL is considered as a coupled system that consists of one microstrip line and two HM-SIWs. Coupled-mode theory and normal-mode analysis are combined and developed to analytically treat this coupled system. It has been found that a large change in the coupling coefficient with frequency causes a significant field spreading from the microstrip line to HM-SIWs. As a result, the dominant mode of MSTL undergoes a shape change, from resembling a quasi-TEM microstrip mode to resembling a quasi-TE_{10} waveguide mode as frequency increases. Excellent agreement between the approximate fields (analytical

solutions) and the exact fields (full-wave solutions) affirms the correctness and effectiveness of the normal- and coupled-mode analysis for MSTL. While this approximate analysis cannot give the complete exact modal solutions (eigenmode solutions) for MSTL, it provides an in-depth physical understanding and theoretical foundation on how the dominant mode of a coupled-mode system changes with frequency under certain conditions for mode selectivity or conversion. The parametric behavior of MSTL has been analyzed, providing helpful information for MSTL design considerations.

Appendix Mutual relation between coupled-mode formalism and normal-mode solution

To derive the mutual relation between coupled-mode formalism and normal-mode solution to the same problem, we treat a longitudinally uniform, codirectionally coupled system that is constructed from two single-mode transmission elements (see Fig. 5.4). Based on this relation, the normal modes (i.e., eigenmodes) of the uniform system can be represented approximately by uncoupled modes of the individual constituent elements.

A. Coupled-mode formalism

In the coupled-mode theory, electromagnetic (vector) fields of the coupled system can be expressed as the sum of the eigenmodes in each constituent element

$$\vec{E}(x,y,z) = e_a(z)\vec{E}_a(x,y,z) + e_b(z)\vec{E}_b(x,y,z) \tag{5.15a}$$

$$\vec{H}(x,y,z) = e_a(z)\vec{H}_a(x,y,z) + e_b(z)\vec{H}_b(x,y,z) \tag{5.15b}$$

where $e_a(z)$ and $e_b(z)$ are the amplitudes of individual constituent elements, a and b, respectively. It is worthwhile to mention that in (5.15), we ignore the contributions of radiation modes [102]. The electromagnetic fields of each element can be expressed as

$$\vec{E}_{a,b}(x,y,z) = \vec{E}_{a,b}(x,y)e^{-j\beta_{a,b}z} \tag{5.16a}$$

$$\vec{H}_{a,b}(x,y,z) = \vec{H}_{a,b}(x,y)e^{-j\beta_{a,b}z} \tag{5.16b}$$

where β_a and β_b are the longitudinal propagation constants of individual constituent elements. By ignoring the butt couplings and the change in the propagation constants, we obtain the following

simplified mode-coupled equations:

$$\frac{de_a(z)}{dz} = -jK_{ab}e_b(z)e^{-j(\beta_b-\beta_a)z} \tag{5.17a}$$

$$\frac{de_b(z)}{dz} = -jK_{ba}e_a(z)e^{+j(\beta_b-\beta_a)z} \tag{5.17b}$$

where K_{ab} and K_{ba} are the coupling coefficients and satisfy $K_{ab} \approx K_{ba} = K$ [see (5.3)]. The detailed derivation of (5.17) is not presented here; the interested reader is referred to [101], [102], and [111]. Note that (5.17a) and (5.17b) correspond to (5.1a) and (5.1b) by defining

$$a(z) = e_a(z)e^{-j\beta_a z} \tag{5.18a}$$

$$b(z) = e_b(z)e^{-j\beta_b z}. \tag{5.18b}$$

B. Normal-mode solution

According to the definition, a normal mode of the coupled system obeys the relation

$$\frac{d\vec{E}(x,y,z)}{dz} = -j\beta_e\vec{E}(x,y,z) \tag{5.19}$$

where β_e is the propagation constant of the normal mode (eigenmode). Substituting (5.15)-(5.18) into (5.19) gives

$$[Kb(z)+(\beta_a-\beta_e)a(z)]\vec{E}_a(x,y)+[Ka(z)+(\beta_b-\beta_e)b(z)]\vec{E}_b(x,y) = 0. \tag{5.20}$$

It has nontrivial solutions if the following equations are satisfied:

$$Kb(z)+(\beta_a-\beta_e)a(z) = 0 \tag{5.21a}$$

$$Ka(z)+(\beta_b-\beta_e)b(z) = 0. \tag{5.21b}$$

We can get the eigenvalues of the coupled system by solving (5.21) as follows:

$$\beta_{e1,2} = \frac{\beta_a+\beta_b}{2} \pm \frac{1}{2}\sqrt{4K^2+(\beta_a-\beta_b)^2}. \tag{5.22}$$

Corresponding to the first eigenvalue β_{e1}, the first normal mode is expressed as

$$\vec{E}_{e1}(x,y,z) \approx \vec{E}(x,y,z=0)e^{-j\beta_{e1}z} = [a(0)\vec{E}_a(x,y) + b(0)\vec{E}_b(x,y)]e^{-j\beta_{e1}z}. \tag{5.23}$$

For normalization, coefficients $a(0)$ and $b(0)$ need to satisfy the following condition:

$$a(0)^2 + b(0)^2 = 1. \tag{5.24}$$

Equations (5.21) and (5.24) are simultaneously solved to yield

$$a(0) = \sqrt{\frac{1}{2}\left(1 + \frac{x}{\sqrt{1+x^2}}\right)} = m \tag{5.25a}$$

$$b(0) = \sqrt{\frac{1}{2}\left(1 - \frac{x}{\sqrt{1+x^2}}\right)} = n \tag{5.25b}$$

where

$$x = \frac{\beta_a - \beta_b}{2K}. \tag{5.26}$$

Note that coefficients m and n can be rewritten in the form presented in the main text [see (5.6)] by substituting (5.26) into (5.25). Finally, the vector fields for the first normal mode (i.e., the dominant mode) of the coupled system are approximated as

$$\vec{E}_{e1}(x,y,z) \approx [m\vec{E}_a(x,y) + n\vec{E}_b(x,y)]e^{-j\beta_{e1}z} \tag{5.27a}$$

$$\vec{H}_{e1}(x,y,z) \approx [m\vec{H}_a(x,y) + n\vec{H}_b(x,y)]e^{-j\beta_{e1}z}. \tag{5.27b}$$

Similarly, the electromagnetic fields for the second normal mode (i.e., the first higher-order mode) are given by

$$\vec{E}_{e2}(x,y,z) \approx [-n\vec{E}_a(x,y) + m\vec{E}_b(x,y)]e^{-j\beta_{e2}z} \tag{5.28a}$$

$$\vec{H}_{e2}(x,y,z) \approx [-n\vec{H}_a(x,y) + m\vec{H}_b(x,y)]e^{-j\beta_{e2}z}. \tag{5.28b}$$

CHAPTER 6 ARTICLE 4: MODE-SELECTIVE TRANSMISSION LINE——PART II: EXCITATION SCHEME AND EXPERIMENTAL VERIFICATION

Desong Wang and Ke Wu

Published in the *IEEE Transactions on Components, Packaging and Manufacturing Technology*, vol. 11, no. 2, pp. 260-272, Feb. 2021.

In Part I of this two-part work (Chapter 5), we have presented the theoretical foundation and physical mechanism of the mode-selective transmission line (MSTL). The present part is devoted to its excitation scheme, practical transition design, and experimental verification. The MSTL excitation is first explained by comparison with a conductor-backed coplanar waveguide (CBCPW). To produce the specific mode excitation, an ultra-broadband transition between CBCPW and MSTL is proposed. It has a tapered structure operating as a tapered-mode coupler, which supports smooth evolution from the fixed CPW mode of CBCPW to the frequency-dependent dominant mode of MSTL. This modal evolution along the transition is analytically treated based on a local normal mode theory. Couplings between the local normal modes are negligible as a result of gradual tapering, thereby effectively suppressing higher order modes in MSTL and sustaining a mode purity over an ultra-broad frequency range. For experimental demonstration purposes, back-to-back CBCPW-to-MSTL transition circuits are physically realized. The measured results are in agreement with the prediction, showing a return loss of 15 dB from 3 to 109 GHz; the single transition introduces a relatively low insertion loss of 1.84 dB at 100 GHz. The propagation characteristics of MSTL are also extracted from the measured S-parameters, which provides an excellent validation of the proposed structure.

6.1 Introduction

Mode-selective transmission line (MSTL) has recently been proposed, which meets the stringent requirements for high-quality guided-wave signal propagation judging from propagation loss,

frequency dispersion, operating bandwidth, field confinement, and so on [47], [48], [87]. In Part I of this work (Chapter 5) [112], a typical MSTL [Fig. 6.1(a)] is considered as a coupled system consisting of one microstrip line and two half-mode substrate-integrated waveguides (HM-SIWs) [113]. The large change in the coupling coefficient with frequency results in the frequency-enabled mode selectivity, the most distinguished feature of MSTL. Specifically, the dominant mode of MSTL can be converted from a quasi-TEM microstrip mode into a quasi-TE_{10} waveguide mode [25] as frequency increases [53], [86]. This unique feature offers MSTL combined advantages of the two dissimilar modes: the microstrip mode is known to get rid of a low-frequency cutoff phenomenon and thus to have low dispersion, whereas the waveguide mode allows for relatively low signal attenuation and improved frequency dispersion in a higher frequency range. Nevertheless, the mode selectivity of MSTL implies that both its characteristic impedance and field distributions experience strong variations with frequency, thus presenting a technical challenge to excite the variable dominant mode. In practical applications, an efficient excitation of MSTL may be produced with the help of a specially designed ultra-broadband transition between MSTL and conventional transmission medium. It requires that the transition maintain a smooth evolution between the fixed dominant mode of the conventional transmission medium and the frequency-dependent dominant mode of MSTL over the desired frequency range.

Transitions are usually implemented using a single- or multi-section transformer constructed from quarter-wavelength sections [114]. This kind of design generally leads to a short and simple transition structure, but it suffers from a limited bandwidth conditioned by its frequency-related size. As it is well-known, tapered transitions are popular for broadband applications, benefitting from their structural characteristics [81], [115]; they are suitable for TEM (or quasi-TEM) transmission lines and non-TEM waveguides [116], [117]. This work uses a tapered structure to form an ultra-broadband transition between conductor-backed coplanar waveguide (CBCPW) and MSTL. CPW is one of the most popular transmission media for microwave and millimeter-wave integrated circuits and systems [118]. Since its one variant, CBCPW with two bilateral sidewalls (called CBCPW herein for simplicity) [61], [62], is similar in geometry to MSTL, it is straightforward to construct a tapered transition via a linear connection of their transverse cross sections with the same shape. This tapered transition operates as a tapered-mode coupler (also called tapered-velocity coupler) [93], [119], [120]. Gradual enough tapering meeting the adiabatic invariance condition prevents mode couplings

between local normal modes and minimizes power transfer to unguided radiation modes. It guarantees a smooth modal evolution from the fixed dominant CPW mode of CBCPW to the frequency-dependent dominant mode of MSTL. With the transitions integrated into the prototype, MSTL can be conveniently characterized using a probe-based measurement technique. It facilitates the experimental characterization of MSTL and expedites its potential applications in antennas and circuits. This CBCPW-to-MSTL transition has been mentioned in [96]. In this article, much attention will be paid to the excitation scheme of MSTL, modal evolution along the transition, design considerations of the transition, suppression of higher-order modes in MSTL, and experimental verification.

The rest of this article is organized as follows. In Section 6.2, MSTL is briefly described in terms of structural and field characteristics as well as excitation scheme. The CBCPW-to-MSTL transition is then presented in Section 6.3. Its design considerations such as transition length, insertion loss, return loss, and ripple level are discussed. The modal evolution along the tapered transition is analytically treated using a local normal mode theory and is subsequently verified by examining the field distributions in both the single transition and the back-to-back configuration. Section 6.4 is concerned with the suppression of higher-order modes in MSTL. Symmetric higher-order modes existing in the operating frequency range are examined and identified; their suppression effect by the tapered transition is also demonstrated. It is followed by experimental verification of the proposed transition in Section 6.5. A refined simulation model is presented to better emulate the practical situations. Both the measured S-parameters of the back-to-back transition and the extracted propagation characteristics of MSTL are obtained and compared with the simulation results. In Section 6.6, a further discussion about a special MSTL case is presented to get a better physical understanding of the mode selectivity of MSTL. Finally, conclusions are given in Section 6.7.

6.2 MSTL and its excitation scheme

In this section, we will first briefly describe the typical MSTL and its unique phenomenon of frequency-enabled mode selectivity that has been treated in detail in Part I of this work (Chapter 5) [112]. We will then discuss the excitation scheme of the variable dominant mode of MSTL. Unlike CPW and microstrip line, MSTL requires a special excitation to ensure that its variable dominant mode can be efficiently excited throughout.

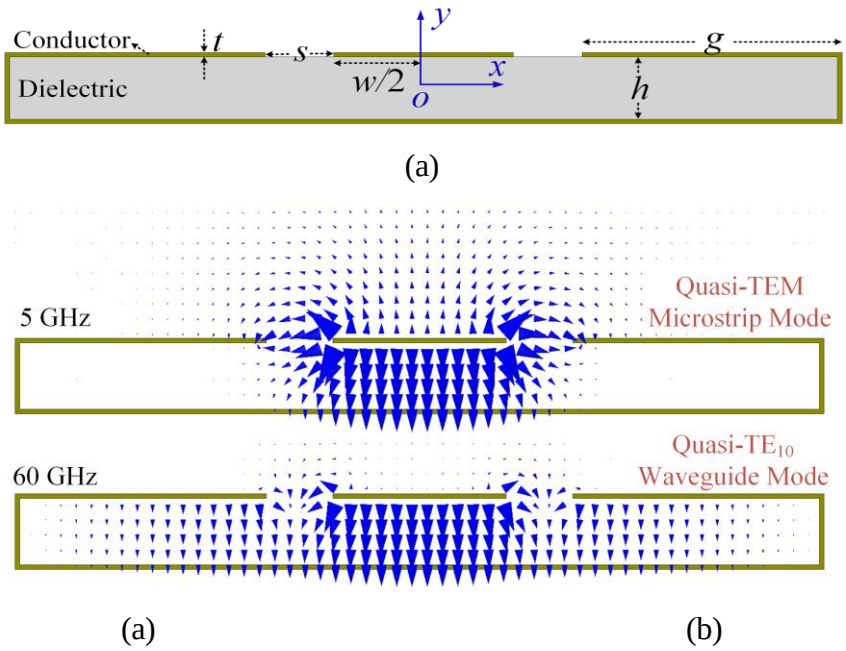

Figure 6.1 (a) Transverse cross section of MSTL with geometrical parameters: h = 0.254 mm, g = 0.925 mm, w = 0.65 mm, s = 0.25 mm, and t = 17.5 μm. (b) E-field distributions of the dominant mode of MSTL at 5 and 60 GHz

Dielectric substrate is set to be transparent to clearly show the fields.

6.2.1 Typical MSTL

The geometry of a typical MSTL is shown in Fig. 6.1(a), labeled with its geometrical parameters including substrate thickness h, side conductor width g, center strip width w, slit width s, and conductor thickness t. In Part I of this work (Chapter 5) [112], MSTL is analyzed as a coupled system that is composed of one microstrip line and two HM-SIWs to account for its physical mechanism. In this part, we turn our attention to the required excitation scheme and practical transition design. For this purpose, the dc-to-110-GHz MSTL mentioned in [96] is introduced for the following analysis and transition design. The dimensions of this MSTL are listed in the caption of Fig. 6.1. The dielectric substrate used (Rogers RT/duroid 6010 substrate) has a relative permittivity of ε_r = 10.2 and a loss tangent of tanδ = 0.0023. The conductors have a conductivity of σ = 5.8 × 10^7 S/m. A full-wave analysis is performed in a finite-element method software

package, ANSYS Electronics Desktop 2017 [57], [121]. For simplicity, the bilateral sidewalls [Fig. 6.1(a)] are modeled by continuous metal walls unless otherwise stated.

As we have seen in [53] and [86], the dominant mode of MSTL can be converted from a quasi-TEM microstrip mode into a quasi-TE_{10} waveguide mode as frequency increases. This frequency-enabled mode selectivity satisfies the orthogonality relations [86], [72], and is related to the phenomenon of "leakage" [122], [123]. Its physical mechanism has been presented in Part I of this work (Chapter 5) using the normal- and coupled-mode analysis [112]. The dominant mode of MSTL behaves as the microstrip mode and the waveguide mode at frequencies considerably below and above f_c, respectively. The specific frequency f_c is the cutoff frequency of the constituent HM-SIWs [112]; we have f_c = 22 GHz in this case. This unique feature can be reflected directly in the field variations of the dominant mode, which has been discussed in detail in [53]. Here, we concentrate merely on two different frequencies chosen arbitrarily, 5 and 60 GHz, at which the electric fields (*E*-fields) are quite different as a result of the different modal behavior. As shown in Fig. 6.1(b), the *E*-fields at 5 GHz concentrate primarily around the center strip; at 60 GHz, they are distributed over the entire cross section of MSTL. It can be concluded that the frequency-dependent modal behavior of MSTL causes strong frequency dependence of the field properties and thus poses a practical difficulty in exciting the variable dominant mode of MSTL.

6.2.2 Excitation scheme

To thoroughly understand the excitation scheme of MSTL and the distributed field evolution behavior, let us first consider a general multi-conductor system with embedded dielectric materials. Shown in Fig. 6.2 is an arbitrarily spatially separated *N*-conductor coupled transmission system ($N \geq 1$) that is uniform in the direction of propagation. The geometric parameters l_1, l_2, l_3, $l_{(N-1)}$, and l_N labeled in Fig. 6.2 represent the maximum physical dimensions of individual conductors; their maximum value is denoted by l_m. In general, (*N*-1) TEM modes are described for this coupled multi-conductor system, but this assumption is not rigorous and, in some cases, could even be erroneous. In fact, dominant modes and field distributions of this system can be determined and conditioned by frequency f (wavelength λ) with reference to structure topology and dielectric properties: 1) when $f = 0$ and $\lambda = +\infty$ (dc, static case), there exist (N–1) distinct TEM dominant modes in the coupled system; 2) when $f \neq 0$ and $\lambda >> l_m$ (low frequency, quasi-static case), there

are (N–1) TEM and/or quasi-TEM dominant modes; 3) when $f \neq 0$ and $\lambda \sim l_m$ (high frequency, distributed case), up to N but at least (N-1) TEM and/or non-TEM dominant modes may be anticipated, depending on frequency and structure; 4) when $f \neq 0$ and $\lambda << l_m$ (extremely high frequency, quasi-optical case), every single conductor supports TE and/or TM modes with more than N TE and/or TM dominant modes appearing in the entire system. Similarly, our MSTL has two electrically separate conductors, as shown in Fig. 6.1(a), including the center strip and the bent conductor constructed from the top side conductors connected to the bottom conductor. It has only one dominant mode which behaves as a quasi-TEM mode at low frequencies [case (2)] and as a quasi-TE_{10} mode at extremely high frequencies [case (4)]. This feature requires a special method to feed the dominant mode of MSTL in the ultra-broad frequency range.

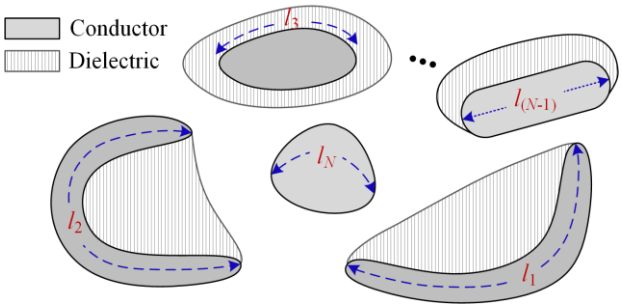

Figure 6.2 Transverse cross section of arbitrary N-conductor coupled transmission system with embedded dielectric materials ($N \geq 1$)

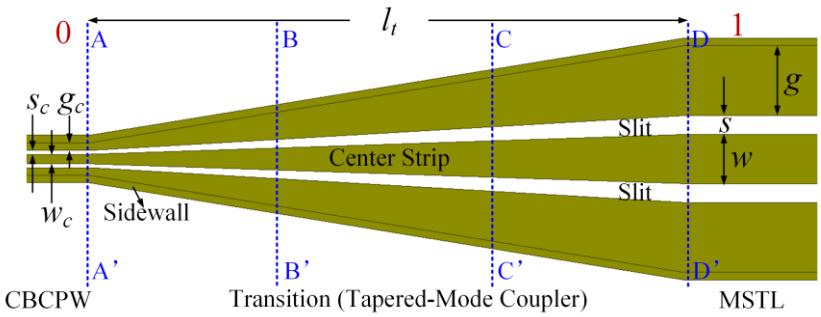

Figure 6.3 Top view of the transition model that is made up of a CBCPW, a single CBCPW-to-MSTL transition, and an MSTL

The CBCPW has parameters: g_c = 101.6 μm, w_c = 127 μm, and s_c = 50.8 μm. Bottom conducting plane and dielectric substrate are set to be transparent in order to clearly show this transition design.

To efficiently excite a specific mode requires that the signal source have a distribution that matches perfectly the mode transverse distribution. In general, a voltage excitation of CBCPW has a signal on the center strip with the side conductors at zero potential, denoted by the vector

$$V_{\mathrm{CBCPW}} = \begin{pmatrix} 0 \\ 1 \\ 0 \end{pmatrix}. \tag{6.1}$$

This excitation was analyzed in [124] as the sum of propagating modes denoted by equivalent voltage eigenvectors. As frequency increases, a mode coupling or leakage may occur in this CBCPW [100], [124]. The laterally spreading fields could give rise to serious resonances or leakages and thus degrade and even ruin the performance of CBCPW at high frequencies, due to the fact that a practical CBCPW usually has open- or short-ended side conductors [107]. Therefore, CBCPW operates in a limited frequency range, in which it has a dominant CPW mode; parasitic microstrip [104] and waveguide modes [59], [73] are usually suppressed.

In contrast to CBCPW, MSTL requires a special voltage signal which should be frequency dependent to excite its variable dominant mode. This signal source is different from that for a conventional CBCPW, albeit with similar geometry, given by

$$V_{\mathrm{MSTL}} = \begin{pmatrix} q \\ p \\ q \end{pmatrix} \tag{6.2}$$

where at low frequencies ($\leq f_c$ = 22 GHz), the signal has $p = 1$ and $q = 0$ to excite the quasi-TEM microstrip mode of MSTL, which is the same as for the CBCPW case [see (6.1)]; at higher frequencies ($> f_c$), both p and q are nonzero ($0 < p < 1$ and $0 < q < 1$), and satisfy $p^2 + 2q^2 = 1$ required by normalization, meaning that this is a signal on the center strip with the side conductors at finite potentials with respect to the bottom conductor, which can be used to excite the quasi-TE_{10} waveguide mode of MSTL [Fig. 6.1(b)]. The vector V_{MSTL} corresponds to the transverse field profile ψ_{E11} [see (6.6), it is denoted by ψ_{E1} in (5.11a)] of the first normal mode (i.e., dominant mode) of MSTL. This frequency-dependent excitation can be realized with the help of a specially designed transition.

6.3 Transition design

A tapered transition between CBCPW and MSTL is presented in this section, capable of providing a practical excitation of MSTL and of facilitating its characterization using widely available ground-signal-ground (GSG) probes. Since MSTL and the CPW variant, CBCPW with bilateral sidewalls, have similar geometries, the CBCPW-to-MSTL transition is constructed directly by linearly connecting their cross sections with the same shape, as shown in Fig. 6.3. The CBCPW on one side of the transition has a fixed dominant CPW mode; the MSTL on the other side has a frequency-dependent dominant mode. This difference in their dominant modes is the result of the different physical sizes [47], [86], [104], which will be discussed in more detail later. The taper maintains a gradual enough change in the physical boundary conditions; the electromagnetic fields of relevance can thus be smoothly transformed when the signal propagates along the transition. In other words, this transition ensures good and concurrent impedance and field matching between the fixed dominant CPW mode of CBCPW and the variable dominant mode of MSTL.

6.3.1 Local normal mode analysis

The local normal mode theory [94] is used to analytically treat the modal evolution along the CBCPW-to-MSTL transition. For a nonuniform structure, local normal modes at a specific z point in the propagation direction are defined as the normal modes of a uniform transmission structure with the cross-sectional parameters of the point z. They are nonorthogonal, meaning that couplings may exist among them. Physically, the tapered transition operates as a tapered-mode coupler [93], [119], [120] and may support several local normal modes. The modal evolution of interest involves the first local normal mode which behaves quite differently on both sides of the transition despite the same geometrical cross-sectional shapes. We use the subscripts 0 and 1 to indicate the CBCPW side and the MSTL side of the transition, respectively, as shown in Fig. 6.3. Due to reciprocity, we can assume an input signal applied on the CBCPW side of the transition.

At the input, it is possible to simultaneously excite many local normal modes by different amounts, and the incident field profile is then expressed as

$$\psi_0 = a_{10}\psi_{E10} + a_{20}\psi_{E20} + \ldots + a_{(N-1)0}\psi_{E(N-1)0} + a_{N0}\psi_{EN0} \tag{6.3}$$

where ψ_{Ei0} (i = 1, 2, …, N, and $N \geq 1$) represent the field profiles of the first Nth-order local normal modes at the input of the tapered-mode coupler, and the coefficients a_{i0} (i = 1, 2, …, N) satisfy $a_{10}^2 + a_{20}^2 + \ldots + a_{(N-1)0}^2 + a_{N0}^2 = 1$. The sidewalls on the CBCPW side are quite close to the center strip; therefore, all the higher-order local normal modes are at cutoff in the frequency range of interest (dc to 110 GHz herein). Note that the parasitic odd slotline mode on the CBCPW side is not considered since it is usually suppressed in practice. The result is that only the first local normal mode is excited efficiently at the input, and it behaves as a quasi-TEM CPW mode throughout, namely,

$$\psi_0 = \psi_{E10} \approx \frac{N_0}{\sqrt{2}}\psi_{B0} + M_0\psi_{A0} + \frac{N_0}{\sqrt{2}}\psi_{C0} \approx \psi_{A0} \tag{6.4}$$

where ψ_{B0} (= ψ_{C0}) and ψ_{A0} are the fields of the uncoupled quasi-$TE_{0.5,0}$ and quasi-TEM modes, respectively (referring to (5.11a)). The coefficients M_0 and N_0 satisfy $M_0^2 + N_0^2 = 1$. In this case, the uncoupled quasi-$TE_{0.5,0}$ modes of the constituent HM-SIWs of CBCPW (Fig. 6.3) are at cutoff because of the close sidewalls. As a result, we have $N_0 = 0$ and $M_0 = 1$. Note that on the CBCPW side of the transition, the slits are considerably narrow relative to the substrate thickness ($s_c < h$ and $w_c/2 + s_c < h$, referring to the caption of Fig. 6.3), thereby resulting in the dominant quasi-TEM CPW mode rather than a microstrip mode [104]. The bilateral sidewalls on the CBCPW side of the transition are mainly used to eliminate waveguide modes [59], [73] and to prevent power leakage [100].

At the output (i.e., MSTL side of the transition), there may exist several local normal modes, as will be discussed in Section 6.4. However, not all of these modes can be excited. In fact, the incident signal propagates mainly in the first local normal mode along the transition. Here, we restrict attention to the first and second local normal modes on the MSTL side; the field profile is then expressed as

$$\psi_1 = (1-P_t)^{1/2}\psi_{E11} + P_t^{1/2}\psi_{E21} \tag{6.5}$$

where ψ_{E11} and ψ_{E21} represent the field profiles of the first two local normal modes at the output of the transition, and P_t denotes the power transfer from the first local normal mode to the second one. As long as the tapered transition meets the adiabatic invariance condition [119], [120], the sufficiently gradual tapering prevents mode couplings between local normal modes. Thus, the

power launched from the input into the first local normal mode [see (6.4)] remains in that mode while the mode propagates along the transition, indicating $P_t \approx 0$. The field profile at the output can be rewritten as

$$\psi_1 \approx \psi_{E11} \approx \frac{N_1}{\sqrt{2}}\psi_{B1} + M_1\psi_{A1} + \frac{N_1}{\sqrt{2}}\psi_{C1} \tag{6.6}$$

where ψ_{B1} (= ψ_{C1}) and ψ_{A1} are the fields of the uncoupled quasi-$TE_{0.5,0}$ waveguide mode (individual HM-SIW) and quasi-TEM microstrip mode (individual microstrip line) on the MSTL side, respectively. The coefficients M_1 and N_1 are frequency dependent, and satisfy $M_1^2 + N_1^2 = 1$, expressed as in (5.12a) and (5.12b) (denoted by M and N there). They correspond to the signal variables p and q in (6.2), respectively. The first local normal mode on the MSTL side of the transition is the first normal mode (i.e., dominant mode) of MSTL ($h < w$ and $h < w/2 + s$, referring to the caption of Fig. 6.1), which behaves as a quasi-TEM microstrip mode at low frequencies ($\leq f_c$ = 22 GHz herein) and as a quasi-TE_{10} waveguide mode at higher frequencies [112].

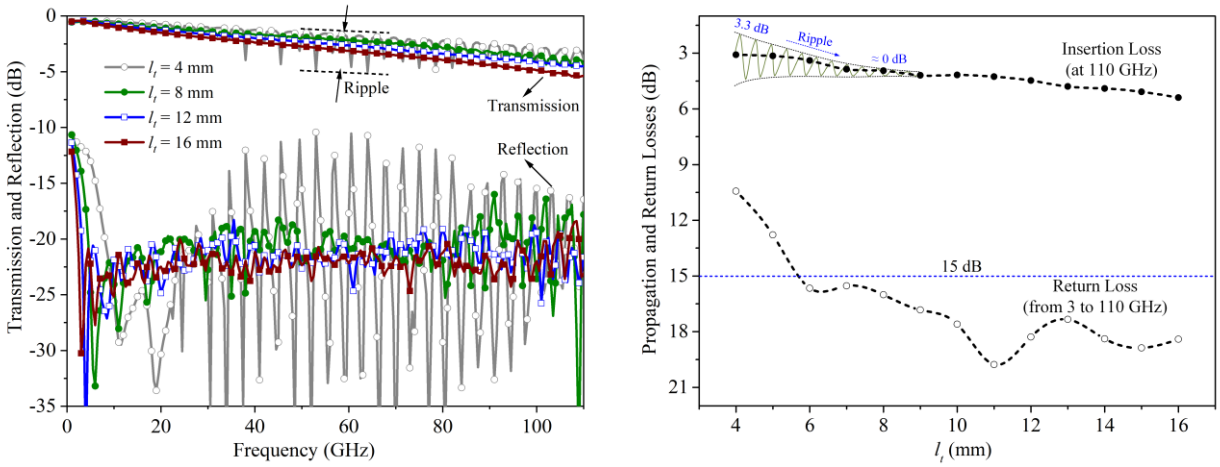

(a) (b)

Figure 6.4 Transmission and reflection responses of the simulation model shown in Fig. 6.3 (which is made up of a 1-mm-long CBCPW, a single transition, and an 8.5-mm-long MSTL) as functions of (a) frequency and (b) transition length l_t

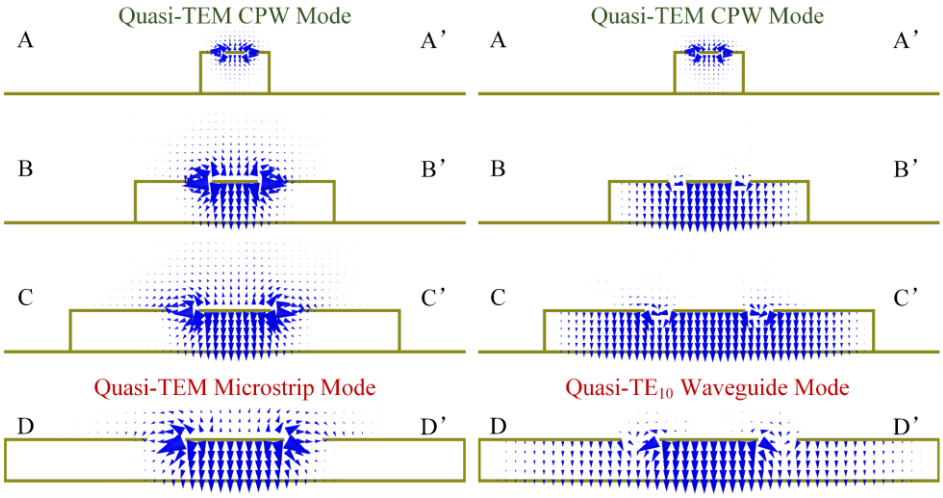

(a) (b)

Figure 6.5 *E*-field distributions in various cross sections (labeled in Fig. 6.3) of the CBCPW-to-MSTL transition at (a) 5 and (b) 60 GHz

Dielectric substrate is set to be transparent to clearly show the fields.

Even though the guided power remains in the first local normal mode [see (6.4) and (6.6)], this mode itself undergoes a smooth field evolution along the transition. From being concentrated primarily around the two slits of CBCPW at the input (quasi-TEM CPW mode), the fields at low frequencies ($\leq f_c$ = 22 GHz) evolve to be confined between the top center strip and the bottom conductor at the output (quasi-TEM microstrip mode); at higher frequencies, they evolve to be distributed over the entire cross section of MSTL at the output (quasi-TE_{10} waveguide mode). This will be confirmed in Section 6.3.3 by examining the *E*-field distributions in the transition. The field evolution results in the large change in the modal behavior of the first local normal mode and corresponds to the mode splitting behavior of a separating waveguide [125]. The spatial power transfer within a local normal mode was termed "normal mode warping" by Fox [126].

A continuous tapered-mode coupler can be approximated as a series of discontinuous, abrupt steps, which can be used to evaluate the cumulative power conversion using an iterative computer calculation [127]. This method is widely used for coupled dielectric waveguides. For our tapered transition, the coupling is a function of position and frequency [112]; the above approximate

method will become quite complicated. In this work, it is preferable to use the frequency-dependent numerical technique to evaluate the performance of the transition, which has the advantage of much greater simplicity. As will be discussed in Section 6.3.2, the adiabatic invariance condition in the presented transition is

$$\Delta\beta_t \Delta z_t \geq 60 \tag{6.7}$$

where $\Delta\beta_t$ is the maximum value of the total phase difference between the uncoupled, individual guided modes of the transition over the taper length of Δz_t in the operating frequency range. With this design requirement, the cumulative power transfers from the first local normal mode to higher-order local normal modes are negligible, which will be estimated in Section 6.4.

6.3.2 Design considerations

The CBCPW-to-MSTL transition (Fig. 6.3) needs to be developed carefully with several design considerations including transition length, insertion loss, return loss, and ripple level. In general, the dimensions of MSTL can be determined based on a given specification; they are listed in the caption of Fig. 6.1. The dimensions of CBCPW should be determined to realize a characteristic impedance of about 50 Ω, and to meet specific measurement requirements (e.g., probe pitch) and fabrication limitations. In addition, on the CBCPW side of the transition, the cutoff frequency of the individual HM-SIWs must be beyond the desired frequency range (dc to 110 GHz herein) to avoid exciting the second and other higher-order local normal modes. Finally, the dimensions of CBCPW are determined, as listed in the caption of Fig. 6.3, and the cutoff frequency of each HM-SIW is about 122 GHz (> 110 GHz). As a consequence, only the transition length l_t, as labeled in Fig. 6.3, needs to be determined for the design and optimization of the CBCPW-to-MSTL transition. This reduces the design complexity of the transition.

For a conventional tapered transition, a long structure would cause a small signal reflection but at the expense of a high-power loss. It applies to the presented CBCPW-to-MSTL transition as well. The effect of the transition length l_t on the frequency characteristics is discussed with the help of the simulation model presented in Fig. 6.3, which is made up of a 1-mm-long CBCPW, a single CBCPW-to-MSTL transition, and an 8.5-mm-long MSTL. It can be seen from Fig. 6.4(a) that as l_t increases from 4 to 16 mm in increments of 4 mm, both the reflection level (return loss) and ripple

level of the transmission curves [labeled in Fig. 6.4(a)] improve but inevitably cause degradation in the attenuation level (insertion loss), as expected. This requires a delicate balance between the reflection level, ripple level, and attenuation level. Their relationship curves with l_t are depicted in Fig. 6.4(b), which can help figure out a trade-off transition length. As can be seen, the insertion loss at 110 GHz continues to increase from 3 to 5.4 dB as l_t gradually increases from 4 to 16 mm. There is an approximate positive linear relationship between l_t and the insertion loss. It should be noted that the insertion loss at 110 GHz contains the propagation loss of 1.7 dB introduced by the 8.5-mm-long MSTL and the loss of 0.42 dB in connection with the 1-mm-long CBCPW. The in-band ripple level is reduced to about 0 dB when l_t increases to 8 mm, and the return loss is better than 15 dB from 3 to 110 GHz when l_t increases to 6 mm. Notably, the transition performance deteriorates [Fig. 6.4(a)] when the frequency is relatively low (< 3 GHz), limited by the taper itself [81], [117]. Finally, the transition length of l_t = 8 mm is determined after balancing the above-discussed factors, which causes a maximum power loss of 1.82 dB (3.94 - 1.7 - 0.42 dB) up to 110 GHz. This CBCPW-to-MSTL transition is much shorter than the microstrip-to-MSTL transition with a length of 21 mm presented in [86]. This is due to the stronger coupling in the CBCPW-to-MSTL transition that helps to meet the adiabatic invariance condition more easily while facilitating a shorter length device. With these results, the adiabatic invariance condition in the proposed transition is given in (6.7). The above analysis shows that the proposed transition can achieve an ultra-broadband (from 3 to 110 GHz) performance with relatively low insertion loss and good return loss.

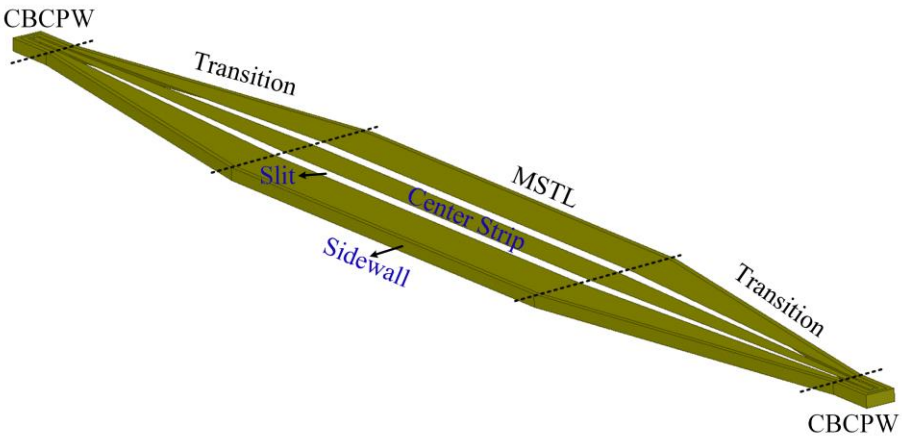

(a)

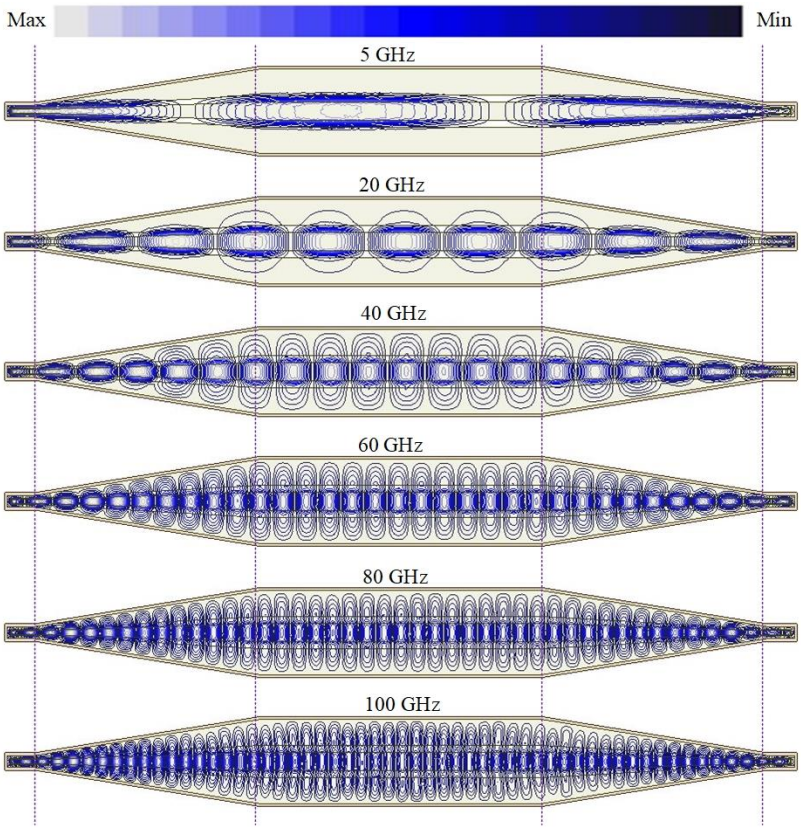

(b)

Figure 6.6 (a) Back-to-back transition model. Bottom conducting plane and dielectric substrate are set to be transparent in order to clearly show the structure. (b) *E*-field distributions in the back-to-back transition at 5, 20, 40, 60, 80, and 100 GHz

6.3.3 Field analysis

A succinct evolution from the fixed dominant mode of CBCPW to the variable dominant mode of MSTL is critical to the transition design. This modal evolution is directly related to the field evolution along the transition; it has been analyzed in Section 6.3.1 using the local normal mode theory. In this subsection, this modal evolution is confirmed by examining the *E*-field distributions in both the single transition and the back-to-back configuration. To this end, various cross sections of the transition are chosen, namely A-A', B-B', C-C', and D-D' as labeled in Fig. 6.3. We may note that A-A' and D-D' are also the cross sections of CBCPW and MSTL on each side of the transition, respectively. Two different frequencies, 5 and 60 GHz, are chosen, at which the

dominant mode of MSTL behaves as the quasi-TEM microstrip mode and the quasi-TE_{10} waveguide mode, respectively. The *E*-field distributions in the cross sections are depicted in Fig. 6.5. At 5 GHz [Fig. 6.5(a)], the *E*-fields in A-A' concentrate around the narrow slits, meaning that the mode is a quasi-TEM CPW mode. As the signal propagates toward the MSTL side of the transition, the most *E*-fields are being distributed between the top center strip and the bottom conducting plane [see D-D' in Fig. 6.5(a)], indicating that the mode is being transformed to a quasi-TEM microstrip mode. At 60 GHz [Fig. 6.5(b)], the *E*-fields in A-A' concentrate around the narrow slits, which illustrates that the mode is still the quasi-TEM CPW mode, as at 5 GHz. As the signal propagates toward the MSTL side, the *E*-fields gradually spread over the entire cross section [see D-D' in Fig. 6.5(b)]; this implies that the mode is being transformed to a quasi-TE_{10} waveguide mode. The *E*-field distributions in A-A' are for the fixed dominant CPW mode of CBCPW; there are no obvious changes at different frequencies. The *E*-field distributions in D-D' are for the variable dominant mode of MSTL, which are significantly different at the two frequencies; this can be confirmed by comparing them with the field distributions in Fig. 6.1(b). Shown in B-B' and C-C' are the "evolving" fields in the proposed transition.

The above phenomenon reveals that at low frequencies (e.g., 5 GHz), the quasi-TEM CPW mode of CBCPW [see A-A' in Fig. 6.5(a)] is smoothly transformed to the quasi-TEM microstrip mode of MSTL [see D-D' in Fig. 6.5(a)]. In this case, the transition provides a signal source as in (6.2) with $p = 1$ and $q = 0$ to feed MSTL at the launch point D-D'. On the other hand, at higher frequencies (e.g., 60 GHz), the quasi-TEM CPW mode of CBCPW [see A-A' in Fig. 6.5(b)] is gradually transformed to the quasi-TE_{10} waveguide mode of MSTL [see D-D' in Fig. 6.5(b)]. The transition in this case provides a signal source as in (6.2) but with nonzero p and q to feed MSTL. From these field distributions in Fig. 6.5, one can find that the modal evolution between CBCPW and MSTL can be realized by the transition. In other words, this transition can provide an excitation as in (6.2) to MSTL.

As Fig. 6.6(a) shows, a back-to-back transition is constructed from two 8-mm-long tapered transitions, two 1-mm-long CBCPWs, and one MSTL. The *E*-field distributions in this back-to-back configuration are examined, as vividly depicted in Fig. 6.6(b). It can be observed that at different frequencies including 5, 20, 40, 60, 80, and 100 GHz, which are chosen arbitrarily, the *E*-fields are delivered or formed smoothly along the entire structure. The phenomenon of mode

selectivity occurs in the middle MSTL, as expected. These field distributions further demonstrate that the transition sustains smooth field and modal evolutions between CBCPW and MSTL. They also reveal, directly or indirectly, the capability of the CBCPW-to-MSTL transition in support of well-behaved impedance and field matchings between CBCPW and MSTL.

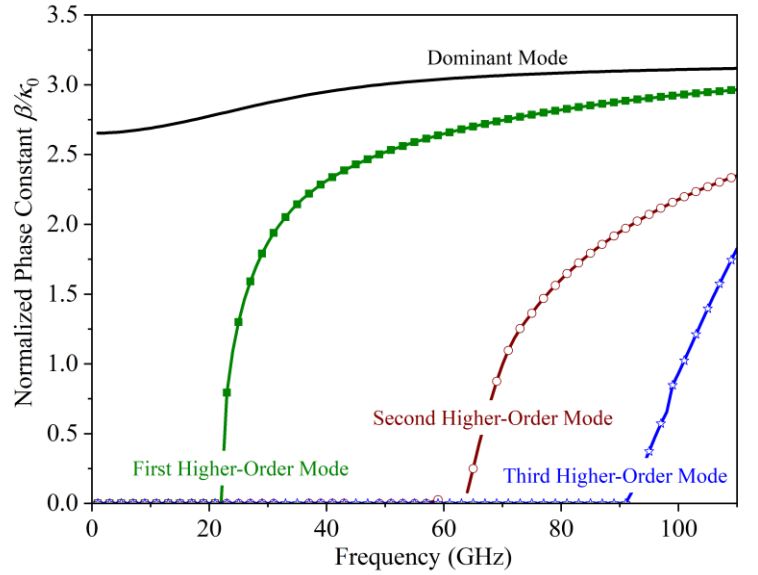

(a)

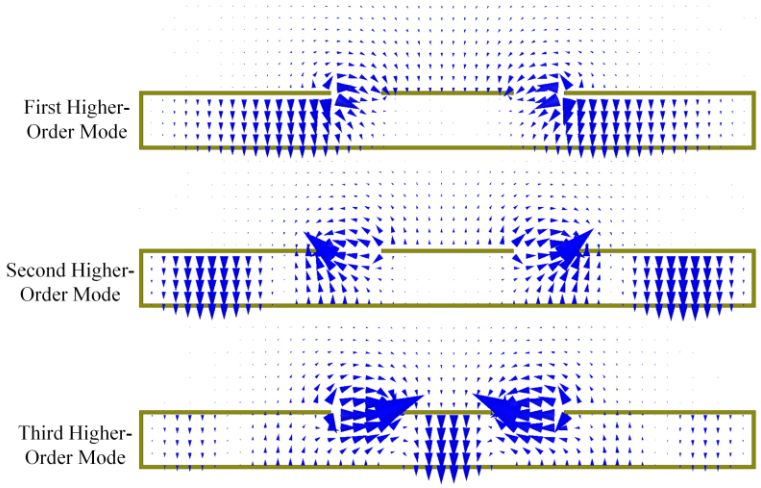

(b)

Figure 6.7 (a) Normalized phase constants and (b) cross-sectional *E*-field distributions for three symmetric higher-order modes in MSTL

Dielectric substrate is set to be transparent to clearly show the fields.

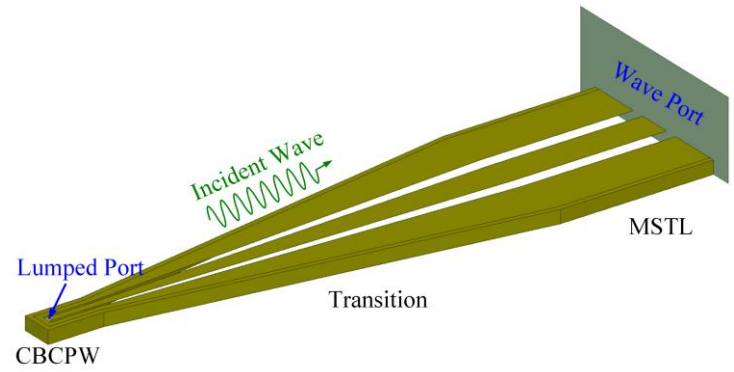

(a)

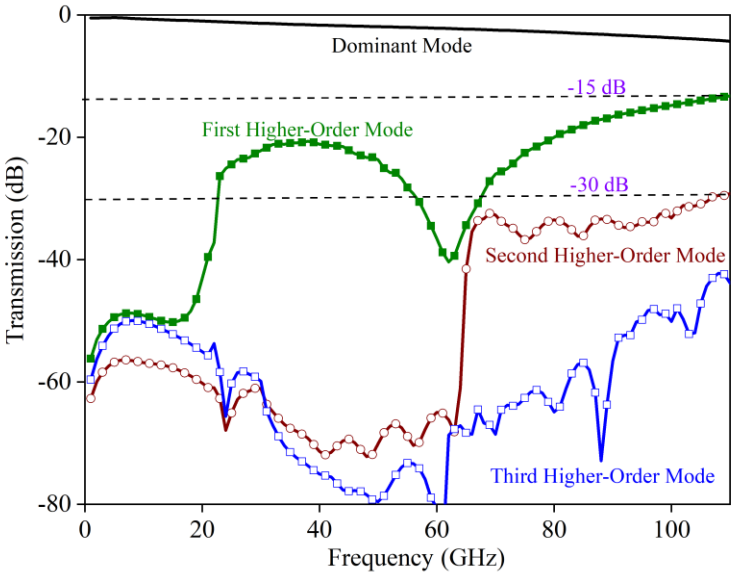

(b)

Figure 6.8 (a) Full-wave simulation model of single transition. Bottom conducting plane and dielectric substrate are set to be transparent in order to clearly show the transition structure. (b) Suppression effect of higher-order modes in MSTL

6.4 Suppression of higher-order modes

MSTL may support many higher-order normal modes (i.e., eigenmodes), especially at very high frequencies, which correspond to the higher-order local normal modes in the transition. This is a result of the fact that MSTL is a composite transmission line [Fig. 6.1(a)], from which we can see the

footprints of several well-known transmission media, such as microstrip line, slotline, CPW, dielectric-filled rectangular waveguide (RWG, i.e., SIW [128]), half-mode SIW [113]. At frequencies up to 110 GHz, the presented MSTL supports the variable dominant mode as well as several higher-order modes. Since asymmetric modes are not excited effectively by a practical symmetric excitation (see Section 6.2.2), we prefer to focus on the symmetric higher-order modes for simplicity. In the frequency range of dc to 110 GHz, there are three symmetric higher-order modes above cutoff; their *E*-field distributions are symmetric about the *yz* plane [see Fig. 6.1(a)]. Fig. 6.7(a) plots their phase constants β, normalized to the free-space wave number k_0, and Fig. 6.7(b) shows the corresponding *E*-field distributions. The first and second higher-order modes are even quasi-$TE_{0.5,0}$ and quasi-$TE_{1.5,0}$ modes; their fields reside mostly inside the side HM-SIWs. The third higher-order mode is a hybrid waveguide mode whose fields are distributed over the entire cross section of MSTL. Similar to the dominant mode of MSTL, these higher-order modes may undergo mode conversion as frequency increases much further, which is beyond the scope of this article.

To sustain a mode purity and to broaden the operating bandwidth of MSTL, we need to suppress the unwanted higher-order modes. The amplitudes of different modes depend on the nature of the signal source used to excite the MSTL. As discussed above, the tapered CBCPW-to-MSTL transition can provide the required signal source [see (6.2)] for the variable dominant mode of MSTL, and the gradual enough tapering minimizes the cumulative power transfer from the first local normal mode excited in the transition to higher-order modes. It means that the tapered transition is capable of suppressing the higher-order modes over the desired bandwidth, in addition to the requirements for practical measurement and circuit integration of MSTL. A full-wave simulation model of the single transition was built to demonstrate the suppression effect. As explained in Fig. 6.8(a), on the MSTL side of the transition, an external wave port is assigned, with multiple modes including the dominant mode and three symmetric higher-order modes (Fig. 6.7); on the CBCPW side, an internal 50-Ω lumped port is assigned. Fig. 6.8(b) plots the transmission responses between the lumped port and the wave port. For the dominant mode of MSTL, there is a flat transmission curve with a small loss. In contrast, the transmissions of the higher-order modes, except for the first higher-order mode, are still suppressed under -30 dB at frequencies up to 110 GHz. Since the propagation constant (or velocity of propagation) and the field distributions of the first symmetric higher-order mode of MSTL become similar to those of the dominant mode as

frequency increases [112], the transmission of this higher-order mode experiences a slight increase at high frequencies, while still remaining below -15 dB. Asymmetric modes in MSTL have also been treated in a similar manner, which are well suppressed throughout (not shown). These results imply that in the tapered transition, no appreciable power transfers from the lowest-order local normal mode to the higher-order modes.

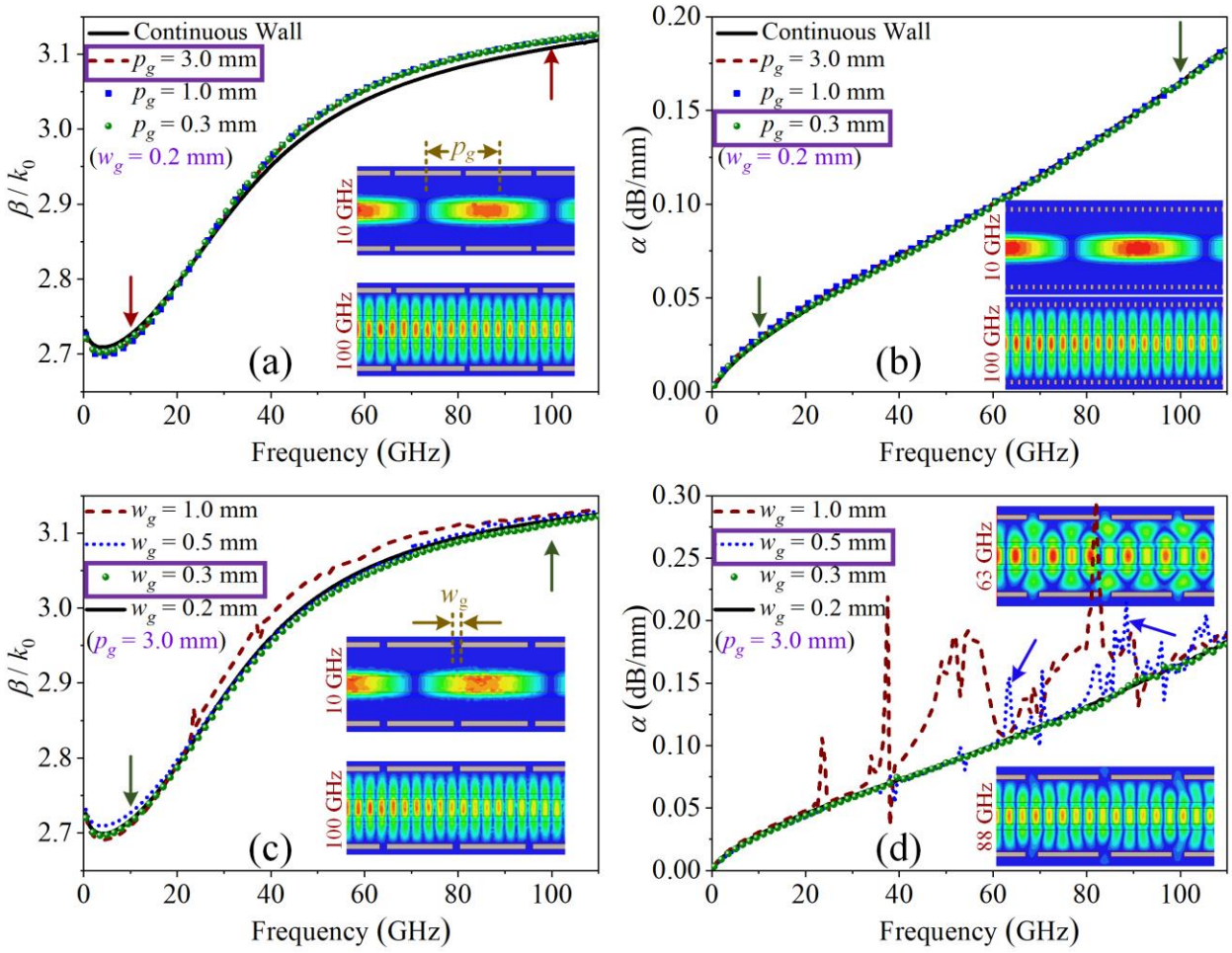

Figure 6.9 Numerically extracted propagation constants of periodic MSTL. (a) Normalized phase and (b) attenuation constants versus gap periodicity p_g (w_g = 0.2 mm), in which results for the continuous-sidewall case are also plotted for comparison. (c) Normalized phase and (d) attenuation constants versus gap width w_g (p_g = 3 mm)

p_g and w_g are defined in the insets of (a) and (c), respectively. *E*-field distributions at specific frequencies for p_g = 3 and 0.3 mm as well as w_g = 0.3 and 0.5 mm are shown in the insets of (a)-(d), respectively.

On the basis of the above-executed analysis, we can draw a conclusion that the CBCPW-to-MSTL transition is able to avoid the excitation of higher-order modes in MSTL by preventing the power transfer between the local normal modes in the transition. This sustains a high-quality mode purity over an ultra-broad frequency range. In other words, with the help of the tapered transition, the dominant mode of MSTL can be selectively excited, to the exclusion of all other modes. Thus, a veritable full-pass operation is realized. These facts about the CBCPW-to-MSTL transition presented in Sections 6.3 and 6.4 indicate that the upper frequency limit of this tapered transition is controlled primarily by the suppression of higher-order modes on both the CBCPW and MSTL sides.

6.5 Experimental verification

To verify the validity of our analysis and transition design, the proposed back-to-back CBCPW-to-MSTL transition [Fig. 6.6(a)] was fabricated and measured. Given the microscale CBCPW feedline, as shown in Fig. 6.3, a high-precision printed circuit board (PCB) process available in our Poly-Grames Research Center was used for realizing the high-frequency structure. The bilateral sidewalls of MSTL were implemented using periodic metal-filled trenches to accommodate the fabrication requirements based on the SIW technology [69], [129]-[131]. As a matter of practical design procedure, it will be necessary to slightly modify the previous MSTL simulation model prior to the final fabrication.

6.5.1 Refined simulation model

In the refined MSTL model, the continuous sidewalls are replaced by the periodic metal-filled trenches to simulate the practical structure. The resulting periodic MSTL has two additional parameters to choose, including gap periodicity p_g and gap width w_g. Their definitions and effects on the phase and attenuation constants of a periodic MSTL are shown in Fig. 6.9. Here, the width of the sidewalls is set to be 0.2 mm. The complex propagation constants are evaluated using a numerical calibration technique [132], [133]. The results for the periodicity p_g (w_g = 0.2 mm) are shown in Fig. 6.9(a) and (b). It can be seen that the propagation constant curves for the periodic MSTL with different periodicities (3, 1, and 0.3 mm) are indistinguishable from each other, which are also quite close to those for the continuous-sidewall MSTL. This relation holds true for the *E*-field distributions

for the dominant mode of operation [see the insets and Fig. 6.6(b)]. This fact implies that when w_g = 0.2 mm, the change in p_g has little effect on the performance of the periodic MSTL. The results for the gap width w_g (p_g = 3 mm) are shown in Fig. 6.9(c) and (d). It can be seen that w_g = 0.3 mm yields almost the same results, including the propagation constants and field distributions, as those for w_g = 0.2 mm. For w_g = 0.5 and 1 mm, however, the extracted propagation constants (especially the attenuation constants) excessively deviate from the usual values at some frequencies. This deviation is reflected in the field distributions, for example, at 63 and 88 GHz for w_g = 0.5 mm [Fig. 6.9(d)]. Now let us define parameter λ_{mg} as the guided wavelength at the maximum operating frequency, λ_{mg} = 0.87 mm at 110 GHz here, for example. We can then conclude that when $w_g < \lambda_{mg}/2$ (e.g., w_g = 0.2 or 0.3 mm), the results for the periodic MSTL are desirable and stable; otherwise, the MSTL performance will be degraded severely.

We will now see why the wide trench gaps (e.g., w_g = 0.5 or 1 mm) could ruin the performance of the periodic MSTL. With the introduction of the periodic gaps, the final MSTL is a sort of periodic guided-wave structures. It may be subject to an electromagnetic bandgap phenomenon and/or a potential leakage problem [31], [133]. Furthermore, periodic discontinuities may allow for the phenomenon of mode coupling to occur [134], [135]. All these problems may affect the propagation properties and field patterns of the periodic MSTL. The bandgap phenomenon occurs in a periodic structure in accordance with the following condition:

$$\beta_0 p_g = n_1 \pi \tag{6.8}$$

where β_0 is the phase constant of the dominant mode of operation, and n_1 is a positive integer. If (6.8) is satisfied, successive reflections from the periodic discontinuities interfere constructively, and more and more waves travel in the opposite direction, thus giving rise to the bandgaps. As discussed earlier, several higher-order modes are above cutoff over the operating bandwidth of MSTL, but they are not excited by the proposed transition. In the periodic MSTL case, however, the presence of such longitudinal discontinuities may lead to coupling among the modes of different propagation constants. To simplify our discussion, we only treat those associated with the dominant mode of operation. They occur if the following condition is met:

$$(\beta_0 + \beta_i) p_g = 2 n_2 \pi \tag{6.9}$$

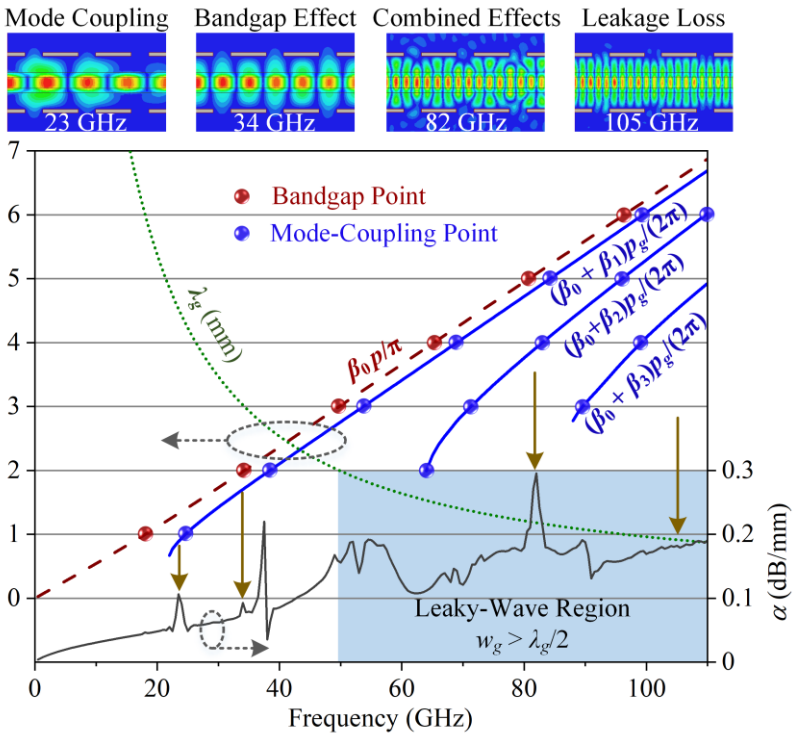

Figure 6.10 Conditions of electromagnetic bandgap, mode coupling, and leakage loss, as well as their effects on the performance of the periodic MSTL with w_g = 1 mm and p_g = 3 mm

where β_i is the phase constant of the ith symmetric higher-order mode, and n_2 is a positive integer. It means that at some specific frequencies, there is energy exchange between the forward dominant mode and the backward propagating ith mode, through space harmonics [134]. In addition to the bandgap effect and mode coupling, the periodic MSTL may suffer from leakage loss. The existence of the trench gaps may open up to let power to leak into transverse directions in the form of a parallel-plate wave. We have found from the parametric study that leakage is very significant when the width of the periodic gaps is larger than half a guided wavelength, namely,

$$w_g > \lambda_g/2. \tag{6.10}$$

As an example, we treat the case of w_g = 1 mm and p_g = 3 mm to illustrate how the above problems could affect the MSTL performance. Fig. 6.10 describes the conditions of (6.8)-(6.10), in which the attenuation constant curve is again plotted, together with the E-field distributions at some specific frequencies. It is easy to find out the corresponding bandgap points, mode-coupling points,

and also leak-wave region. One can then observe that they correspond to the peaks in the attenuation constant curve, and they can even be identified from the field distributions, such as the mode coupling at 23 GHz, bandgap effect at 34 GHz, and leakage loss at 105 GHz. Certainly, these phenomena may occur simultaneously, for example, at 82 GHz. It should be pointed out that there may also exist back and forth periodic power exchange between the symmetric and asymmetric higher-order modes. To circumvent these canonical problems of a periodic structure, we can reduce the periodicity to avoid the bandgap effect as well as mode coupling and narrow down the periodic gaps to reduce power leakage to an acceptable level. The periodic MSTL case with w_g = 0.2 mm and p_g = 0.3 mm, which is shown in Fig. 6.9, is such a design in this work. The parametric study in Fig. 6.9 has revealed that as long as the trench gaps are narrow enough ($w_g < \lambda_{mg}/2$), all the undesirable discontinuity effects (see Fig. 6.10) can be ignored. From design and prototyping considerations (fabrication tolerances and mechanical strength), we choose w_g = 0.2 mm and p_g = 3 mm for the final MSTL design.

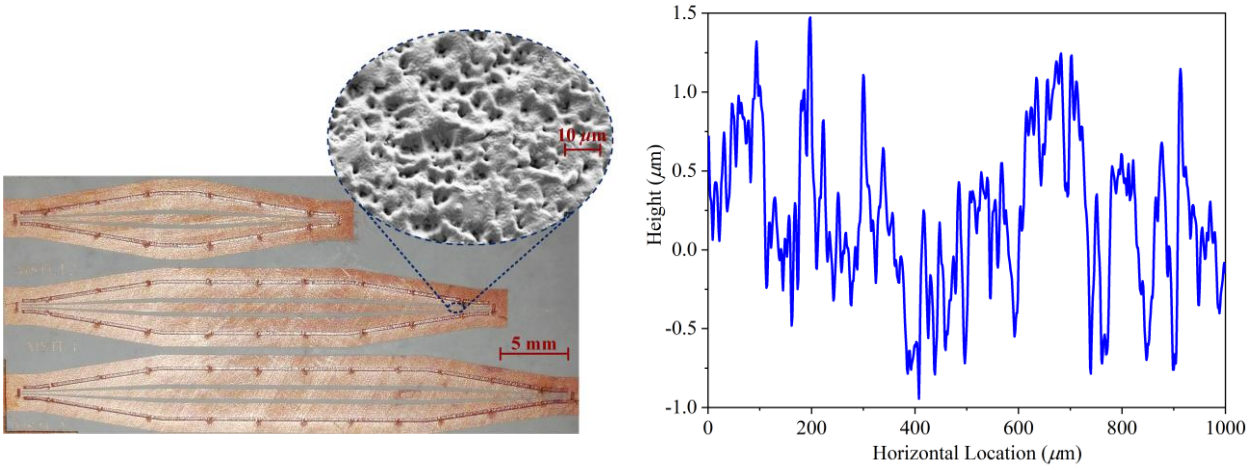

(a) (b)

Figure 6.11 (a) Optical microscope image of the fabricated samples and scanning electron micrograph (SEM) of the rough copper surface. (b) Measured 2-D surface roughness profile

The periodic MSTL was fabricated by our high-precision PCB process. Fig. 6.11(a) shows an optical microscope image of the fabricated samples. A precise examination shows that these samples have such average parameter values, including g = 0.91 mm (1.62% error), w = 0.63 mm (4.1% error), and

s = 0.27 mm (8% error) (referring to the caption of Fig. 6.1). The two-dimensional (2-D) surface roughness profile was measured using a DekTak profilometer with a precision of 4 Å, as shown in Fig. 6.11(b). It can be observed that the conductor surfaces suffer from a certain amount of roughness, which would cause an additional power loss. The surface roughness can be modeled as a pyramidal stack-up of conducting spherical "snowballs" on a conductor surface, which is illustrated by the scanning electron microscope (SEM) in Fig. 6.11(a). This is the well-known Huray's snowball model [121], [136]. Its parameters were evaluated from the measurement data to give a surface ratio of 0.5 and a sphere radius of 1.8 μm. The slight material dispersion is also taken into account in the refined simulation model. These measures help better emulate the practical situations.

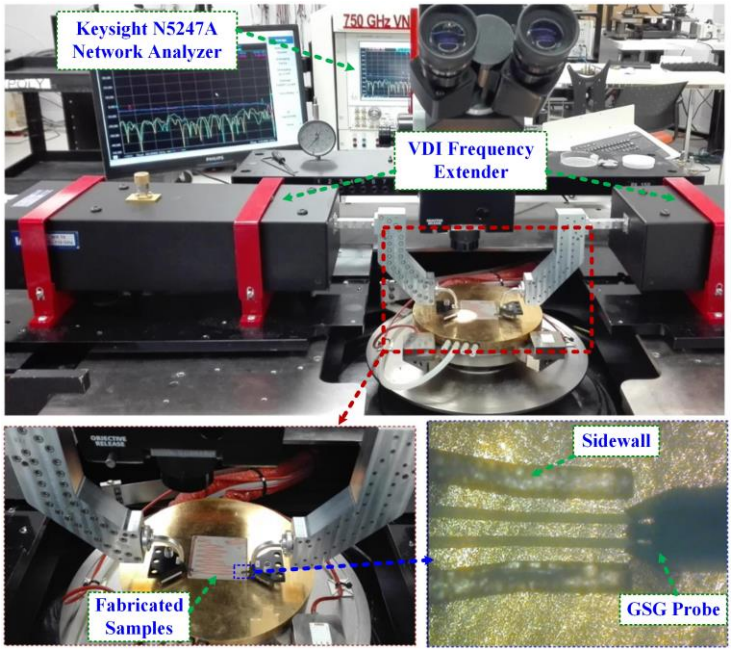

Figure 6.12 Measurement setup and fabricated samples

6.5.2 Experimental measurements

A PNA-X network analyzer N5247A (Keysight Technologies) was used to directly perform a full two-port S-parameter measurement from 1 to 65 GHz. This network analyzer was then connected to VDI transmitting and receiving frequency extenders, which can test the performance of the samples

from 68 to 110 GHz. Several photographs of the measurement setup and fabricated samples under test are shown in Fig. 6.12. The measurements were carried out using pairs of 170-μm-pitch GSG probes on a probe test platform. With CS-5 calibration kits from GGB Industries Inc., a short-open-load-thru (SOLT) calibration method was used to remove the effect of the test system.

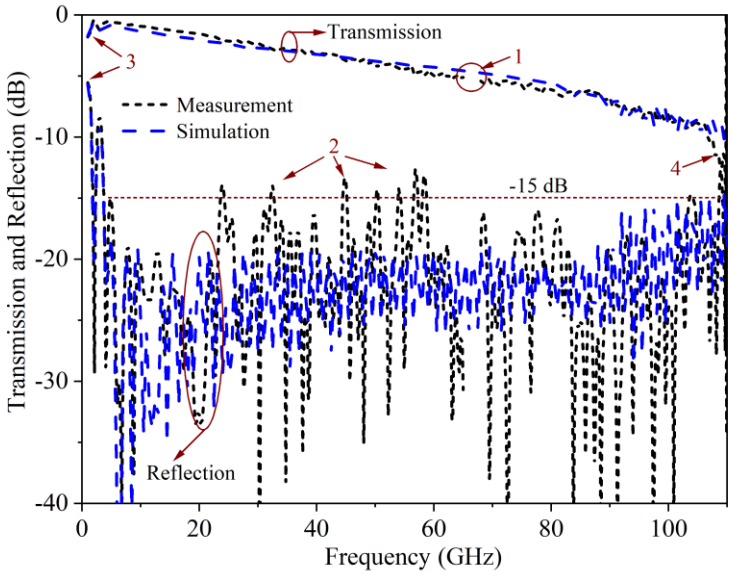

Figure 6.13 Comparison between measured and simulated transmission and reflection responses of the back-to-back transition in Fig. 6.6(a)

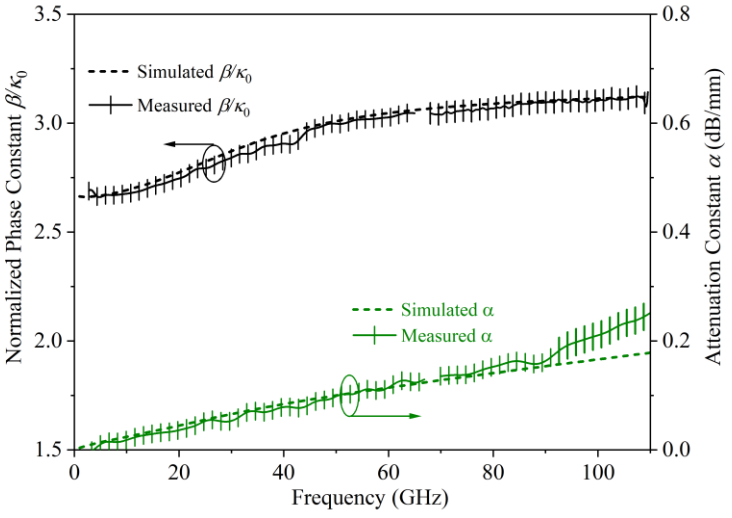

Figure 6.14 Measured and simulated phase and attenuation constants of MSTL

The error bars constitute an indication for statistical errors of the measurement approach.

The transmission and reflection responses of the back-to-back transition with a 17-mm-long MSTL [Fig. 6.6(a)] were measured and compared with the simulated results, as plotted in Fig. 6.13. The measured transmission curve is observed to be flat and agreeable with the simulated one. Its two parts in the different frequency ranges of the measurement (1-65 GHz and 68-110 GHz) remain consistent with regard to their magnitudes and slopes, especially around the break points labeled as 1 in Fig. 6.13. The average measured power loss at 100 GHz, introduced by the single CBCPW-to-MSTL transition, is about 1.84 dB. This is evaluated by removing the losses of the two feeding CBCPWs (about 0.8 dB in total at 100 GHz) and of the 17-mm-long MSTL (about 3.78 dB at 100 GHz, referring to Fig. 6.14). We will continue to further reduce this loss by shortening the transition structure. Furthermore, this loss can be reduced by using some low-loss dielectric materials, such as high-resistivity silicon [137], alumina [138], crystal quartz [47], etc. Thickening the dielectric substrate can also reduce the power dissipated by the Joule effect, thanks to the reduced amplitude of electric current density. The measured return loss as a whole is better than 15 dB, from 3 to 109 GHz. Slight fluctuations appear at several frequency points (labeled as 2) but do not significantly degrade the transition performance. Due to the limitation of the taper itself [81], [117], the performance deteriorates at relatively low frequencies (i.e., < 3 GHz in this case, labeled as 3). On the other hand, when the frequency approaches the upper frequency limit (110 GHz), several sharp fluctuations appear (labeled as 4). The fluctuations (labeled as 2 and 4) are mainly caused by the calibration and measurement errors [139].

As we have explained in Section 6.4, the transition can effectively suppress the undesired higher-order modes to an acceptable level. The propagation characteristics of MSTL are extracted to indirectly examine the suppression effect of the proposed transition. To this end, six MSTLs of different lengths connected to the same transitions [referring to Fig. 6.6(a)] were fabricated and measured. The phase and attenuation constants of the individual MSTL were extracted from the measured S-parameters based on a multiline method [82], [132], as shown in Fig. 6.14. The simulated results of MSTL are also plotted in Fig. 6.14 for comparison. The maximum percent deviation between the measured and simulated phase constants is about 2% (at about 41 GHz). The percent deviation between the attenuation constants is below 10% at frequencies below 90 GHz; nevertheless, the deviation increases rapidly as frequency further increases. This is mainly attributed to the measurement errors; a shorter MSTL sample was found to experience more drastic fluctuations

especially near 110 GHz. This discrepancy is reasonable and is within an acceptable level. In other words, the experimentally extracted propagation characteristics of MSTL agree with the simulated results. The error bars in Fig. 6.14 constitute an indication for the statistical errors of the reported measurement approach. It can also be observed that there is not a significant difference in the attenuation properties over different frequency ranges (e.g., 3-22 GHz and 22-110 GHz, f_c = 22 GHz). Physically, this is due to the fact that in spite of the frequency-dependent modal behavior of MSTL, the main fields are still concentrated around the central microstrip region [Fig. 6.1(b)]. Typical performance comparisons with microstrip line, CPW, and RWG have been carried out in [86] and [96]. In [86], we compared the simulated frequency performance of MSTLs and their CBCPW and RWG counterparts; specific feedlines were included for the comparisons to emulate practical situations. In [96], we compared the measured responses of MSTL and its microstrip and RWG counterparts. These comparisons have shown that MSTL can operate in a frequency range much wider than the conventional transmission media, with a relatively low power loss throughout. In summary, these measurement results verify the effectiveness of the proposed CBCPW-to-MSTL transition.

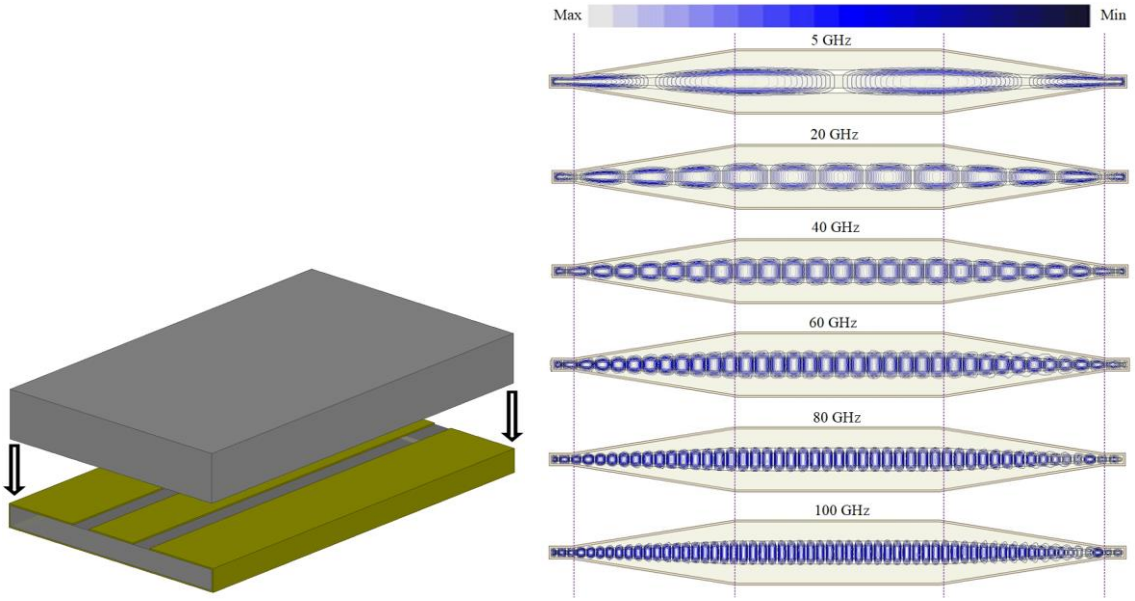

(a) (b)

Figure 6.15 (a) MSTL loaded with a dielectric superstrate. (b) *E*-field distributions in the corresponding back-to-back transition at 5, 20, 40, 60, 80, and 100 GHz

6.6 Discussion

To sustain a single guided mode of propagation (i.e., first local normal mode) in the presented tapered transition requires the tapered coupling path with a length of many wavelengths, that is, the adiabatic invariance condition of (6.7) needs to be satisfied over the desired frequency range. This leads to the transition being insensitive to wavelength within the limit of the adiabatic regime and having relaxed fabrication tolerances, which may be practical especially in the THz regime. If the adiabatic invariance condition is not satisfied, more than one local normal mode may be copropagating in the transition. Consequently, some oscillations will appear at the output, as can be seen from Fig. 6.4(a) (when l_t = 4 mm), which are caused by interferences between the local normal modes [119].

In Part I of this work (Chapter 5) [112], we have reported a special case of MSTL that is the original MSTL loaded with a dielectric superstrate; it is redrawn in Fig. 6.15(a). The phenomenon of mode selectivity would disappear in this special MSTL, as long as the superstrate is thick enough and its relative permittivity is fairly close or equal to that of the bottom (original) substrate. This has been discussed in detail in Section 5.6.2 of Chapter 5 [112]. Its corresponding tapered back-to-back transition is constructed here, as for the original MSTL [Fig. 6.6(a)]. For comparison, its geometry and size are kept the same as the presented CBCPW-to-MSTL transition, but with a superstrate of permittivity 10.2 and thickness 1 mm loaded in its design. The *E*-field distributions in the back-to-back transition at 5, 20, 40, 60, 80, and 100 GHz are shown in Fig. 6.15(b). As can be seen, the fields still concentrate around the center strip at these different frequencies, indicating the propagating mode of MSTL is still the microstrip mode over the operating bandwidth, in contrast to the phenomenon of mode selectivity shown in Fig. 6.6(b). This is consistent with our discussion in [112], which helps get a better physical understanding of the mode selectivity of MSTL.

6.7 Conclusion

The specific excitation scheme for MSTL has been presented in this article. To realize this mode excitation, a tapered transition between CBCPW and MSTL has been proposed and investigated, which can operate in an ultra-broad frequency range (3-109 GHz) with a relatively low loss (about 1.84 dB at 100 GHz) and a good return loss (better than 15 dB). This transition operates as a tapered-mode coupler, whose operation has been analyzed from the point of view of mode coupling between local normal modes. The design considerations and modal evolution have been presented

in detail, together with physical mechanisms and explanations. This transition has a simple tapered structure and is easy to implement. It can facilitate the experimental characterization and practical circuit integration of MSTL. In addition, it can effectively suppress higher-order modes to sustain a high-quality pure mode operation. With the help of this transition, the MSTL has been experimentally characterized. The extracted propagation characteristics of MSTL, in agreement with the simulated results, have verified the effectiveness of the proposed transition. This transition is expected to play an important role in the practical integration of MSTL with CPW circuits for microwave, millimeter-wave, and terahertz applications.

CHAPTER 7 ARTICLE 5: SYNTHESIZED ALL-PASS WAVEGUIDE FOR ULTRAFAST ELECTRONICS TOWARDS PICOSECOND TRANSMISSION AND BEYOND

Desong Wang and Ke Wu

Submitted to *Physical Review Letters*, Oct. 2021.

Ultrashort pulse transmission has been recognized as a primary issue that fundamentally hampers the development of ultrafast electronics beyond the current timescale of nanoseconds. Here, we present a synthesized all-pass waveguide that demonstrates record guided-wave controlling capabilities, including eigenmode reshaping, polarization rotation, loss reduction, and dispersion improvement. We experimentally develop two such waveguides for use in ultra-broad frequency ranges (dc to millimeter wave and to terahertz), capable of efficiently transmitting picosecond electrical pulses. This waveguide technology provides a path towards a frequency-engineered ultrashort pulse for low-loss and low-dispersion transmission.

7.1 Introduction

Ultrafast electronics stands out in emerging ultrafast phenomenon-focused sciences and technologies, particularly on the picosecond timescale and below [140], [141]. It has a wide range of implications and applications in many fields such as basic science [142], terahertz (THz) detection [143], imaging [144], high-frequency measurement [145], high-capability communications [146], as well as biology and medicine [147]. This has drawn extensive attention to the most critical issue, that is, ultrashort electrical pulse transmission [148]-[150]. It particularly needs a transmission line or waveguide to support low-loss, low-dispersion, and all-pass guidance for ultra-broadband signals (dc-to-millimeter-wave or dc-to-THz) [47], [151]. However, this type of waveguiding structure has not yet been known to practically exist; all conventional ones suffer from the prohibited effects of dispersion and loss in connection with low-frequency cutoff (high-pass) [152] and/or high-frequency attenuation (low-pass) [153].

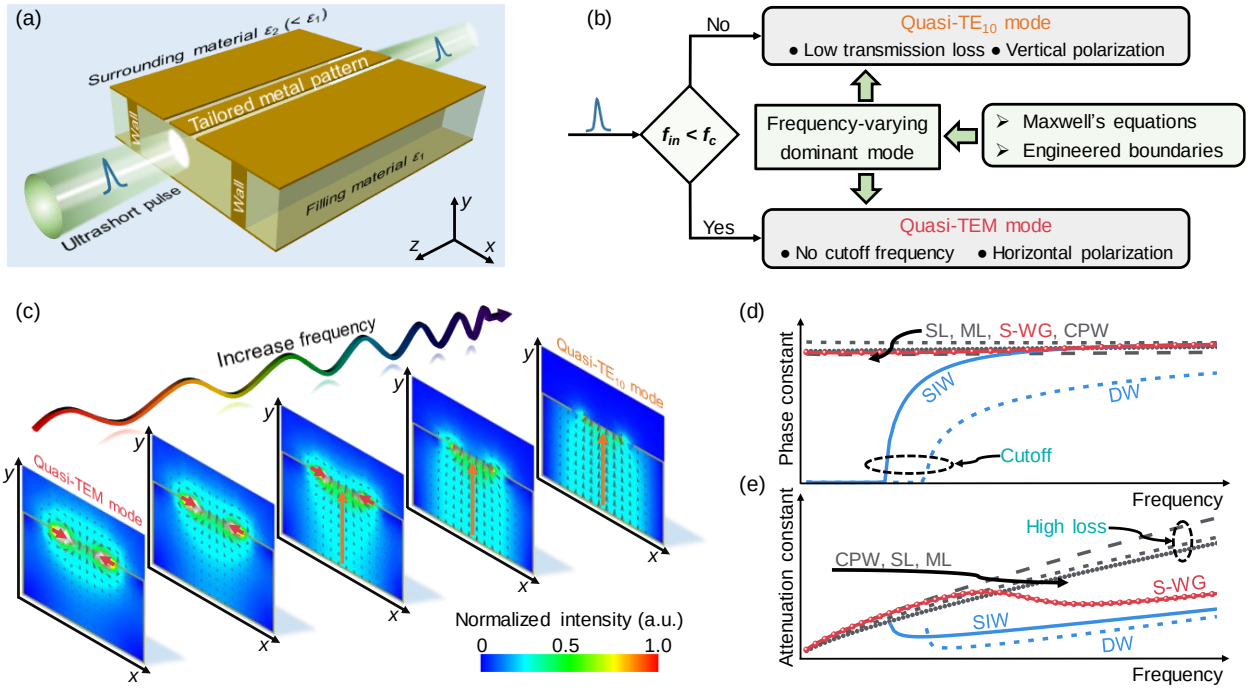

Figure 7.1 Concept of synthesized all-pass waveguide. (a) Schematic of synthesized waveguide. (b) Frequency-dependent mode-conversion mechanism. The frequency-varying dominant mode behaves as a quasi-TEM or quasi-TE_{10} mode depending on whether the frequency of a guided wave f_{in} is lower or higher than the specific frequency f_c, as a solution of the Maxwell's equations together with engineered boundaries. (c) Evolution of cross-sectional electric fields with frequency. The red and orange arrows represent the direction of main electric fields at different frequencies. (d), (e) Comparison of (d) phase and (e) attenuation constants of synthesized waveguide (S-WG) and common transmission media including substrate-integrated waveguide (SIW), dielectric waveguide (DW), coplanar waveguide (CPW), stripline (SL), and microstrip line (ML)

Commonly used planar transmission lines, such as microstrip lines [154], coplanar waveguides (CPWs) [155], and striplines [156], which operate in a ground-plane referenced transverse electromagnetic (TEM) or quasi-TEM mode, present an inherent low-pass ability to transmit broadband signals starting from dc (or very low frequency). Nevertheless, they suffer from weak field confinement and near-monotonically increasing attenuation with frequency. This is contrasted

by the most popular integrated waveguides in use today, including dielectric waveguides [157], [158] and substrate-integrated waveguides (SIWs) [17], [159], which operate in a dominant transverse electric (TE) or transverse magnetic (TM) mode, or even in a hybrid mode. They have a relatively lower attenuation but possess low-frequency cutoff, thus yielding a strong dispersion over a certain frequency range. These fundamental properties are primarily a result of the guided-wave nature of the respective dominant eigenmodes (eigen fields) that are generally assumed to remain unchanged for a given waveguide cross section. That is to say, none of these conventional transmission media is capable of creating an all-pass distortion-free signal transmission that covers a dc-to-THz ultra-broad bandwidth in the frequency domain. Groundbreaking innovations and advances in signal transmission technology are urgently needed to remedy this situation [44], [160], [161]. In fact, this is the most fundamental challenge in the future development of ultrafast electronics in support of picosecond or shorter pulse generation [162], transmission [163], and processing [164], which requires to break through the current nanosecond electronics barrier.

The information-carrying capacity of a transmission system is basically limited by the dispersion and attenuation characteristics of a dominant propagating mode over a bandwidth of interest. Given the aforementioned nonidealities of the specific eigenmodes, it is rather intuitive to come up with an idea that if we could reshape a propagating mode as desired, we would be able to deliberately control the propagation of guided waves. For a given guide, modal eigenvalues are the unique solutions of Maxwell's equations corresponding to specific boundary conditions [165]. It is nevertheless of interest to note that these solutions are a function of frequency, which makes it possible to "construct" particular eigenmodes with frequency [53] and thus obtain various desired modal behavior. In our previous work, an attempt was made to change the dominant mode of a uniform transmission line [47], [96]. The mode change, however, is not well reflected in the related frequency characteristics (especially high-frequency attenuation and wave polarization).

In this Letter, we demonstrate a synthesized waveguide technology in support of ultrashort electrical pulse transmission towards the unprecedented picosecond scale. This waveguide has a dominant mode that is fully reshaped with frequency. We can therefore manipulate its guided wave properties, including polarization rotation, loss reduction, and dispersion improvement. These findings are revealed using two waveguide examples that are separately realized in the millimeter-wave (mmW) [166], [167] and THz frequency ranges [28], [168]. The numerical and experimental results of these

synthesized waveguides demonstrate their capabilities of guiding picosecond electrical pulses efficiently while maintaining signal integrity effectively.

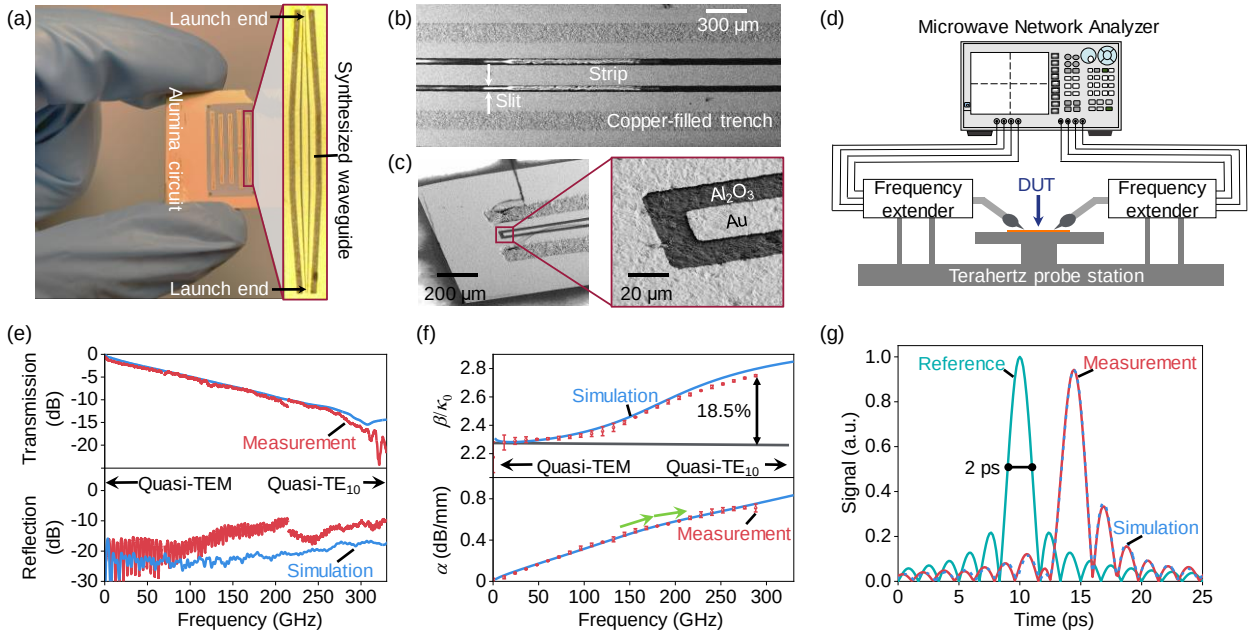

Figure 7.2 Implementation of THz synthesized waveguide. (a) Micrographs of the fabricated samples on an alumina substrate. The single sample is magnified for clear demonstration. Several back-to-back circuits of different lengths [including through-reflect-line (TRL) calibration kits] were fabricated for experimental characterization. (b) A scanning electron microscope (SEM) image of the THz synthesized waveguide. (c) SEM images of the grounded CPW (GCPW) launch end. (d) Schematic of the experimental set-up for frequency-domain characterization of the THz device under test (DUT). Note that for the measurement at frequencies below 67 GHz, the microwave network analyzer was connected directly to radio frequency probes using 1.85 mm coaxial cables without the use of frequency extenders. (e) Measured and simulated (by finite-element modelling) transmission and reflection responses. These results are for a 14.4-mm long back-to-back circuit (including effects of tapered transitions and GCPW launch ends). (f) Experimentally extracted and numerically simulated attenuation α and (normalized) phase constants β/k_0. Error bars indicate the experimental extraction uncertainty (±1 s.d. of three independent extractions). (g) Evolution of an ultrashort pulse with a 2-ps FWHM pulse duration as it propagates along the synthesized waveguide for 0.5 mm

7.2 Synthesized waveguide

The synthesized waveguide is constructed by symmetrically etching two narrow slits over the top plane of a rectangular waveguide filled with a dielectric of permittivity ε_1 and then covering them with another dielectric (or air) of permittivity ε_2. This simple geometric setting, as shown in Fig. 7.1(a), has important characteristics: transverse inhomogeneity ($\varepsilon_2 < \varepsilon_1$) and longitudinal invariance. It is compatible with planar fabrication processes and convenient for integration with other devices. Thanks to the engineered boundaries, this particular waveguide supports a frequency-varying dominant eigenmode that undergoes a gradual-to-complete conversion from a quasi-TEM CPW mode (horizontal polarization) to a quasi-TE_{10} waveguide mode (vertical polarization) as the operating frequency increases (see Supplemental Material [169] for eigenmode analysis). Hence, this synthesized waveguide merges the desired waveguiding properties offered by both the CPW (no cutoff frequency) and rectangular waveguide (low transmission loss). This special scenario is briefly described in the schematic block diagram of Fig. 7.1(b).

To illustrate the frequency-dependent mode conversion, electric fields are examined over the cross section of the waveguide at different frequencies. As shown in Fig. 7.1(c), both the field pattern and polarization direction are subject to vivid changes with frequency, which are significantly different from their relatively stationary counterparts in conventional waveguiding structures (Supplemental Fig. 7.1 [169]). The special modal characteristics offer the synthesized waveguide many unique advantages over common guiding structures, such as ultra-broad operating bandwidth, reduced high-frequency loss, and low signal dispersion. Figures 7.1(d) and 7.1(e) compare the propagation constants of the synthesized waveguide and its counterparts. As expected, both the SIW and dielectric waveguide exhibit a cutoff phenomenon [Fig. 7.1(d)]; the CPW, stripline, and microstrip line suffer from relatively high losses, especially at high frequencies [Fig. 7.1(e)]. However, our synthesized waveguide overcomes these disadvantages, thus becoming a promising candidate for transmitting ultra-broadband ultrashort pulses. To demonstrate the proof-of-principle, we developed two such waveguides for use in ultra-broad frequency ranges, from dc to terahertz (dc to 300 GHz) and to millimeter wave (dc to 67 GHz).

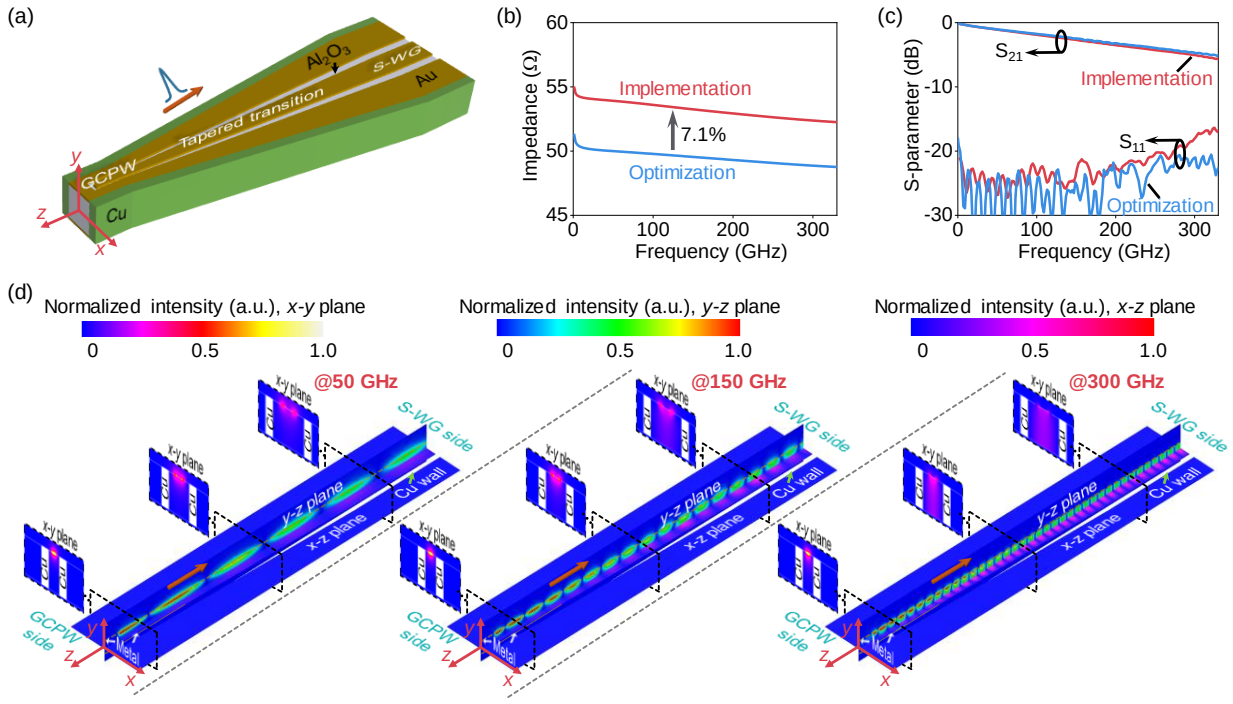

Figure 7.3 Tapered transition design. (a) Schematic of tapered transition design. The taper connects the synthesized waveguide (S-WG) to a GCPW. (b) Characteristic impedance of GCPW launch end. The finally implemented GCPW has a 7.1% increase in characteristic impedance as compared with the originally optimized value. (c) Simulated transmission (S_{21}) and reflection (S_{11}) responses of the tapered transition. At frequencies up to 300 GHz, the S_{21} curve is very flat, and the S_{11} curve remains below -20 dB, meaning smooth power delivery and good matching between the synthesized waveguide and GCPW. (d) Electric field distributions in the *x-z*, *y-z*, and *x-y* planes of the transition at 50, 150, and 300 GHz

The transition model is hidden to clearly show fields in which the positions of metal layers and copper walls are marked for reference. The orange arrows indicate the propagation direction of guided waves. The fields on the GCPW side (CPW mode) are almost the same at different frequencies, whereas those on the S-WG side (frequency-varying mode) undergo a significant shape change.

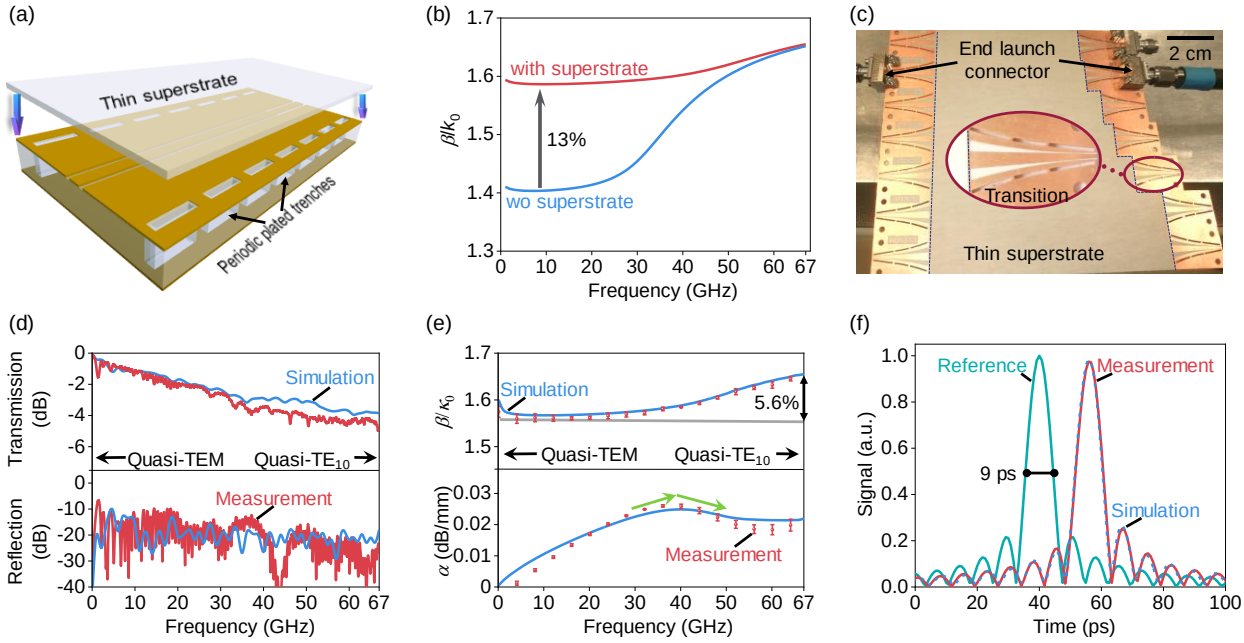

Figure 7.4 Implementation of mmW synthesized waveguide. (a) Schematic of mmW synthesized waveguide. (b) Dispersion curve of the synthesized waveguide, with and without a thin superstrate. The thin superstrate contributes significantly to increasing the normalized phase constant β/k_0 (or effective permittivity) in low frequency range (quasi-TEM mode) but has no obvious effect on it at higher frequencies (quasi-TE_{10} mode). The flatter curve for the superstrate case indicates an improvement in signal dispersion. (c) A micrograph of the fabricated samples. A tapered transition is magnified for better demonstration. Several back-to-back circuits of different lengths (including TRL calibration kits) were fabricated for experimental characterization. (d) Measured and simulated (by finite-element modelling) transmission and reflection responses. These results are for a 124-mm long back-to-back circuit (including effects of tapered transitions and end launch connectors). (e) Experimentally extracted and numerically simulated attenuation α and (normalized) phase constants β/k_0. Error bars indicate the experimental extraction uncertainty (±1 s.d. of three independent extractions). (f) Evolution of an ultrashort pulse with a 9-ps FWHM pulse duration as it propagates along the synthesized waveguide for 3 mm

7.3 Realization in terahertz spectrum

We first implemented a micro-scale synthesized waveguide on an alumina substrate for THz-wave guidance [Figs. 7.2(a)-(c)]. To characterize its ultra-broad frequency response, experiments were carried out separately over different frequency ranges on a THz probe station [Fig. 7.2(d)]. Detailed fabrication and measurement procedures are illustrated in Supplemental Material [169]. Figure 7.2(e) shows the measured transmission and reflection responses of the fabricated circuit from 10 MHz (near dc) to 325 GHz. It is found that the transmission response is flat at frequencies up to 300 GHz; the reflection curve remains below -10 dB. Figure 7.2(f) plots the propagation constants of this synthesized waveguide, which were extracted from the measured scattering parameters. The normalized phase constant experiences an 18.5% change throughout the entire operating range, attributable to the variable modal behavior. The attenuation constant increases monotonically with frequency and reaches a maximum value of 0.72 dB/mm; however, there is a noticeable sign of slowing down at frequencies above roughly 170 GHz. This phenomenon becomes much more pronounced in the larger distance between the bilateral sidewalls (Supplemental Fig. 7.2 [169]). The derived time-domain results [Fig. 7.2(g)] demonstrate that this waveguide supports an efficient transmission of an ultrashort pulse with a 2-ps full width at half maximum (FWHM) pulse duration. The numerical simulation results are also plotted in Figs. 7.2(e)-(g), which are found to be in close agreement with the experimental data.

To facilitate the experimental characterization, we designed a continuously tapered transition [Fig. 7.3(a)] to directly connect the synthesized waveguide to a grounded CPW (GCPW) that remains a fixed characteristic impedance of 50 Ω [Fig. 7.3(b)]. This taper provides good impedance and field matching between the synthesized waveguide and GCPW [170], thus guaranteeing a smooth power delivery [Fig. 7.3(c)]. As illustrated in Fig. 7.3(d), an ultrashort pulse is launched on the GCPW side into the CPW mode whose electric fields concentrate primarily around the narrow slits. As the pulse propagates down the taper, the power is smoothly delivered into the frequency-varying dominant mode of the synthesized waveguide on the other side. These results suggest that the variable dominant mode of the synthesized waveguide is excited with the aid of the taper.

7.4 Realization in millimeter-wave spectrum

We now evaluate the waveguiding capabilities in the mmW frequency range (dc to 67 GHz) to further verify the validity and generality of the synthesized waveguide concept. To this end, an mmW waveguide was implemented on a low-loss dielectric substrate and then loaded with an electrically thin sheet on the top [Fig. 7.4(a)]. The primary purpose of the additional superstrate is to increase the effective permittivity ε_2 of the surrounding material. The resulting ε_2 does increase to approach but still be less than that of the filling material ε_1 (i.e., $\varepsilon_2 < \varepsilon_1$). It means that the frequency dispersion of this waveguide is improved [Fig. 7.4(b)], while the geometric characteristic of transverse inhomogeneity is preserved. The bilateral sidewalls in this case are implemented with periodic plated trenches, which act as continuous electric walls (Supplemental Fig. 7.3 [169]). This mmW synthesized waveguide does not lose any generality and can be easily fabricated by a low-cost printed circuit board (PCB) process [169].

Similar to the THz synthesized waveguide, this mmW demonstration has a frequency-varying dominant mode [169] and thus shows superior performance. We conducted the experimental confirmation of broadband signal transmission (10 MHz to 67 GHz, see Supplemental Material [169]) with the help of tapered transitions [Fig. 7.4(c)] constructed in the same manner as the THz case. Figure 7.4(d) compares the numerically simulated and experimentally measured frequency responses of the fabricated back-to-back circuit [Fig. 7.4(c)]. One can observe from the transmission responses that the insertion loss increases gradually with frequency, but this increase slows down in the right half of the frequency plane. The reflection level is still maintained below -10 dB, indicating good matching over the operating bandwidth. Figure 7.4(e) shows the extracted propagation constants of the individual synthesized waveguide. This mmW waveguide has a smaller change (< 5.6%) in its normalized phase constant as compared with the THz case [Fig. 7.2(f)], implying an improvement in signal dispersion. The attenuation constant is found to first increase with frequency but then, surprisingly, it decreases steadily after reaching a maximum value of 0.026 dB/mm near 38 GHz, which ensures a low dissipative loss throughout. This is an attribute of the frequency-dependent mode conversion occurring in the synthesized waveguide. This distinctive attenuation phenomenon is reflected in thermal effects (Supplemental Fig. 7.4 [169]). Figure 7.4(f) plots the derived pulse responses, displaying that a 9-ps FWHM pulse can be well transmitted through the mmW synthesized waveguide without distortion.

7.5 Conclusions

We have introduced a synthesized waveguide that enables the efficient guidance and proper manipulation of ultrashort electrical pulses. By elaborate geometric tailoring, we have conceived the waveguide whose dominant eigenmode is fully reshaped with frequency. As a result, the guided wave undergoes a total polarization rotation of 90° (horizontality to verticality) and an anomalous but significant reduction in high-frequency loss while attaining a superior dispersion property. To validate and exhibit the potential and generality of this technology, we have presented two simple waveguide prototypes operating in different frequency ranges. Our results suggest that the synthesized waveguides are capable of efficiently transmitting picosecond pulses while maintaining signal integrity. Despite the initial implementations in the mmW (dc to 67 GHz) and THz (dc to 300 GHz) frequency ranges, the synthesized waveguide is highly scalable, possibly extending its applicability to frequencies above 1 THz and beyond (i.e., picosecond or sub-picosecond pulse bandwidth).

This work has offered new horizons for the future development of ultrafast electronics especially in connection with ultrashort pulse transmission. The presented waveguide technology is an important breakthrough in the evolution of ultrafast electronics, which is set to become the backbone of future ultrafast electronic circuits, interconnects, and systems [171], [172]. Despite the conspicuous superiority of this technology, practical applications still require more efforts to improve the excitation of the variable dominant mode and the suppression of undesired modes.

Supplemental material

A. Eigenmode analysis

The synthesized waveguide supports a frequency-varying dominant mode (Fig. 7.1). This is attributed to the fact that the dimensionality of the engineered boundaries is conditioned by frequency or wavelength. In other words, the boundary conditions "seen" by the dominant eigenmode vary with frequency [112]. At low frequencies, the surrounding conductor [Fig. 7.1(a)] functions as a folded ground plane for the center strip on the top. In this case, the synthesized waveguide, whose dominant mode behaves as a quasi-TEM CPW mode, acts like a conventional GCPW. In contrast, the surrounding conductor behaves like a slitted waveguide [25] at higher frequencies; the resulting dominant mode in this case becomes a quasi-TE_{10} waveguide mode. Here, specific field components of the synthesized waveguide are examined using two types of eigenmode analysis [173], [174], namely exact full-wave solution [175], [176] and approximate analytical solution [94], [177].

Let us treat the mmW synthesized waveguide (Fig. 7.4) as an example for the eigenmode analysis. The full-wave eigenmode analysis was carried out using the finite-element numerical technique [173], [175], whereas the approximate analytical solution was obtained using the coupled-mode theory [77], [178] combined with the normal-mode analysis [94], [179]. From the viewpoint of mode coupling, the synthesized waveguide is regarded as a coupled transmission system consisting of two constituent elements: the central GCPW and surrounding slitted waveguide [18], [25], as indicated by the subscripts 1 and 2 in Supplemental Fig. 7.5(a). The electromagnetic fields of the entire transmission system can be expressed approximately as a linear superposition of fields of the individual constituent elements [22]. For example, the fields for the dominant eigenmode of the synthesized waveguide are given by

$$\vec{E}_e(x,y,z) \approx [m\vec{E}_1(x,y) + n\vec{E}_2(x,y)]e^{-j\beta_e z} \tag{7.1}$$

and

$$\vec{H}_e(x,y,z) \approx [m\vec{H}_1(x,y) + n\vec{H}_2(x,y)]e^{-j\beta_e z}, \tag{7.2}$$

where β_e is the propagation constant of the dominant mode of the synthesized waveguide; the coefficients m and n are related to the coupling strength between the constituent elements [178].

The modal analysis results show that *m* and *n* have fixed though differing values at low frequencies ($m \approx 1$ and $n \approx 0$) and then start to vary inversely with frequency [Supplemental Fig. 7.5(b)]. This points to a large variation in electromagnetic fields of the synthesized waveguide [see Eqs. (7.1) and (7.2)], which can be easily verified by examining either the approximate fields derived from the theoretical analysis or the exact fields obtained from the rigorous full-wave numerical calculation (Supplemental Fig. 7.6). A close and precise examination of all the field components affirms that the dominant mode of the synthesized waveguide fully converts from a quasi-TEM mode to a quasi-TE_{10} mode as the operating frequency increases.

B. Device fabrication

The THz synthesized waveguide (Fig. 7.2) was fabricated on a 250-μm thick alumina substrate by a microfabrication process [Supplemental Fig. 7.7(a)]. This process began by laser-drilling trenches through the alumina substrate. Then, a 20-nm thick titanium (for adhesion purpose) and a 1-μm thick copper were sputtered successively on the bottom, followed by an electroplating operation to fill the trenches completely with copper. After removing the excess copper and polishing the surfaces, a bimetal titanium-gold coating (~1-μm thick) was sputter-deposited atop the substrate. It was then coated with positive photoresist whose pattern was defined by lithography. Next, the top metal pattern was formed by removing the exposed titanium-gold using wet etching prior to removing the photoresist using acetone. This operation caused the copper film preformed on the bottom to lift off. Finally, the bottom was again metallized by sputtering a 1-μm thick titanium-aluminum.

The mmW waveguide (Fig. 7.4) was fabricated on two stacked RT/duroid 6002 laminates (0.5-oz copper cladding) using a standard low-cost printed circuit board (PCB) process [Supplemental Fig. 7.7(b)]. For the top laminate (5-mil thick), we just needed to completely remove the copper claddings on both sides by wet etching. For the bottom laminate (30-mil thick), the plated trenches were realized by first laser drilling and then metallization. It was followed by patterning the top metal plane using a photolithography process. After being suitably tailored by laser cutting, these two laminates were bonded together with a two-component epoxy glue by thermocompression (pressed and heated at 50 °C for two hours).

C. Waveguide characterization

To evaluate the practical performance of the synthesized waveguides, we conducted a series of frequency-domain measurements using a Keysight PNA-X network analyzer N5247A. Here, we adopted both the multiline short-open-load-through (SOLT) and through-reflect-line (TRL) calibration techniques [82], [180] to eliminate the unwanted effects of the measurement set-up chain. By the two-port measurements, we measured the transmission and reflection responses (scattering parameters) [Figs. 7.2(e) and 7.4(d)]. Then, we extracted the propagation constants of the synthesized waveguides [Figs. 7.2(f) and 7.4(e)] and derived the time-domain pulse responses [Figs. 7.2(g) and 7.4(f)] using the inverse fast Fourier transform (IFFT) [181].

For the THz synthesized waveguide, experimental measurements were conducted on a THz probe station shown in Fig. 7.2(d) [90]. After completing the calibration procedure, we first measured the two-port scattering parameters from 10 MHz to 67 GHz. Note that the lowest measurement frequency limited by our test set was 10 MHz at which the performance of the synthesized waveguide was assumed to be analogous to that at dc. To obtain the results at higher frequencies, we then connected the network analyzer to different pairs of frequency extenders, ground-signal-ground (GSG) radiofrequency probes, and waveguide transitions. The subsequent measurements were performed separately over the frequency ranges of 75-110 GHz, 90-140 GHz, 140-220 GHz, and 220-325 GHz. All the SOLT calibrations were carried out at the probe tips using commercial calibration substrates (GGB CS-15 and GGB CS-5), whereas the TRL calibrations were made using the fabricated calibration standards [182].

For the mmW synthesized waveguide, the frequency responses from 10 MHz to 67 GHz were measured using 1.85-mm end launch connectors [Fig. 7.4(c)]. The aforementioned calibration procedures were used to characterize the error boxes before measuring the two-port waveguide [183].

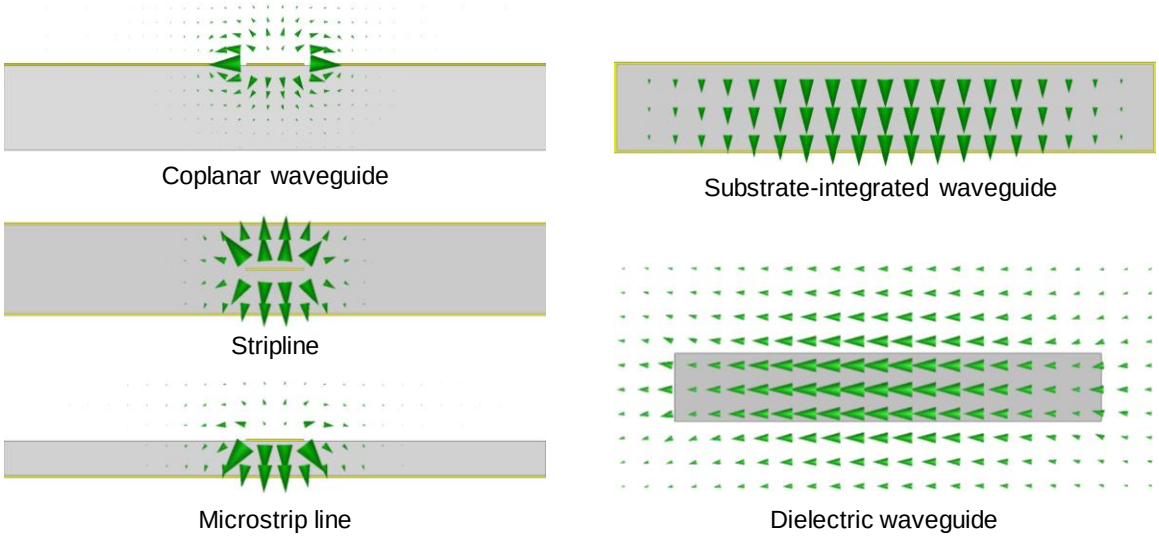

Supplemental Figure 7. 1 Cross-sectional electric field distributions for each dominant eigenmode of conventional waveguiding structures

These field patterns do not vary significantly with frequency.

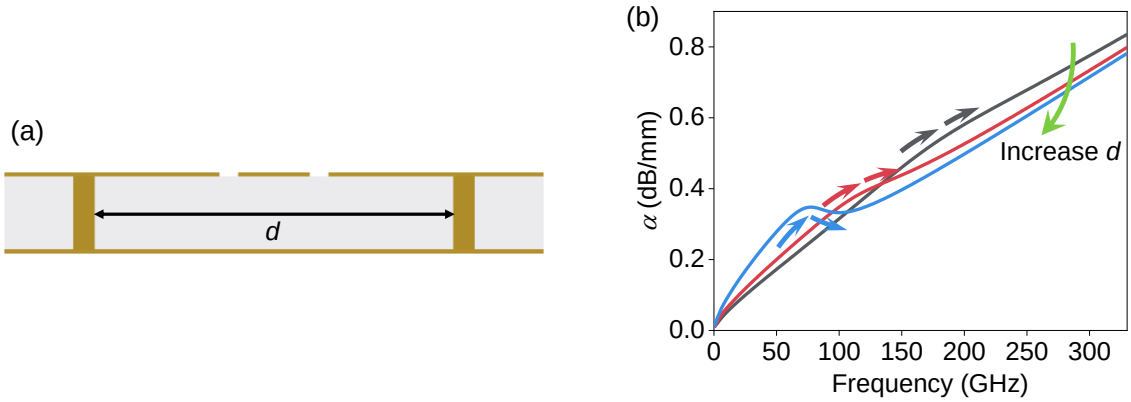

Supplemental Figure 7. 2 Attenuation evaluation for different distances between bilateral sidewalls of THz synthesized waveguide. (a) Definition of distance *d*. (b) Effects of *d* on attenuation constant α

The value of *d* increases from 420 to 820 μm in an increment of 200 μm. The increase in α with frequency slows down after a specific frequency. The tendency of slowing down becomes more pronounced for a larger *d*, and there is even a slight decrease in α over a narrow frequency range (78-100 GHz) when d = 820 μm.

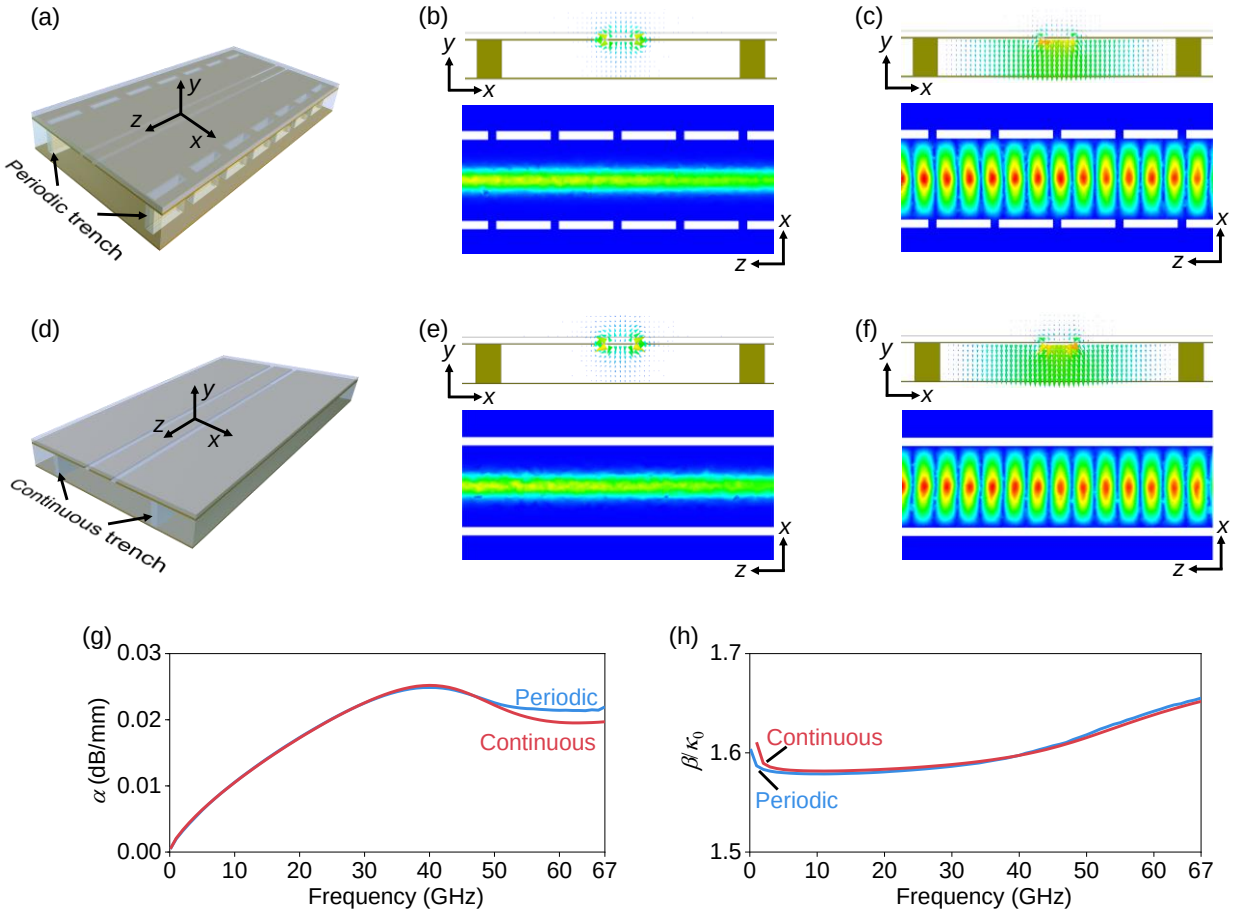

Supplemental Figure 7. 3 Implementations of bilateral sidewalls of mmW synthesized waveguide. (a) Schematic of mmW synthesized waveguide with bilateral walls implemented using periodic plated trenches. (b), (c) Electric field distributions of the waveguide [see (a)] at (b) 1 GHz and (c) 67 GHz. (d)-(f) Same as (a)-(c) but the bilateral walls are implemented using continuous plated trenches. (g) Attenuation constant α and (h) normalized phase constant β/k_0 for the two implementations

No significant difference in modal fields and propagation constants between these implementation approaches is observed.

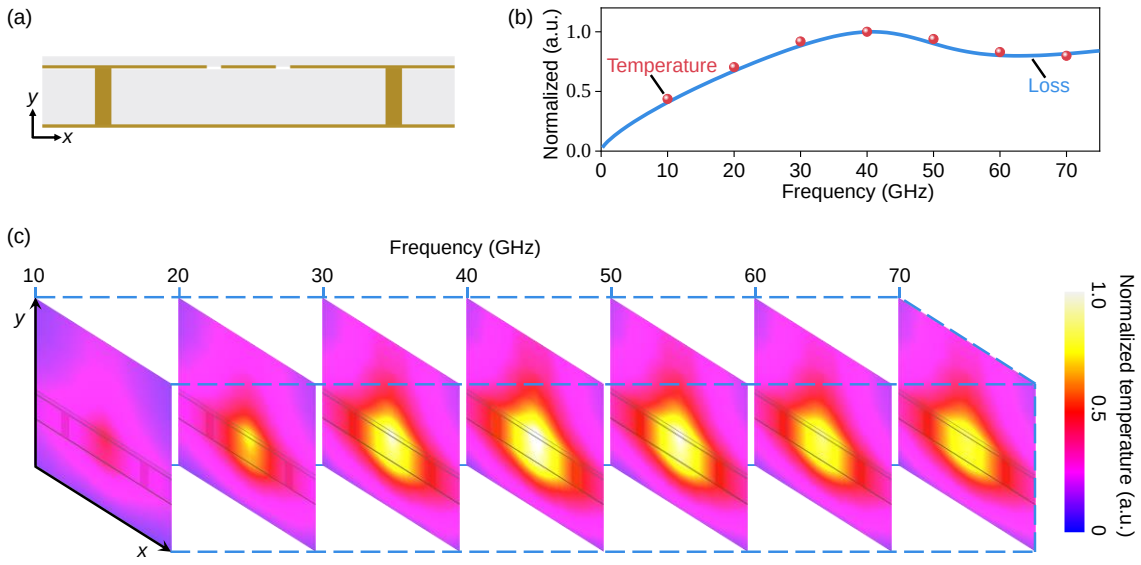

Supplemental Figure 7. 4 Dissipative loss versus thermal effect. (a) Transverse cross section of the mmW synthesized waveguide. (b) Comparison between normalized temperature and loss as a function of frequency. (c) Cross-sectional (normalized) temperature distributions

It should be noted that the temperature shown here is the one caused by thermal noise generated internally by dissipative loss. The change in internal temperature with frequency further verifies that the transmission loss of the synthesized waveguide can be reduced at high frequencies.

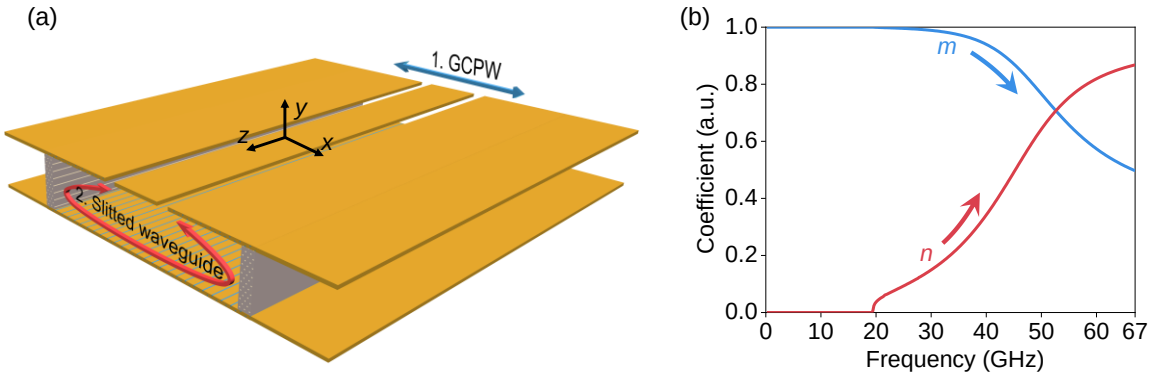

Supplemental Figure 7. 5 Schematic of synthesized-waveguide system. (a) Illustration of the mmW synthesized waveguide as a coupled transmission system. Dielectrics are hidden to clearly show the geometry. The transmission system consists of the central GCPW and the surrounding slitted waveguide. (b) Calculated coefficients *m* and *n* versus frequency

The coefficient m has a fixed value of $m \approx 1$ at low frequencies and then starts to decrease gradually with frequency; n has a fixed value of $n \approx 0$ at low frequencies and increases greatly with frequency.

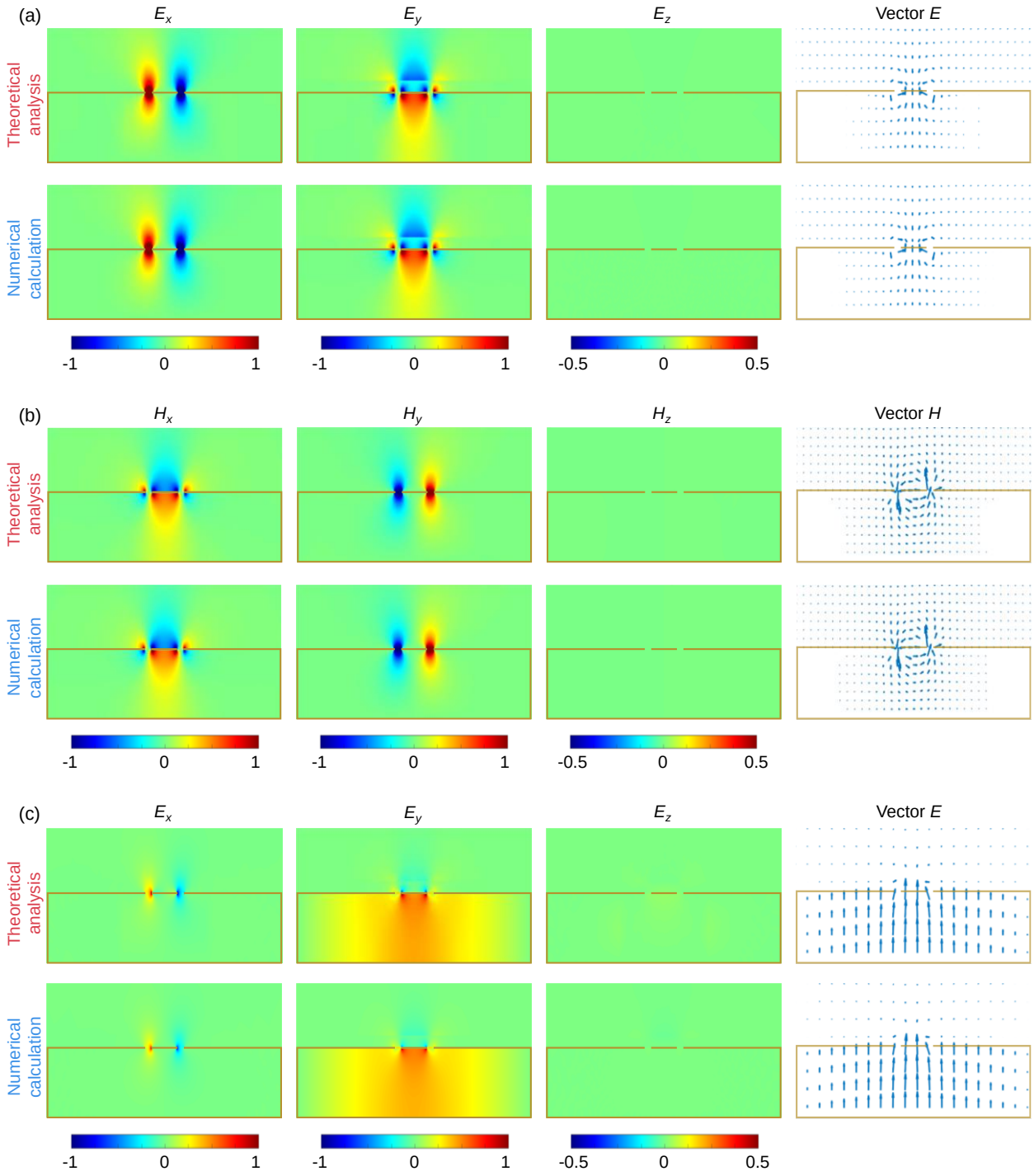

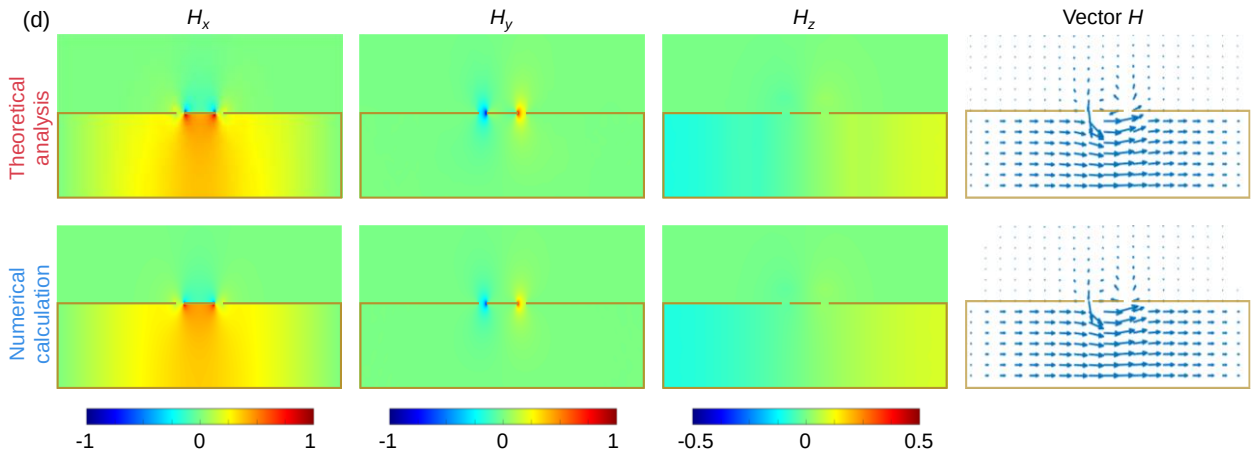

Supplemental Figure 7. 6 Cross-sectional electromagnetic fields of the mmW synthesized waveguide. (a) Electric fields at 1 GHz. (b) Magnetic fields at 1 GHz. (c) Electric fields at 67 GHz. (d) Magnetic fields at 67 GHz

The field components for the frequency-varying dominant mode are obtained from both the approximate theoretical analysis and the rigorous full-wave numerical calculation (Methods). They are normalized to the corresponding maximum electric and magnetic field magnitudes. Dielectrics are hidden to show the field patterns. The fields at 1 GHz (including field pattern and direction) are significantly different from those at 67 GHz, which correspond to the quasi-TEM and quasi-TE_{10} modes, respectively.

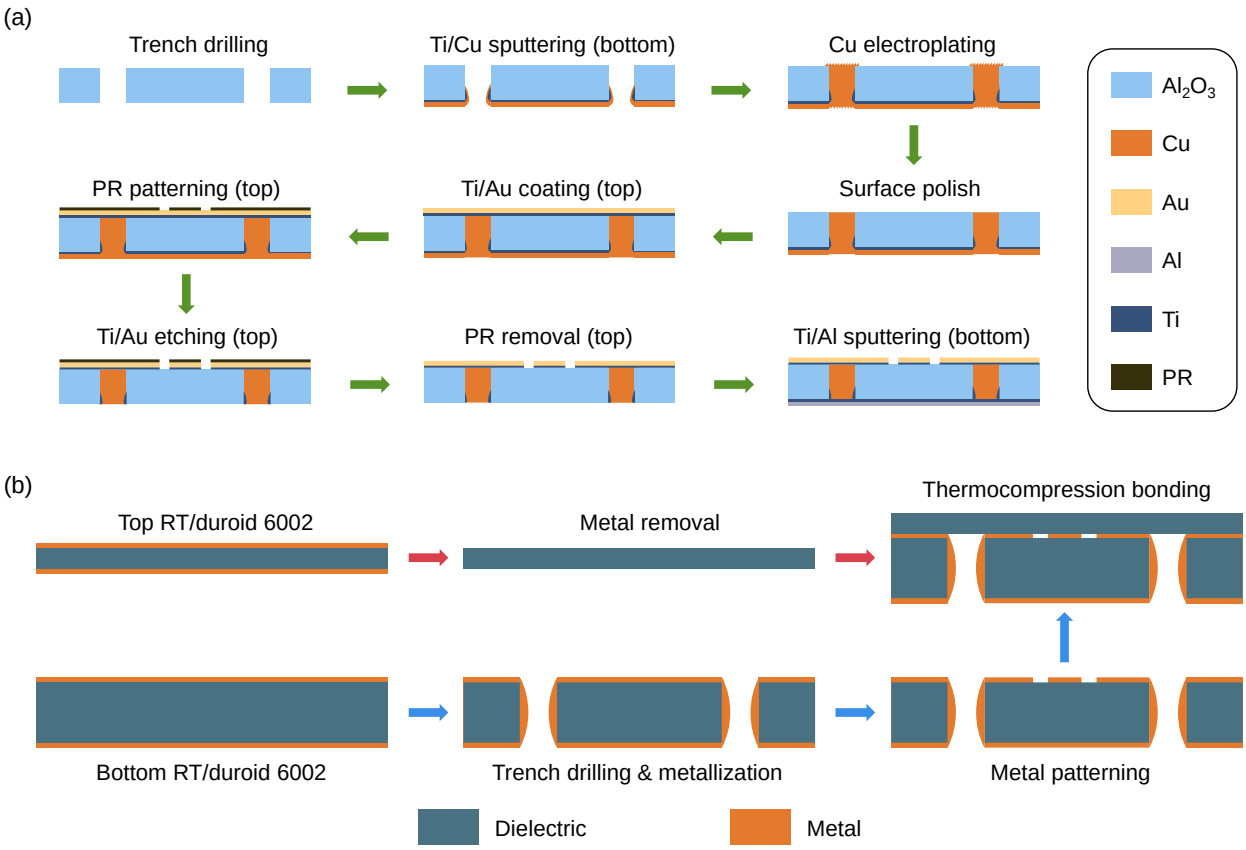

Supplemental Figure 7. 7 Fabrication processes of the synthesized waveguides. (a) Microfabrication process of THz synthesized waveguide. (b) PCB process of mmW synthesized waveguide

In (a), PR represents the photoresist. Four metallic materials (gold, aluminum, copper, and titanium) were involved in this microfabrication process; gold and aluminum were sputtered to form the top and bottom conducting layers, respectively; copper was electroplated to fill the trenches; titanium was used for adhesion purpose.

CHAPTER 8 GENERAL DISCUSSION

This Ph.D. research is an attempt to explore and demonstrate an advanced signal-guiding technology for transmitting ultrafast ultra-broadband electromagnetic waves starting from dc to mmW, THz, or even optical frequencies. To this end, several synthesized waveguides have been presented and treated, which show superior frequency performance including low loss, low dispersion, ultra-broad bandwidth, etc. Some issues involved in this research are worthwhile for discussions, as presented below. Through a general discussion, it is the major goal of this chapter to provide a better understanding of the studied synthesized waveguide technology and potential applications.

Research strategy: Beginning with a comprehensive treatment of MSTL, this Ph.D. research is to investigate and develop the synthesized waveguide technology for a wide range of ultrafast electronics and broadband systems including high-speed interconnects in future Internet of Things (IoT)-based wireless systems. MSTL is a kind of synthesized waveguides, which was first proposed and investigated preliminarily by our research group. As its name suggests, MSTL operates in a dominant eigenmode with frequency-varying behavior, and it thus exhibits low loss and low dispersion over a wide frequency range. To realize the research objectives (see Chapter 1), advanced modeling and parameter extraction techniques have been utilized together with experimental verifications. This research has paved the way for future integration of circuits and antennas in a unified way; the synthesized waveguides will play an important role in multi-mode wireless designs and applications.

Research resources: Different software and hardware resources were used to complete this research activities and achieve the research objectives. Several high-frequency simulation tools including High Frequency Structure Simulator (HFSS), CST Microwave studio, Advanced Design System (ADS), and COMSOL were utilized to model, simulate, optimize, and analyze the synthesized waveguides; MATLAB, Origin, and Microsoft Office Suite were used to support the theoretical analysis and extract the useful data from simulation and measurement results.

Furthermore, we made an effort to choose, validate, and then adopt some low-loss dielectric materials such as silicon, alumina, and Rogers substrates for the high-frequency waveguide realizations. Microfabrication and PCB fabrication processes were adopted to implement the synthesized waveguides according to their sizes and operation frequencies. Standard PCB circuit tests and high-frequency probing tests on a THz measurement platform were conducted to characterize the ultra-broadband waveguide performance. Vector network analyzer (10 MHz to 67 GHz), frequency extenders (up to 325 GHz), 1.85-mm end launch connectors, coaxial lines, GSG probes, and standard waveguide connectors were all deployed for the experimental verifications. In addition, academic discussions, teamwork, cooperation, and spirit of scientific research are considerably critical throughout the research process.

Problems and solutions: A systematic investigation on the synthesized waveguide technology has been carried out, revealing superior signal transmission performance. Over the course of this exhaustive study, some problems or difficulties were met, including material selection, suppression of undesired modes, fabrication accuracy, measurement feasibility, etc, which are briefly described as follows. (1) Most of commercially available dielectric materials do not meet the requirements for low loss and stable performance over an ultra-broad frequency range. We compared and analyzed several available materials that are popularly used in optics, and then tried some of them (such as high-resistivity silicon and low-loss alumina) for implementing the designed dc-THz waveguides. In addition, we used the Rogers 6002 and 6010 substrates with a relatively low loss for implementing the dc-67-GHz and dc-110-GHz waveguides. (2) As frequency increases, higher-order modes may emerge and ruin the frequency characteristics of the wideband waveguides, especially the high-frequency performance. These undesired modes are difficult to remove completely. In this research, tapered transitions were designed to excite the dominant mode and also to suppress the undesired modes to an acceptable level. (3) Since the designed waveguides operate in an ultra-broad frequency range, there is a large difference in their sizes of different parts. It results in a difficulty in the practical fabrication. To solve the problem, we utilized a high-accuracy PCB process and a microfabrication process together with SIW technology to physically realize the waveguides. (4) Furthermore, the experimental characterization of the ultra-broadband waveguides is labor-intensive and time-consuming, requiring pairs of advanced measurement instruments for tests in different frequency bands. With the measurement setups available in our

lab, the frequency responses of the waveguides in the ranges of 10 MHz-67 GHz, 75-110 GHz, 90-140 GHz, 140-220 GHz, and 220-325 GHz were tested, which almost cover the desired ranges of dc-67 GHz, dc-110 GHz, and dc-300 GHz. In addition to these solutions, we also cooperated with the Department of Engineering Physics for the measurements. For promising applications of the synthesized waveguides in integrated THz systems, we cooperated with the Institute of Optoelectronics at the University of Duisburg-Essen for developing possible reliable THz source systems, which would be realized by integrating a photodiode with our dc-500 GHz waveguide to generate and guide picosecond pulses.

Specific contributions: After solving the problems and difficulties, the research project has been accomplished successfully, with many scientific contributions, as summarized below.

- As a simple example of synthesized waveguides, a coupled-HMSIW system has been proposed and explained based on the coupling-mode theory and has been used to design compact wideband balun for mmW applications.
- The unique mode-selectivity phenomenon occurring in MSTL has clearly been presented by examining the detailed field components of MSTL at different frequencies, as the first-hand physical evidence.
- The physical mechanism of MSTL has been revealed by conducting a joint normal- and coupled-mode analysis, providing an in-depth understanding of how the frequency-varying dominant mode changes with frequency.
- The excitation scheme of MSTL has been presented, which helps guide the tapered transition design for efficiently exciting the variable dominant mode of MSTL and also for effectively suppressing undesired modes that possibly appear at high frequencies.
- Another synthesized all-pass waveguide has been proposed, which demonstrates record guided wave controlling capabilities, including eigenmode reshaping, polarization rotation, loss reduction, and dispersion improvement. It is capable of efficiently transmitting picosecond electrical pulses.
- Last but not least, the well-explained synthesized waveguides have been demonstrated to have huge potential in the realization of different wideband components such as

antennas, couplers, multi-mode filters. They are also a good candidate for high-speed chip interconnects.

Impacts and benefits: Suffering from high loss and high dispersion, conventional transmission lines and waveguides cannot satisfy the demand for sophisticated high-performance applications over the dc-to-THz range. This strongly motivates researchers to devise an alternative transmission medium. However, few revolutionary research results have been reported up to now (see Chapter 2). This situation drives us to change a way of thinking. Finally, we have realized a groundbreaking synthesized waveguide technology with sustained low loss and low dispersion, possessing the following benefits:

- **Short-term benefit**: Low-loss and low-dispersion synthesized waveguides such us MSTL have been implemented, which can operate well over the dc-to-THz frequency range and are suitable for high-speed chip interconnects and many other applications.
- **Mid-term benefit**: Based on the presented waveguide technology, promising applications will be thought and developed, such as wideband antennas, filters, couplers, etc.
- **Long-term benefit**: The ultra-broadband waveguides seem to be a promising candidate that enables and empowers current and future integrated-circuit developments and applications toward high-performance, high-density, and broadband dc-to-THz modules, as well as high-speed interconnects. This research will also drive countless research activities in mode-conversion transmission structures and passive as well as active components.

CHAPTER 9 CONCLUSION AND FUTURE WORK

9.1 Conclusion

This research work has presented and developed several synthesized waveguide structures for ultra-broadband signal transmission and applications. In addition to the MSTL on which this work focuses (Chapters 4-6), other two synthesized waveguides including the coupled-HMSIW system (Chapter 3) and synthesized all-pass waveguide (Chapter 7) have been investigated and analytically treated. In our opinion, this synthesized waveguide technology is an important breakthrough in electromagnetic waveguide evolution, providing a path to realize low-loss and low-dispersion transmission for ultrafast electromagnetic waves or signals. We expect that it may become the backbone of future ultra-broadband ultrafast electronic circuits, interconnects, and systems.

This research has started with the analysis of coupled HMSIWs, a very simple coupled-mode transmission system, which aids our understanding of a synthesized waveguide system. Given the frequency-independent out-of-phase property of its odd $TE_{0.5,0}$ mode, a low-cost and compact balun has been proposed in Chapter 3. This balun operates over K-, Ka-, and Q-bands with superior performance such as wide bandwidth, low power loss, and good in-band amplitude and phase imbalances. The presented slotline excitation facilitates the integration with other planar circuits and expedites its potential applications in microwave and mmW circuits and systems.

Chapter 4 has presented a comprehensive treatment of typical MSTLs, including numerical examination, theoretical analysis, and experimental verification. To verify the applicability of the MSTL design, we have treated two MSTLs as practical examples that operate in quite different frequency ranges. The unique mode selectivity of MSTLs has been validated by both the physical evidence and theoretical foundation. It has been treated rigorously by defining the characteristic frequencies and then specifying several frequency regions, which would be useful for meeting given MSTL specifications. Furthermore, the propagation characteristics of MSTLs have been analyzed; unwanted higher-order modes have been briefly discussed, which are suppressed effectively by the proposed microstrip-to-MSTL tapered transition to sustain a pure mode operation. The comparison between the frequency characteristics of MSTLs and conventional transmission media has indicated

that MSTLs are capable of supporting low-loss and low-dispersion transmission of ultra-broadband signals. This work has also revealed the possibility to realize other frequency-enabled mode conversions among other modes (such as CPW mode and waveguide mode) in consideration of mode-selectivity conditions, paving the way of the subsequent evolutions of MSTL.

To achieve an in-depth physical understanding of how the frequency-enabled mode conversion occurs in the MSTL, we have performed an approximate theoretical analysis in Chapter 5. The longitudinally uniform MSTL has been treated as a coupled-mode system that consists of one microstrip line and two HM-SIWs and has been investigated by the joint coupled- and normal-mode analysis. It has been found that a large change in the coupling coefficient with frequency causes a significant field spreading from the individual microstrip line to HM-SIWs. A direct result is that the dominant mode of MSTL undergoes a shape or modal evolution, from resembling a quasi-TEM microstrip mode to a quasi-TE_{10} waveguide mode as frequency increases. Excellent agreement between the approximate fields (analytical solutions) and the exact fields (full-wave solutions) affirms the correctness and effectiveness of the theoretical analysis of MSTL. The final parametric study of MSTL has provided helpful information for MSTL design considerations.

Although the special mode selectivity offers MSTL many advantages, it also presents a technical challenge in the excitation of the variable dominant mode. Chapter 6 has focused on a specific excitation scheme for MSTL, which has been explained by comparison with a CBCPW. A tapered transition between CBCPW and MSTL has been presented to produce this excitation, whose operation has been analyzed from the point of view of mode coupling between local normal modes. The design considerations and modal evolution have been presented, together with physical mechanisms and explanations. The tapered transition has a simple tapered structure and is easy to implement. It facilitates the experimental characterization and practical circuit integration of MSTL. Another function of this taper is to effectively suppress undesired higher-order modes to sustain a high-quality pure mode operation.

Finally, we have introduced another synthesized waveguide in Chapter 7 for transmitting and manipulating picosecond ultrafast electrical pulses. This waveguide has demonstrated record guided-wave controlling capabilities including eigenmode reshaping, polarization rotation, loss reduction, and dispersion improvement. To exhibit the potential and generality of this technology, we have showcased two waveguide designs operating in different frequency ranges (dc to 67 GHz

and dc to 300 GHz). This synthesized waveguide is highly scalable, possibly extending its applicability to frequencies beyond 1 THz and even to optical frequencies (i.e., picosecond or subpicosecond pulse bandwidth). Despite the conspicuous superiority of the presented waveguide technology, certainly, its practical application still requires future efforts on the excitation of the variable dominant mode and on the suppression of undesired modes.

9.2 Future work

This research work offers new horizons for future developments of ultra-broadband signal transmission and applications; synthesized waveguide technologies and applications would become an important research topic. Despite the high performance of the presented synthesized waveguides, their practical applications may require future efforts on the following aspects:

- It is necessary to further optimize or redesign the feed lines of synthesized waveguides to efficiently excite the frequency-varying dominant mode of interest and to suppress undesired modes over the ultra-broad bandwidth of operation. In the current research, tapered transitions are used to provide the specific mode excitation. The tapers must have a length of many wavelengths for meeting the adiabatic invariance condition, thus resulting in a large circuit size and high additional loss.
- A more comprehensive and rigorous analysis of the synthesized waveguides is required to guide future design improvements and applications. This work has used the joint normal- and coupled-mode theory to analyze the modal behavior of the presented waveguides, providing a rather straightforward physical explanation of the mode-selectivity phenomenon. Nevertheless, this is an approximate analysis; more rigorous modeling and treatment such as spectral domain analysis are still needed. In addition, systematic parametric studies are meaningful to provide preliminary guidance in the design of synthesized waveguides.
- It is worth exploring multilayered waveguide designs that are expected to achieve better performance such as wider operating bandwidth, lower transmission loss, and improved frequency dispersion. In this work, attempt has been made to improve frequency dispersion by loading an additional thin superstrate (see Chapter 7). This is a simple and

straightforward realization of multilayered synthesized waveguide whose superior performance has indicated that multilayered designs would be a promising research direction towards high-quality ultra-broadband-signal guidance.

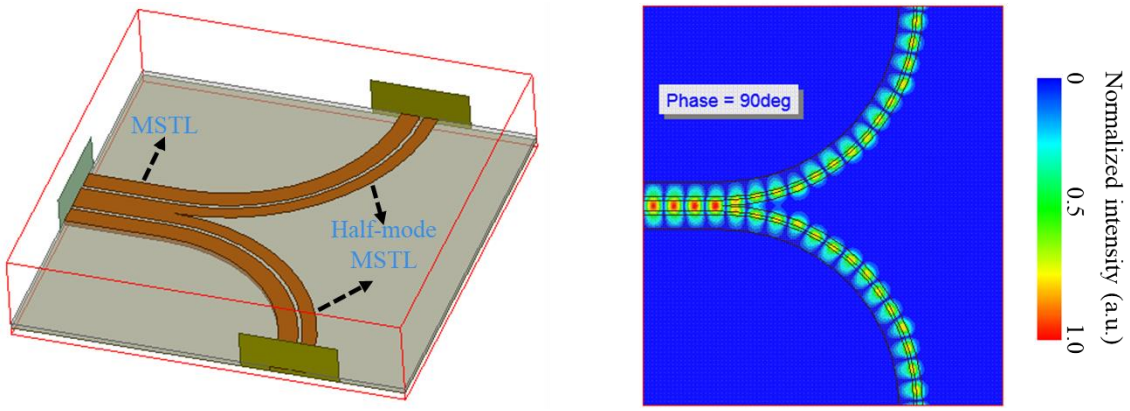

(a) (b)

Figure 9.1 (a) Schematic of MSTL-based power divider and (b) electric field distributions

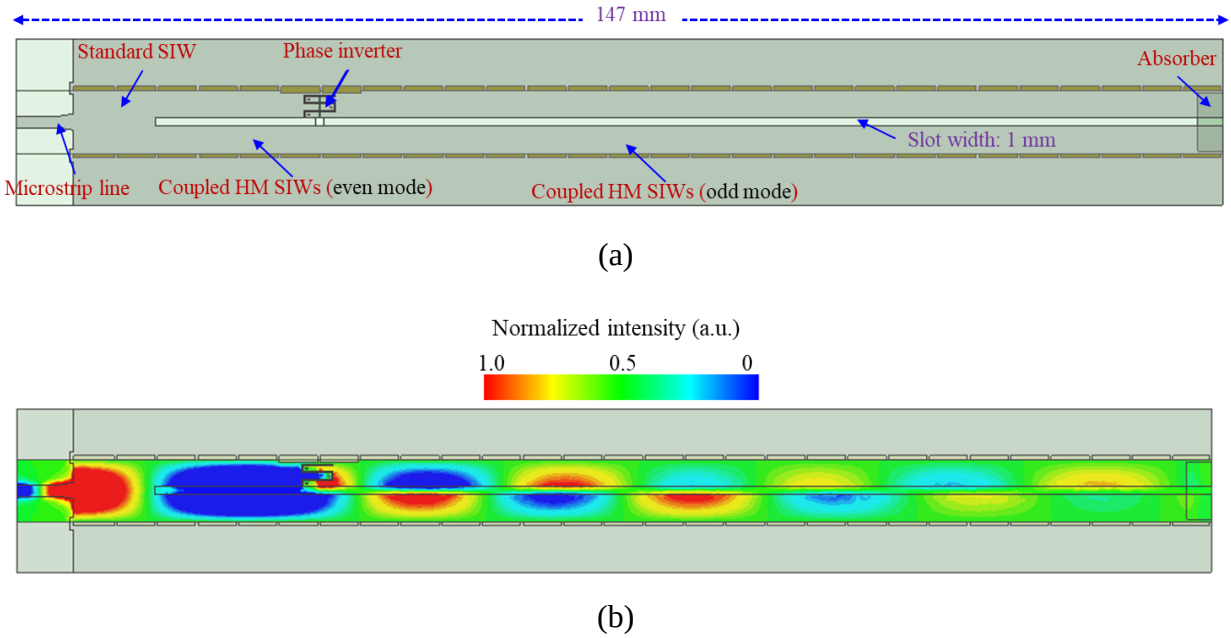

(a)

(b)

Figure 9.2 (a) Schematic of coupled-waveguide-based leaky-wave antenna and (b) electric field distributions

- Based on the presented synthesized waveguides, wideband or multiband passive components such as power dividers, filters, and antennas are possible to realize, which would have huge application potentials in wideband circuits and systems. Several ideas have been conceived, including MSTL-based power divider (Fig. 9.1) and coupled-waveguide leaky-wave antenna (Fig. 9.2); preliminary results have revealed many advantages over their counterparts. Continuous efforts need to be devoted to further improving the structures and exploring more wideband designs.
- Another promising research topic would be the monolithic integration of photonic devices (such as photodiode and photoconductive switch) and the synthesized waveguides to generate reliable guided ultrafast pulses. It involves cutting-edge THz/optical technologies in photonics and electronics, including semiconductor materials, accurate numerical modeling, and advanced fabrication and measurement techniques. Synthesized waveguides such as MSTL have shown advantages of transmitting ultra-broadband waves; photodiode (or photoconductive switch) is promising to generate such ultrafast signals. Their compact integration (Fig. 9.3) would be useful for applications in integrated chip-scale THz systems.

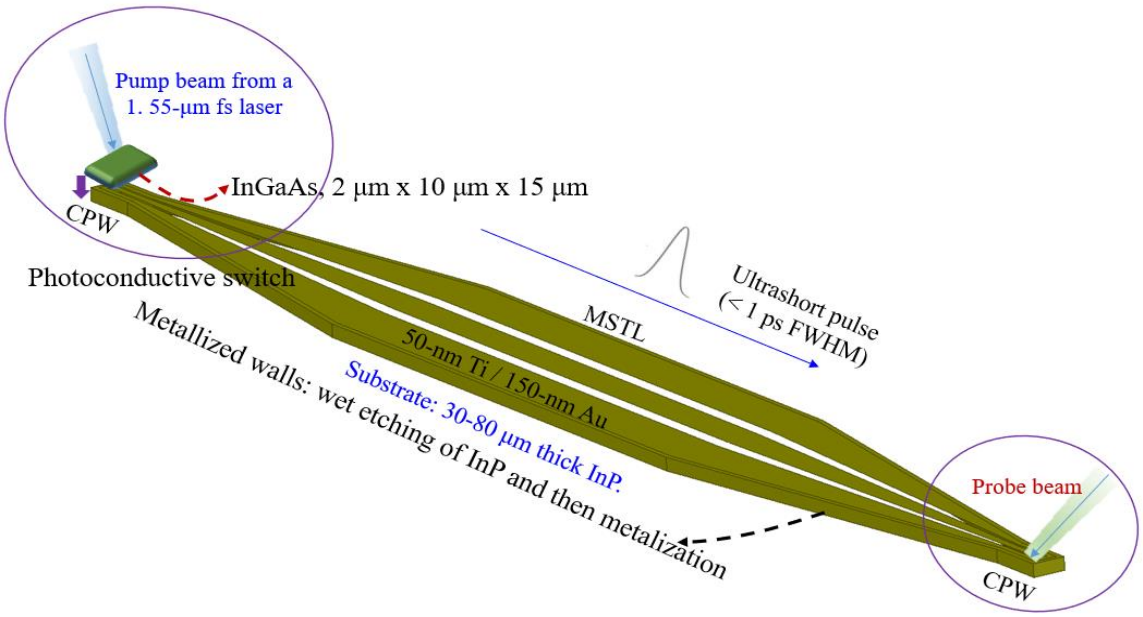

Figure 9.3 Schematic of integrated photodiode and MSTL for generation and guidance of ultrashort pulses

REFERENCES

[1] S. Laurette, A. Treizebre, and B. Bocquet, “Corrugated Goubau lines to slow down and confine THz waves,” *IEEE Trans. THz Sci. Technol*., vol. 2, no. 3, pp. 340–344, May 2012.

[2] Y. Liang, H. Yu, H. C. Zhang, C. Yang, and T. J. Cui, “On-chip sub-terahertz surface plasmon polariton transmission lines in CMOS,” *Sci. Rep.*, vol. 5, Oct. 2015, Art. no. 14853.

[3] M. Ahmadi-Boroujeni, K. Altman, B. Scherger, C. Jansen, M. Shahabadi, and M. Koch, “Terahertz parallel-plate ladder waveguide with highly confined guided modes,” *IEEE Trans. THz Sci. Technol.*, vol. 3, no. 1, pp. 87–95, Jan. 2013.

[4] A. Malekabadi, S. Charlebois, D. Deslandes, and F. Boone, “High-resistivity silicon dielectric ribbon waveguide for single-mode low-loss propagation at F/G-bands,” *IEEE Trans. THz Sci. Technol*., vol. 4, no. 4, pp. 447–453, Jul. 2014.

[5] Z. Wu, W.-R. Ng, M. E. Gehm, and H. Xin, “Terahertz electromagnetic crystal waveguide fabricated by polymer jetting rapid prototyping,” *Opt. Exp*., vol. 19, no. 5, pp. 3962–3972, Feb. 2011.

[6] M. D’Auria *et al*., “3-D printed metal-pipe rectangular waveguides,” *IEEE Trans. Compon., Packag., Manuf. Technol*., vol. 5, no. 9, Sep. 2015.

[7] K. Wu, M. Bozzi, and N. J. G. Fonseca, ‘‘Substrate integrated transmission lines: Review and applications,’’ *IEEE J. Microw*., vol. 1, no. 1, pp. 345–363, Jan. 2021.

[8] Y. Yang *et al*., “Terahertz topological photonics for on-chip communication,” *Nature Photon.*, vol. 14, no. 7, pp. 446–451, Jul. 2020.

[9] Y. Li and N. Engheta, “Supercoupling of surface waves with ε-near-zero metastructures,” *Phys. Rev. B*, vol. 90, no. 20, Nov. 2014, Art. no. 201107.

[10] F. Fesharaki, “Integrated guided-wave structures and techniques for millimeter-wave and terahertz electronics and photonics,” Ph.D. dissertation, Dept. Elect. Eng., Polytechnique Montreal, Montreal, QC, 2016.

[11] L. Xu, H. Sjoland, M. Tormanen, T. Tired, T. Pan, and X. Bai, “A miniaturized Marchand balun in CMOS with improved balance for millimeter-wave applications,” *IEEE Microw. Wireless Compon. Lett*., vol. 24, no. 1, pp. 53-55, Jan. 2014.

[12] K. W. Hamed, A. P. Freundorfer, and Y. M. M. Antar, “A monolithic double-balanced direct conversion mixer with an integrated wideband passive balun,” *IEEE J. Solid-State Circuits*, vol. 40, no. 3, pp. 622-629, Mar. 2005.

[13] K. S. Ang, I. D. Robertson, K. Elgaid, and I. G. Thayne, “40 to 90 GHz impedance-transforming CPW Marchand balun,” in *IEEE MTT-S Int. Microw. Symp. Dig.*, Jun. 2000, pp. 1141-1144.

[14] J. L. Chen, S. F. Chang, and B. Y. Laue, "A 20-40 GHz monolithic doubly-balanced mixer using modified planar Marchand baluns," in *Proc. Asia Pacific Microw. Conf*., Dec. 2001, vol. 1, pp. 131-134.

[15] T. Zhang, L. Li, Z. Zhu, and T. J. Cui, "A broadband planar balun using aperture-coupled microstrip-to-SIW transition," *IEEE Microw. Wireless Compon. Lett*., vol. 29, no. 8, pp. 532-534, Aug. 2019.

[16] J. Moghaddasi and K. Wu, "Hybrid structure-based broadband field-rotation balun for millimeter-wave applications," in *IEEE MTT-S Int. Microw. Symp. Dig.*, May 2015, pp. 1-3.

[17] K. Wu, Y. J. Cheng, T. Djerafi, and W. Hong, "Substrate-integrated millimeter-wave and terahertz antenna technology," *Proc. IEEE*, vol. 100, no. 7, pp. 2219-2232, Jul. 2012.

[18] Q. Lai, C. Fumeaux, W. Hong, and R. Vahldieck, "Characterization of the propagation properties of the half-mode substrate integrated waveguide," *IEEE Trans. Microw. Theory Techn*., vol. 57, no. 8, pp. 1996-2004, Aug. 2009.

[19] Z. Y. Zhang and K. Wu, "Broadband half-mode substrate integrated waveguide (HMSIW) Wilkinson power divider," in *IEEE MTT-S Int. Microw. Symp. Dig.*, June 2008, pp. 879-882.

[20] G. F. Cheng and C. K. C. Tzuang, "A differentially excited coupled half-width microstrip leaky EH_1 mode antenna," *IEEE Trans. Antennas Propag*., vol. 61, no. 12, pp. 5885-5892, Dec. 2013.

[21] B. C. Wadell, *Transmission Line Design Handbook*. Norwood, MA, USA: Artech House, 1991, pp. 181-252.

[22] E. Marom, O. G. Ramer, and S. Ruschin, "Relation between normal-mode and coupled-mode analyses of parallel waveguides," *IEEE J. Quantum Electron.*, vol. 20, no. 12, pp. 1311-1319, Dec. 1984.

[23] P. Wu, J. Liu, and Q. Xue, "Wideband excitation technology of TE_{20} mode substrate integrated waveguide (SIW) and its applications," *IEEE Trans. Microw. Theory Techn*., vol. 63, no. 6, pp. 1863-1874, June 2015.

[24] R. Saleh *et al*., "System-on-chip: reuse and integration," *Proc. IEEE*, vol. 94, no. 6, pp. 1050-1069, Jul. 2006.

[25] J. W. Holloway, L. Boglione, T. M. Hancock, and R. Han, "A fully integrated broadband sub-mmwave chip-to-chip interconnect," *IEEE Trans. Microw. Theory Techn.*, vol .65, no. 7, pp. 2373-2386, Jul. 2017.

[26] E. Mortazy, X. Zhang, M. Chaker, and K. Wu, "Mode coupling between substrate integrated waveguide and coplanar waveguide for traveling-wave electrooptical modulator," *IEEE Trans. Microw. Theory Techn.*, vol. 59, no. 5, pp. 1258-1264, May 2011.

[27] J. Capmany and D. Novak, "Microwave photonics combines two worlds," *Nature Photon.*, vol. 1, no. 6, pp. 319-330, 2007.

[28] M. Tonouchi, “Cutting-edge terahertz technology,” *Nature Photon.,* vol. 1, no. 2, pp. 97-105, 2007.

[29] G. Gallot, S. P. Jamison, R. W. McGowan, and D. Grischkowsky, “Terahertz waveguides,” *J. Opt. Soc. Amer. B,* vol. 17, no. 5, pp. 851-863, May 2000.

[30] O. Mitrofanov, R. James, F. A. Fernández, T. K. Mavrogordatos, and J. A. Harrington, “Reducing transmission losses in hollow THz waveguides,” *IEEE Trans. THz Sci. Technol.,* vol. 1, no. 1, pp. 124-132, Sep. 2011.

[31] D. Deslandes and K. Wu, “Accurate modeling, wave mechanisms, and design considerations of a substrate integrated waveguide,” *IEEE Trans. Microw. Theory Techn.,* vol. 54, no. 6, pp. 2516-2526, June 2006.

[32] S. Atakaramians, S. Afshar, T. M. Monro, and D. Abbott, “Terahertz dielectric waveguides,” *Adv. Opt. Photon.,* vol. 5, no. 2, pp. 169-215, 2013.

[33] C. Yeh and F. Shimabukuru, *The Essence of Dielectric Waveguides*. New York: Springer-Verlag, 2008.

[34] N. Dolatsha, C. Chen, and A. Arbabian, “Loss and dispersion limitations in mm-wave dielectric waveguides for high-speed links,” *IEEE Trans. THz Sci. Technol.,* vol. 6, no. 4, pp. 637-640, Jul. 2016.

[35] C. P. Wen, “Coplanar waveguide: a surface strip transmission line suitable for nonreciprocal gyromagnetic device applications,” *IEEE Trans. Microw. Theory Techn.,* vol. MTT-17, no. 12, pp. 1087-1090. Dec.1969.

[36] R. W. Jackson, “Consideration in the use of coplanar waveguide for millimeter-wave integrated circuits,” *IEEE Trans. Microw. Theory Techn.,* vol. MTT-34, no. 12, pp. 1450-1456. Dec. 1986.

[37] H.-M. Heiliger *et al.*, “Low-dispersion thin-film microstrip lines with cyclotene (benzocyclobutene) as dielectric medium,” *Appl. Phys. Lett.,* vol. 70, no. 17, pp. 2233-2235, 1997.

[38] A. D. Fund *et al.*, “Metal layer losses in thin-film microstrip on LTCC,” *IEEE Trans. Compon., Packag., Manuf. Technol.,* vol. 4, no. 12, pp. 1956-1962, Dec. 2014.

[39] J. Kim and H. H. Park, “A novel IC-stripline design for near-field shielding measurement of on-board metallic cans,” *IEEE Trans. Electromagn. Compat.,* vol. 59, no. 2, pp. 710-716, Apr. 2017.

[40] F. David, M. Chatras, C. Dalmay, L. Lapierre, L. Carpentier, and P. Blondy, “Surface-micromachined rectangular micro-coaxial lines for sub-millimeter-wave applications,” *IEEE Microw. Wireless Compon Lett.,* vol. 26, no. 10, pp. 756-758, Oct. 2016.

[41] D. M. Pozar, *Microwave Engineering*. New York: Wiley, 2012, ch. 3.

[42] R. Mendis and D. Grischkowsky, “THz interconnect with low-loss and low-group velocity dispersion,” *IEEE Microw. Wireless Compon Lett.,* vol. 11, no. 11, pp. 444-446, Nov. 2001.

[43] R. Mendis and D. Grischkowsky, "Undistorted guided-wave propagation of subpicosecond terahertz pulses," *Opt. Lett.,* vol. 26, no. 11, pp. 846-848, 2001.

[44] K. Wang and D. M. Mittleman, "Metal wires for terahertz wave guiding," *Nature,* vol. 432, no. 7015, pp. 376-379, Nov. 2004.

[45] K. Wang and D. M. Mittleman, "Guided propagation of terahertz pulses on metal wires," *J. Opt. Soc. Amer. B, Opt. Phys.,* vol. 22, no. 9, pp. 2001-2008, 2005.

[46] F. Fesharaki, T. Djerafi, M. Chaker, and K. Wu, "Mode-selective transmission line for DC-to-THz super-broadband operation," in *IEEE MTT-S Int. Microw. Symp. Dig.*, San Francisco, May 2016, pp. 1-4.

[47] F. Fesharaki, T. Djerafi, M. Chaker, and K. Wu, "Low-loss and low-dispersion transmission line over DC-to-THz spectrum," *IEEE Trans. THz Sci. Technol.,* vol. 6, no. 4, pp. 611-618, June 2016.

[48] F. Fesharaki, T. Djerafi, M. Chaker, and K. Wu, "Guided-wave properties of mode-selective transmission line," *IEEE Access,* vol. 6, pp. 5379-5392, 2018.

[49] D. Deslandes and K. Wu, "Integrated microstrip and rectangular waveguide in planar form," *IEEE Microw. Wireless Compon Lett.,* vol. 11, no. 2, pp. 68-70, Feb. 2001.

[50] R. S. Fan and R. B. Hooker, "Tapered polymer single-mode waveguides for mode transformation," *J. Lightwave Technol.,* vol. 17, no. 3, pp. 466-474, Mar. 1999.

[51] M. Thumm, "Modes and mode conversion in microwave devices," in *Generation and Application of High Power Microwaves,* R. A. Cairns and A. D. R. Phelps, Eds. Bristol, U.K.: IOP, 1997, pp. 121-171.

[52] J. Liu, R. Mendis, and D. M. Mittleman, "The transition from a TEM-like mode to a plasmonic mode in parallel-plate waveguides," *Appl. Phys. Lett.,* vol. 98, no. 23, Jun. 2011, Art. no. 231113.

[53] D. Wang, F. Fesharaki, and K. Wu, "Physical evidence of mode conversion along mode-selective transmission line," in *IEEE MTT-S Int. Microw. Symp. Dig.,* June 2017, pp. 491-494.

[54] A. Patrovsky, M. Daigle, and K. Wu, "Coupling mechanism in hybrid SIW-CPW forward couplers for millimeter-wave substrate integrated circuits," *IEEE Trans. Microw. Theory Techn.,* vol. 56, no. 11, pp. 2594-2601, Nov. 2008.

[55] J. Guo, T. Djerafi, and K. Wu, "Mode composite waveguide," *IEEE Trans. Microw. Theory Techn.,* vol. 64, no. 10, pp. 3187-3197, Oct. 2016.

[56] J. A. Deibel, M. Escarra, N. Berndsen, K. Wang, and D. M. Mittleman, "Finite-element method simulations of guided wave phenomena at terahertz frequencies," *Proc. IEEE,* vol. 95, no. 8, pp. 1624-1640, Aug. 2007.

[57] *ANSYS HFSS products*. Accessed: Jan. 15, 2018. [Online]. Available: http://www.ansys.com/Products/Electronics/ANSYS-HFSS

[58] R. N. Simons, *Coplanar Waveguide Circuits, Components, and Systems*. Hoboken, NJ, USA: Wiley, 2004.

[59] W. H. Haydl, "On the use of vias in conductor-backed coplanar circuits," *IEEE Trans. Microw. Theory Techn.*, vol. 50, no. 6, pp. 1571-1577, Jun. 2002.

[60] G. Leuzzi, A. Silbermann, and R. Sorrentino, "Mode propagation in laterally bounded conductor-backed coplanar waveguides," in *IEEE MTT-S Int. Microw. Symp. Dig.*, May 1983, pp. 393-395.

[61] K. Wu, Y. Xu, R. G. Bosisio, "Theoretical and experimental analysis of channelized coplanar waveguide (CCPW) for wideband applications of integrated microwave and millimeterwave circuits," *IEEE Trans. Microw. Theory Techn.*, vol. 42, no. 9, pp. 1651-1659, Sep. 1994.

[62] A. Sain and K. L. Melde, "Impact of ground via placement in grounded coplanar waveguide interconnects," *IEEE Trans. Compon., Packag., Manuf. Technol.*, vol. 6, no. 1, pp. 136-144, Jan. 2016.

[63] C. C. Tien, C. K. C. Tzuang, S. T. Peng, and C. C. Chang, "Transmission characteristics of finite-width conductor-backed coplanar waveguide," *IEEE Trans. Microw. Theory Techn.*, vol. 41, no. 9, pp. 1616-1624, Sep. 1993.

[64] Y. Shih and T. Itoh, "Analysis of conductor-backed coplanar waveguide," *Electron. Lett*, vol. 18, no. 12, pp. 538-440, June 1982.

[65] M. A. Magerko, L. Fan, and K. Chang, "A discussion on the coupling effects in conductor-backed coplanar waveguide MIC's with lateral sidewalls," in *IEEE MTT-S Int. Microw. Symp. Dig.*, 1993, pp. 947-950.

[66] W. T. Lo *et al*., "Resonant phenomena in conductor-backed coplanar waveguides (CBCPW's)," *IEEE Trans. Microw. Theory Techn.*, vol. 41, no. 12, pp. 2099-2107, Dec. 1993.

[67] H. Shigesawa and M. Tsuji, "Dominant mode power leakage from printed-circuit waveguides," *Radio Sci.*, vol. 26, no. 2, pp. 559-564, Mar./Apr. 1991.

[68] D. Deslandes, "Design equations for tapered microstrip-to-substrate integrated waveguide transitions," in *IEEE MTT-S Int. Microw. Symp. Dig.*, May 2010, pp. 704-707.

[69] A. Suntives and R. Abhari, "Design and application of multimode substrate integrated waveguides in parallel multichannel signaling systems," *IEEE Trans. Microw. Theory Techn.*, vol. 57, no. 6, pp. 1563-1571, Jun. 2009.

[70] R. Garg, I. Bahl, and M. Bozzi, *Microstrip Lines and Slotlines*. Artech house, 2013.

[71] A. W. Snyder, "Coupled-mode theory for optical fibers," *J. Opt. Soc. Amer.*, vol. 62, no. 11, pp. 1267-1277, 1972.

[72] J. L. Gomez-Tornero and A. Alvarez-Melcon, "Nonorthogonality relations between complex hybrid modes: an application for the leakywave analysis of laterally shielded top-

open planar transmission lines," *IEEE Trans. Microw. Theory Techn*., vol. 52, no. 3, pp. 760-767, Mar. 2004.

[73] N. K. Das, "Methods of suppression or avoidance of parallel-plate power leakage from conductor-backed transmission lines," *IEEE Trans. Microw. Theory Techn*., vol. 44, pp. 169-181, Feb. 1996.

[74] Y.-W. Hsu and Y.-C. Lin, "Modeling and characterization of slitted parallel-plate waveguide with applications for slit-based planar structures," *IEEE Trans. Microw. Theory Techn.,* vol. 65, no. 7, pp. 2228-2239, Jul. 2017.

[75] Y. H. Chou and S. J. Chung, "Attenuation of the parasitic modes in a shielded microstrip line by coating resistive films on the substrate," *IEEE Trans. Microw. Theory Techn.,* vol. 43, no. 7, pp. 1610-1613, Jul. 1995.

[76] P. Lampariello and A. A. Oliner, "New equivalent networks with simple closed-form expressions for open and slit-coupled E-plane tee junctions," *IEEE Trans. Microw. Theory Techn.,* vol. 41, no. 5, pp. 839-847, May 1993.

[77] H. A. Haus and W. Huang, "Coupled-mode theory," *Proc. IEEE,* vol. 79, no. 10, pp. 1505-1518, Oct. 1991.

[78] T. Sauer, *Numerical Analysis*. Upper Saddle River, NJ: Pearson Educ., 2006, pp. 230-235.

[79] D. Grischkowsky, S. Keiding, M. Van Exter, and C. Fattinger, "Far-infrared time-domain spectroscopy with terahertz beams of dielectrics and semiconductors," *J. Opt. Soc. Amer. B,* vol. 7, no. 10, pp. 2006-2015, Oct. 1990.

[80] Y. Ding and K. Wu, "Substrate integrated waveguide-to-microstrip transition in multilayer substrate," *IEEE Trans. Microw. Theory Techn.,* vol. 55, no. 12, pp. 2839-2844, Dec. 2007.

[81] W. R. Klopfenstein, "A transmission line taper of improved design," *Proc. IRE,* pp. 31-35, June 1956.

[82] R. B. Marks, "A multiline method of network analyzer calibration," *IEEE Trans. Microw. Theory Techn.,* vol. 39, no. 7, pp. 1205-1215, Jul. 1991.

[83] W. R. Eisenstadt and Y. Eo, "S-parameter-based IC interconnect transmission line characterization," *IEEE Trans. Compon. Hybrids Manuf. Technol.,* vol. 15, no. 4, pp. 483-490, Aug. 1992.

[84] S. J. Orfanidis, *Electromagnetic Waves and Antennas*. Piscataway: Rutgers Univ. Press, 2002, ch. 9.

[85] F. Fesharaki, T. Djerafi, M. Chaker, and K. Wu, "High-integrity terabitper-second signal interconnects with mode-selective transmission line," in *IEEE MTT-S Int. Microw. Symp. Dig*., May 2016, pp. 1-4.

[86] D. Wang, F. Fesharaki, and K. Wu, "Longitudinally uniform transmission lines with frequency-enabled mode conversion," *IEEE Access*, vol. 6, pp. 24089-24109, 2018.

[87] F. Fesharaki, T. Djerafi, M. Chaker, and K. Wu, "Mode-selective transmission line for chip-to-chip terabit-per-second data transmission," *IEEE Trans. Compon., Packag., Manuf. Technol.*, vol. 8, no. 7, pp. 1272-1280, Jul. 2018.

[88] J. M. Perez-Escudero, A. E. Torres-Garcia, R. Gonzalo, and I. Ederra, "A chebyshev transformer-based microstri-to-groove-gap-waveguide inline transition for MMIC packaging," *IEEE Trans. Compon., Packag., Manuf. Technol*., vol. 9, no. 8, pp. 1595-1602, Aug. 2019.

[89] M. Daigle and K. Wu, "Photoimageable thick-film micro-coaxial line for DC-to-millimeter-wave broad band applications," *IEEE Trans. Compon., Packag., Manuf. Technol*., vol. 4, no. 1, pp. 117-122, Jan. 2014.

[90] D. Wang and K. Wu, "Mode-selective transmission line—part II: Excitation scheme and experimental verification," submitted to *IEEE Trans. Compon., Packag., Manuf. Technol*., June 2020.

[91] W. K. Burns and A. F. Milton, "Waveguide transitions and junctions," in *Guided-Wave Optoelectronics*, T. Tamir, Ed. Berlin, Germany: Springer-Verlag, 1988, pp. 89-144.

[92] W.-P. Huang, "Coupled-mode theory for optical waveguides: An overview," *J. Opt. Soc. Amer. A, Opt. Image Sci*., vol. 11, no. 3, pp. 963-983, March 1994.

[93] W. H. Louisell, "Analysis of the single tapered mode coupler," *Bell Syst. Tech. J*., vol. 34, pp. 853-870, Jul. 1955.

[94] W. K. Burns, "Normal mode analysis of waveguide devices. Part I: Theory," *J. Lightw. Technol*., vol. 6, no. 6, pp. 1051-1057, Jun. 1988.

[95] N. Nguyen-Trong and C. Fumeaux, "Half-mode substrate-integrated waveguides and their applications for antenna technology: A review of the possibilities for antenna design," *IEEE Antennas Propag. Mag*., vol. 60, no. 6, pp. 20-31, Dec. 2018.

[96] D. Wang and K. Wu, "Propagation characteristics of mode-selective transmission line," in *IEEE MTT-S Int. Microw. Symp. Dig.*, June 2018, pp. 1057-1060.

[97] W. Jiang, X.-D. Cai, B. Sen, and G. Wang, "Equation-based solutions to coupled, asymmetrical, lossy, and nonuniform microstrip lines for tabrouting applications," *IEEE Trans. Electromagn. Compat*., vol. 61, no. 2, pp. 548-557, Apr. 2019.

[98] B. Snyder and P. O'Brien, "Packaging process for grating-coupled silicon photonic waveguides using angle-polished fibers," *IEEE Trans. Compon., Packag., Manuf. Technol*., vol. 3, no. 6, pp. 954-959, Jun. 2013.

[99] N. K. Das and D. M. Pozar, "Full-wave spectral-domain computation of material radiation and guided wave losses in infinite multilayered printed transmission lines," *IEEE Trans. Microw. Theory Techn*., vol. 39, no. 1, pp. 54-63, Jan. 1991.

[100] A. A. Oliner, "Types and basic properties of leaky modes in microwave and millimeter-wave integrated circuits," *IEICE Trans. Electron*., vol. E83-C, no. 5, pp. 675-686, May 2000.

[101] K. Okamoto, *Fundamentals of Optical Waveguides*. 2nd ed. Burlington, MA, USA: Elsevier, 2006, pp. 159-168.

[102] A. Hardy and W. Streifer, "Coupled mode theory of parallel waveguides," *J. Lightwave Technol.*, vol. LT-3, no. 5, pp. 1135-1146, Oct. 1985.

[103] W. K. Bums and A. F. Milton, "3 × 2 channel-waveguide gyroscope couplers: Theory," *IEEE Trans. Microw. Theory Techn*., vol. 30, no. 10, pp. 1778-1784, Oct. 1982.

[104] R. N. Simons, *Coplanar Waveguide Circuits, Components, and Systems*. Hoboken, NJ, USA: Wiley, 2001, ch. 3.

[105] L. Carin, G. W. Slade, K. J. Webb, and A. A. Oliner, "Packaged printed transmission lines: Modal phenomena and relation to leakage," in *IEEE MTT-S Int. Microw. Symp. Dig.*, June 1993, pp.1195-1198.

[106] D. Nghiem, J. T. Williams, D. R. Jackson, and A. A. Oliner, "Existence of a leaky dominant mode on microstrip line with an isotropic substrate: Theory and measurement," *IEEE Trans. Microw. Theory Techn*., vol. 44, pp. 1710-1715, Dec. 1996.

[107] S.-J. Kim, H.-S. Yoon, and H.-Y. Lee, "Suppression of leakage resonance in coplanar MMIC packages using a Si submount layer," *IEEE Trans. Microw. Theory Techn*., vol. 48, no. 12, pp. 2664-2669, Dec. 2000.

[108] T. Rozzi and M. Mongiardo, *Open Electromagnetic Waveguides*, London, U.K.: Inst. Elect. Eng., 1997.

[109] Robert E. Collin, *Foundations for Microwave Engineering*, 2nd ed. Hoboken, NJ, USA: Wiley, 2001, pp. 117-125.

[110] S. Ishino and S. Matsumoto, "Waveguide structure compatible with TE, TM, and TEM modes," in *Proc. Asia–Pacific Microw. Conf. (APMC)*, Nov. 2018, pp. 309-311.

[111] S.-L. Chuang, "A coupled-mode formulation by reciprocity and a variational principle," *J. Lightw. Technol*., vol. 5, no. 1, pp. 5-15, Jan. 1987.

[112] D. Wang and K. Wu, "Mode-selective transmission line—part I: Theoretical foundation and physical mechanism," *IEEE Trans. Compon., Packag., Manuf. Technol*., vol. 10, no. 12, pp. 2072-2086, Dec. 2020.

[113] Y. Shao, X.-C. Li, N. Wang, L.-S. Wu, M. Tang, and J.-F. Mao, "Theoretical and experimental investigation of HMSIW-based high-speed data transmission system using QPSK scheme," *IEEE Trans. Compon., Packag., Manuf. Technol*., vol. 8, no. 11, pp. 1938-1947, Nov. 2018.

[114] G. L. Matthaei, L. Young, and E. M. T. Jones, *Microwave Filters, Impedance-Matching Networks, and Coupling Structures*. Norwood, NJ, USA: Artech House, 1980.

[115] N. Ghassemi, I. Boudreau, D. Deslandes, and K. Wu, "Millimeter-wave broadband transition of substrate integrated waveguide on high-to-low dielectric constant substrates," *IEEE Trans. Compon., Packag., Manuf. Technol*., vol. 3, no. 10, pp. 1764-1770, Oct. 2013.

[116] M. Moallem, J. East, and K. Sarabandi, “A broadband, micromachined rectangular waveguide to cavity-backed coplanar waveguide transition using impedance-taper technique,” *IEEE Tran. THz Sci. Technol*., vol. 4, no. 1, pp. 49-55, Jan. 2014.

[117] S. Cogollos, J. Vague, V. E. Boria, and J. D. Martínez, “Novel planar and waveguide implementations of impedance matching networks based on tapered lines using generalized superellipses,” *IEEE Trans. Microw. Theory Techn*., vol. 66, no. 4, pp. 1874-1884, Apr. 2018.

[118] I. Wolf, *Coplanar Microwave Integrated Circuits*. Hoboken, NJ, USA: Wiley, 2006.

[119] A. F. Milton and W. K. Burns “Tapered velocity couplers for integrated optics: Design,” *Appl. Optics*., vol. 14, no. 5, pp. 1207-1212, May 1975.

[120] H. S. Kim and R. V. Ramaswamy, “Tapered, both in dimension and in index velocity coupler: Theory and experiment,” *IEEE J. Quantum Electron.*, vol. 29, no. 4, pp. 1158-1167, Apr. 1993.

[121] G. M. Jeronimo, S. C. Sejas-Garcia, and R. Torres-Torres, “Modeling and parameter extraction for the metal surface roughness loss effect on substrate integrated waveguides from S-parameters,” *IEEE Trans. Microw. Theory Techn*., vol. 66, no. 2, pp. 875-882, Feb. 2018.

[122] F. Mesa, C. Di-Nallo, and D. R. Jackson, “The theory of surface-wave and space-wave leaky-mode excitation on microstrip lines,” *IEEE Trans. Microw. Theory Techn*., vol. 47, no. 2, pp. 207-215, Feb. 1999.

[123] H. Shigesawa, M. Tsuji, and A. A. Oliner, “Simultaneous propagation of bound and leaky dominant modes on printed-circuit lines: A new general effect,” *IEEE Trans. Microw. Theory Techn*., vol. 43, no. 12, pp. 3007-3019, Dec. 1995.

[124] M. Riaziat, R. Majidi-Ahy, and I.-J. Feng, “Propagation modes and dispersion characteristics of coplanar waveguides,” *IEEE Trans. Microw. Theory Techn*., vol. 38, no. 3, pp. 245-251, Mar. 1990.

[125] W. K. Burns and A. F. Milton, “Mode conversion in planar dielectric separating waveguides,” *IEEE J. Quantum Electron*., vol. QE-l1, no. 1, pp. 32-39, Jan. 1975.

[126] A. G. Fox, “Wave coupling by warped normal modes,” *Bell Syst. Tech. J.*, vol. 34, pp. 823-852, Jul. 1955.

[127] D. Marcuse, “Radiation losses of tapered dielectric slab waveguides,” *Bell Sys. Tech. J*., vol. 49, pp. 273-290, 1970.

[128] B. Youzkatli El Khatib, T. Djerafi, and K. Wu, “Substrate-integrated waveguide vertical interconnects for 3-D integrated circuits,” *IEEE Trans. Compon., Packag., Manuf. Technol*., vol. 2, no. 9, pp. 1526-1535, Sep. 2012.

[129] M. Bozzi, A. Georgiadis, and K. Wu, “Review of substrate-integrated waveguide circuits and antennas,” *IET Microw., Antennas Propag*., vol. 5, no. 8, pp. 909-920, Jun. 2011.

[130] K.-S. Chin, C.-C. Chang, C.-H. Chen, Z. Guo, D. Wang, and W. Che, "LTCC multilayered substrate-integrated waveguide filter with enhanced frequency selectivity for system-in-package applications," *IEEE Trans. Compon., Packag., Manuf. Technol*., vol. 4, no. 4, pp. 664-672, Apr. 2014.

[131] W. Xu, K. Ma, S. Xu, and Y. Wang, "Ka-band SISL-to-AFSIW transitions with fabrication tolerance characteristics," *IEEE Trans. Compon., Packag., Manuf. Technol*., vol. 9, no. 10, pp. 2097-2103, Oct. 2019.

[132] M. D. Janezic and J. A. Jargon, "Complex permittivity determination from propagation constant measurements," *IEEE Microw. Guided Wave Lett.*, vol. 9, no. 2, pp. 76-78, Feb. 1999.

[133] F. Xu and K. Wu, "Guided-wave and leakage characteristics of substrate integrated waveguide," *IEEE Trans. Microw. Theory Techn*., vol. 53, no. 1, pp. 66-73, Jan. 2005.

[134] C. Elachi, "Waves in active and passive periodic structures: A review," *Proc. IEEE*, vol. 64, pp. 1666-1698, Dec. 1976.

[135] E. Abaei, E. Mehrshahi, and H. Sadreazami, "The influence of periodic discontinuities on propagation characteristic of substrate integrated waveguide," in *Proc. IEEE Asia–Pacific Conf. Appl. Electromagn. (APACE)*, Nov. 2010, pp. 1-4.

[136] P. G. Huray, *The Foundations of Signal Integrity*, Hoboken, NJ, USA: Wiley, 2009, ch. 6.

[137] R.-L. Wang, Y.-K. Su, and C.-J. Chen, "Transmission performances of CPW lines on a laser-crystallization polysilicon passivated high-resistivity silicon substrate," *IEEE Trans. Compon., Packag., Manuf. Technol*., vol. 2, no. 5, pp. 847-851, May 2012.

[138] M. S. Hilario *et al*., "W-band complex permittivity measurements at high temperature using free-space methods," *IEEE Trans. Compon., Packag., Manuf. Technol*., vol. 9, no. 6, pp. 1011-1019, Jun. 2019.

[139] L. Jing, W. Wang, Z. Li, and R. Murch, "Detecting impedance and shunt conductance faults in lossy transmission lines," *IEEE Trans. Antennas Propag*., vol. 66, no. 7, pp. 3678-3689, Jul. 2018.

[140] N. Li, B. Zhang, Y. He, and Y. Luo, "Sub-picosecond nanodiodes for low-power ultrafast electronics," *Adv. Mater*., vol. 33, 2021, Art. no. 2100874.

[141] M. Samizadeh Nikoo *et al*., "Nanoplasma-enabled picosecond switches for ultrafast electronics," *Nature*, vol. 579, pp. 534–539, 2020.

[142] Y. Yang *et al*., "Ultrafast magnetization reversal by picosecond electrical pulses," *Sci. Adv*., vol. 3, no. 11, Nov. 2017, Art. no. e1603117.

[143] B. Ferguson and X.-C. Chang, "Materials for terahertz science and technology," *Nature Mater*., vol. 1, pp. 26–33, 2002.

[144] T. L. Cocker, D. Peller, P. Yu, J. Repp, and R. Huber, "Tracking the ultrafast motion of a single molecule by femtosecond orbital imaging," *Nature*, vol. 539, pp. 263–267, 2016.

[145] M. Kahrs, "50 years of RF and microwave sampling," *IEEE Trans. Microw. Theory Techn.*,

vol. 51, no. 6, pp. 1787–1805, Jun. 2003.

[146] S. Koenig *et al*., "Wireless sub-THz communication system with high data rate," *Nature Photon*., vol. 7, pp. 977–981, Oct. 2013.

[147] P. H. Siegel, "Terahertz technology in biology and medicine," *IEEE Trans. Microw. Theory Techn*., vol. 52, no. 10, pp. 2438–2447, 2004.

[148] K. Jhuria *et al*., "Spin–orbit torque switching of a ferromagnet with picosecond electrical pulses," *Nature Electron*., vol. 3, pp. 680–686, 2020.

[149] T. Spencer, T. Osborn, and P. Kohl, "High-frequency chip connections," *Science*, vol. 320, pp. 756–757, 2008.

[150] T. Y. Hsiang *et al*., "Propagation characteristics of picosecond electrical transients on coplanar striplines," *Appl. Phys. Lett*., vol. 51, pp. 1551–1553, 1987.

[151] X. Yu *et al*., "Simultaneous low-loss and low-dispersion in a photonic-crystal waveguide for terahertz communications," *Appl. Phys. Express*, vol. 12, no. 1, 2019, Art. no. 012005.

[152] R. W. McGowan, G. Gallot, and D. Grischkowsky, "Propagation of ultrawideband short pulses of terahertz radiation through submillimeter-diameter circular waveguides," *Opt. Lett*., vol. 24, pp. 1431–1433, 1999.

[153] J. J. Zhang, S. Alexandrou, and T. Y. Hsiang, "Attenuation characteristics of coplanar waveguides at subterahertz frequencies," *IEEE Trans. Microw. Theory Techn.*, vol. 53, no. 11, pp. 3281–3287, Nov. 2005.

[154] H. Roskos *et al*., "Propagation of picosecond electrical pulses on a silicon-based microstrip line with buried cobalt silicide ground plane," *Appl. Phys. Lett*., vol. 58, pp. 2604–2606, Mar. 1991.

[155] S. D. Hogan *et al*., "Driving Rydberg-Rydberg transitions from a coplanar microwave waveguide," *Phys. Rev. Lett*. vol. 108, 2012, Art. no. 063004.

[156] M. Burchett, S. Pennock, and P. Shepherd, "A rigorous analysis of uniform stripline of arbitrary dimensions," *IEEE Trans. Microw. Theory Tec*hn., vol. 41, no. 12, pp. 2074–2080, Dec. 1993.

[157] C. Yeh *et al*., "Communication at millimeter-submillimeter wavelengths using a ceramic ribbon," *Nature*, vol. 404, pp. 584–588, Apr. 2000.

[158] P. Chaisakul *et al*., "Integrated germanium optical interconnects on silicon substrates," *Nature Photon*., vol. 8, pp. 482–488, 2014.

[159] Z. Zhou *et al*., "Substrate-integrated photonic doping for near-zero-index devices," *Nature Commun*., vol. 10, Sep. 2019, Art. no. 4132.

[160] Z. Zhang *et al*., "Manipulation of polarizations for broadband terahertz waves emitted from laser plasma filaments," *Nature Photon*., vol. 12, no. 9, pp. 554–559, Aug. 2018.

[161] F. Lemoult, N. Kaina, M. Fink, and G. Lerosey, "Wave propagation control at the deep subwavelength scale in metamaterials," *Nature Phys*., vol. 9, pp. 55–60, Oct. 2013.

[162] D. S. Chemla, D. A. B. Miller, and S. Schmitt-Rink, "Generation of ultrashort electrical

pulses through screening by virtual populations in biased quantum wells," *Phys. Rev. Lett*., vol. 59, no. 9, pp. 1018–1021, Aug. 1987.

[163] M. Y. Frankel, S. Gupta, J. A. Valdmanis, and G. Mourou, "Terahertz attenuation and dispersion characteristics of coplanar transmission lines," *IEEE Trans. Microw. Theory Techn.*, vol. 39, pp. 910–916, 1991.

[164] Q. Hu and R. P. Joshi, "Transmembrane voltage analyses in spheroidal cells in response to an intense ultrashort electrical pulse," *Phys. Rev. E*, vol. 79, 2009, Art. no. 011901.

[165] I. Liberal, A. M. Mahmoud, and N. Engheta, "Geometry-invariant resonant cavities," *Nature Commun*., vol. 7, Mar. 2016, Art. no. 10989.

[166] A. Anferov *et al.*, "Millimeter-wave four-wave mixing via kinetic inductance for quantum devices," *Phys. Rev. Appl*., vol. 13, Feb. 2020, Art. no. 024056.

[167] C. M. Krowne, "Physics of propagation in left-handed guided wave structures at microwave and millimeter-wave frequencies," *Phys. Rev. Lett*., vol. 92, no. 5, 2004, Art. no. 053901.

[168] R. Han *et al*., "Filling the gap: Silicon terahertz integrated circuits offer our best bet," *IEEE Microw. Mag.*, vol. 20, no. 4, pp. 80–93, Apr. 2019.

[169] See Supplemental Material for additional figures and details of eigenmode analysis, device fabrication, and waveguide characterization.

[170] S. G. Johnson, P. Bienstman, M. Skorobogatiy, M. Ibanescu, E. Lidorikis, and J. Joannopoulos, "Adiabatic theorem and continuous coupled-mode theory for efficient taper transitions in photonic crystals," *Phys. Rev. E*, vol. 66, 2002, Art. no. 066608.

[171] K. Sengupta, T. Nagatsuma, and D. M. Mittleman, "Terahertz integrated electronic and hybrid electronic–photonic systems," *Nature Electron*., vol. 1, no. 12, pp. 622–635, Dec. 2018.

[172] H. Tataria *et al*., "6G wireless systems: Vision, requirements, challenges, insights, and opportunities," *Proc. IEEE*, vo. 169, pp. 1166–1199, 2021.

[173] M. Memarian and G. V. Eleftheriades, "Dirac leaky-wave antennas for continuous beam scanning from photonic crystals," *Nature Commun*., vol. 6, Jan. 2015, Art. no. 5855.

[174] E. Lustig *et al*., "Photonic topological insulator in synthetic dimensions," *Nature*, vol. 567, pp. 356–360, 2019.

[175] I. Carmeli *et al*., "Spatial modulation of light transmission through a single microcavity by coupling of photosynthetic complex excitations to surface plasmons," *Nature Commun*., vol. 6, Jun. 2015, Art. no. 7334.

[176] J. G. N. Rahmeier, V. Tiukuvaara, and S. Gupta, "Complex eigenmodes and eigenfrequencies in electromagnetics," *IEEE Trans. Antennas Propag*., vol. 69, pp. 4644–4656, 2021.

[177] D. Scarlat, S. Ruschin, and D. Brooks, "Experimental characterization of coupled waveguides by normal-mode excitation," *IEEE J. Quantum Electron.*, vol. 33, pp. 1132–

1140, Jul. 1996.

[178] Q. Li, G. Moille, H. Taheri, A. Adibi, and K. Srinivasan, “Improved coupled-mode theory for high-index-contrast photonic platforms,”. *Phys. Rev. A*, vol. 102, 2020, Art. no. 063506.

[179] K. Ogusu and H. Li, “Normal-mode analysis of switching dynamics in nonlinear directional couplers,” *J. Lightw. Technol.*, vol. 31, no. 15, pp. 2639–2646, Aug. 2013.

[180] S. Fregonese, M. Deng, M. D. Matos, C. Yadav, S. Joly, B. Plano, C. Raya, B. Ardouin, and T. Zimmer, “Comparison of on-wafer TRL calibration to ISS SOLT calibration with open-short de-embedding up to 500 GHz,” *IEEE Trans. THz Sci. Technol*., vol. 9, no. 1, pp. 89–97, Jan. 2019.

[181] E. A. Anashkina *et al*., “Single-shot laser pulse reconstruction based on self-phase modulated spectra measurements,” *Sci. Rep*., vol. 6, 2016, Art. no. 33749.

[182] S. Pi, M. Ghadiri-Sadrabadi, J. C. Bardin, and Q. Xia, “Nanoscale memristive radiofrequency switches,” *Nature Commun*., vol. 6, Jun. 2015, Art. no. 7519.

[183] C. Seguinot *et al*., “Multimode TRL—a new concept in microwave measurements: Theory and experimental verification,” *IEEE Trans. Microw. Theory Techn*., vol. 46, no. 5, pp. 536–542, May 1998.

APPENDIX A LIST OF PUBLICATIONS

1. Journal papers:

[1] **D. Wang** and K. Wu, "Synthesized all-pass waveguide for ultrafast electronics towards picosecond transmission and beyond," submitted to *Phys. Rev. Lett.*, Oct. 2021.

[2] C.-M. Liu, S.-Qiu Xiao, **D. Wang**, and K. Wu "Wideband via-loaded cylindrical open-ended SIW cavity antenna," *IEEE Open J. Antennas Propag*., vol. 2, pp. 1001-1019, 2021.

[3] **D. Wang** and K. Wu, "Mode-selective transmission line—part II: Excitation scheme and experimental verification," *IEEE Trans. Compon., Packag., Manuf. Technol*., vol. 11, no. 2, pp. 260-272, Feb. 2021.

[4] **D. Wang** and K. Wu, "Mode-selective transmission line—part I: Theoretical foundation and physical mechanism," *IEEE Trans. Compon., Packag., Manuf. Technol*., vol. 10, no. 12, pp. 2072-2086, Dec. 2020.

[5] **D. Wang**, F. Fesharaki, and K. Wu, "Longitudinally uniform transmission lines with frequency-enabled mode conversion," *IEEE Access,* vol. 6, pp. 24089-24109, Apr. 2018.

2. Conference papers:

[1] **D. Wang** and K. Wu, "Compact wideband coupled-waveguide balun for millimeter-wave applications," in *IEEE Int. Wireless Symp.,* Sep. 2020, pp. 1-3.

[2] **D. Wang** and K. Wu, "Propagation characteristics of mode-selective transmission line," in *IEEE MTT-S Int. Microw. Symp. Dig*., Jun. 2018, pp. 1057-1060.

[3] **D. Wang**, F. Fesharaki, and K. Wu, "Physical evidence of mode conversion along mode-selective transmission line," in *IEEE MTT-S Int. Microw. Symp. Dig.,* Jun. 2017, pp. 491-494.